Study and development of localised surface plasmon resonance based sensors using anisotropic spectroscopy

William L. Watkins

SORBONNE UNIVERSITÉ

CRÉATEURS DE FUTURS
DEPUIS 1257

INSP
INSTITUT DES NANOSCIENCES DE PARIS

SORBONNE UNIVERSITÉ

ÉCOLE DOCTORALE
Physique et chimie des matériaux
ED397

LABORATOIRE - EQUIPE DE RECHERCHE
Institut des nanosciences de Paris
Physico-chimie et dynamique des surfaces

Study and development of localised surface plasmon resonance based sensors using anisotropic spectroscopy

Par M. WILLIAM L. WATKINS

Thèse de doctorat de PHYSICO-CHIMIE

Dirigée par Dr. YVES BORENSZTEIN

Présentée et soutenue publiquement le 8 OCTOBRE 2018

Devant un jury composé de :

Dr. HYND REMITA	Directrice de recherche	LCP - Université Paris Sud	Rapporteur
Dr. LIONEL SIMONOT	Maître de conferences	Pprime - Université de Poitiers	Rapporteur
Dr. RAMDANE BENFERHAT	Directeur de la stratégie	Horiba	Examinateur
Pr. DIDIER GOURIER	Professeur	IRCP - Chimie ParisTech	Examinateur
Pr. CHRISTOPHE PETIT	Professeur	MONARIS - Sorbonne Université	Examinateur
Dr. VIRGINIE PONSINET	Chargée de recherche	CRPP - Université de Bordeaux	Examinateur
Dr. YVES BORENSZTEIN	Directeur de recherche	INSP - Sorbonne Université	Directeur de thèse

À ma grand-mère, Nani…

"Those who cannot do, teach, and those who cannot teach do a PhD."

First thing my grand-dad said when I told him I wanted to be a doctor - Bertram Watkins 2010

Acknowledgements

WRITING THE ACKNOWLEDGEMENTS FOR THIS THREE-YEAR WORK is possibly the most difficult part of this manuscript. Indeed, a lot of people have helped through this accomplishment, and I wish not to forget any of them. Although I know this is not customary, I wish to first send my best regards and thank my mother, Malvina, whom has supported me throughout my university and indeed my PhD. She has especially been very supportive the last few months before my viva whilst I was writing this manuscript. It is without saying that she has made this step much more agreeable hence why I wanted to mention her first.

Needless to say how working with Yves Borensztein, my supervisor, has been enjoyable. His help and guidance were exemplary and made this doctoral journey indeed memorable and exceptional. Regardless of the ups and downs of academic research, the team and relationship we have built enabled us to accomplish the work presented in this thesis. I am glad to say that these last three years I had the best boss one could hope for. Yet academic research is not a one man or two men job and a key character was Sebastien Royer, whom, as a technician has help me throughout the technical challenges of the experimental work. Although most of his work was indispensable, I indeed do feel guilty that, at times, I had requested his help on the fabrication of equipment which I ended up not using. Academic research is not limited to hard work, but also the enjoyment of a great work environment which was the Physico-Chimie et dynamique des surfaces team at INSP. I want to thank Loïc Becerra for helping me in using the clean room as well as Dominique Demaille whom has trained me on the valuable scanning electron microscope allowing me to record high quality images. Generally, I want to thank everyone in the team for welcoming me and being supportive and showing encouragement as well as giving scientific advice when approached.

I am also glad that I was not alone undertaking this work as many PhD candidates were also going through this challenge. This made the atmosphere delightful and very much collaborative as we did help each other out and did take some time off playing cards (after work hours of course). Hence why I want to send my thanks to Alberto Curcella whom has sat on my side throughout these three years. Although an excellent photographic model, I indeed had to help him out a few times such as with the LaTeX template (he indeed waited for me to write it up and sneakily pinched it), or that time when his laptop died whilst he was in the middle of writing his manuscript. Yet the exoticism of this Italian boy enlighten my days through the good and bad. Léo Bossard-Giannesini, on the other hand brought sanity and decency in the office. Throughout the last mile, Léo and I worked around the clock through the month of August which drastically helped motivation wise. I would not dare forget the other students in the lab such as Silvia Pandolfi, Ju-Hyeon Lee, Danilo Longo, Clement Livache, and the-girl-who-speaks-a-lot for their kind support.

I want to send my gratitute to Fabienne Testard from IRAMIS at CEA for the collaborating work with have done on strain gauge sensors, even though it did not appear in this manuscript. I also wish to thank Christian Serre, Antoine Tissot and Shan Dai from the materials institute of Paris (ENS - ESPCI) for the help in preparing samples, and expertise on metal oxide frameworks.

I wish to specifically thank Emmanuel Puig, whom I have met at Cardiff Uni during my third year of undergraduate, and whom unexpectedly did his PhD two halls away. I am happy to consider Emmanuel as a great friend thanks to whom I knew what awaited me during my final year (as we were one year apart). Adrien Bussard whom has given me advices regarding the patent applications and steps through the valorisation but also helped me find this doctoral subject. Carole Thomas, with whom I was glad to work on her film production for “Les chercheurs font leur cinéma”. Salome Fabri-Ruiz whose PhD in

marine biology has given me dreams of travelling around the globe in places such as Antarctica. And the list goes on.

I want to send my gratitude to my family, my father Gareth, and grandparents Bertram and Merril, as well as to my aunt and grand-mother, Nadia and Anna. I wish to thank my loving brother Alexis, whom has made me drop tears when dancing Black swan, and filled me with pride when accomplishing is undergraduate studies in forest management. I wish to express my recognition to Judith for her support, help, kindness and affection.

Lastly, I wish to send my thanks to the jury members: Christophe Petit, Ramdane Benferhat, Didier Gourier and Virginie Ponsinet for honouring me by evaluating my PhD work, as well as Hynd Remita and Lionel Simonot for reffering the manuscript.

ÉCRIRE LES REMERCIEMENTS DE CE TRAVAIL DE TROIS ANS est peut-être la partie la plus délicate de ce manuscrit. En effet, beaucoup de personnes ont contribué à cet aboutissement et je ne veux en oublier aucune. Bien que ce ne soit pas habituel, je souhaite d'abord remercier ma mère, Malvina, qui m'a soutenu tout du long de mes études universitaires et bien sûr durant ma thèse. Elle m'a apporté son appui soutenu ces derniers mois, pendant la rédaction de ce manuscrit.

C'est sans dire que travailler avec Yves Borensztein, mon directeur de thèse, a été exceptionnel. Son aide et ses conseils ont été exemplaires et ont rendu ce parcours doctoral inoubliable. Indépendamment des hauts et des bas de la recherche universitaire, l'équipe et la relation que nous avons formées nous ont permis d'accomplir le travail présenté dans cette thèse.

Pourtant, la recherche académique n'est pas un travail d'une ou deux personnes et un personnage clef a été Sébastien Royer, qui, en tant que technicien, m'a aidé à surmonter les difficultés techniques du travail expérimental. Bien que l'essentiel de son travail ait été indispensable, je me sens néanmoins coupable d'avoir parfois demandé son aide pour la fabrication de matériel que je n'ai au final pas utilisé. Cette recherche universitaire ne s'est limitée pas à un travail acharné, mais aussi à présence dans un environnement de travail formidable, qui est l'équipe Physico-Chimie et dynamique des surfaces de l'INSP. Je tiens à remercier Loïc Becerra pour m'avoir aidé à utiliser la salle blanche ainsi que Dominique Demaille, qui m'a formé sur le microscope électronique à balayage me permettant d'enregistrer des images de haute qualité. Je tiens à remercier, en règle générale, tous les membres de l'équipe pour m'avoir accueilli et encouragé, ainsi que donné des conseils scientifiques.

Je suis également heureux de ne pas avoir été seul à entreprendre ce travail de doctorat, car de nombreux doctorants ont également été confrontés à ce défi en même temps que moi. Cela a permis de développer une ambiance de complicité, et favorisé des moments de détente. C'est pourquoi je souhaite adresser mes remerciements à Alberto Curcella, qui est resté à mes côtés tout au long de ces trois années. Bien qu'il soit un excellent modèle pour la photographie, j'ai dû l'aider à plusieurs reprises, notamment avec le modèle LaTeX (il a en effet attendu que je l'écrive avant de le chiper « sournoisement »), ou à un moment où son ordinateur ne démarrait pas du tout alors qu'il était en pleine rédaction. Léo Bossard-Giannesini, d'autre part, a apporté bon sens et décence au bureau.

Au cours du dernier mois d'août, Léo et moi avons travaillé ensemble d'arrachepied, ce qui a considérablement renforcé notre motivation. Je ne veux pas oublier les autres étudiants du laboratoire tels que Clément Livache, Silvia Pandolfi, Ju-Hyeon Lee, Danilo Longo et la-fille-qui-parle-beaucoup pour leurs soutiens.

Je souhaite remercier Fabienne Testard du laboratoire IRAMIS du CEA pour la collaboration sur les capteurs de déformation, même si ces travaux ne figurent pas dans ce manuscrit. Je tiens également à remercier Christian Serre, Antoine Tissot et Shan Dai de l'institut des matériaux poreux de Paris (ENS - ESPCI) pour leur aide dans la préparation des échantillons et leur expertise sur les MOF.

Je tiens à remercier tout particulièrement Emmanuel Puig, que j'ai rencontré à Cardiff pendant de ma troisième année et qui a fait sa thèse de doctorat dans le laboratoire voisin. Je suis heureux d'avoir comme ami Emmanuel, grâce à qui je savais ce qui m'attendrait au cours de ma dernière année, car nous avions un an d'écart dans nos cursus. Adrien Bussard qui m'a donné des conseils concernant le dépôt de brevet et les étapes de la valorisation. Carole Thomas, avec qui j'ai eu le loisir de travailler sur son film pour "Les chercheurs font leur cinéma". Salome, dont le doctorat en biologie marine m'a fait rêver de voyager autour du monde dans des endroits comme l'Antarctique. Et la liste continue.

Je veux témoigner ma gratitude à ma famille, mon père Gareth et mes grands-parents Bertram et Merril, ainsi que ma tante et ma grand-mère, Nadia et Anna. Je tiens à remercier mon frère bien-aimé, Alexis,

qui m'a fait verser plus d'une larme en dansant le lac des cygnes, et m'a rempli de fierté en accomplissant ses études en gestion forestière. Je souhaite exprimer ma reconnaissance à Judith pour son soutien, son aide et son affection.

Finalement je souhaite remercier les membres du jury : Christophe Petit, Ramdane Benferhat, Didier Gourier et Virginie Ponsinet qui me font l'honneur d'évaluer ce travail que j'ai effectué pendant mon doctorat, ainsi que Hynd Remita et Lionel Simonot pour avoir accepté d'être rapporteur du manuscrit.

Contents

SORBONNE UNIVERSITÉ

ED397

Institut des nanosciences de Paris

Doctor of Physics

Study and development of localised surface plasmon resonance based sensors using anisotropic spectroscopy

by William L. WATKINS

Foreword

THE PROPERTIES OF GOLD have always been of high interest as it does exhibit peculiar behaviours. Amongst many, it undergoes localised surface plasmon resonance (LSPR) which gives the characteristic ruby colour to colloidal gold nanoparticles. At the nanoscale, the inertness of the metal vanishes and new chemical and physical mechanism arise. Research in this field has seen exponential growth, should it be for catalysis, energy, biological and biomedical applications as well as chemical sensing. Albeit, a lot was promised about the capabilities of this noble metal, but obstacles were encountered along the way revealing the difficulties these developments brought with them.

Regarding sensing applications of LSPR in general, it has been rather quickly realised that the abilities of gold or other LSPR metals are strongly limited to the spectroscopic equipment necessary to reach detection limits or practicality in contrast to competitive methods. Efforts were put into synthesising complex nanoparticle shapes in order to push these constraints without actually attending to the intrinsic limit. This is where an alternative spectroscopic technique may have the potential to break the limitation barrier and enable to benefit from the full potential of LSPR-based sensing.

The method undertaken in this scientific research was to couple the use of anisotropic nanoparticles with a differential spectroscopic technique known as transmission anisotropy spectroscopy (TAS). The aim of this, was to take advantage of the polarisation dependence of anisotropic LSPR nanostructures with this simple and effective optical apparatus to move beyond the spectral limitations of conventional methods.

This goal inevitably bears challenges. The first one was the anisotropic sample fabrication. Indeed, with industrial scalability in mind, we wanted a method that produced nanometric structures as well as showing reproducible and usable results. Furthermore, the chemistry of nanoparticles dictates that the features should be as small as possible whilst still exhibiting a workable optical response. This means particles around 5 to 20nm in size must be fabricated. This poses a challenge as particles in these sizes are difficult to organise in order to yield anisotropic samples should it be through bottom-up or top-down approaches. The second difficulty relies in the theoretical understanding of the observed phenomena. Indeed, scientific research requires the investigation of the physical and chemical observation i.e. go beyond a rudimentary phenomenological study. However, in the cases studied in this work, the conditions are difficult to control which is a consequence of the working scale. This is in contrast to more fundamental work undertaken in ultra high vacuum for example. Yet, throughout this work, efforts were given into reminding a theoretical model to better understand and thus predict the experimental observations. Analytical expressions, though requiring simplification of the systems, enabled just this, by giving the tools to grasp which phenomena are taking place in the mechanisms. Other times, numerical methods come in handy for more complex systems, though do have their own limitations.

This thesis is laid out in five chapters. Each of them comprises of a small introduction to set the scientific context, the motivations as well as a state of the art. It then discusses the work that was undertaken and is ended by a small summary. Each chapter, to some extent, is self consistent though at times, necessary references to other sections are inevitable. The references of each chapter are written at the end as well as

reprinted at the end of the manuscript after an appendix which contains non crucial but still interesting information.

The first chapter lays the theoretical foundations to understand the basic principles at play. A lot of effort was given into providing the reader with the necessary tools not only to understand the theoretical models used in the experimental sections, but also to allow to underline the behaviour and limitations of each models should it be analytical or numerical.

In the second chapter, the experimental instruments are described, though nothing new is discussed, I wanted to remind the limitations as well as the capabilities associated with each experimental method.

The third chapter deals with the anisotropic sample fabrication process. Although the method chosen was oblique angle deposition, that is evaporation of the metal under vacuum, efforts was given into modelling the optical properties of the less than ideal LSPR nanostructures. The word *metal* is indeed used instead of simply gold as investigation with palladium was also a major focus of this research.

The last two chapters are devoted to the detailed investigation of two study cases. The first one, in chapter four, discusses the use of anisotropic gold nanoparticles to study their hydrogenation reactivity with dihydrogen as it is of key interest in hydrogenation processes. The methodology revealed such sensitivity, that the understanding of the reaction mechanism between the two species was deepened.

The fifth and last chapter demonstrates sensing applications of the anisotropic method using both gold-palladium and pure palladium samples for dihydrogen detection. The results revealed the high sensitivity of the method in ideal circumstances as well as preliminary work into more *real-world* conditions which do increase the challenges due to the presence of containments such as dioxygen and water.

This work is by no means exhaustive and much more research is required to truly achieve and benefit from the technique. In the final conclusion, a couple glimpses into the possibilities and capabilities of the technique are revealed paving the path for new and innovative uses of LSPR.

Chapter 1

General introduction and state of the art

1.1 First observations of surface plasmon resonance

> "The unique feature of the Lycurgus cup is that it appears red by transmitted light, but the glass exhibits a degree of turbidity, the scattered light being markedly greenish in hue."
>
> - 1963
>
> *R.C. Chirnside*
> *P.M.C. Proffitt*

EVERY LECTURE DEVOTED TO PLASMONIC RESONANCE starts by presenting the Lycurgus cup. This Roman glass cup, shown in figure 1.1, dates back to the 4^{th} century AD. The sculpture depicts an episode from the Greek myth of Lycurgus, a king of the Thracians, around 800 BC. It shows the moment when Dionysus, the god of grape harvest and one of his maenads, Ambrosia, are attacked by Lycurgus. Ambrosia called out to Mother Earth, who transformed her into a vine. She then coiled herself about the king, and held him captive. The cup shows this moment when Lycurgus is entrapped by the branches of the vine [i1]. The object itself is well known for exhibiting a peculiar optical characteristic. That is being red when light is shone through the glass, and green when light is reflected on its surface [i2].

This masterpiece, exhibited at the British Museum has been readily studied by 20^{th} century scholars such as Harden et al., though, they were unable to explain the very nature of the phenomenon at hand [i1]. One has to wait Chirnside et al. who, in 1963, were requested, by the British Museum Research Laboratory, to carry out a deeper scientific analytical investigation of the glass in order to elucidate its chemical composition [i3]. They have established that the material was composed of many oxides such as SiO_2, Na_2O, as well as Mn_2O_3. However, traces of metallic gold, in extent of about 50 parts per million were also found. They concluded that "the unusual optical properties of the glass may well be connected with the presence in the glass of colloidal gold" though acknowledging that the presence of Mn_2O_3 may also contribute to the colour. The influence of Au has now been confirmed and light has been shed on the possible manufacturing process [i2], [i4].

FIGURE 1.1: Photograph of the Lycurgus cup. The photograph of the left hand side shows the green tint of the glass when light is shun from the outside whilst the photograph of the right hand side shows the ruby red colour from when light is transmitted through the glass - British museum

This ancient example illustrates the physical properties of gold nanoparticles in relation to electromagnetic fields. The study of such aspects have been famously discussed by Faraday at the Bakerian lecture

at the Royal Institute in a 1857 [i5]. In this work, Faraday investigated the optical properties of gold colloid solutions, and observed "a beautiful ruby fluid" as well as accounting for the influence of the size of the dispersion noting "a mere variation in the size of particles gave rise to a variety of resultant colours", though he was unable to explain these phenomena as the physics had not yet been established.

In the beginning of the 20 th century Mie, inspired by Faraday's work, published a paper developing an analytical solution to Maxwell's equations in order to describe the scattering and absorption of light by very small spherical particles due to resonance modes generated within the particle by the interaction of an electromagnetic wave [i6]. These solutions were later generalised to spheroidal shaped particles by Gans based on Drude's model which describes in a purely classical model the electronic transport in conductors [i7]–[i9]. The term *plasmon* arrived later as Pines et al. published a paper in 1952 discussing a quantised bulk plasma oscillation of electrons in a metallic solid[i10].

Alongside these advances, a new field of physics was being established by Feynman at the annual meeting of the American Physical Society at Caltech in 1960, he coined the now famous phrase "there's plenty of room at the bottom" establishing the foundation for what is to become the *nanosciences* [i11]. Today, nanoparticles are in the centre of new technologies finding applications in physics, medicine, chemistry, &c... and the optical properties of gold nanoparticles are extensively used for various applications which is the general subjective of this doctoral thesis.

1.2 Electromagnetic properties of metals

In this section, the mathematical fundamentals related to the electromagnetic properties of metals are described. Although not exhaustive, these set of equations should give the reader the necessary knowledge to understand the physics of plasmonics in nanoparticles. This section references multiple sources which are [i12]–[i15]. In this introduction, the system is simplified to exclude magnetism as the materials used in latter work is not magnetic.

1.2.1 A few elements of electromagnetism

At the microscopic level, that is the scale of the atom, the optical properties of matter can be described by Maxwell's microscopic equations.

$$\nabla \cdot \boldsymbol{e} = \rho^{micro} \tag{1.1a}$$

$$\nabla \wedge \boldsymbol{b} = \frac{1}{c^2}\frac{\partial \boldsymbol{e}}{\partial t} + \boldsymbol{j}^{micro} \tag{1.1b}$$

The vectors $\boldsymbol{e} = \boldsymbol{e}(\boldsymbol{r}, t)$ and $\boldsymbol{b} = \boldsymbol{b}(\boldsymbol{r}, t)$ are the microscopic electric and magnetic fields respectively. $\rho^{micro}(\boldsymbol{r}, t)$ and $\boldsymbol{j}^{micro}(\boldsymbol{r}, t)$ are the microscopic charge and current densities, respectively. These equations apply to dielectrics media including metals. In the following, there is no distinction made between the free i.e. conduction electrons (metals) and bound electrons (*pure* dielectrics). With these equations, one considers the contribution of each charged particle. Charges in a system should it be electrons and nuclei are considered as point charges. Therefore, the charge density at the microscopic level is given by:

$$\rho^{micro}(\boldsymbol{r}) = \sum_i q_i \delta(\boldsymbol{r} - \boldsymbol{r_i}) \tag{1.2}$$

where q_i is the charge of the i^{th} particle and $\delta(\boldsymbol{r} - \boldsymbol{r_i})$ is the Dirac delta function. At the atomic level, one should account for quantum effects and thus the point charge should really be treated in terms of spatial probabilities distributions. Yet, this classical model approximation does help to understand and still well represent the physical phenomenon. The electric dipole moment $\boldsymbol{p}^{micro}$ of an entity such as an atom or a molecule is given by

$$\boldsymbol{p}^{\boldsymbol{micro}}(\boldsymbol{r}) = \int \boldsymbol{r}\, \boldsymbol{\rho}^{micro}(\boldsymbol{r})\, d^3\boldsymbol{r} \tag{1.3}$$

An assembly of such entities are interpreted at the macroscopic level where the different densities are averaged over a given volume. Such a volume is large enough to contain a large number of polarisable entities ($\approx$ thousands) but yet still small with respect to the light wavelength. Typically a sphere with a diameter of a few nanometres for the case of atoms. If an electric field is applied to a medium made up of a large number of these microscopic entities, the electronic charge distribution of each entity is displaced with respect to the nucleus. In the case of a non-uniform polarisation in the applied field, a net charge is generated within the region (Fig 1.2). The global dipole moment per unit volume is given by the sum of the microscopic dipole moments

$$\boldsymbol{P}(\boldsymbol{r}) = \sum_i N_i \boldsymbol{p}_i^{micro} \tag{1.4}$$

where $\boldsymbol{p}_i^{micro}$ is the dipole moment of the i^{th} entity in the medium, the average is taken over a small volume centred at $\boldsymbol{r}$ and N_i is the average number per unit volume of the i^{th} type of entity at the point $\boldsymbol{r}$ This leads to a polarisation of the charge and current densities, ρ^{pol} and $\boldsymbol{j}^{pol}$ respectively at the macroscopic level. A second source of extra net charge can come from an external source and is written ρ^{ext}. When considering only the case of interaction with light though, $\rho^{ext} = 0$.

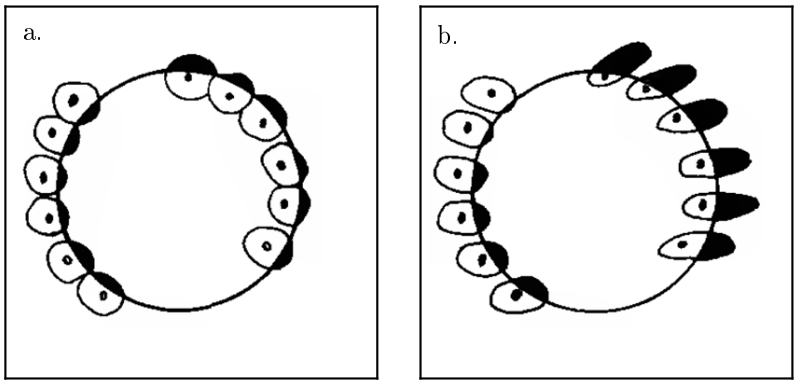

FIGURE 1.2: Origin of polarisation charge density a. no electric field b. polarisation in presence of a spatially varying electric field. Only entities near the boundary are shown [i12], [i14].

The Maxwell equations at the macroscopic level are given in terms of the total charge and current densities of the macroscopic region, ρ^{total} and $\boldsymbol{j}^{total}$ respectively.

$$\nabla \cdot \boldsymbol{E} = \frac{\rho^{total}}{\varepsilon_0} \tag{1.5a}$$

$$\nabla \wedge \boldsymbol{B} = \frac{1}{c^2}\frac{\partial \boldsymbol{E}}{\partial t} + \mu_0 \boldsymbol{j}^{total} \tag{1.5b}$$

where $\boldsymbol{E}$ and $\boldsymbol{B}$ are the macroscopic electric and magnetic fields, respectively. ε_0 is the electric permittivity of free space, μ_0 the magnetic permeability of vacuum. The relation between the charge and current densities is given by

$$\nabla \cdot \boldsymbol{j}^{total} + \frac{\partial \rho^{total}}{\partial t} = 0 \tag{1.6}$$

In the case of a dielectric material, the total charge and current densities are given by the sum of the polarisation densities and the external densities

$$\rho^{total} = \rho^{pol} + \rho^{ext} \tag{1.7}$$

$$\boldsymbol{j}^{total} = \boldsymbol{j}^{pol} + \boldsymbol{j}^{ext} \tag{1.8}$$

The polarisation charge density is equal to the divergence of the dipole moment per unit volume

$$\rho^{pol} = -\nabla \cdot \boldsymbol{P} \tag{1.9}$$

thus from eq. 1.6 and eq. 1.9, the current density is given as

$$\boldsymbol{j}^{pol} = \frac{\partial \boldsymbol{P}}{\partial t} \tag{1.10}$$

Adding these equations to the macroscopic Maxwell equations leads to

$$\nabla \cdot \boldsymbol{E} = \frac{\rho^{pol} + \rho^{ext}}{\varepsilon_0} \Leftrightarrow \nabla \cdot (\varepsilon_0 \boldsymbol{E} + \boldsymbol{P}) = \rho^{ext} \tag{1.11}$$

The electric displacement is therefore defined as

$$\boldsymbol{D}(\boldsymbol{r}, t) = \varepsilon_0 \boldsymbol{E}(\boldsymbol{r}, t) + \boldsymbol{P}(\boldsymbol{r}, t) \tag{1.12}$$

which leads to the familiar equality between the divergence of the electric displacement and the external charge density. In the case where no external charge densities are introduced ($\rho^{ext} = 0$), then

$$\nabla \cdot \boldsymbol{D} = \rho^{ext} = 0 \tag{1.13}$$

In the same way, the second Maxwell macroscopic equation can be written as

$$\nabla \wedge \boldsymbol{B} = \frac{\partial \boldsymbol{D}}{\partial t} + \mu_0 \boldsymbol{j}^{ext} \tag{1.14}$$

which in a non magnetic medium with no current applied $\mu_0 = 1$ and $\boldsymbol{j}^{ext} = 0$.

In the case of metals, one must account for the valence and conduction electrons which are represented by bound and free charge densities, thus the polarisation charge density is given by

$$\rho^{pol} = \rho^{bound} + \rho^{free} \tag{1.15}$$

The constitutive properties of matter connects the polarisation $\boldsymbol{P}(\boldsymbol{r}, t)$ with the field $\boldsymbol{E}(\boldsymbol{r}', t')$ existing at all other positions and all earlier times. In general it is given as

$$\boldsymbol{P}(\boldsymbol{r}, t) = \int d\boldsymbol{r}' \int_{\infty}^{t} dt' \chi(\boldsymbol{r}, \boldsymbol{r}', t, t') \boldsymbol{E}(\boldsymbol{r}', t') \tag{1.16}$$

where χ is the electric susceptibility of the medium. In the following, we shall neglect any spatial dispersion which is equivalent to using the local approximation such as

$$\boldsymbol{P}(\boldsymbol{r}, t) = \int_{\infty}^{t} dt' \chi(\boldsymbol{r}, t, t') \boldsymbol{E}(\boldsymbol{r}, t') \tag{1.17}$$

At this point the plane wave electric field, written as

$$\boldsymbol{E}(\boldsymbol{r}, t) = \boldsymbol{E}_0 e^{i(\boldsymbol{k}\cdot\boldsymbol{r} - \omega t)} \tag{1.18}$$

enables, after a Fourier transform, to consider $\chi(\omega)$. The polarisation can thus be given as

$$\boldsymbol{P}(\omega) = \varepsilon_0 \chi(\omega) \boldsymbol{E}(\omega) \tag{1.19}$$

Three assumptions are made within this expression. As indicated above, the assumption of locality is applied. This relationship applies to linear optics, which means that the polarisation is linearly proportional to the electric field, which does not apply for large intensity of the electric field. Finally, the medium is taken

as isotropic. Indeed in the case of anisotropic materials, the polarisation $\boldsymbol{P}$ might not align with the electric field $\boldsymbol{E}$. Therefore the displacement can be written as

$$\boldsymbol{D} = \varepsilon_0 \varepsilon(\omega)\, \boldsymbol{E} \qquad with \quad \varepsilon(\omega) = 1 + \chi(\omega) \tag{1.20}$$

where $\varepsilon(\omega)$ is the complex dielectric function of the material. $\varepsilon(\omega)$ describes the response to an electromagnetic wave and is equal to $\varepsilon = \tilde{n}^2$. The demonstration of these equations is not shown in the manuscript but can be found in [i15]. From these equations, the complex reactive index is described as:

$$\sqrt{\varepsilon(\omega)} = \tilde{n}(\omega) = n + i\kappa \tag{1.21}$$

The real and imaginary part of the dielectric function can thus be written as:

$$\varepsilon(\omega) = \varepsilon_1(\omega) + i\varepsilon_2(\omega) \tag{1.22}$$

where

$$\varepsilon_1 = n^2 - \kappa^2 \tag{1.23a}$$
$$\varepsilon_2 = 2n\kappa \tag{1.23b}$$

which can be written as:

$$n = \frac{1}{\sqrt{2}} \left(\varepsilon_1 + \sqrt{\varepsilon_1^2 + \varepsilon_2^2} \right)^{1/2} \tag{1.24a}$$
$$\kappa = \frac{1}{\sqrt{2}} \left(-\varepsilon_1 + \sqrt{\varepsilon_1^2 + \varepsilon_2^2} \right)^{1/2} \tag{1.24b}$$

Within a medium, the dielectric function accounts for the electronic transitions of all types and for their oscillating forces, the effects of polarisation, the effect of shielding and the phenomenon of electron collision and diffusion. The imaginary part of the refraction index is responsible for the absorption of electromagnetic waves by the medium as it propagates through the material. The real part modifies the speed and wavelength of the wave passing through the medium.

Both the real and imaginary parts are related to one another by Kramers-Kronig relations. This comes from the principle of causality and enables one to theoretically determine the real part of the dielectric

function from its imaginary part and vice versa through these two relations:

$$\varepsilon_1(\omega) = 1 + \frac{2}{\pi}\mathcal{P}\int_0^\infty \frac{\varepsilon_2(\omega')}{\omega' - \omega}d\omega' \tag{1.25a}$$

$$\varepsilon_2(\omega) = -\frac{2}{\pi}\mathcal{P}\int_0^\infty \frac{\varepsilon_1(\omega') - 1}{\omega' - \omega}d\omega' \tag{1.25b}$$

where $\mathcal{P}$ denotes the Cauchy principal value of the integral and ω the energy. The demonstration of the statement is well defined in the literature cf ref. [i15].

However, the relationship does infer that the values are known on the entire spectrum, which is thus a limiting factor for numerical calculations. A possible solution was proposed by Catra, F and Nabet, B. They proposed a procedure that "calculates the real component of the dielectric function from its imaginary component by making use of the Hilbert transform properties of the Kramers-Kronig relations."[i16]. The point is that numerical resolution of the Kramers-Kronig relation is one of the main method undertaken by late XX^{th} century researchers to experimentally determine dielectric function of different material.

1.2.2 Experimental determination of dielectric functions

One way to experimentally determine the complex dielectric function of a metal is to measure two independent quantities, for instance, ellipsometric quantities or the transmittance, T, and reflectance, R, of a sample consisting of a thin, few nanometres, film of material evaporated on a transparent substrate. T and R can be related to n and κ though still dependent on the wavelength and the film thickness. These relations allows one to obtain the $n - \kappa$ plane of R and T countours, which in turn can be computed to find the physical values of n and κ [i17], [i18].

The early way of determining the optical properties of a material was to use Drude's polarimetric method which gives explicit expressions for the optical constants n and κ derived from measured quantities such as T and/or R. However, it is very much dependent on the quality of the sample elaboration [i19]. Neverthless, in the late sixtees, the solutions were mainly obtained through approximate formulas and graphical methods as expressed by Nilsson [i17]. The advent of computational power enabled researchers to use numerical techniques which could compute methods less sensitive to the surface conditions. An instance of this is Kramers-Kronig analysis of the data in order to discriminate the final dielectric function. This method was for instance undertaken by Nilsson to determine the optical properties of AgIn and CuGe [i20]. Yet, issues arise from the necessity to extrapolate the wavelength outside the measured range which leads to large effects on the magnitude of the optical constant. This was tackled by Nilsson by using a dispersion relation and no extrapolations outside the measured region from only transmission data.

Using multiple measurement was done by Pells to determine the dielectric constant of gold and metal alloys such as $\mathrm{Au} - \mathrm{Mn}$ and copper alloys [i21]. His method consisted in measuring the intensities of reflection at four different azimuths. The intensities were measured normal, parallel and at $\pm 45^\circ$ with respect to the plane of incidence. From these four measurements and the angle of incidence, the real and imaginary parts of the complex dielectric constant can be calculated. However, the accuracy of his measurements are weaken due to uncertainty of the thickness of the film surface. No information is given in his paper whether the relation used satisfy the Kramers-Kronig relation. Though early computational power was indeed used as the dielectric function determined by Pells were done on an IBM 7030 computer.

In 1971, Nestell and Christy published a paper presenting "a complete coherent discussion of the equations for the reflectance and transmittance of a thin absorbing film for arbitrary angle of incidence of light" [i18]. The problem they intended to resolve is first to solve the Maxwell-equation boundary-value problem which predict R and T in terms of the material constants n and κ and second to invert these solutions to obtain the wanted values of n and κ in terms of the measured R and T. Their mathematical model described in [i22] requires computer inversion techniques for practical utility as a method for determining the optical constants of metals. In their later paper Johnson and Christy have applied this method to determine the optical constants of copper, silver and gold. These results are amongst the most used in analytical and numerical calculation today and is described as a reference by many researchers [i19]. This can be attributed to the accuracy of the measurements undertaken but also to the availability of the data as they also published numerical tables of the result making them easier to use.

Yet, the increase computational power also enabled theoreticians to apply new theoretical models such as density functional theory (DFT) and time-dependent DFT to determine the dielectric function of materials which would be difficult to determine experimentally such as palladium hydride at different degrees of hydrogenation [i23], [i24]. Figure 1.3.a shows the dielectric function of silver calculated with DFT-LDA compared to experimental values. It can be seen that the calculation only gives an estimate to the experimental values but are not yet capable of producing exact results [i25]. Other functionals such as GW do yield appreciable results as shown by A. Marini et al. whom have calculated the reflectivity spectrum of silver using GW and LDA functionals and compared them to experimental values [i26]. The results are shown in figure 1.3.b. It can be seen from these results that although good results are obtain from both functionals, it is only on a specific energy interval. Indeed, GW shows good agreement from 0 to $6eV$ and then underestimates the experimental values whereas LDA only shows good agreement from $\approx 10eV$ onwards. In spite of the better results obtained with GW, it is a much more demanding computationally wise. Such results are used in a latter chapter discussing the use of palladium as a hydrogen optical sensor (cf. chapter 5).

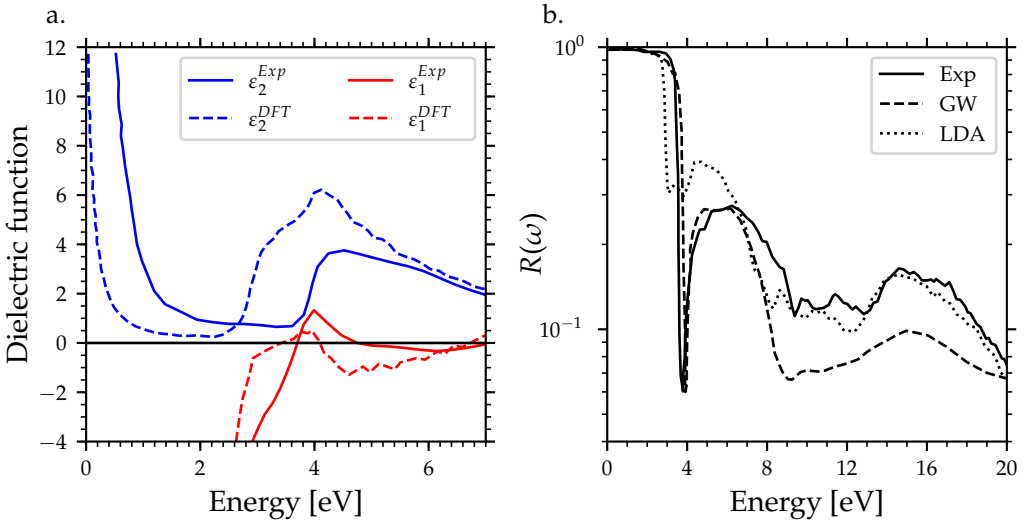

FIGURE 1.3: a. Reflectivity spectrum of Ag. Dashed line: GW, dotted: LDA, solid: experiment [i26]. b. Dielectric function of bulk Ag. Dashed line: experimental from Johnson and Christy [i19], dashed line: DFT-LDA calculation from Hogan et al. [i25].

1.2.3 Simple analytical expression: Drude model

Taking a closer look at the dielectric function, obtained by Johnson and Christy, plotted in figure 1.4, shows that for each metal the first low energy values represent intraband transitions. Then, at a specific threshold, interband transitions occur. The latter are more visible for the imaginary part of the dielectric function which occurs at $\approx 2eV$ for copper, around $\approx 2.2eV$ for gold and $\approx 3.9eV$ for silver. To understand these transitions, one must look at the band structure of a metal. For the case of argument, gold is taken as a working example. Figure 1.5 shows the band structure for bulk gold. The Fermi energy level is shown in red and the inset illustrates the two types of transition that can occur: intraband and interband transitions

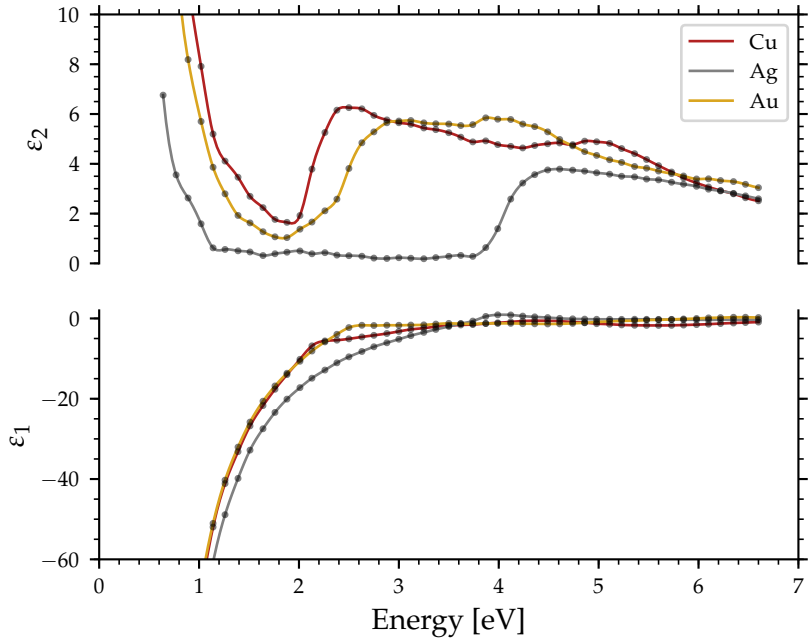

FIGURE 1.4: Experimental dielectric functions for Au, Ag and Cu determined by Johnson and Christy [i19]. The values are also tabulated in the appendix A.1.

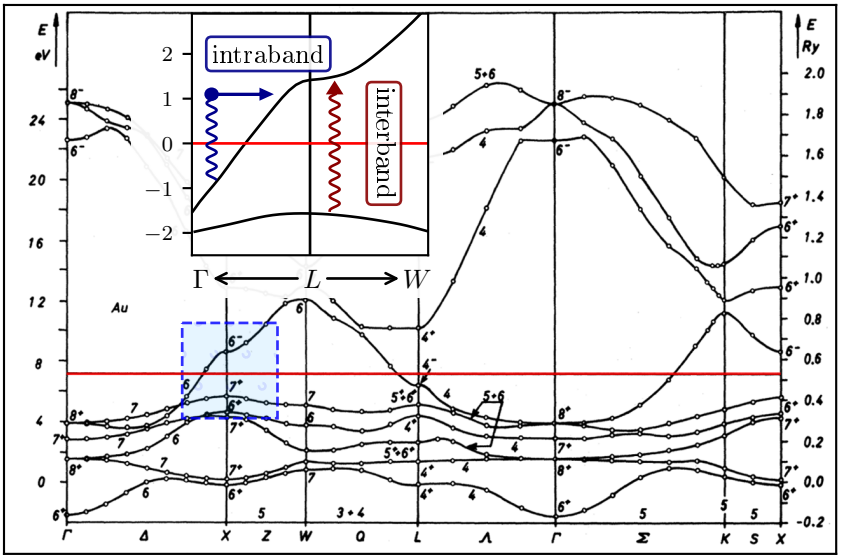

FIGURE 1.5: Band diagram for bulk Au . The insert schematically shows interband and intraband transitions.

Analytical interpretation of the dielectric function of a noble metal can be done by dissociating the interband transitions from the intraband transitions. This was first proposed by Ehrenreich et al. in 1962 [i27], [i28] and is written as:

$$\varepsilon_{bulk}(\omega) = \varepsilon^{D}(\omega) + \delta\varepsilon_{ib}(\omega) \tag{1.26}$$

where ε_{bulk} is the dielectric function of a bulk metal, ε^{D} and $\delta\varepsilon_{ib}$ are the intraband & interband contribution to the dielectric function respectively. The intraband contribution can explicitly be written using the Drude model for free-electron metals approximates. This model considers an ionic network representing the metallic atoms and a free electron cloud. These electrons interact with different elements of the network via elastic collisions with a damping factor defined as $\Gamma = \frac{1}{\tau}$. τ is the relaxation time given by $\tau = \frac{l_{bulk}}{v_{Fermi}}$ where l_{bulk} is the electron mean free path within the metal bulk and v_{Fermi} the electron Fermi velocity. These interactions, taken as independent of one another, occur with the ionic network, as well as other interactions leading to an increase in the damping factor such as interactions with other electrons, phonons, defects, impurities, &c... as shown in the following equation

$$\Gamma = \Gamma_{e-e} + \Gamma_{e-ph} + \Gamma_{e-defects} + \Gamma_{e-impurities} + \dots \tag{1.27}$$

As the material is subjected to an electromagnetic field, the free electrons are induced to oscillate around their equilibrium position. This is known as the plasma frequency Ω_p. This leads to a macroscopic polarisation of the metal and is described by the Drude dielectric function written as:

$$\varepsilon^{D}(\omega) = 1 - \frac{\Omega_p^2}{\omega(\omega + i\Gamma)} \tag{1.28}$$

where

$$\Omega_p = \left(\frac{Ne^2}{\varepsilon_0 m}\right)^{1/2} \tag{1.29}$$

where N is the density of conduction electrons, e is their charge, and m the effective electron mass. Thus the real and imaginary parts can be written as:

$$\varepsilon_1^D(\omega) = 1 - \frac{\Omega_p^2}{\omega^2 + \Gamma^2} \tag{1.30a}$$

$$\varepsilon_2^D(\omega) = \frac{\Omega_p^2 \Gamma}{\omega(\omega^2 + \Gamma^2)} \tag{1.30b}$$

To calculate the interband transition contribution, $\delta\varepsilon_{ib}$, a sum of Lorentz oscillators can be used:

$$\delta\varepsilon_{ib}(\omega) = (\varepsilon_\infty - 1) + \sum_j \frac{f_j \Omega_p^2}{\omega_j^2 - \omega^2 - i\omega\Gamma_j} \tag{1.31}$$

where ω_j is the resonance frequency of the oscillator, Γ_j its damping factor and f_j the oscillator strength. ε_∞ is the high-frequency value of the permittivity which permits to satisfy Kramers-Kronig relation as it accounts for higher energy interband transitions. These are adjustable parameters which describe the interband transitions. In practice, determining the correct values for these parameters can be a challenging task. For instance Sehmi et al. have proposed a method to optimise the fit of experimentally determined dielectric functions with multiple Lorentz oscillators and even then discrepancies exist with the experimental results [i29].

For noble metals, as indicated above, it is feasible to separate the interband and intraband transitions from the experimental data. For this, one needs to subtract a fitted Drude model from the experimental data effectively isolating the interband transitions. Let us apply the Drude model from eq. 1.26 and eq. 1.28 and fit Johnson and Christy's dielectric function of gold. This enables one to study the optical response of a particle in detail such as the effect of interband transitions as well as the effect of confinement by modifying the parameters of the Drude model. The parameter used to fit the experimental data are recapitulated in table 1.1. Plotting the intraband contribution (figure 1.6.a) with the experimental dielectric function shows how well the Drude model is able to fit the first part of the dielectric function of Au. However, beyond $\approx 2.5eV$ the interband transition occur making the Drude model erroneous.

TABLE 1.1: Parameters of the Drude dielectric function chosen to fit Johnson and Christy for Au [i19]

ε_∞	$\Omega_p\,[eV]$	$\Gamma\,[eV]$	$v_{FERMI}\,[m/s]$	$l_{bulk}\,[m]$
9.4	8.94	0.073	$1.4 \cdot 10^6$	$1.27 \cdot 10^{-8}$

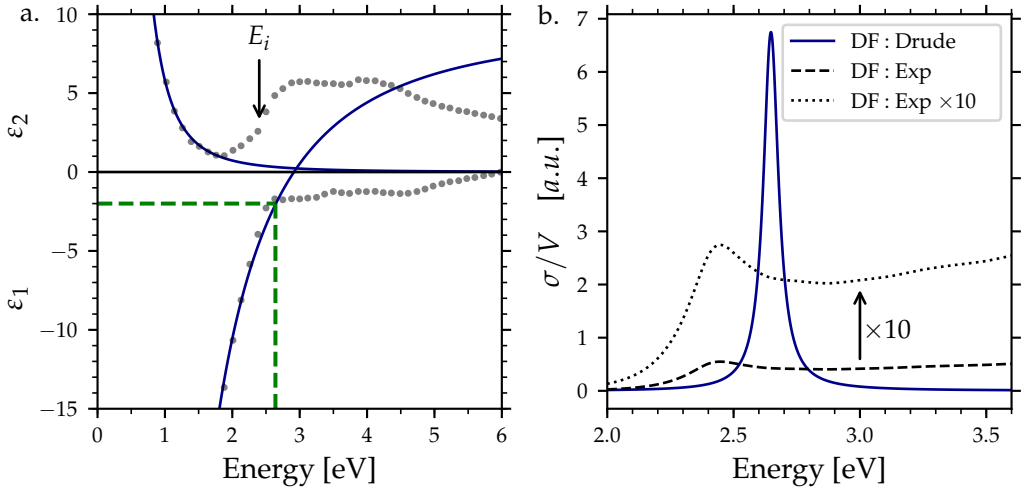

FIGURE 1.6: a. Grey dots: experimental dielectric function for Au by Johnson and Christy [i19]. Blue solid line Drude fit of the experimental data. b. Absorption cross-section of a Au sphere normalised to the volume calculated using the experimental dielectric function and a pure Drude fitted dielectric function i.e. with the interband transition are not accounted for by setting $\delta\varepsilon_{ib}(\omega) = 0$

1.2.4 Drude Model: confinement in a nanoparticle

One last point to note when using these dielectric functions is that they represent the optical properties of thin films. This means that for rigorous applications when studying the optical response of nanoparticles, one must account for the dampening factor induced by the particle's surface as its size decreases. This parameter can be included in the damping parameter (eq. 1.27).

$$\Gamma = \Gamma_{e-e} + \Gamma_{e-ph} + \Gamma_{e-defects} + \Gamma_{e-impurities} + \Gamma_{e-surface} + \dots \tag{1.32}$$

In practice, the modified dielectric function due to the surface i.e. confinement is calculated by subtracting the Drude contribution for the bulk and adding a modified Drude contribution with the damping factor adapted for the proper conditions. Using this method, the interband transitions are kept unchanged and only the intraband transitions are modified as shown in the following expression:

$$\varepsilon_M^{mod}(\omega) = \varepsilon_M^{bulk}(\omega) + \frac{\Omega_p^2}{\omega^2 + \omega i\Gamma_{bulk}} - \frac{\Omega_p^2}{\omega^2 + \omega i\Gamma_{mod}} \tag{1.33}$$

where M is the metal, and Γ_{mod} is the modified damping factor accounting for the scattering of the conduction electrons at the surface of the nanoparticle. Its value is increased with respect to the Γ_{bulk} as the electron's mean free path, described by $l_{bulk} = v_{Fermi}/\Gamma_{bulk}$ is reduced. In the case of a spherical nanoparticle, the modified mean free path can be described as:

$$l_{mod}^{-1} = l_{bulk}^{-1} + \frac{A}{R} \tag{1.34}$$

where R is the radius of the sphere and A a phenomenological parameter whose values is close to 1 [i13], [i30].

To relate the now obtained dielectric functions to the optical response of a given particle, we must account for its size compared to the electromagnetic wavelength. Indeed, the quasi-static approximation can be used when the size of the particle is much smaller compared to the wavelength: $R \ll \lambda$. In this case, the electric field *seen* by the particle can be considered as uniform as it is illustrated on the right hand side of figure 1.7. Furthermore, if the particle is isolated, then the local field can be considered as uniform as well, in which case the dipole approximation applies. Indeed, as two or more particles are brought close to one another, the local electric field seen by a single particle is a combination of both the external electric field and the electric field of the neighbouring particles. The local field is thus non-uniform and although the quasi-static approximation applies, the response of the system is not dipolar.

If the particle is not very small or even larger compared to the wavelength, as shown on the left hand side of figure 1.7, the electric field is not uniformed thus the quasi-static approximation cannot apply. The non-uniform electric field leads to multipolar effects. Describing the optical response of larger particles requires different regimes to be applied such as the theory of Mie [i6], [i15]. This is addressed in a later section though not in great details as the particle studied in the experimental work of this thesis generally satisfy the quasi-static approximation.

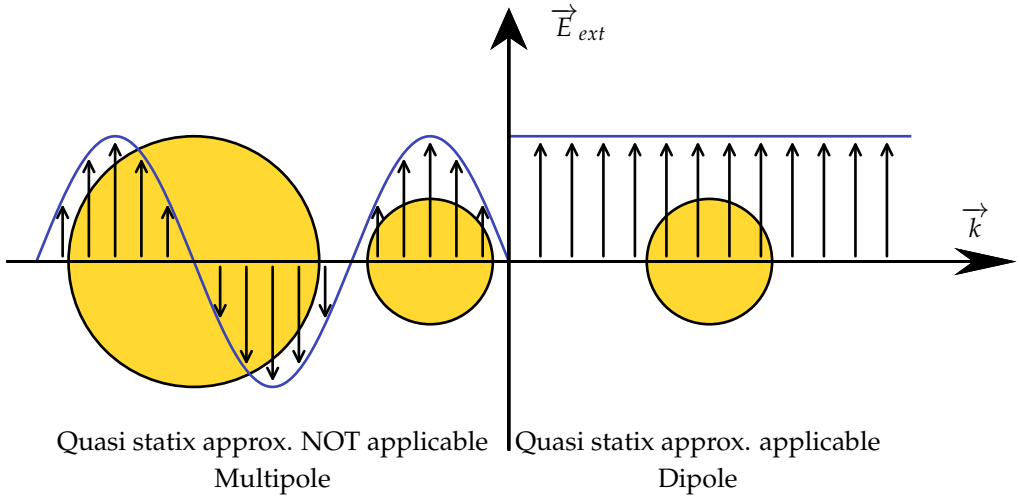

FIGURE 1.7: Schematic example of the quasi-static approximation. Left hand side shows particles which cannot be considered in the quasi-static approximation as they are too large with respect to the wavelength. On the right hand side, the electric field of the applied wave is considered as uniform and thus can be considered within the quasi-static approximation.

1.3 Localised surface plasmon resonance (LSPR)

1.3.1 Fundamental principal of LSPR

Localised surface plasmon resonance (LSPR) is defined as the collective oscillation of the electron cloud induced by an external electric field. Considering an isolated small metallic spheric nanoparticle subjected to a standing electromagnetic wave, the particle reacts to the external electric field by displacing its electronic cloud (Fig. 1.8). Within the quasi-static approximation, the positive charges of the particle e.g.

atom's nucleus are considered as immobile and the negative charges e.g. the electron cloud, are allowed to move under the influence of the electric field. This regime is characterised by only keeping the time dependence and not the spatial dependence of the electromagnetic field as illustrated in figure 1.8.

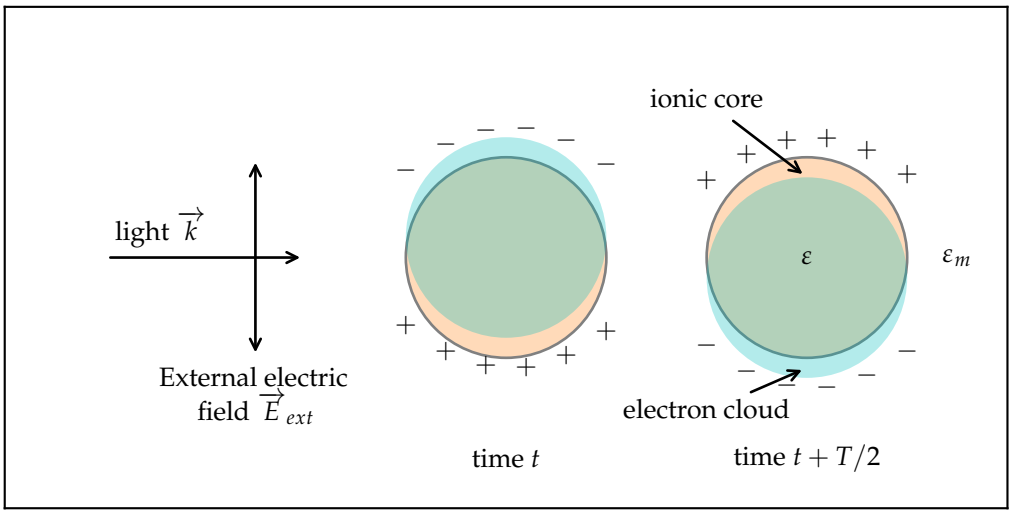

FIGURE 1.8: Schematic of the oscillation of the conduction electrons in a plasmonic particle induced by an incident electric field.

In the quasi-static approximation, the internal electric field, $\boldsymbol{E}_{int}$ is expressed as:

$$\boldsymbol{E}_{int} = \boldsymbol{E}_{ext} \frac{3\varepsilon_m}{\varepsilon + 2\varepsilon_m} \tag{1.35}$$

where ε_m is the dielectric constant of the embedding medium. The polarisability of a sphere, defined by $\boldsymbol{p}_{sphere} = \varepsilon_m \alpha_{sphere} \boldsymbol{E}_0$, is given as:

$$\alpha_{sphere} = 4\pi R^3 \varepsilon_0 \frac{\varepsilon - \varepsilon_m}{\varepsilon + 2\varepsilon_m} \tag{1.36}$$

The absorption cross-section of a particle can be calculated from the polarisability described above and is formulated as:

$$\sigma_{abs} = \frac{2\pi\omega}{\lambda} \sqrt{\varepsilon_m} \times Im(\alpha) \tag{1.37}$$

It is noteworthy that the absorption cross-section is proportional to the volume of the particle. It is conventional to also calculate the efficiency factors for the absorption of a system which is defined as:

$$Q_{abs} \equiv \frac{\sigma_{abs}}{\pi a_{eff}^2} \tag{1.38}$$

$$\tag{1.39}$$

where a_{eff} is the effective radius i.e. the radius of a sphere of equal volume V, to the nanoparticle.

A resonance behaviour of the polarisability of the sphere occurs when the denominator, $|\varepsilon + 2\varepsilon_m|$ reaches a minimum. This is referred to as the localised surface plasmon resonance (LSPR) which is thus defined as the collective oscillation of conduction electrons excited by an electric field. Hence in the case of a spheric particle in vacuum i.e. $\varepsilon_m = 1$ this occurs for $\varepsilon = -2$.

Plotted in figure 1.6.b are the absorption cross-section of an isolated Au sphere in air calculated using both the Drude intraband dielectric function and the experimental dielectric function. In the case of a pure intraband gold material, the LSPR peak is very narrow, symmetric and positioned at $\hbar\omega \approx 2.7eV$. The broadness of the spectrum is led by the damping factor Γ which is fixed to be $\approx 0.1eV$ as can be read at the full width at mid hight on the spectrum. On the other hand, the LSPR calculated using the experimental dielectric function, which includes the interband transitions, is not symmetrical and red shifted, with a position of the peak at $\hbar\omega \approx 2.4eV$, but most importantly, the intensity is much lower. On the figure, it was multiplied by ten in order to increase readability. The reduction and broadening of the spectrum is due to the absorption induced by the interband transitions in ε_2. For comparison, the absorption cross-section for the three noble metals: copper, silver and gold from the dielectric function measured by Johnson and Christy (cf Fig. 1.4) are plotted in figure 1.9 [i19].

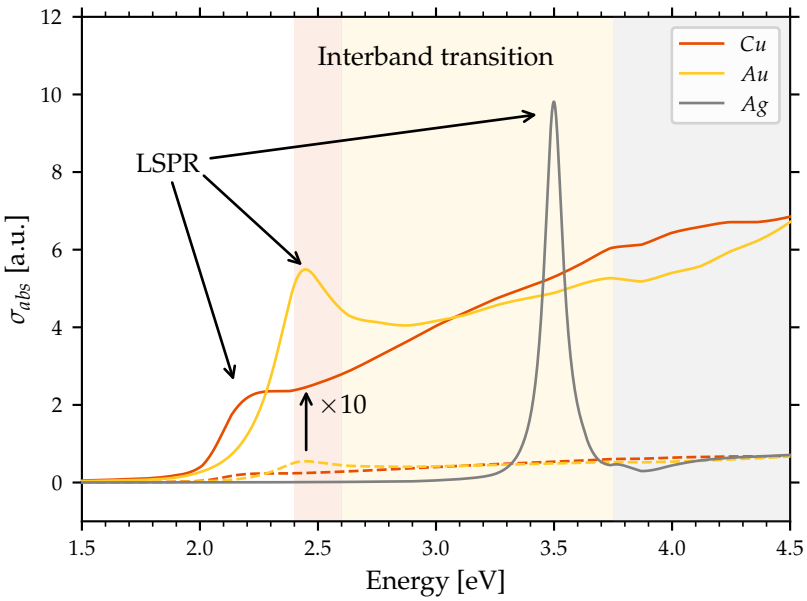

FIGURE 1.9: LSPR spectra for spheres of Cu, Au and Ag using the dielectric function experimentally determined by Johnson and Christy [i19]. The spectra for Cu and Au have been multiplied by ten for readability.

On the spectra we can see that all three metals exhibit a peak more or less defined in the visible range and then a steady increase in extinction as the energy is increased. The LSPR of silver is very intense and much narrower than that of gold or copper and reaches a maximum at $\hbar\omega_{Ag} \approx 3.5eV$. On the other hand, gold and copper have a much less intense peak (indeed, their spectra is multiplied by ten for visibility of

the figure). They are also much wider compared to silver with a maximum at $\hbar\omega_{Cu} \approx 2.2eV$ and $\hbar\omega_{Au} \approx 2.45eV$. Moreover, from these results, we can see the effect of the interband transitions on the LSPR, indeed, the interband transitions for silver are much further away from the resonance energy compared to copper and gold. This is why the resonance for copper and gold are so quenched.

To deeper visualise the effect of the interband transitions, it is possible to modify by simulation the energy at which the interband transition begin i.e. the threshold. This is simply done by first calculating the interband transition $\delta\varepsilon_{ib}$ and then reconstructing the full dielectric function for the metal from the Drude part and the interband, however this time, a value $\Delta\hbar\omega$ can be added in the interband part to change its position in energy:

$$\delta\varepsilon_{ib}(\omega) = \varepsilon_{bulk}(\omega) - \varepsilon^{D}(\omega) \tag{1.40a}$$

$$\varepsilon_{mod}(\omega) = \varepsilon^{D}(\omega) + \delta\varepsilon_{ib}(\omega + \Delta\omega) \tag{1.40b}$$

From this modified dielectric function, the absorption cross-section is calculated with different values for $\Delta\hbar\omega$ for Au. The calculations are plotted on figure 1.10.a.c. On the first figure 1.10.a the modified dielectric function is plotted and one can see that the interband transitions are translated in energy without moving the intraband part. On the real part (ε_1) it can be seen that the interband transition greatly disturb the dielectric function. Figure 1.10.c. shows the calculated absorption cross-section for each dielectric function. It can be seen that when displacing the interband transitions' energy threshold from lower to higher energies, the LSPR is blue shifted, the intensity increases and the peak becomes narrower. Looking at the red spectrum ($\Delta\hbar\omega = -0.5eV$), the interband transition actually causes the LSPR peak to be quenched to the point where there is no LSPR. It is thus interesting to note that for application of LSPR, it is more interesting to move away from the interband transition in order to get a more intense LSPR peak. This can be done also by changing the embedding medium (cf. 1.3.2).

A second observation that can be done with the Drude model, is to see the effect of confinement on the LSPR peak. As discussed in the previous section, the dielectric function determined by Johnson and Christy is for bulk metal. When calculating the optical properties of a finite particle, one must account for the confinement of the electrons in the particle by adjusting the damping parameter Γ. From eq. 1.33 and eq. 1.34, the dielectric function can be adjusted by calculating the modified damping parameter according to the radius of the nanoparticle. For the sake of demonstration, let's first only consider the intraband transitions. The calculations are plotted in figure 1.10.b.d. The dielectric function (figure 1.10.b) is mainly modified in the imaginary part and the confinement induces a blue shift. On the real part, the effect is much lower. An inset plots a zoomed in view of the graph to show the order of displacement of the curve which is opposite to that of the imaginary part. This induces only a very small, almost null, shift in the LSPR. Yet when looking at LSPR cross-section, which is normalised to the volume of the nanoparticle, the effect of the damping leads mainly to a decrease in intensity of the resonance as well as a widening of the resonance compared to bulk. This can be understood by considering the mean free path of electrons within gold. Indeed, the value for gold is $l_{bulk} = 12.7nm$ which tells that when reducing the radius of a particle below this size, the collisions with the surface of the particle become non negligible and also infers that when the particle is too small resonance cannot occur. On the other hand, increasing the size of the particle does indeed increase the intensity and narrows the peak. However, it is important to remember that the quasi-static approximation is in use in these example. In other words, increasing the size of the particle also means that the approximation becomes erroneous. More details of this point is discussed in section 1.3.3.

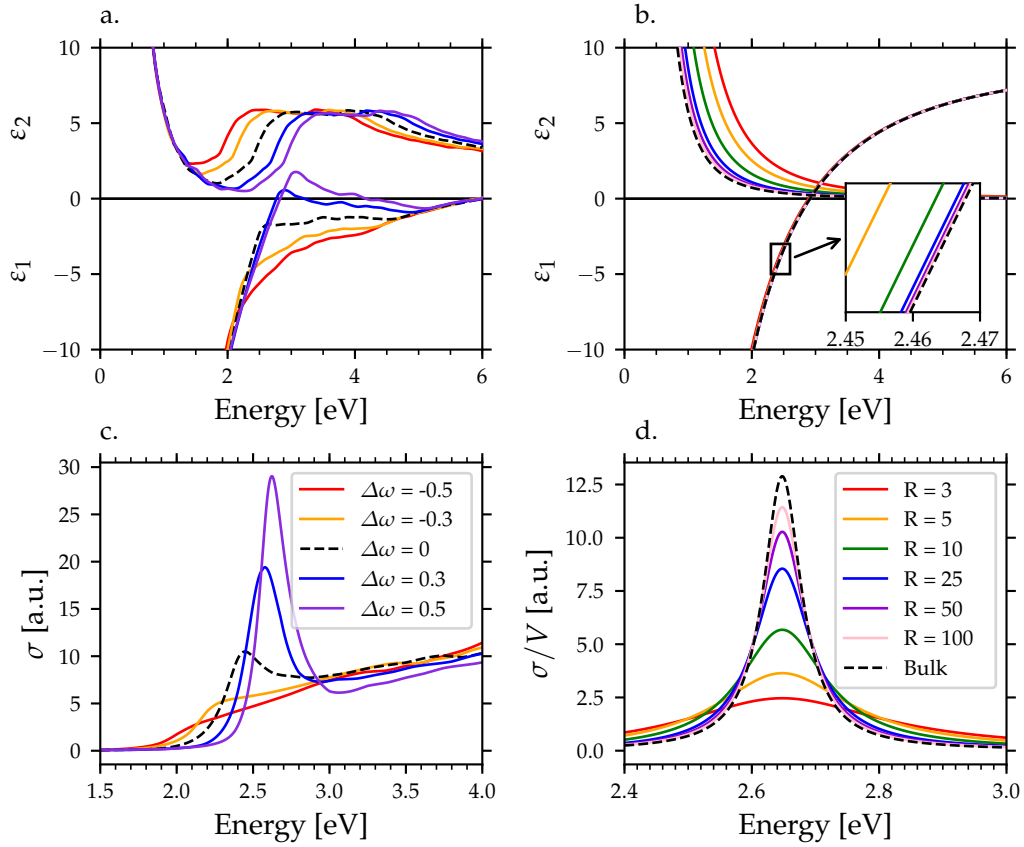

FIGURE 1.10: a. Dielectric function for Au with the interband transition shifted at different energies from $\Delta\hbar\omega = -0.5eV$ to $\Delta\hbar\omega = 0.5eV$. b. Drude fitted dielectric function of Au modified to account for the confinement of a particle size from $R = 3$ to the bulk dielectric function. c. LSPR spectra of Au using the different dielectric functions displayed in (a.). d. LSPR spectra of Au using the different dielectric functions displayed in (b.).

The effect of the radius also has a small spectral shift effect when taking into account the interband transitions. In figure 1.11, the same procedure is done to calculate the absorption cross-section of a spheric particle using the experimental dielectric function for gold decomposed in a Drude and interband dielectric function. This enables the modification of the damping factor but keep the interband transitions. On figure 1.11.b. one can see that decreasing the radius leads to a decrease in the intensity, and broadening of the LSPR spectrum, but also, due to the interband transition, it also leads to a red shift which is not seen when only considering the intraband transition (cf figure 1.10.d.)

Thus, going back to figure 1.9, it is clear why the LSPR of copper is much less pronounced than that of silver. Indeed, the interband transitions of silver being much further away, it behaves much like a Drude function whereas copper has its interband transitions starting near its LSPR frequency which thus quenches the spectrum. For the case of gold, its dielectric function is intermediate with the interband transition starting just after the LSPR peak. In practise, silver would be a better candidate for LSPR-base technologies, however, its chemical reactivity makes it difficult to work with. Thus is why in spite of the proximity of its interband transitions, gold is better suited thanks to its chemical stability.

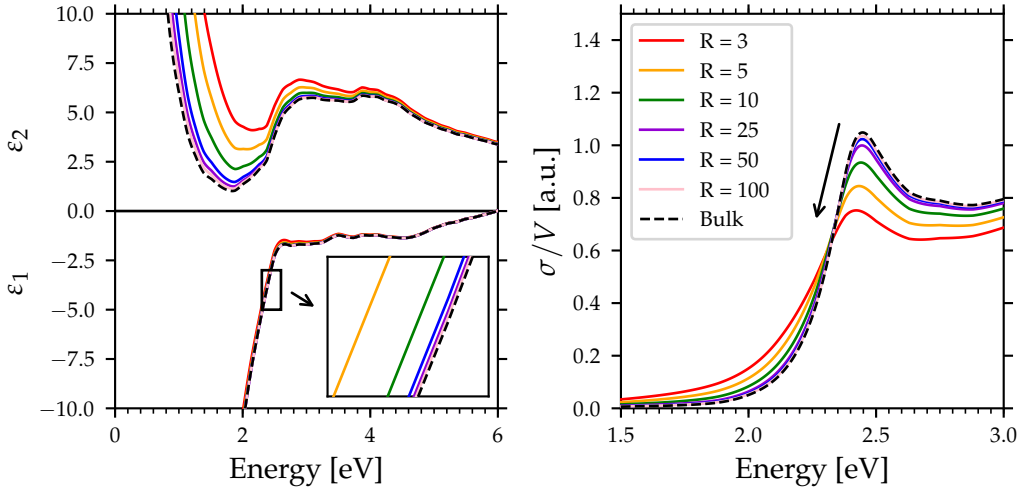

FIGURE 1.11: a. Experimental dielectric function of Au modified to account for the confinement of a particle. b. LSPR spectra of Au using the different dielectric functions displayed in (a.).

These examples thus theoretically show the behaviour of the confinement and interband transitions on the LSPR of a plasmonic metal. Although these examples are not experimentally feasible, they enable one to better understand how these effects might combine to modify the final LSPR response.

Thus one can clearly see how the metal's dielectric function greatly influence the position of the LSPR, however, the polarisability equation (eq: 1.36) shows that the LSPR is also dependent on the dielectric function of the medium ε_m as well as the radius of the particle R.

1.3.2 Factors influencing the LSPR

• Influence of the medium

The polarisability described in eq. 1.36 not only shows that the extinction spectrum is dependent on the dielectric function of the metal, but also on that of the medium. To illustrate this dependence, let's consider a gold sphere first in vacuum ($\varepsilon_m = 1$) and then in water ($\varepsilon_m = 1.33^2$). We use the example of gold as well as a pure Drude fitted on gold which allows a clearer understanding of the effect of the surrounding medium. Figure 1.12.a. shows the two LSPR spectra in the media depicted above. The effect of increasing the external refraction index leads to a red shift of the LSPR spectrum which in turn, due to the proportionality of the absorption cross-section with the dielectric function of the medium, leads to an increase in intensity (cf eq. 1.37).

When calculating the effect on the gold with interband transitions (Fig. 1.12.c.) a similar behaviour is observed with a red shift and increase in intensity. However, this time, the increase in intensity is also due to the fact that the LSPR is shifted away from the interband transitions.

If we were to simulate the effect of a slight change in refractive index of the medium, the effect would prove to be less pronounced. This is illustrated in figure 1.12.b where the extinction is calculated for a gold sphere in pure water ($\varepsilon_m = 1.33^2$) and in water with 20% sugar ($\varepsilon_m = 1.36^2$). In this case a similar red shift is observed but much weaker with a $\Delta\hbar\omega \approx 0.006eV \Leftrightarrow \Delta\lambda = 1.13nm$. For a gold sphere with interband transitions (Fig. 1.12.d.) the effect is the same though the shift $\Delta\hbar\omega \approx 0.003eV \Leftrightarrow \Delta\lambda = 0.65nm$ is smaller and harder to determine due to the broadness of the LSPR. This theoretical example illustrates a key aspect

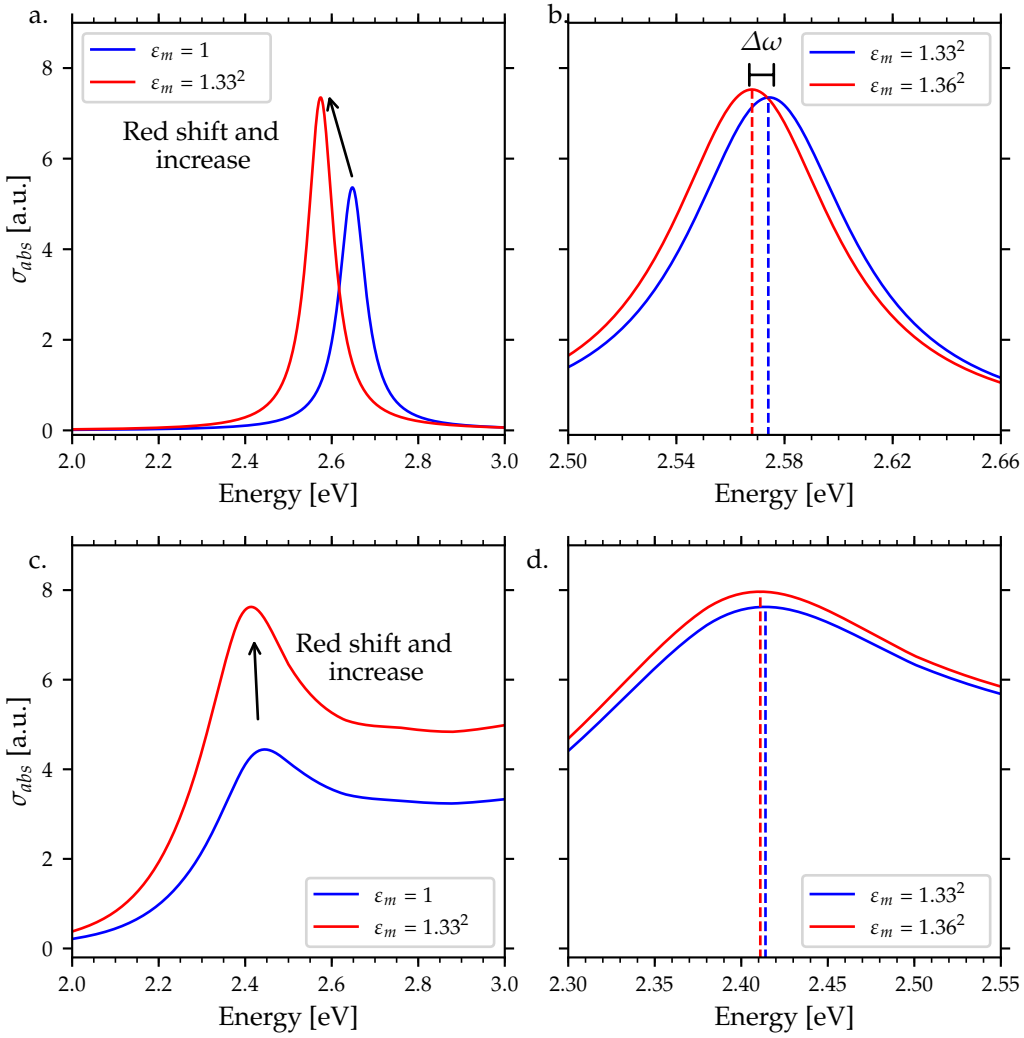

FIGURE 1.12: a. LSPR spectra using a Drude dielectric function fitted on Au calculated for spheres with $\varepsilon_m = 1$ representing vacuum or gas and $\varepsilon_m = 1.33^2$ representing the spheres in water. b. Same as a. but with a difference in the refractive of the medium with $\varepsilon_m = 1.33^2$ and $\varepsilon_m = 1.36^2$. c. Same calculation as a. but using the experimental dielectric function for Au i.e. with interband transitions. d. Same as b. but using the experimental dielectric function of Au.

of LSPR, that is the large field of application of LSPR for sensing applications which is the core theme of the next chapters.

- **Influence of the shape**

Other parameters also have an affect on the position of the LSPR. Indeed, eq. 1.36 shows the simplified polarisability for the case of a sphere, but a more general equation can be written for an ellipsoid. In this latter case, a depolarisation factor L_j is added to account for the effect of the ellipsoid's dimension and is given by:

$$\alpha_{ellispoid} = \frac{4}{3}\pi a_1 a_2 a_3 \frac{(\varepsilon - \varepsilon_m)}{\varepsilon_m + L_j(\varepsilon - \varepsilon_m)} \tag{1.41}$$

where a_1, a_2 and a_3 are the semi-axis of the ellipsoid as shown in the drawing in figure 1.13, and L_j is given by:

$$L_j = a_1 a_2 a_3 \int_0^\infty \frac{dq}{(a_i^2 + q) f(q)} \tag{1.42}$$

$$f(q) = \sqrt{(a_1^2 + q)(a_2^2 + q)(a_3^2 + q)} \tag{1.43}$$

$$\sum_{j=1}^{3} L_j = 1 \tag{1.44}$$

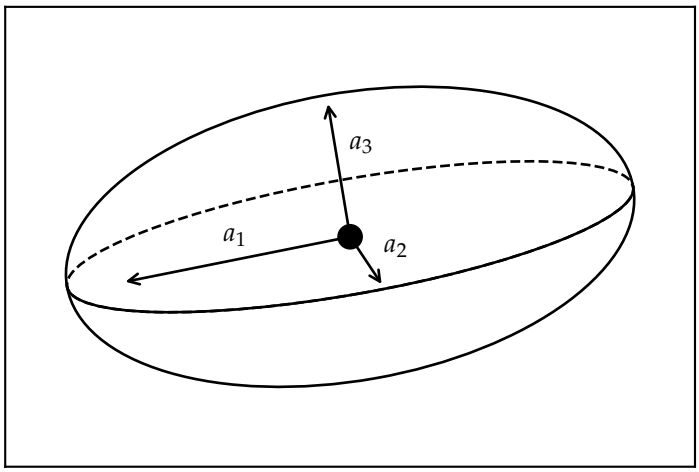

FIGURE 1.13: Schematic of an ellipsoid showing the three axis used in equation 1.41.

Thus when $L_j = 1/3$ one can see that eq. 1.41 simplifies back to the polarisability of a sphere as described by eq. 1.36. In the particular case of oblate or prolate spheroids, L can be described using Gans set of equations[i31].

• For a prolate particle $a_2 = a_3$:

$$L_1 = \frac{1 - e^2}{e^2} \left[-1 + \frac{1}{2e} ln \left(\frac{1 + e}{1 - e} \right) \right] \tag{1.45}$$

$$with \quad e = \sqrt{1 - \frac{a_2^2}{a_1^2}} \tag{1.46}$$

• For an oblate particles $a_1 = a_2$:

$$L_1 = \frac{g}{2e^2} \left[\frac{\pi}{2} - ArcTan\,(g) \right] - \frac{g^2(e)}{2} \tag{1.47}$$

$$with \quad g = \sqrt{\frac{1 - e^2}{e^2}} \quad and \quad e = 1 - \frac{a_3^2}{a_1^2} \tag{1.48}$$

The depolarisation factor L_j leads to an anisotropy when the two radius normal to the wave vector are not equal. Hence, the poles of the polarisability equations are given by:

$$\varepsilon_m + L_j\left(\varepsilon - \varepsilon_m\right) = 0 \Leftrightarrow \varepsilon = \varepsilon_m\left(1 - \frac{1}{L_j}\right) \tag{1.49}$$

Therefore looking at this relationship, the LSPR is directly related to the depolarisation factor. Let's consider a flat ellipsoid with $a_1 = 1$, $a_2 = 1.2$ and $a_3 = 0.61$. The depolarisation factors are thus $L_1 = 0.28$, $L_2 = 0.22$ and $L_3 = 0.5$. If we consider a non polarised incident wave along a_3, only the resonances along a_1 and a_2 are excited and thus visible. Figure 1.14.a. shows the dielectric function of silver with the dotted lines representing the resonances values for L_1 and L_2. This yields a LSPR spectrum with two maxima corresponding to both orthogonal axis (Fig 1.14.b.). It is interesting to note that if polarised light was used, than one could isolate both LSPR maxima. This combination of using polarised light and anisotropic particle is the main point of this thesis and is discussed in more details in the second part of this chapter.

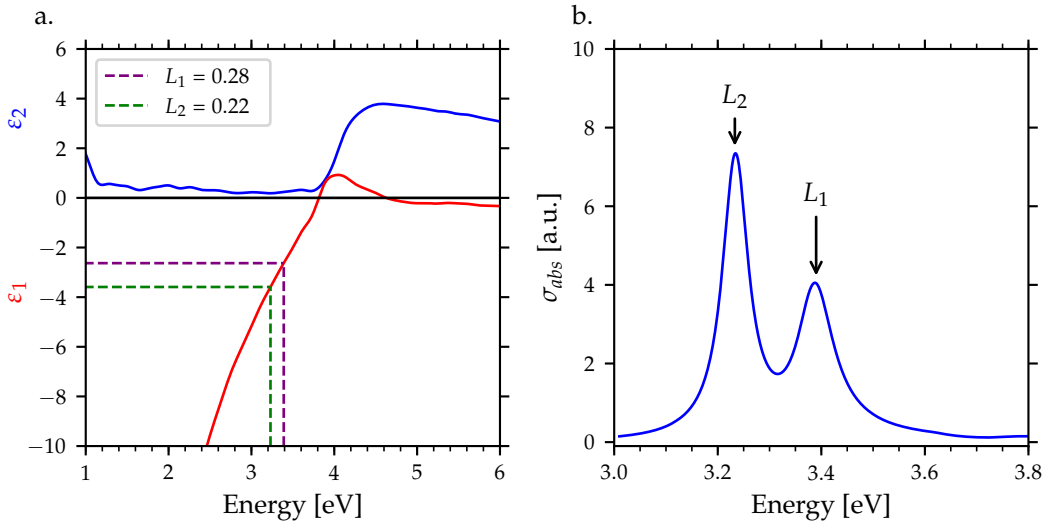

FIGURE 1.14: a. Experimental dielectric function of Ag determined by Johnson and Christy [i19]. b. Absorption cross-section for a an ellipsoid calculated using the dielectric function in (a.) with parameters: $a_1 = 1$, $a_2 = 1.2$ and $a_3 = 0.61$. Only the polarisation along a_1 and a_2 are excited.

• Case of core-shells particles

We have seen how the dielectric function of the metal influences the LSPR with the case of copper, silver and gold (cf. figure 1.9). However, these cases only consider a homogeneous metal. For heterogeneous particles, analytical equations are also capable of rigorously describing more complex systems such has core-shell particles [i15]. The general equation for core-shell ellipsoids is given as:

$$\alpha = V\frac{\left\{\left(\varepsilon_s - \varepsilon_m\right)\left[\varepsilon_s + \left(\varepsilon_c - \varepsilon_s\right) \times \left(L_j^{(1)} - f\,L_j^{(2)}\right)\right] + f\varepsilon_s\left(\varepsilon_c - \varepsilon_s\right)\right\}}{\left\{\left[\varepsilon_s + \left(\varepsilon_c - \varepsilon_s\right)\,\left(L_j^{(1)} - f\,L_j^{(2)}\right)\right]\left[\varepsilon_m + \left(\varepsilon_s - \varepsilon_m\right)\,L_j^{(2)}\right] + f\,L_j^{(2)}\varepsilon_s\left(\varepsilon_c - \varepsilon_s\right)\right\}} \tag{1.50}$$

where $V = 4\pi a_1^{(2)} a_2^{(2)} a_3^{(2)}/3$ is the total volume of the particle and $f = a_1^{(1)} a_2^{(1)} a_3^{(1)} / a_1^{(2)} a_2^{(2)} a_3^{(2)}$ is the ratio between the radii of the core (1) and shell (2). The depolarisation factor $L_j^{(k)}$ is given by:

$$L_j^{(k)} = a_1^{(k)} a_1^{(k)} a_1^{(k)} \int_0^\infty \frac{dq}{\left\{ \left(a_1^{(k)} \right)^2 + q \right\} f^{(k)}(q)} \quad (k = 1,\ 2) \tag{1.51}$$

with

$$f^{(k)}(q) = \sqrt{\left[\left(a_1^{(k)} \right)^2 + q \right] \left[\left(a_2^{(k)} \right)^2 + q \right] \left[\left(a_3^{(k)} \right)^2 + q \right]} \tag{1.52}$$

where (k) is either 1 or 2 for the core and shell respectively. An important fact about this model however is that the shell is not of constant thickness due to the way the depolarisation factor is calculated. This is illustrated in figure 1.15. Though not a big issue for a quantitative analysis or thin shells, it is a limitation to take into account when considering such systems. To simulate a shell of constant thickness other means need to be used such as numerical analysis (cf. section 1.3.3).

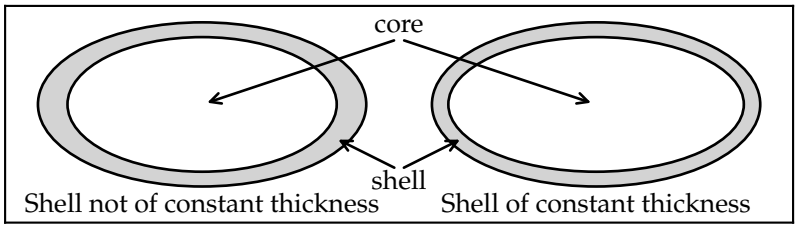

FIGURE 1.15: Schematic showing a core-shell ellipsoid with a. a shell not of constant thickness and b. with a shell of constant thickness.

The same way the polarisability of an ellipsoid (eq. 1.41) simplifies back to the polarisability of a sphere as described by eq. 1.37. The description for a core-shell sphere is written as:

$$\alpha = V \frac{(\varepsilon_s - \varepsilon_m)(\varepsilon_c + 2\varepsilon_s) + f(\varepsilon_c - \varepsilon_s)(\varepsilon_m + 2\varepsilon_s)}{(\varepsilon_s + 2\varepsilon_m)(\varepsilon_c + 2\varepsilon_s) + f(2\varepsilon_s - 2\varepsilon_m)(\varepsilon_c - \varepsilon_s)} \tag{1.53}$$

where ε_c and ε_s are the dielectric function of the core and the shell respectively. V is the volume of the core-shell particle given by $V = 4\pi a_2^3$ and $f = a_1^3/a_2^3$.

Such an approach can be used for bimetallic particles. For instance, figure 1.16 shows a simple core-shell system composed of increasing amount of Au in a Ag sphere. The spectrum shows that for the pure metals, the respective LSPR spectra are displayed. For the core-shell system, the overall spectrum displays two maxima due to the contribution of each metals. Increasing the ratio of silver leads to a decrease in intensity as well as a blue shift of the gold contribution whereas the silver contribution increases with a red shift. It is worth noting though that the intensity of the silver contribution in a core-shell particle is much weaker than for pure silver due to the absorption of Au. Moreover, in this layout, the contribution of silver displays an asymmetric LSPR which is known as a *Fano* resonance [i32]. This phenomena is one of the paths

undertaken in LSPR based system to use meta-materials with asymmetric LSPR. The goal being that this asymmetry leads to a sharp drop in extinction which could increase sensitivity of a system. Though in this simple case, it can be seen that the steepest slope at $\hbar\omega \approx 3.8eV$ for silver is reached for the pure metal. This observation therefore questions the effectiveness of using Fano resonances to improve plasmonic sensors. Though an exhaustive investigation should be undertaken, it is out of the scope of this work.

Another point to consider regarding Ag and Au is the fact that they are miscible in all proportions. In the case of an alloy, the LSPR does not behave as the core-shell where the LSPR peak of one metal increases whilst the other decreases as the composition changes. Instead the LSPR shifts continuously from the response of the first pure metal to the other [i33].

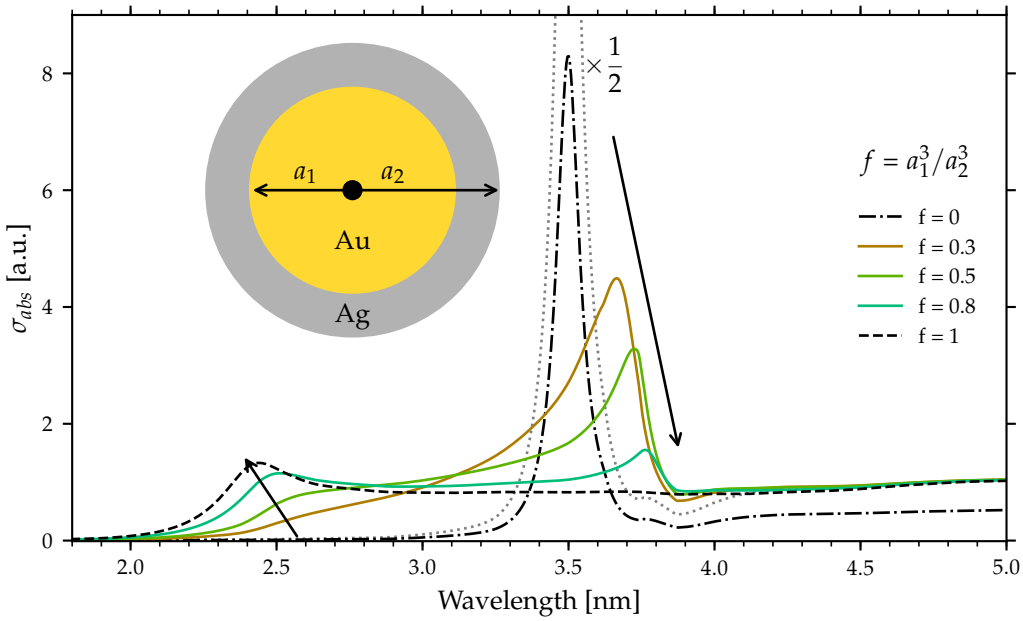

FIGURE 1.16: Absorption cross-section for a core-shell sphere constituted of a core Au and Ag shell with varying ratio for the size of the thickness of the shell.

Nevertheless, these equations are not limited to bimetallic particles. For example, let's consider the case of nanoparticles of gold dispersed as a colloidal suspension in water. In soft chemistry organic surfactants are functionalised around the nanoparticles to stabilise them and prevent aggregation. This kind of system could be modelled using the core-shell equations. The approximations used in this situation, on top of the requirements for the quasi-static approximation to be applicable, are the following:

- The surfactant covers the particle in a homogeneous layer and can thus be represented with a specific dielectric function.
- The dielectric function of the gold needs to be adjusted to account for any charge transfers induced by the adsorbate.

This model can easily be applied to practical examples. Indeed, the fabrication of metallic nanoparticles via chemical synthesise such as the Turkevich method enables to fashion small ($\geqslant 5nm$ in diameter) spherical nanoparticles of homogeneous radius. The typical chemical route is to react a gold acid such as chloroauric acid ($HAuCl_3$) with a reducing agent such as trisodium citrate ($Na_3C_6H_5O_7$). The elegance of this synthesis is the fact the citrate plays both the role of the reducing agent and stabiliser as it bonds to the

surface of the gold nanoparticle and prevent aggregation. This last point is indeed of importance as different type of stabiliser better known as surfactant can be used. Bossard et al. have studied the effect of the surfactant on the electronic properties of the Au nanoparticles. The organic compounds they have chosen were 16-mercaptohexadecanoic acid ($HS-(CH_2)_{16}-COOH$) and 8-amino-1-octanethiol ($H_2N-(CH_2)_8-SH$), which are two surfactants which bond to the gold and form a nanometre thick layer. The refractive index of both molecules is around n = 1.48, however, the acid forms a $2nm$ shell compared to $1nm$ for the amine. To determine the effect on the LSPR of these surfactant, the system can be interpreted as a core-shell system with the core being calculated with the dielectric function of Au and the shell as having the dielectric constant of the organic molecules. The calculated absorption cross-sections for the three systems are plotted in figure 1.17.a. The Au nanoparticle was taken with a radius of $10nm$. The effect of the surface leads to a red shift and intensity increase of the LSPR compared to the bare Au nanoparticle. Furthermore, the acid covered particle oversees a higher red shift than the amine system. As the refractive index of both molecules are the same, this is due to the thickness of the shell which is higher in the case of the acid. Experimentally, this is confirmed as the shift measured between the bare Au and the Au functionnalised with the acid are about the same as shown in figure 1.17.b. [i34].

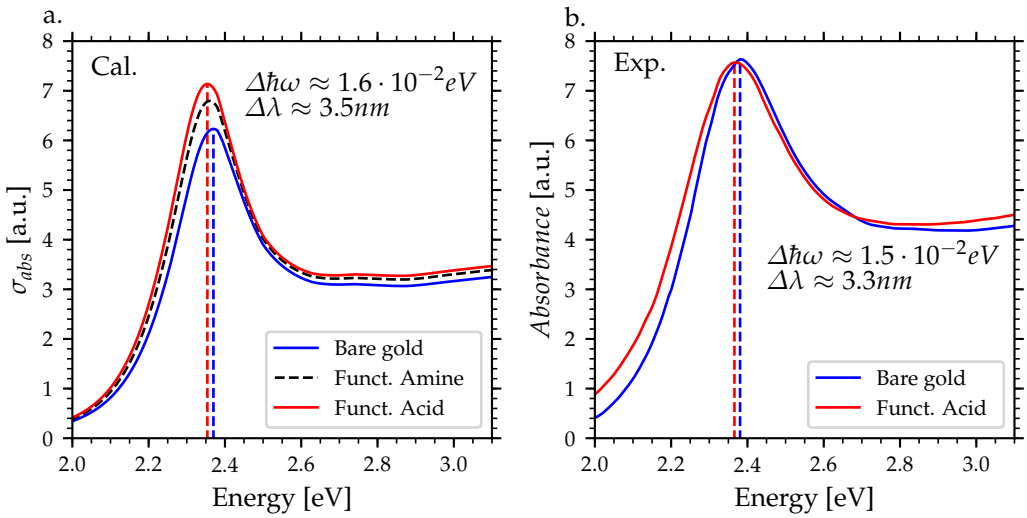

FIGURE 1.17: a. Calculated absorption cross-section for a $15nm$ in diameter Au sphere (solid blue) in 50% ethanol. The black and red spectra are for a core-shell system constituted of a Au core of $15nm$ in diameter core and a 1 and $2nm$ shells representing the functionalisation of 8-amino-1-octanethiol and 16-mercaptohexadecanoic acid respectively. b. Experimental absorbance of the the bare and acid functionnalised $15nm$ diameter particles in 50% ethanol exhibiting the same spectral shift as the theoretical calculation [i34].

It is for this property that LSPR-based sensing applications are conceivable. Indeed, functionnalising a plasmonic nanoparticle with a molecular sensor which would selectively bind to an analyte would induce a change in the refractive index in the vicinity of the nanoparticle and thus induces a shift of the LSPR peak. This statement is the core interest of this thesis and will be discussed in much more details in the second part of this chapter. It is important to note though that other contributions than the change in refractive index may occur when adsorbing molecules on the surface of plasmonic nanoparticles. Indeed as brought forward by Goldmann et al. the surfactant can also lead to charge transfers which would modify the dielectric function of the plasmonic metal as well as change in the refractive index in the vicinity of the particle [i35].

• **Charge transfers: modification of the metal's dielectric function**

The polarisability shows how the LSPR spectrum of a plasmonic metal is related to the change in the dielectric function in the vicinity of a nanoparticle (cf eq. 1.36). However, it is also possible to inherently modify the dielectric function of a metal by inducing charger transfers i.e. increasing or decreasing the electron density within the plasmonic particle. Indeed, the Drude model shows that the dielectric function is related to the plasma frequency, Ω_p as shown in eq. 1.28, which is in turn proportional to the square root of the conduction electron density, N within the particle (eq. 1.29). Thus varying N within a particle changes the plasma frequency and is related as:

$$\frac{\Delta\Omega_p}{\Omega_p} = \frac{1}{2}\frac{\Delta N}{N} \tag{1.54}$$

This can be related to the position of the LSPR peak which we denote ω_{LSPR}. The condition of resonance is approximatively given at the poles of the polarisability e.g. for an ellipsoid eq. 1.49. A slight change in the plasma frequency $\Delta\Omega_p$ leads to a corresponding change of the LSPR energy $\Delta\omega_{LSPR}$ given by the following relation

$$\frac{\Delta\omega_{LSPR}}{\omega_{LSPR}} \approx \frac{\Delta\Omega_p}{\Omega_p} \tag{1.55}$$

This approximation is true if we consider the interband contribution to remain constant around ω_{LSPR} and when $i\Gamma$ is small (cf. box page 28). Thus varying the electron density, N in a plasmonic particle will directly influence the dielectric function of the metal. The change in wavelength is related to the change in energy by

$$\frac{\Delta\lambda_{LSPR}}{\lambda_{LSPR}} = -\frac{\Delta\omega_{LSPR}}{\omega_{LSPR}} \tag{1.56}$$

The first approximation taken into account is to consider resonance condition to be given at the pole of the polarisability; for an ellipsoid it is

$$Re\left(\varepsilon(\omega_{LSPR})\right) \equiv \epsilon(\omega_{LSPR}) \approx \epsilon_m \left(1 - \frac{1}{L_j}\right)$$

where $\epsilon = Re(\varepsilon)$. Using the Drude model plus interband showed in eq. 1.26, we may write

$$\epsilon(\omega_{LSPR}) = 1 - \frac{\Omega_p^2}{\omega^2 + \Gamma^2} + \delta\epsilon^{ib} \approx \epsilon_m \left(1 - \frac{1}{L_j}\right)$$

The partial derivation gives

$$\frac{\partial\epsilon}{\partial\Omega_p} d\Omega_p + \frac{\partial\epsilon}{\partial\omega_{LSPR}} d\omega_{LSPR} = 0$$

which when solved is

$$-\frac{2\Omega_p}{\omega_{LSPR}^2 + \Gamma^2} d\Omega_p + \frac{2\omega_{LSPR}\Omega_p^2}{\left(\omega_{LSPR}^2 + \Gamma^2\right)^2} d\omega_{LSPR} + \frac{\partial\epsilon^{ib}}{\partial\omega_{LSPR}} d\omega_{LSPR} = 0$$

We neglect the last parameter which relates to the interband transitions and is expected not to vary much with small changes in energy. By simplifying the above expression we get

$$\frac{d\Omega_p}{\Omega_p} = \frac{d\omega_{LSPR}}{\omega_{LSPR}\left(1 + \frac{\Gamma^2}{\omega_{LSPR}^2}\right)}$$

In Au, the resonance occurs around $\omega_{LSPR} \approx 2eV$ and $\Gamma \approx 0.1$. In this case, one can see that the fraction in the denominator is roughly around 0.003 which may be negligible. This allows us to write

$$\frac{d\Omega_p}{\Omega_p} \approx \frac{d\omega_{LSPR}}{\omega_{LSPR}}$$

The relative shift in energy of the LSPR spectrum, ω_{LSPR} can be related to the variation in the conduction electron density ΔN such as:

$$\frac{\Delta\lambda_{LSPR}}{\lambda_{LSPR}} = -\frac{\Delta\omega_{LSPR}}{\omega_{LSPR}} \approx -\frac{\Delta\Omega_p}{\Omega_p} = -\frac{1}{2}\frac{\Delta N}{N} \tag{1.57}$$

This relation thus shows that increasing the electron density in a plasmonic metal leads to a blue shift of the spectrum and descreasing it to a red shift [i36]. Increasing the conduction electron density within

a plasmonic particle can be done in different ways. Ershow et al. have shown that, when exposing a solution of colloidal nanoparticles to dihydrogen, leads to a blue shift of the LSPR spectrum [i37]. Their interpretation is that as the H_2 adsorbs on Au nanoparticles, a dissociation occurs with the H_2 ceding its electrons to the Au nanoparticle and are released as protons in solution. This leads to an increase in the electron density within the Au nanoparticle and hence a blue shift as confirmed by eq. 1.57.

Using capacitive charging, Hoener et al. have shown that on $94 \times 41nm$ nanorods, although very weak, a blue shift of $2meV$ is induced when a potential from $0.1V$ to $-0.3V$ is applied to the nanoparticles [i38]. Again this can be interpreted as an increase in electron density in the nanoparticles which according to eq. 1.57 leads to a decrease in the wavelength resonance i.e. a blue shift. This result correlates with an older paper from Ali et al. whom have shown similar results where a red shift of about $5nm \approx 4meV$ when positivily increasing the potential from $0.05V$ to $0.55V$ (decreasing N) on $9nm$ Au nanoparticles [i39]. Similar observations have be reported by several authors [i40]–[i42].

In these three cases, the electron density in the particle is changed either by injecting or depleting electrons. Would it be possible, in the case of small nanoparticles, to change the distribution of the electron density by adsorbing molecular compounds on their surface ? Indeed, in inorganic chemistry, it is well known that metallic complexes are molecules with a Lewis acid metal core and basic ligands, that is the metal cedes its electron density towards to ligands. This leads to an increase in the oxidation state of the metal which thus becomes positively charged. This however does change the overall charge of the molecule, but only leads to a redistribution in the electron density within the complex. For instance, chloroauric acid $HAuCl_4$ has its gold at a degree of oxidation of 3 (denoted Au^{III}). Each of the chlorine ligands have a degree of oxidation of -1 and the hydrogen of $+1$. Thus the total charge of the gold complex is neutral, but the charge density is redistributed towards to the electronegative ligands.

It is therefore conceivable that as molecular species adsorb on a gold nanoparticles to form a *pseudo-complex*, it would mobilise the electron density within the newly formed bonds. This would in turn reduce the amount of conduction electrons available to undergo oscillations taking part in the LSPR, in turn reducing N and thus leading to a red shift in of the LSPR. This statement is supported by DFT calculations undertaken by Hu et al. where they have studied the electronic structures of macromolecular complexes obtained upon H adsorption on Au_{85} [i43]. The charge redistributes from the cluster and accumulates within the $\mathrm{metal} - H$ bond as shown in figure 1.18. They concluded that the band structure changes around the adsorption sites. Their results reveal that electrons are donated by H and back donated by metal atoms upon H_2 dissociative adsorption.

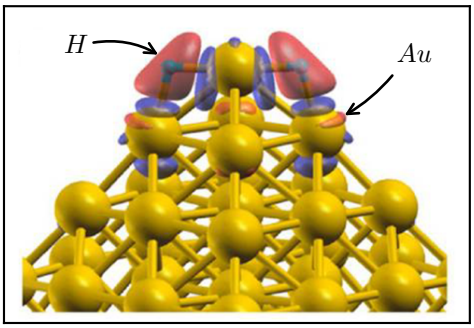

FIGURE 1.18: Au_{85} cluster with adsorbed H atoms calculated by DFT. The electron accumulation and depletion are represented by blue and red surfaces, respectively [i43].

Experimentally Goldmann et al. have shown that adsorbing different organic molecules on a gold surface leads to a modification in the conduction electron distribution at the interface between the metal and the adsorbed molecules [i35]. They have studied the adsorption of dodecanethiol molecules, which are aliphatic chains of 12 carbons terminated with a thiol group, and three different aromatic thiols: phenylthiol, p-biphenilthiol and p-terphenylthiol. Ellipsometric results showed that a 16nm deep layer forms at the surface of the metal where the density in conduction electron is strongly increased and the mobility of the electrons is decreased compared to bulk gold.

These examples show that as well as changing the refractive index in the vicinity of the nanoparticles, inducing a charge transfer by adsorbing molecular species also results in spectral shifts. Furthermore, the amplitude of the shift can quantitatively be related to the changes in conduction electron density which, if the total number of atoms at play is known, give insight into the number of electron charge transferred. This information can be of great value for better understanding catalytic activity, as well as energy transformation such as in solar cells.

• **Influence of the size**

Within the quasi-static approximation, we have seen that because of the confinement of the conduction electrons, decreasing the size of a particle basically leads to a decrease and broadening of the LSPR spectrum (cf Fig. 1.11 & 1.11.b.d.). In this regime, for an isolated nanoparticle with $R \ll \lambda$, the particle's extinction is mainly composed of the absorption spectrum as the particle size is too small to significantly scatter the incident light. When the particle's size increases to the point where it becomes non negligible with respect to the wavelength, multipolar effects occur which cannot be treated within the quasi-static approximation nor with in the dipolar model as expressed in the previous section. Moreover, scattering becomes non negligible and becomes the main component of the extinction spectrum for large particles. The theory of Mie was developed to analytically calculate the optical response of such large particles [i6]. This formulation is still limited to ellipsoids but is classically used for such cases. Other numerical approaches can also be used such as but not limited to discrete dipole approximation (DDA).

To illustrate this, the following spectra drawn in figure 1.19 show the calculated efficiency factors spectra of extinction, absorption and scattering for silver spheric particles of size ranging from 5nm to 50nm in radius. The method chosen was to use the numerical approach DDA, which is suitable to illustrate the phenomena, more information is given in section 1.3.3.

As we can see for particles smaller than 25nm in radius, the extinction is primarily due to the absorption of the silver particle, though the scattering contribution is indeed increasing. Increasing the size of the particle leads to an increase in scattering which becomes the main contribution responsible for the extinction spectrum. This leads to a completely different spectrum with many different peaks which are due to multipolar resonances as the particle is not small enough for the quasi-static approximation to apply.

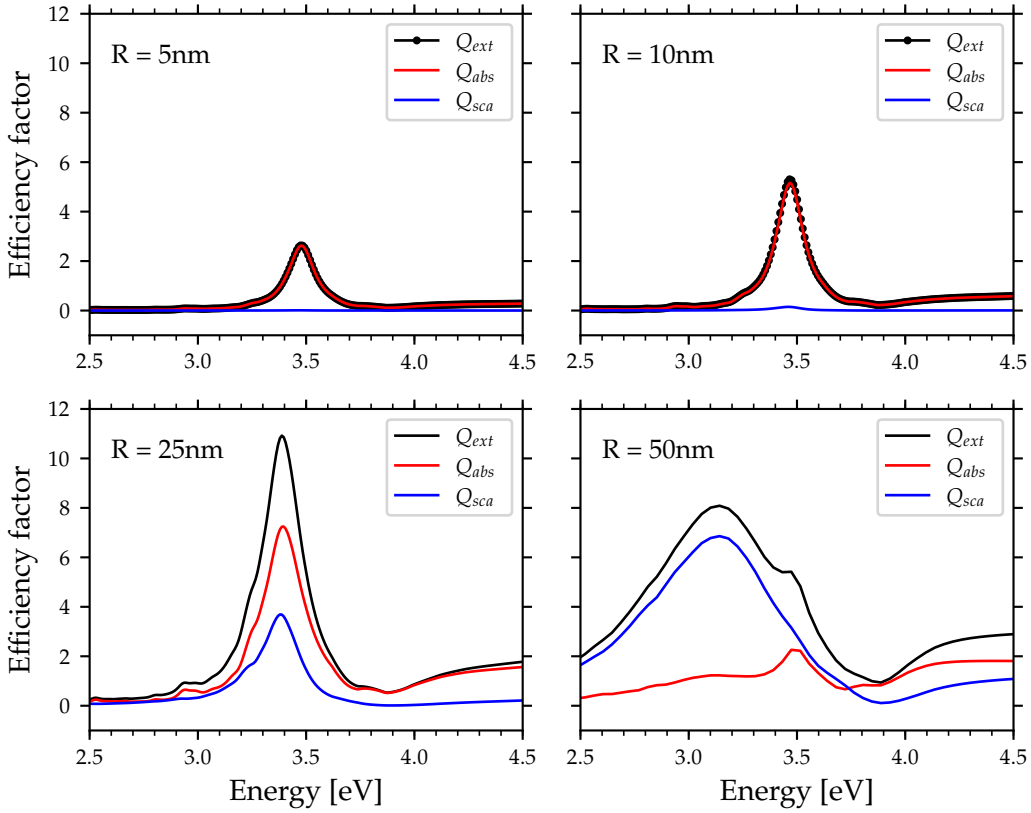

FIGURE 1.19: Efficiency factors calculated by discrete dipole approximation (DDA) for Ag spheres of radii a. $5nm$, b. $10nm$, c. $25nm$ and d. $50nm$, each containing 4 224 dipoles. $Q \equiv \sigma/\pi a_{eff}^2$ cf. 1.3.3. In the latter case, the number of dipoles used is pretty low, however, the general behaviour of the spectrum is reproduced.

• Influence of particle — particle interaction

The effect of two particles in proximity on the global LSPR response can be analytically calculated. Indeed, the dipole induced on a particle by the external electric field induces a polarisability on a particle positioned near to this dipole and vice versa, the other particle induces a polarisation on the first particle. In other words, the electric field *seen* by a single particle is a combination of the external electric field and the perceived field from the particles in vicinity. Although still within the quasi-static approximation, the electric field acting on the particles are not uniform anymore, and multipolar distribution of charges should be considered. However, the main effect of the interaction can be estimated by using the dipolar approximation, both particles being described by a point dipole $\boldsymbol{p}_i$

Looking at the simple particle − particle interaction, the polarisability of the particles can be calculated for the electric field parallel and perpendicular to the direction of alignment of the particle. Lets consider two spheric particles 1 and 2 of radius R, separated by a distance center to center d on which an electric field $\boldsymbol{E}_{ext}$ is applied parallel or perpendicular to the direction of alignment of the particles as shown in figure 1.20.

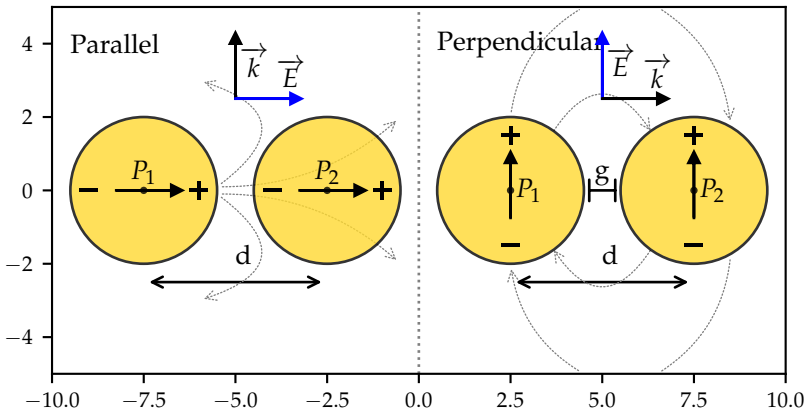

FIGURE 1.20: Schematic showing two dipoles interacting with an external electric field parallel or perpendicular to the alignment of the particles. The line field from p_1 are schematised as grey arrows.

The dipole moment of the system is written as:

$$\boldsymbol{p} = \boldsymbol{p}_1 + \boldsymbol{p}_2 = \varepsilon_0 \varepsilon_m \, \alpha \boldsymbol{E}^{ext} \tag{1.58}$$

The dipole moment of a particle can be written as in terms of its local electric field:

$$\boldsymbol{p}_1 = \varepsilon_0 \varepsilon_m \, \alpha_1 \boldsymbol{E}_1^{loc} \tag{1.59a}$$
$$\boldsymbol{p}_2 = \varepsilon_0 \varepsilon_m \, \alpha_2 \boldsymbol{E}_2^{loc} \tag{1.59b}$$

where the local electric field is the sum of the external electric field and the electric field induced by the neighbouring particle.

$$\boldsymbol{E}_1^{loc} = \boldsymbol{E}^{ext} + \boldsymbol{E}_{2\to1} \tag{1.60a}$$
$$\boldsymbol{E}_2^{loc} = \boldsymbol{E}^{ext} + \boldsymbol{E}_{1\to2} \tag{1.60b}$$

Let's first consider the parallel case. The electric field created by the point dipoles can symmetrically be written as follows:

$$\boldsymbol{E}_{2\to1} = \frac{2}{4\pi d^3} \frac{\boldsymbol{p}_2}{\varepsilon_0 \varepsilon_m} \tag{1.61a}$$
$$\boldsymbol{E}_{1\to2} = \frac{2}{4\pi d^3} \frac{\boldsymbol{p}_1}{\varepsilon_0 \varepsilon_m} \tag{1.61b}$$

Therefore, by combining eq. 1.61a and eq. 1.61b with the initial dipole moments eq. 1.60a and eq. 1.60b to give:

$$\boldsymbol{p}_1 = \varepsilon_0 \varepsilon_m \, \alpha_1 \left(\boldsymbol{E}^{ext} + \frac{2}{4\pi d^3} \frac{\boldsymbol{p}_2}{\varepsilon_0 \varepsilon_m} \right) \tag{1.62a}$$

$$\boldsymbol{p}_2 = \varepsilon_0 \varepsilon_m \, \alpha_2 \left(\boldsymbol{E}^{ext} + \frac{2}{4\pi d^3} \frac{\boldsymbol{p}_1}{\varepsilon_0 \varepsilon_m} \right) \tag{1.62b}$$

for clarity, we define $D_{\parallel} = \frac{2}{4\pi d^3}$. Thus by combining and simplying eq. 1.62a and 1.62b one gets:

$$\boldsymbol{p}_1 = \varepsilon_0 \varepsilon_m \, \alpha_1 \frac{1 + \alpha_2 D_{\parallel}}{1 - \alpha_1 \alpha_2 D_{\parallel}^2} \boldsymbol{E}^{ext} = \varepsilon_0 \varepsilon_m \, \alpha_1^{eff} \boldsymbol{E}^{ext} \tag{1.63a}$$

$$\boldsymbol{p}_2 = \varepsilon_0 \varepsilon_m \, \alpha_2 \frac{1 + \alpha_1 D_{\parallel}}{1 - \alpha_1 \alpha_2 D_{\parallel}^2} \boldsymbol{E}^{ext} = \varepsilon_0 \varepsilon_m \, \alpha_2^{eff} \boldsymbol{E}^{ext} \tag{1.63b}$$

Now that the individual dipole moment can be calculated, the overall dipole moment $\boldsymbol{p}$ of the system is simply their sum. In the special case where the two particles are identical in size and dielectric functions, then $\alpha_1 = \alpha_2 = \alpha$ and $\boldsymbol{p}_1 = \boldsymbol{p}_2$ which gives the effective polarisability of the system as:

$$\alpha_{\parallel}^{eff} = 2 \frac{\alpha}{1 - D_{\parallel} \alpha} = 2 \frac{\alpha}{1 - \frac{2}{4\pi d^3} \alpha} \tag{1.64}$$

$$\tag{1.65}$$

The same demonstration can be done for the electric field perpendicular to the axis of alignment of the particles. In this case:

$$\boldsymbol{E}_{2 \to 1} = \frac{-1}{4\pi d^3} \frac{\boldsymbol{p}_2}{\varepsilon_0 \varepsilon_m} \tag{1.66a}$$

$$\boldsymbol{E}_{1 \to 2} = \frac{-1}{4\pi d^3} \frac{\boldsymbol{p}_1}{\varepsilon_0 \varepsilon_m} \tag{1.66b}$$

In the same way, one can define $D_{\perp} = \frac{1}{4\pi d^3} = \frac{D_{\parallel}}{2}$, which, following the same demonstration as above yields the effective polarisability:

$$\alpha_{\perp}^{eff} = 2 \frac{\alpha}{1 + D_{\perp} \alpha} = 2 \frac{\alpha}{1 + \frac{1}{4\pi d^3} \alpha} \tag{1.67}$$

$$\tag{1.68}$$

To understand the effect of this interaction on the LSPR of the system, let's look at two Au particles at different distances from each other. The distance between the particles is set in the equations center to center. To account for the radius of the particles, but mitigate its effect to only focus on the particle - particle

interaction, the dielectric function chosen was that of bulk Au without the effect of confinement. The gap separating the particle g, is thus written as a percentage of the diameter of the particle.

The spectra are plotted on figure 1.21 for the electric field parallel and perpendicular to the axis of symmetry as shown in figure 1.20. The effect of the particle - particle interaction on the overall spectrum is dependent on the orientation of the electric field. When the electric field is parallel to the axis of symmetry of the system, bringing the particles closer to one another leads to a red shift of the LSPR spectrum with a slight increase in intensity. When the electric field is perpendicular, the opposite effect occurs as the particle interaction leads to a blue shift of the LSPR spectrum as well as a decrease in intensity.

This example shows that the decrease in symmetry of the system leads to a polarisation dependence, similar to that of an ellipsoid.

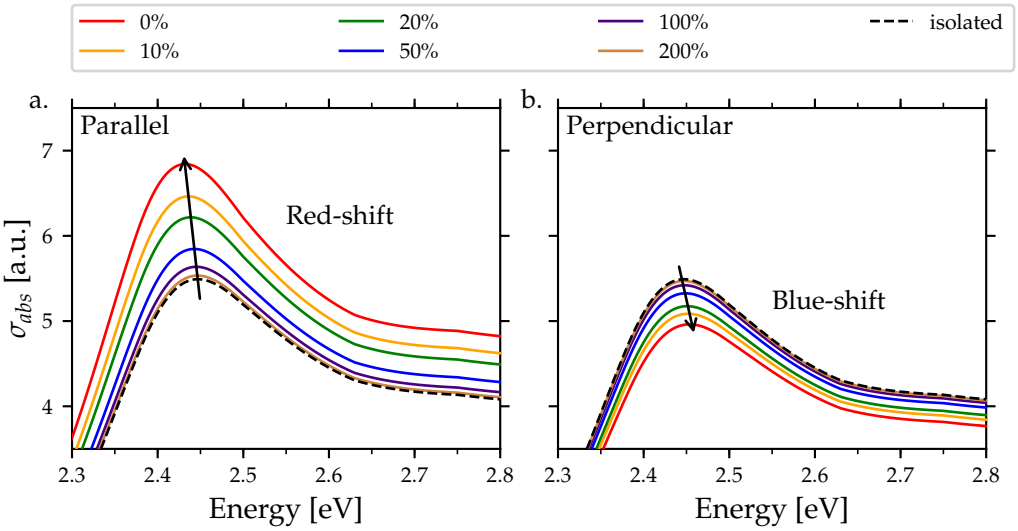

FIGURE 1.21: LSPR spectra for two interaction Au spheres with the electric field (a.) parallel and (b.) perpendicular to the alignment of the particles. The distance if given as a percentage of the radius of the particles

This can be figuratively explained by considering the dipole within the particle as a harmonic oscillator with a restoring force. In both the parallel and perpendicular orientations, the electric field seen by a single particle is the combination of the external electric field and the created field by the other particle. In the parallel case, the dipoles are aligned in the same direction thus the electric field created by depole 1 onto dipole 2 is opposite to the restoring force (Fig. 1.20 parallel). This therefore leads to a red shift of the LSPR response. Whereas, in the perpendicular case, the dipoles are parallel to each other, thus the electric field induced by one particle on the other is in the opposite direction to the dipole (Fig. 1.20 perpendicular). In other words, the induced electric field is in the same direction as the restoring force thus increasing the recoil. This effect leads, in this later cases to a blue shift of the spectrum.

- **Influence of the substrate**

In the case of particles deposited on a substrate, one must account for its effect on the optical response of the particle. There are multiple ways of accounting for a substrate. The most simple way to do so is to use an effective medium approximation. This can be simply done by substituting the spherical particle on a substrate by a spherical particle in a matrix of an averaged dielectric function, ε_{avg} between the medium ε_m and the supporting material, ε_{surf}, effectively writing:

$$\varepsilon_{avg} \approx \frac{1}{2}\left(\varepsilon_m + \varepsilon_{surf}\right) \tag{1.69}$$

This leads to a red shift as explained in p. 20 as long as the medium refractive index is larger than 1. Nevertheless, an alternative method known as the method of image dipoles can be used. The method is analogous to the particle - particle interaction demonstrated above. It proposes to calculate the polarisability of a particle by accounting for the external electric field and an electric field induced by an image particle positioned in the plane of symmetry within the substrate. Figure 1.22 shows a diagram illustrating the image dipoles generated by a particle on a substrate.

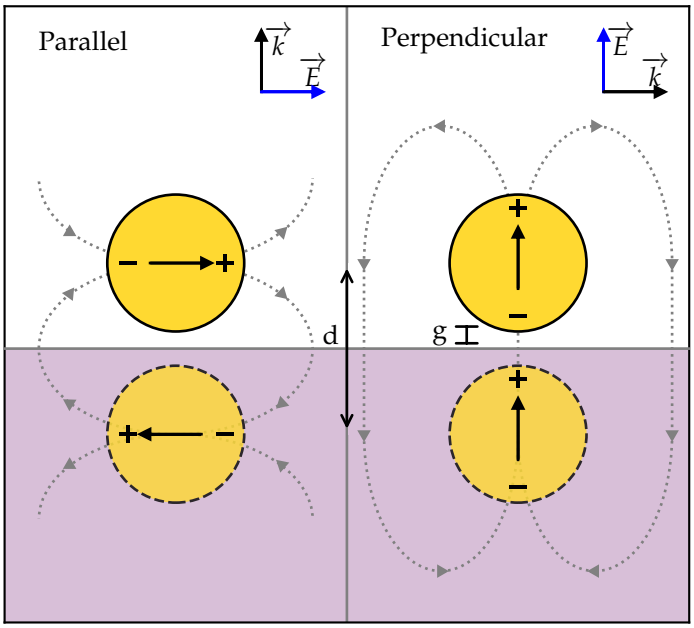

FIGURE 1.22: Schematic of a dipole interacting with a substrate generating an image dipole with the electric field parallel and perpendicular to the surface.

Two cases are considered. On the left hand side, the electric field is parallel to the surface of the substrate. In this situation, the electric field of the particle induces an image dipole oriented in the opposite direction to the dipole of the particle. On the other hand, in the case where the electric field is perpendicular to the substrate, both the dipole and image dipole are oriented in the same direction. Calculating the optical response of the system can be done by considering the effect of the induced dipole, i.e. image dipole on the particle. The dipole moment of a spheric particle near a surface is

$$\boldsymbol{p} = \varepsilon_0 \varepsilon_m \, \alpha \boldsymbol{E}^{loc} \tag{1.70}$$

where the local electric field seen by the particle $\boldsymbol{E}^{loc}$ is defined as the external electric field $\boldsymbol{E}^{ext}$ applied to the particle added to the electric field induced by the image dipole to the particle $\boldsymbol{E}_{id \to part.}$:

$$\boldsymbol{E}^{loc} = \boldsymbol{E}^{ext} + \boldsymbol{E}_{id \to part.} \tag{1.71}$$

Defining the electric field created by the induced dipole depends on the direction of the electric field parallel or perpendicular to the substrate plane as illustrated in figure 1.22. When the external electric field is parallel to the substrate plane, the dipole in the particle aligns to the electric field and the image-dipole, whereas, when the electric field is perpendicular to the substrate plane, both the particle and image dipoles are aligned with the electric field. Mathematically, the electric fields induced by the image dipoles are written as

$$\boldsymbol{E}^{\parallel}_{id\rightarrow part.} = \frac{1}{4\pi d^3}\frac{\boldsymbol{p}^{\parallel}_{id}}{\varepsilon_0\varepsilon_m} \tag{1.72a}$$

$$\boldsymbol{E}^{\perp}_{id\rightarrow part.} = \frac{2}{4\pi d^3}\frac{\boldsymbol{p}^{\perp}_{id}}{\varepsilon_0\varepsilon_m} \tag{1.72b}$$

Therefore, we can write the equation of polarisation for both cases as

$$\boldsymbol{p}^{\parallel} = \varepsilon_0\varepsilon_m\left(\boldsymbol{E}^{ext} - \frac{1}{4\pi d^3}\frac{\boldsymbol{P}^{\parallel}_{id}}{\varepsilon_0\varepsilon_m}\right) \tag{1.73a}$$

$$\boldsymbol{p}^{\perp} = \varepsilon_0\varepsilon_m\left(\boldsymbol{E}^{ext} + \frac{1}{4\pi d^3}\frac{2\boldsymbol{P}^{\perp}_{id}}{\varepsilon_0\varepsilon_m}\right) \tag{1.73b}$$

The polarisability of the image dipole $\boldsymbol{P}_{id}$ is defined as

$$\boldsymbol{p}^{\parallel}_{id} = -F\boldsymbol{p} \tag{1.74a}$$

$$\boldsymbol{p}^{\perp}_{id} = F\boldsymbol{p} \tag{1.74b}$$

$$where \quad F = \frac{\varepsilon_{surf} - \varepsilon_m}{\varepsilon_{surf} + \varepsilon_m} \tag{1.74c}$$

By combining these equations we get the dipole moment of the particle

$$\boldsymbol{P}^{\parallel} = \varepsilon_0\varepsilon_m\frac{\alpha}{1 - \frac{F\alpha}{4\pi d^3}}\boldsymbol{E}^{ext} = \varepsilon_0\varepsilon_m\,\alpha^{eff}_{\parallel}\boldsymbol{E}^{ext} \tag{1.75a}$$

$$\boldsymbol{P}^{\perp} = \varepsilon_0\varepsilon_m\frac{\alpha}{1 - \frac{2F\alpha}{4\pi d^3}}\boldsymbol{E}^{ext} = \varepsilon_0\varepsilon_m\,\alpha^{eff}_{\perp}\boldsymbol{E}^{ext} \tag{1.75b}$$

Thus the effective polarisability for both cases are

$$\alpha^{eff}_{\parallel} = \frac{\alpha}{1 - \frac{1}{4\pi d^3}F\alpha} \tag{1.76a}$$

$$\alpha^{eff}_{\perp} = \frac{\alpha}{1 - \frac{2}{4\pi d^3}F\alpha} \tag{1.76b}$$

To visualise the effect of the substrate on the LSPR, let's plot the absorption cross-section using the effective polarisabilities calculated above for a gold sphere in vacuum on a substrate of dielectric function $\varepsilon_{surf} = 1.5^2$ (Fig 1.23). The LSPR was calculated using the bulk dielectric function of gold. The gap from the substrate, g is calculated as a percentage of the particle's diameter.

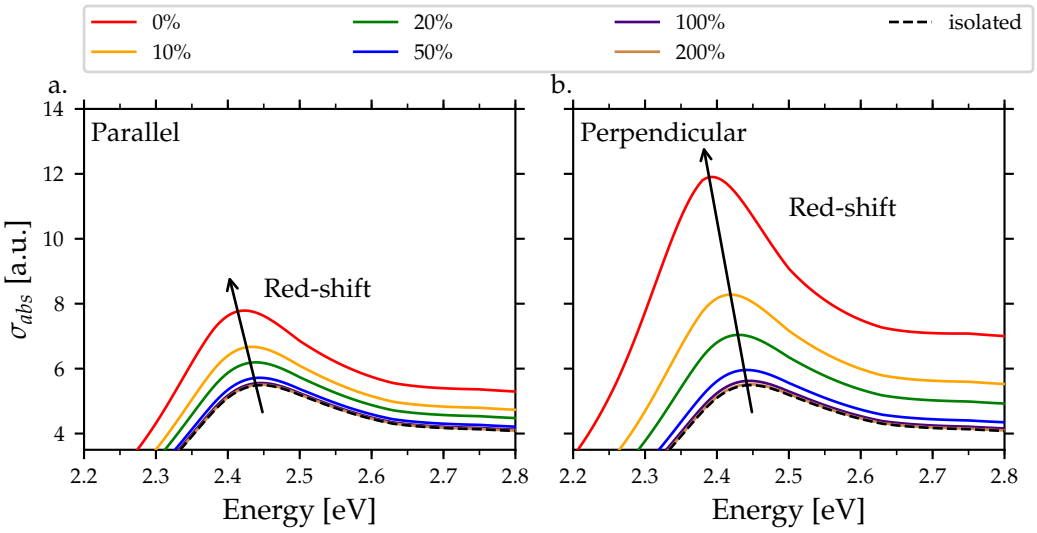

FIGURE 1.23: LSPR spectra Au sphere interacting with a glass substrate with the electric field (a.) parallel and (b.) perpendicular to the surface.

In both cases a red shift is induced as the particles get closer to the surface though the intensity of the shift is dependent on the direction of the electric field. In the parallel case, the intensity of the red shift is lower than for the perpendicular shift. This demonstration shows that, generally, the effect of the substrate on the LSPR is to lead to a red shift on the spectrum regardless of the direction of the electric field. Although this has been analytically demonstrated only for spheres or spheroids, with their resolution axes normal to the surface, it can be inferred that the red shift effect is generalised to particles of any shape.

Through these examples, it is clear how the LSPR response of one or more particles can be influenced. Indeed they are important for understanding and calculating experimental phenomenon. Yet these analytical models reach a limit since they only apply to specific shapes and conditions, and only consider dipolar effects. Thus one might ask, how to deal with more complex systems such as oddly shaped particles, or heterogeneous compositions? Numerical models have been developed to address these problems and the first one we shall focus on is the discrete dipole approximation (DDA).

1.3.3 Determination of the LSPR: beyond analytical calculation

• Introduction to discrete dipole approximation (DDA)

The opportunity of having increased computational power makes it possible to calculate the optical properties of complex particles. We have discussed the possibility of solving simple systems in the previous section, although, they are not capable of calculating the optical response of complex systems. Lets first look at the limitations in shape. So far, the only shape one can easily calculate were mainly variants of ellipsoids. Yet, calculating the polarisability of a arbitrary shaped particle only requires to sum the infinite dipole moments induced by an electric field. Simply stated, this is what the discrete dipole approximation (DDA)

intends to do though its original application had little to do with calculating the LSPR of arbitrary shaped nanoparticles.

"DDA is an approximation of the continuum target by a finite array of polarisable points. The points acquire dipole moments in response to the local electric field. The dipoles of course interact with one another via their electric fields" [i44]. DDA is thus capable of calculating the optical response of particles of arbitrary shape and composition. The accuracy of the result is dependent on what can be considered as the *resolution* of the particle if one were to consider the inter-dipole to be the analogous to a voxel[1]. Increasing the number of dipoles or voxels does increase the accuracy but of course also increase the computational time.

The initial principle for DDA was introduced by DeVoe to study the optical properties of molecular dye aggregates in 1964 [i45]. The main limitation he had to deal with was the fact that *retardation* was not accounted for in his model which meant that only small aggregate could be studied. The retardation effect is where the quasi-static approximation breaks down. Indeed when a particle system extends on a large distance, treating the systems as being subjected to an homogeneous electric field is incorrect even if the individual particle size is smaller compared to the wavelength. The electric field thus changes significantly through the course of a radiation period inducing more complex effects.

The first use of DDA (with retardation effects) was described by Purcell et al. in 1973 published in the Astrophysical Journal [i46]. The problem they proposed to solve was to calculate "the approximate extinction, absorption and scattering cross-sections for dielectric grains of arbitrary shapes with dimensions comparable to or smaller than the wavelength of the incident radiation". The grains in question were interstellar dust which have been studied experimentally but electrostatic models as described in the previous section were not suited for calculating such systems.

The model was later reformulated by Singham et al. to account for superposition of partitionned segments when processing large particles [i47], [i48]. Nevertheless, DDA was only popularised outside the astrophysisist field by Draine et al. with their paper entitled "Discrete dipole approximation for scattering calculations" published in 1994 [i44]. In this paper, they not only covered into details the theoretical background of DDA, but also proposed a FORTRAN implantation: DDSCAT.

• Applications of DDA for calculating the LSPR of metallic nanoparticles

DDSCAT calculates the efficiency factors for the absorption , scattering and extinction of a system which are defined as:

$$Q_{abs} \equiv \frac{\sigma_{abs}}{\pi a_{eff}^2} \tag{1.77a}$$

$$Q_{sca} \equiv \frac{\sigma_{sca}}{\pi a_{eff}^2} \tag{1.77b}$$

$$Q_{ext} \equiv Q_{abs} + Q_{sca} \tag{1.77c}$$

$$where \quad a_{eff} \equiv \sqrt[3]{\frac{3V}{4\pi}} \tag{1.77d}$$

where σ_{abs} and σ_{sca} are the respective absorption and scattering cross-section, a_{eff} is the effective radius i.e. the radius of a sphere of equal volume V, to the nanoparticle.

[1] A voxel stands for a *volume element* which is the 3D analogous to the 2D pixel.

The usual first step when undertaking such intensive calculation is to determine the minimum resolution required to get the best ratio between accuracy of the calculation and the time it takes to converge to the result. In the specific case of DDSCAT, this is represented by the number of dipoles one needs to well represent the particle. Indeed, DDSCAT defines the target as a set of dipoles, hence the more dipoles used the more accurate the target is represented.

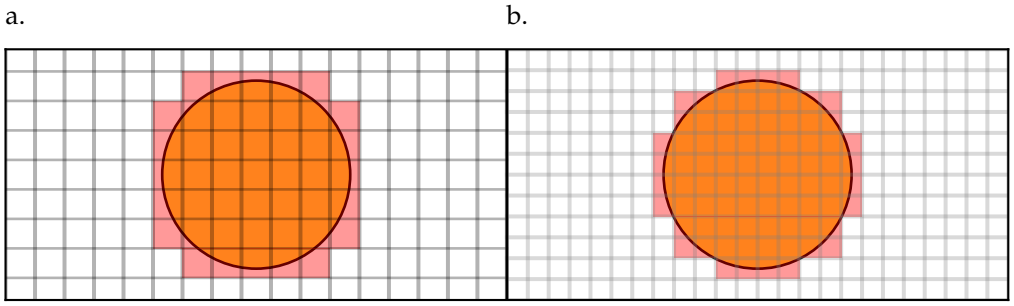

FIGURE 1.24: Schematic showing a disk in a grid and how DDSCAT distributed the dipoles. a. shows a large grid which gives a total of 45 dipoles representing the disk and b. shows a tighter grid which represents the disk with 80 dipoles.

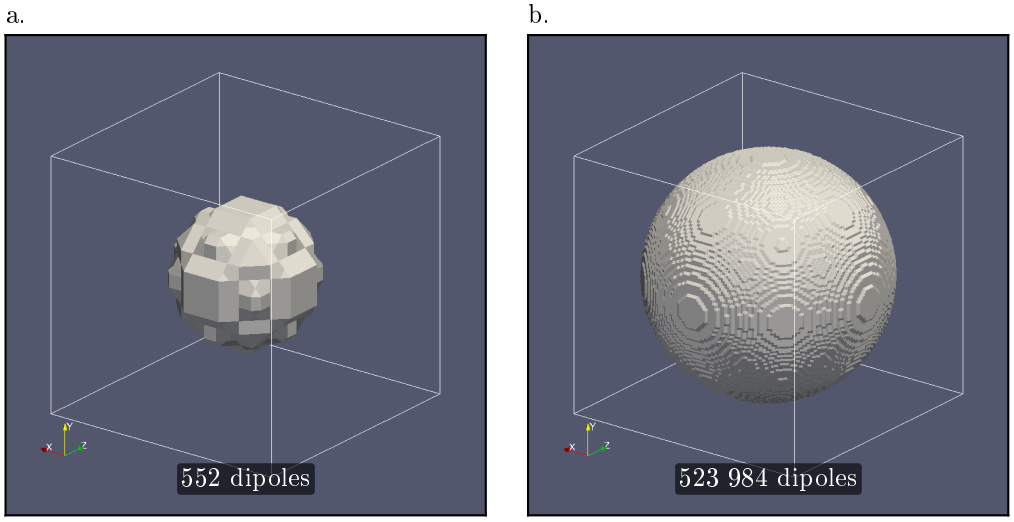

FIGURE 1.25: Three dimensional view of two particles of same volume generated by DDSCAT with a. having 552 dipoles and b. 523 984 dipoles.

This is illustrated in two dimensions in figure 1.24. On this diagram, one can see two disks drawn in two different sized grids. Each square of the grid represents a single dipole. What DDSCAT does is counting the number of squares overlapping the target and counts it as a target dipole. This is represented in red in the diagram. Therefore it is clear in figure 1.24.a that the dipole assembly is far from representing a perfect circle. In this first case the number of dipole representing the target is set to 45. On the right hand side diagram (Fig. 1.24.b), the size of the grid is reduced, thus the target more resembles a circle though still with rough edges even with the number of dipoles increased to 80. In practise the targets are of course represented in three dimensions. Figure 1.25.a and b shows two spherical targets each having 552 and 523 984 dipoles respectively. As it can be seen on these real targets, the sphere with more dipoles has less surface roughness than the small 552 dipoles. However, increasing the number of dipoles does come at a

cost. Figure 1.26 shows the total CPU time against the number of dipoles for an example type of calculation on the machine used at the time of writing. That is a silver sphere of $20nm$ in radius in vacuum, calculated at 24 wavelengths from $300nm$ to $450nm$. The calculations were done on a machine running on a *i7 7600U* which carries a 2 core $2.6Ghz$ processor with $8Gb$ of RAM.

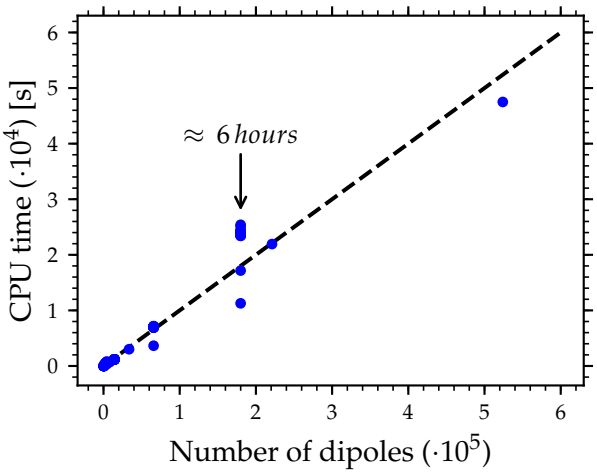

FIGURE 1.26: Plot of the CPU time in seconds to calculate a Ag sphere calculated at 24 wavelengths from $300nm$ to $450nm$ against the number of dipoles constituting the sphere.

This graph shows a linear relationship between the CPU time and the number of dipoles used. The CPU time can therefore increase very fast and calculation can easily take several days if many dipoles are used. The obvious question therefore is: what is the minimum number of dipoles required to get accurate results ? This question does not have a straight forward answer though. Generally, the larger the particle, the greater the number of dipoles required to calculate its optical response. Indeed, considering a small gold particle of $2nm$ in diameter has about $\approx$ 200 atoms. If one is to use 1000 dipoles to represent such a particle, the density is high. On the other hand, for a large particle of $100nm$ in diameter, the number of atoms exceeds 30 millions which means that the dipoles (kept to 1000) becomes very low.

To illustrate the effect of this point, let's compute the efficiency factor for extinction of a $2nm$ in diameter silver nanosphere in vacuum. In figure 1.27 the resulting spectra are plotted for varying quantities of dipoles. Figure 1.27.a shows the Q_{ext} for 552 to 2176 dipoles. Each sample shows a maximum peak at about the correct energy. However, the shape of the curve is pretty chaotic with multiple peaks in some cases. It is most obvious for 81 dipoles which has a maximum at $\approx 3.43eV$ but a shoulders at 3.3, 3.45 and $3.7eV$. Above 4000 dipoles, the spectra are plotted on figure 1.27.b. This spectra are more reproducible and increasing the number of dipoles only leads to a slight shift, increase in intensity and narrowing of the resonance.

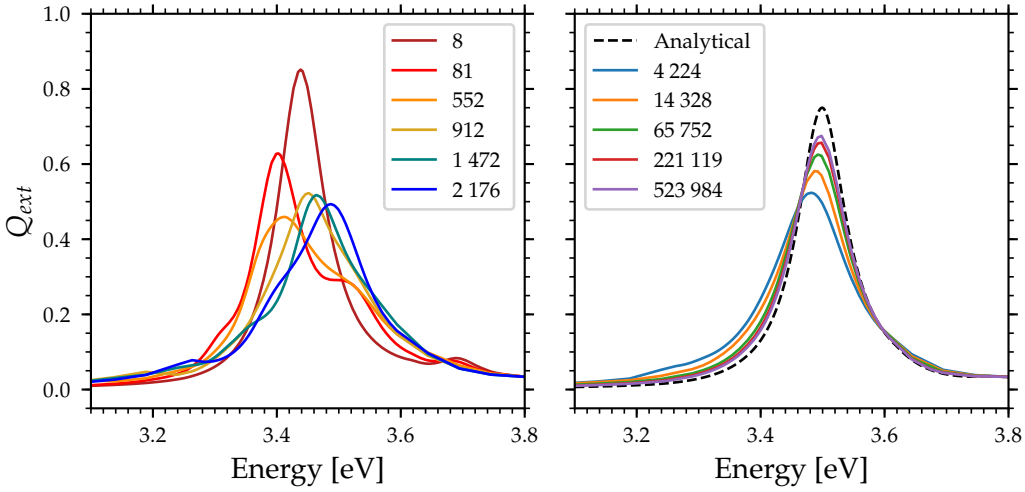

FIGURE 1.27: DDSCAT LSPR spectra calculated for a $2nm$ in diameter Ag sphere with different number of dipoles. The dashed line spectrum on the right hand side shows the analytical calculation for the same system for comparison.

For comparison, the spectrum for the same particle calculated using the analytical model is also plotted on figure 1.27.b. It shows that DDA yields similar result. Yet, even at half a million dipoles, DDA still does not reproduce a perfect sphere, analytically calculated but tends towards it. The origin of this discrepancy does come from the insufficient quantity of dipoles used. More specifically, this likely comes from the shape of the particle which exhibits a structure surface as shown in figure 1.25.b., which induces multipolar effects on the surface ; though small it does contribute in broadening the spectrum. One can still wonder whether using an infinite number of dipoles would yield the same exact result as the analytical calculation. However, this is a computational challenge, and as far the writer's opinion is concern, not a true significance. Indeed, for comparison with experimental fabricated nanosphere, one would need to account for the facets present on the nanoparticles since they are not perfect spheres. What would be interesting, though out of the scope of this work, is to modify the DDSCAT program so it could arrange the dipoles with a face centred cubic lattice structure. This would mimic the structure of metals so each atoms of the particle is represented with a single dipole in which case it could be possible to calculate the nanoparticle containing several hundreds of thousands of dipoles and include the facets and defects. As it is, the dipoles are arranged in cubic lattice structure. It is not known to the writer whether this method would yield reasonable reproduction of experimental data, but could be an interesting path to investigate.

Therefore, to answer the initial question, in the specific case of a particle of $2nm$ in diameter, one can see that the minimum number of dipoles required for accurate results is between 4000 and 14000.

• Enhanced electric field: antenna effects

The key feature of DDSCAT is to be able to calculate the optical response of arbitrary shaped particles. Lets illustrate this point by comparing the optical response of silver particles shaped as a sphere, cube and cylinder but with the same volume of $\approx 4200nm^3$. This yields a sphere of $10nm$ in radius, a cube of side $\approx 16nm$ and a cylinder of radius $10nm$ and height $\approx 13nm$.

Figure 1.28 shows the Q_{ext}, Q_{abs}, & Q_{sca} spectra for each target as well as the electric field at the maximum peak energy. We can see that on every spectra the Q_{ext} and Q_{abs} are super imposed, whereas

the spectra for Q_{sca} is very weak. This is due to the fact that at these dimensions, the particles are too small to scatter light as described earlier. The spectrum for the sphere is the already known single peak at $\approx 3.5eV$ with the interband transitions starting after $\approx 3.9V$. Looking at the near field image, the electric field around the sphere is enhanced in the same direction as the applied external electric field. In the case of the cube, the spectra show multiple peaks with the maximum being at $\approx 3.1eV$ and the second most intense at $\approx 3.3eV$. More less intense peaks are exhibited before the interband transitions which start after $\approx 3.9eV$. The near field image are measured at the maximum peak that is at $3.1eV$. We can see that unlike the case of a sphere, very intense spots are displayed on the corners of the cube. These antenna effects, known as hotspots are induced by sharp features of the particle's shape which induces multipolar effects and thus an high localised electric field. In the last case of a cylinder, the spectra show a maximum peak at $\approx 3.35eV$ with a much lower peak at $\approx 3.5eV$. Looking at the near field images, the cylinder resembles both the sphere and the cube as it has a very intense enhanced field on the rings of the cylinder.

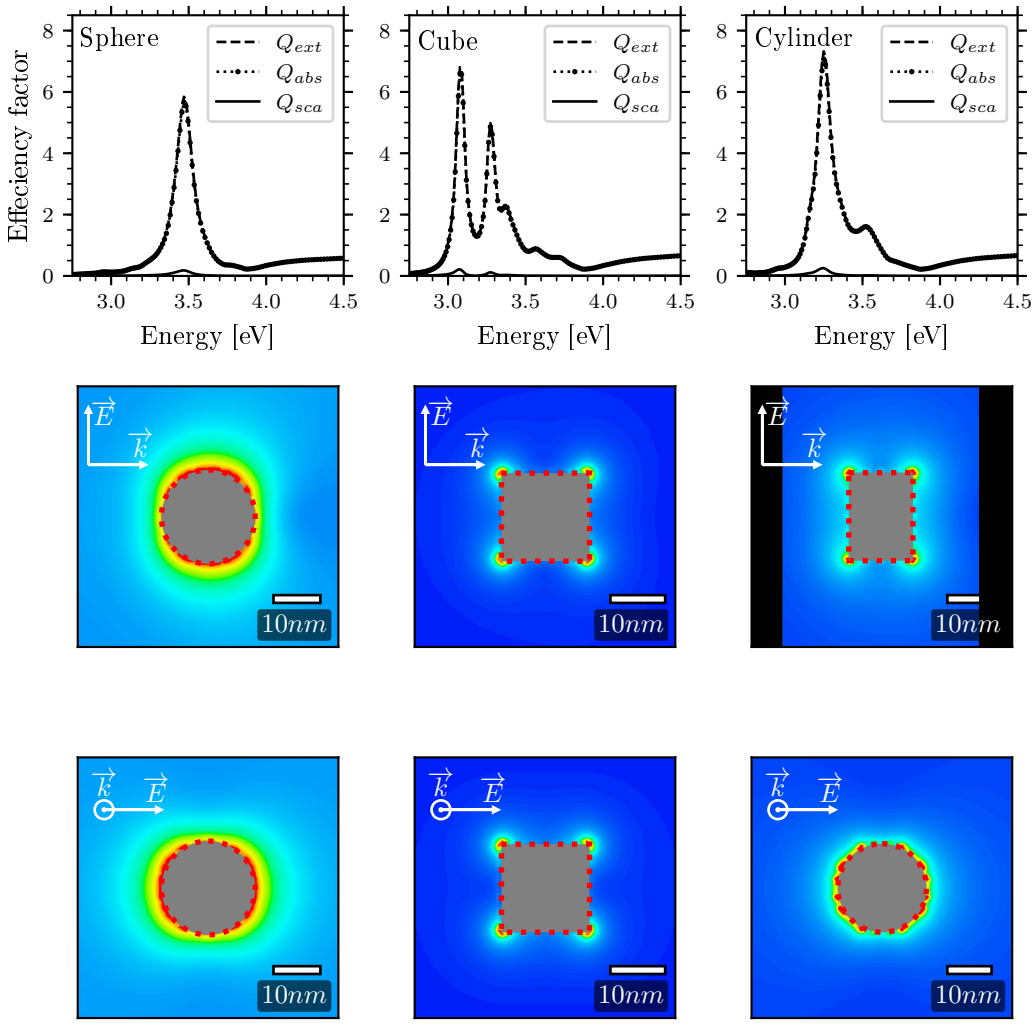

FIGURE 1.28: Efficiency factor spectra calculated for a $10nm$ in radius Ag sphere, a $16 \times 16nm$ Ag cube and a Ag cylinder of $10nm$ in radius and $13nm$ in height. The near electric fields are plotted at the wavelength of maximum intensity beneath the spectra for each system for two orthogonal polarisation.

This set of examples illustrates an important point regarding applications of LSPR for sensing applications. The enhanced field is the region outside the particle where its LSPR is most sensitive to its environment. Therefore, LSPR nanoparticles are mainly sensitive within their close vicinity. The enhanced

field decreases in intensity the further away one gets. The hotspots observed on the cube and cylinder illustrate high intensity regions where the LSPR is even more receptive. Moreover, when bringing two particles near one another, the interaction leads to the generation of such hotspots as illustrated in figure 1.29 where two nanosphere of $10nm$ in radius are brought together with a gap of $8nm$. Indeed, the near field image exhibits a very high intensity hotspot between the two particles. However, only when the electric field is parallel to the alignment of the particles. This latter model finds applications for probing single molecule interaction as a molecule can be inserted in this region of high electric intensity.

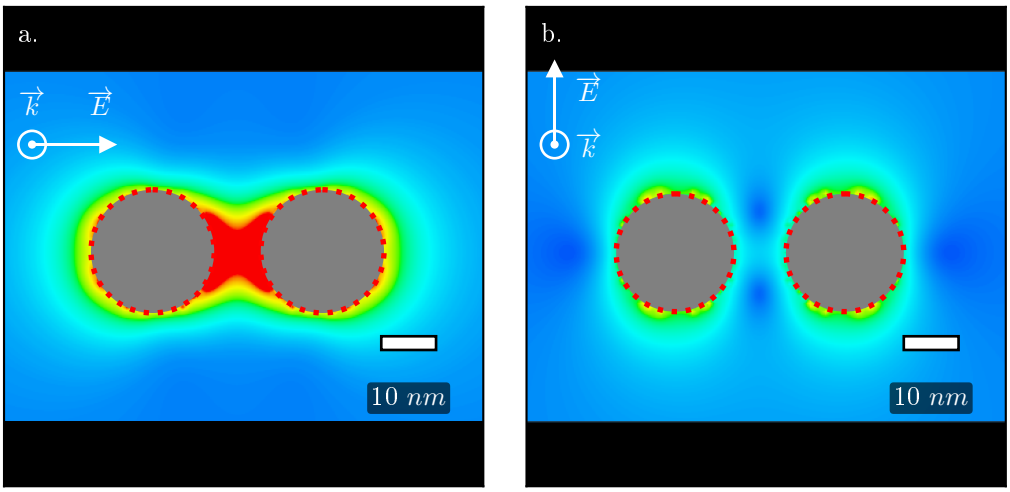

FIGURE 1.29: Near field electric field for two $10nm$ in radius Ag nanoparticles. a. the electric field is aligned with the particle alignment and b. the electric field is perpendicular to the particle alignment.

Throughout these sections, we have discussed the fundamental optical properties of metals, specifically copper, silver and gold which apply to localised surface plasmon resonance. The key points are listed here-after

- Resonance is reached in the visible range for the case of noble metals. Though interband transitions do occur at higher energy and can interfere with the plasmon resonance.
- The LSPR can be modified in several ways, should it be by changes in the medium, charge transfer from or to the particle, variation in the shape of the particle, interaction with either a substrate or other particles, &c....
- Calculating the optical response of either larger particles, particles arbitrary shaped or interacting nanoparticles can be undertaken numerically.
- The enhanced electric field is located in the vicinity of the particle and does not span more than approximately the size of the particle. Which means that the LSPR is mainly sensitive to localised changes within this region.
- sharp features such as edges, vertices or even interacting particles lead to hotspots which are regions of high intensity of the enhanced field.

Lastly, the LSPR of anisotropic particles or particle system shows a dependency on the polarisation of the impinging light. This last point, not discussed in details so far, is a key feature of this writing and is the subject of the next section.

1.4 LSPR-based technologies: sensing applications

1.4.1 Basic principle

From 1997 to 2016, the number of peer reviewed articles devoted to plasmonic systems has increased more than 10 folds as shown in Fig 1.30. Indeed, the use of plasmonic related devices have been studied in various fields such as biomedicine, solar energy, catalysis, &c. . . [i31], [i49]–[i51]. Sensing application is a promising and intensively studied as the properties of LSPR nanoparticles enables one to easily customise them to suite the required needs. The capability of LSPR to sense selectively specific analyte comes from the property of the LSPR spectrum to be dependent on the variation of the refractive index in the vicinity of the particles.

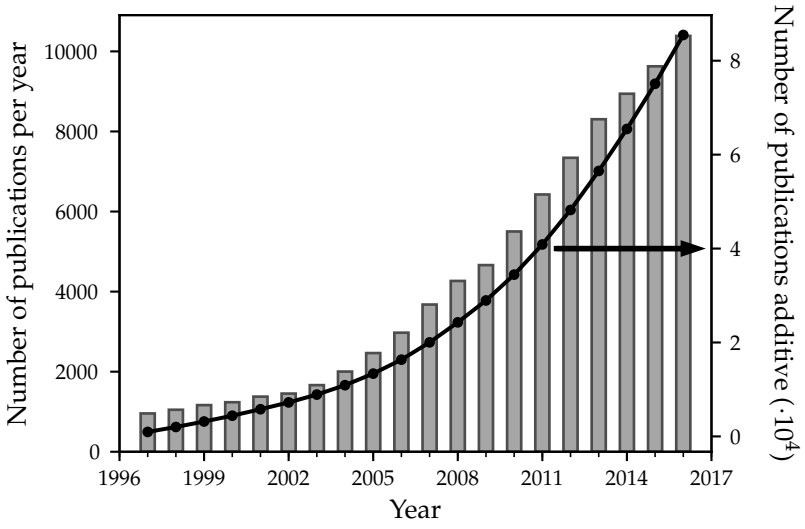

FIGURE 1.30: Bar chart showing on the left y axis the number of publications per year and on the right y axis the cumulative number of publications related to plasmonic nanoparticles from 1996 to 2017. The values were searched from web of science with the terms "*SPR", "plasmon*".

• ELISA, label-free and direct vs. indirect sensors

Many techniques deploy gold nanoparticles for their LSPR properties [i31]. It has found a great use in biological analysis thanks to its relative chemical inertness. The use of this metal as a transducer and antibodies as molecular sensors has made this technique very versatile in terms of possible species to analyse. The method, illustrated in figure 1.31, works as follows [i52]. A layer of antibodies is bonded to a surface. These antibodies are selective to the analyte, hence when they are exposed to the sample containing the analyte, they bind to it. The surface is then exposed to a second solution containing a different antibody compound which plays the role of the transducer by containing a radioactive isotope, a luminescent molecule or in the case of LSPR, a plasmonic nanoparticles. These new antibodies bind to the analyte as well and after washing the surface reveals the presence of the analyte. The washing, known as the separation, is a critical step in the protocol as false positive can occur if unbounded markers are still present. This method is more generally known as the ELISA test standing for *enzyme-linked immunosorbent assay* and is readily used in molecular biology. More sophisticated methods have been developed by adding more steps to generate a higher signal but this is the basic principle.

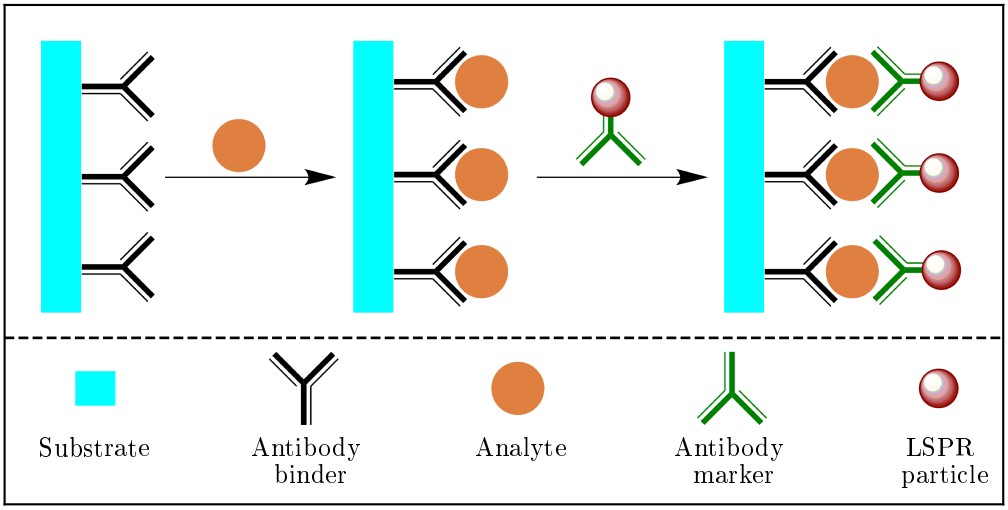

FIGURE 1.31: Diagram illustrating the minimum steps necessary in the ELISA using LSPR nanoparticles as labelled transducers.

The advantages are of course the great sensitivity of the technique as analytes can bond to multiple transducers which greatly amplifys the signal [i53]. Although this method has proven very successful, it does have two main downfalls which are: the need for a laboratory, and of course the multiple steps which can become complicated and difficult to accomplish with good yields. Moreover, the chemical reaction does lead to a denaturation of the analyte which is an issue as in some studies, they require the analyte to be as close as possible to its original state. This is where label-free methods are used with LSPR being a prime candidate for such applications.

The use of nanoparticles which can undergo LSPR has great value. We have already seen how a change in the environment of the particle influences the optical response of the particles (cf section 1.3.2), however, one of the key attributes for sensors is their selectivity towards an analyte. Therefore, gold or silver nanoparticles by themselves are not sufficient for biochemical detection. The label-free method consists in depositing the nanoparticles on a substrate, usually using a self-assembled monolayers (SAM) terminated by amines or thiols which strongly bind to gold nanoparticles. The nanoparticles are then functionalised using a molecular binder usually with one end terminated with a thiol or amine and the other end with an active function. These compounds can be simple organic molecules or complex antibodies depending on the targeted analyte. In this configuration, the spectrum of the LSPR will shift when the analyte binds to the surface of the gold nanoparticle. This principle is known as indirect sensing where the nanoparticle only plays the role of the transducer as shown in figure 1.32.a. The advantages is that the analyte is not modified by a marker, and thus allows the direct study of the chemical reaction occurring between the analyte and the molecular binder [i53].

This method is indeed in opposition with direct sensing where in this latter case, the nanoparticle plays both the role of the optical transducer as well as the chemical probe (Fig. 1.32.b.). However, in this scenario, the chemistry of the metal used is a new factor to take into account. This second method, applied in chapters 4 & 5, generally relies on the modification of the dielectric function of the plasmonic metal itself. These two methods have two different applications. Generally, indirect sensing is applied for chemical detection as in biochemistry which therefore eliminates the step of adding a chemical marker as in the previous labelled methods. Direct sensing on the other hand shows great promise for studying and understanding the chemical properties of a metal surface for instance in the field of catalysis. This

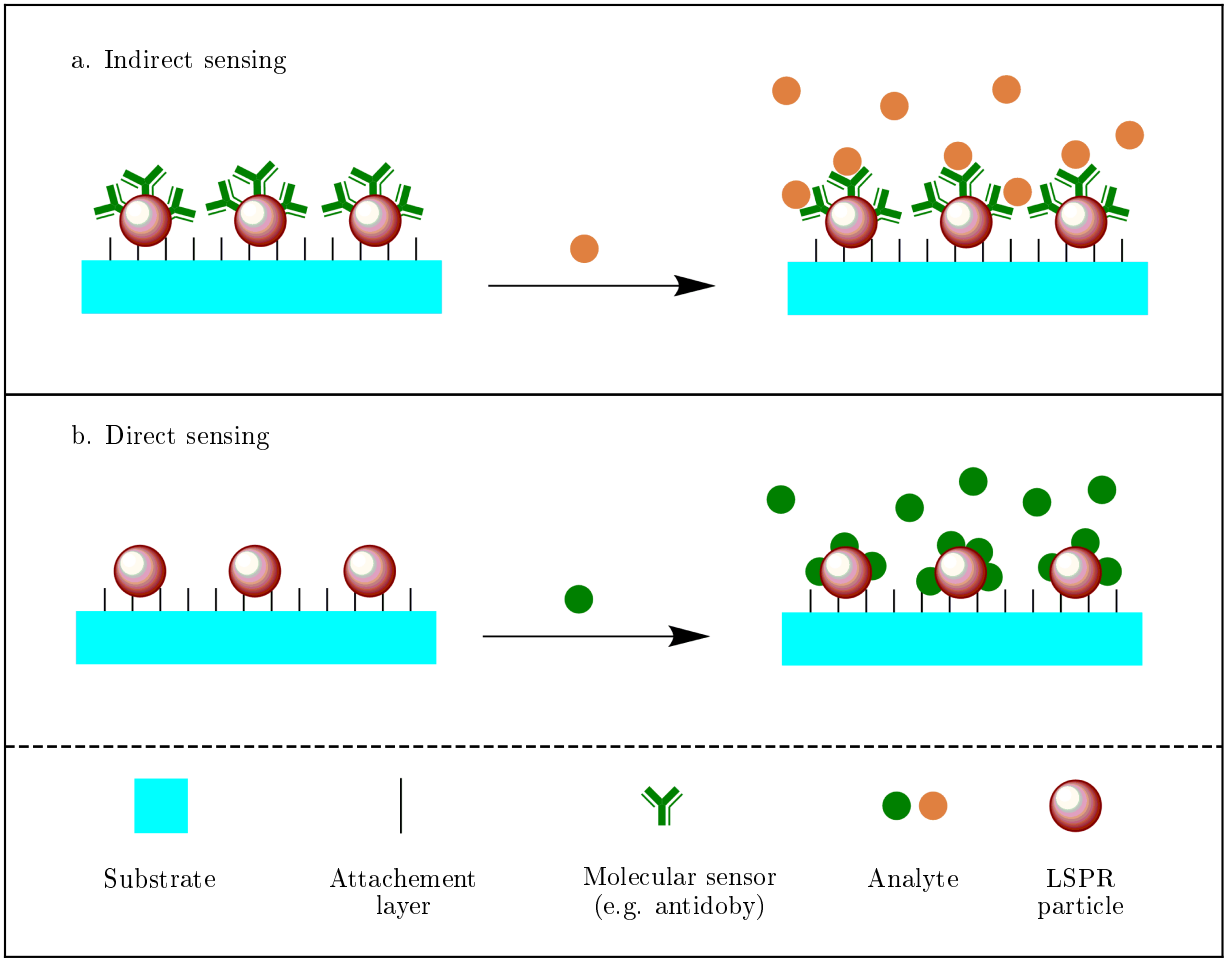

FIGURE 1.32: Diagram illustrating the difference between direct and indirect sensing using LSPR nanoparticles deposited using a self assembled monolayer on a substrate. a. shows indirect sensing were molecular sensors are used to react with the analyte. b. shows the direct sensor method where the analyte directly interacts with the LSPR particles.

is indeed an interesting path especially for sensing gases which tend to have a refractive index very close to 1 regardless of the gas composition. The detection of gas molecules is a promising field where LSPR is capable of great performance in terms of sensitivity, and help understand the mechanism of interaction of gas molecules with metal nanoparticles.

The field we are interested in this work, is applying the sensitivity of LSPR for probing and sensing the interaction of simple gas molecules with noble metals used as direct sensors. However, the key aspect of the system is in using the combination of anisotropic LSPR particles with their sensing capabilities.

• Refractive index sensitivity and figure of merit (FOM)

Experimentally, determining the performance and sensitivity of a LSPR sensor is done by determining the minimum amount of analyte needed to measure a readable change in the optical response. However, it is possible to characterise the general sensitivity of a LSPR system by measuring what is know as the refractive index sensitivity S. This quantity describes a particular LSPR sample by measuring the shift in wavelength induced by a known change in the refraction index around the nanoparticles. In this particular

case, we do not consider the effect of functionalising the plasmonic transducer but only focus on the shape of the plasmonic nanoparticles. The formula is given as

$$S = \frac{\Delta\lambda}{\Delta n} \tag{1.78}$$

where $\Delta\lambda$ is the shift in wavelength of the LSPR spectrum and Δn is the change in the refraction index. S is thus given in $nm \cdot RIU^{-1}$ where RIU stands for refraction index unit.

For example, let's look at the initial example from section 1.3.2 repeated below in figure 1.33. In this example a spheric particle is considered and represented with a Drude fitted on Au. The nanosphere is calculated in two different media at $\varepsilon_m = 1.33^2$ and $\varepsilon_m = 1.36^2$. The difference in wavelength between the two LSPR peaks is $\Delta\lambda_{LSPR} = 1.3nm$ with $\Delta n = 0.03$ giving a sensitivity of $S = 40nm \cdot RIU^{-1}$.

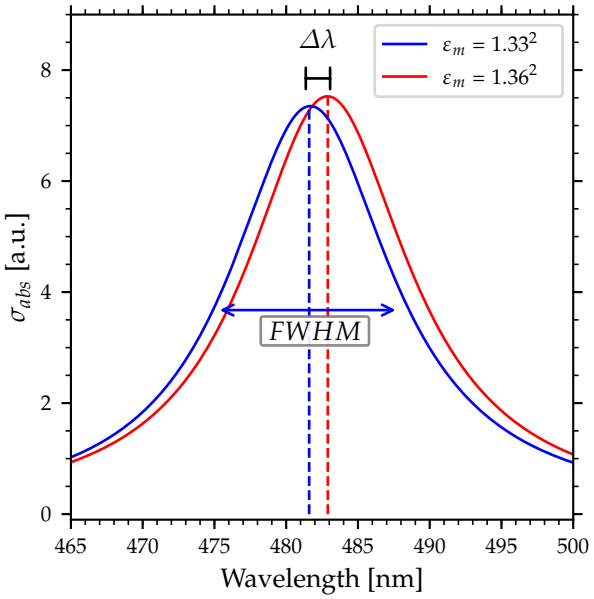

FIGURE 1.33: Calculated absorbance cross section of a spherical Ag nanoparticles with difference values for the medium dielectric function. $\varepsilon_m = 1.33^2$ would be equivalent to water and $\varepsilon_m = 1.36^2$ would be equivalent to pure ethanol.

The spectral shift is generally linear with the change in refractive index. Yet, it is more interesting to work with small particles as, first of all, the surface area is larger which leads to more reactivity [i31]. Furthermore, small particles are more sensitive to their immediate surroundings than larger particles, as the enhanced field is more localised in the former case.

However, we have already seen that decreasing the size of plasmonic particle leads to a broadening on the LSPR spectrum due to confinement effects (cf section 1.3). This broadening increases the difficulty to discern a spectral shift especially if the spectrum has a low signal to noise ratio. It is for this reason that is has become conventional to evaluate the figure of merit (FOM) of a LSPR system. This is done by dividing the refractive index sensitivity by the full width at half maximum (FWHM)

$$FOM = \frac{S}{FWHM} \tag{1.79}$$

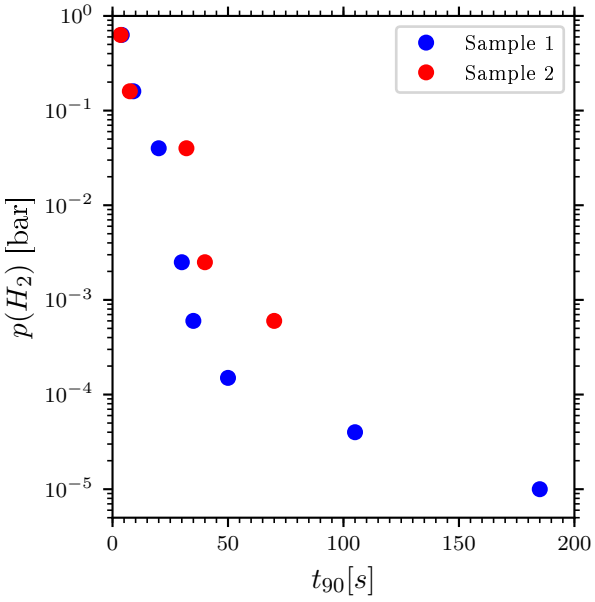

FIGURE 1.34: Write caption

In the case of figure 1.33, the $FWHM = 13.5nm$, thus the $FOM = 3$. The larger the FOM, the more sensitive the sensor is. The value determined in this example is less that ideal but serves only as a demonstration.

This tool enables the comparison in performance of LSPR sensors. The design of the nanoparticle shape and size can increase the FOM and thus the sensitivity of the LSPR sensor. Chen et al. have reviewed the refractive index sensitivity of Au nanoparticles of different size and shape [i54]. They used different concentration of glycerol in water to achieve the different refractive indices from 1.33 to 1.46. The shape they have studied are shown in figure 1.35 which shows four examples of different shaped particles which are nanospheres, branches, rods and bipyramids. For the two latter particle shapes (rods, and bipyramids), one would expect multiple peaks however, in the spectra showed, only the longer wavelength plasmon peak is considered. Figure 1.35 shows the TEM images as well as the LSPR spectra at different refractive indices for each example.

The position and width of the initial spectrum in water is very much dependent on the shape and size of the particle. Indeed, the $15nm$ in diameter nanospheres exhibit a relatively narrow peak at around $530nm$ whereas the nanobranches of effective diameter around $80nm$ displays a broad peak centred around $1150nm$. When the refractive index is increased by introducing glycerol, a red shift is seen on all spectra. The intensity of the shift is clearly strongly dependent on the shape and size of the nanoparticles. Indeed, nanospheres only exhibit a $\Delta\lambda \approx 6nm$, whereas the bipyramids of size $103 \times 26nm$ display a red shift of $\Delta\lambda \approx 50nm$. The characteristic of each system is summarised in table 1.2 where the LSPR peak, the sensitivity S, and the FOM are drawn.

These examples therefore show that for the case of nanobranches for instance, even though the refractive index sensitivity is the largest, the broadness of the spectra leads to a small FOM which is comparable to that of nanospheres. On the other hand, rods and bipyramids display a smaller refractive index sensitivity however, due to the narrowness of the spectra, the FOM are quite large, reaching 4.2 for the latter.

The conventional method to determine the LSPR position is done by fitting the experimental data usually using a Gaussian function as can be seen in ref [i55]. This can be challenging when trying to accurately

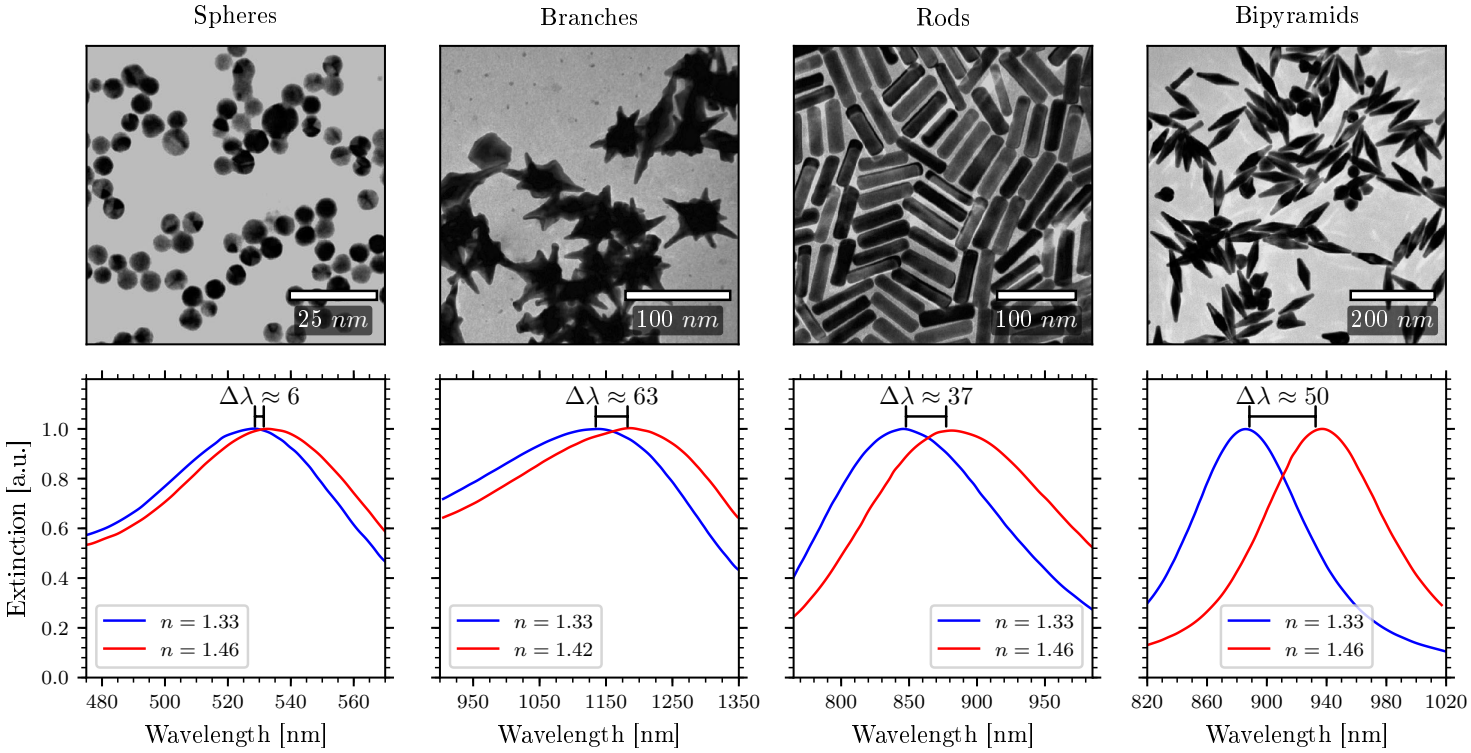

FIGURE 1.35: SEM images and there respective exctinction spectra taken from ref. [i54]. The spectra are measured with non polarised light but at two different refractive index. These were obtained by adding different amount of glycerol in water. For the rods and bipyramids only the resonance at higher wavelength is shown.

determine the maximum of broad spectra, especially if the signal to noise ratio is low. The origin of the noise can come from various sources should it be due to fluctuations in the light or mechanical vibrations. In the reference mentioned above, it comes from the low density in nanoparticles. This fitting procedure makes it mandatory to do spectral measurements which thus poses a problem in terms of reproducibility and stability of the signal. Indeed, the quality and resolution of the monochromator used is a primary matter as high resolution apparatus $\Delta\lambda \approx 0.01nm$ are very bulky and cannot be miniaturised, which means that the resolution of average monochromators, around $\Delta\lambda \approx 0.1$ to $1nm$, might be insufficient. Therefore in the case of small shifts, conventional methods tend to fall short regarding their sensitivity.

For applications in LSPR sensing the ideal requirements would thus be a high resolution monochromator and LSPR particles which exhibit a large shift when they are exposed to the analyte with the narrowest spectrum possible. Tailoring the ideal plasmonic material is a challenging task, especially if one

TABLE 1.2: This table summarises the characterisation of the exctinction spectra from figure 1.35 with the LSPR peak, the sensitivity S and the figure of merit for each geometry seen in the related figure. The values were taken from ref. [i54].

Shape	LSPR peak $[nm]$	S $[nm \cdot RIU^{-1}]$	FOM
spheres	527	44	0.6
branches	1141	703	0.8
rods	846	288	1.7
bipyramids	886	392	4.2

wants to make the process scalable. Yet in the next section we will see how taking advantage of anisotropic nanoparticles greatly increases the sensitivity whilst keeping a lower level of requirement regarding the sample morphology.

1.4.2 Using anisotropy for differential spectroscopy

• Theoretical understanding of microscopic anisotropy

Anisotropy is defined as "the quality of exhibiting properties with different values when measured along axes in different directions"[i56]. Applied to LSPR, it arises when the particle is of anisotropic shape such as an ellipsoid, cuboid, cylinder, &c... An interesting property of these anisotropic shapes is that the LSPR is dependent on the polarisation of the electric field.

Let use the case of an ellipsoid to illustrate this point. The reason for this choice is only because analytical sets of equations can easily be used to calculate the spectrum. The equation for the polarisability is reminded below (see p. 21 for more details):

$$\alpha = \frac{4}{3}\pi a_1 a_2 a_3 \frac{(\varepsilon - \varepsilon_m)}{\varepsilon_m + L_j(\varepsilon - \varepsilon_m)} \tag{1.80}$$

The depolarisation factors L are the same as those chosen in the previous section (cf section 1.3.2) that is: $L_1 = 0.28$, $L_2 = 0.22$ and $L_c = 0.5$ which correspond to a particle with axes $a_1 = 1$, $a_2 = 1.2$ and $a_3 = 0.61$. Combining the two polarisabilities calculated leads to a spectrum, for a silver particle with two maxima for both orthogonal axes a_1 and a_2 (Fig. 1.36.a.).

These LSPR peaks are solely dependent on the polarisation of the applied electric field. It is thus possible to separate both spectra by using polarised light which gives two spectra with a LSPR peak at different energies when the electric field is aligned to either the a_1 or a_2 axes.

This is true no matter the shape of the particle as long as it is anisotropic. However, so far, we have only considered a single particle. Anisotropy can also be achieved when a pattern of particles made of anisotropic or isotropic particles is overall anisotropic. For instance, let's consider the case where two isotropic silver particles i.e. spheres, were brought close to each other. The overall spectrum shown in figure 1.36.b. exhibits a major peak at about $357nm$ and a shoulder at about $353nm$ in the case of non polarised light, but with polarisation parallel and normal to the axis of alignment of the particle, the maxima can be separated just like in the case of an ellipsoid. The dashed black spectra shows the LSPR spectrum for the isolated nanoparticle. Albeit, the separation of the maximum is much narrower, and is dependent on the distance separating the particles (cf section 1.3.2 for more details). In the case of this calculation the two particles are touching each other. It is true that this would also induce quadripolar interaction and other complex phenomena, but for the sake of demonstration, only the dipole-dipole interaction is accounted for.

At the microscopic level (one or two nanoparticles), the anisotropic spectrum can be decomposed by considering either the polarisation perpendicular or parallel to the main axis of the particle(s). Yet, at the macroscopic level (array of nanoparticles), if the particles are not organised, the spectrum of the system always displays both maxima regardless of the polarisation of the electric field. This is due to the fact that even though the particles are microscopically anisotropic, the macroscopic system is isotropic, since there is no preferential axis of symmetry.

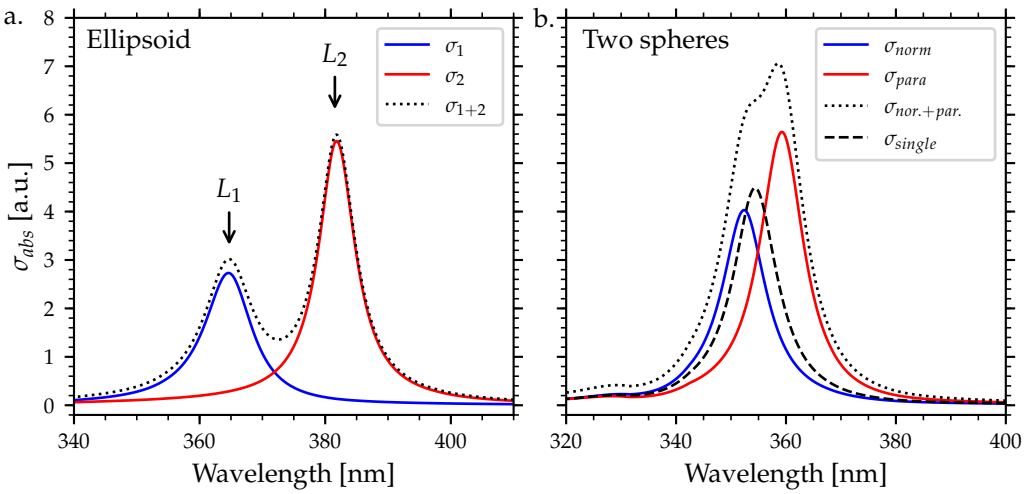

FIGURE 1.36: Calculation of the absorbance cross-section for Ag particle system. a. considers an ellipsoid Ag particles with the σ_{abs} along both the a_1 and a_2 axes using the model discussed in p. 21. b. considers two spherical Ag particles using the model discussed in p. 31. To enhanced the effect for illustrative purposes, the particles were taken touching each other as discussed in the main text. The dashed line in both spectra is the sum of both orthogonal absorption cross-sections.

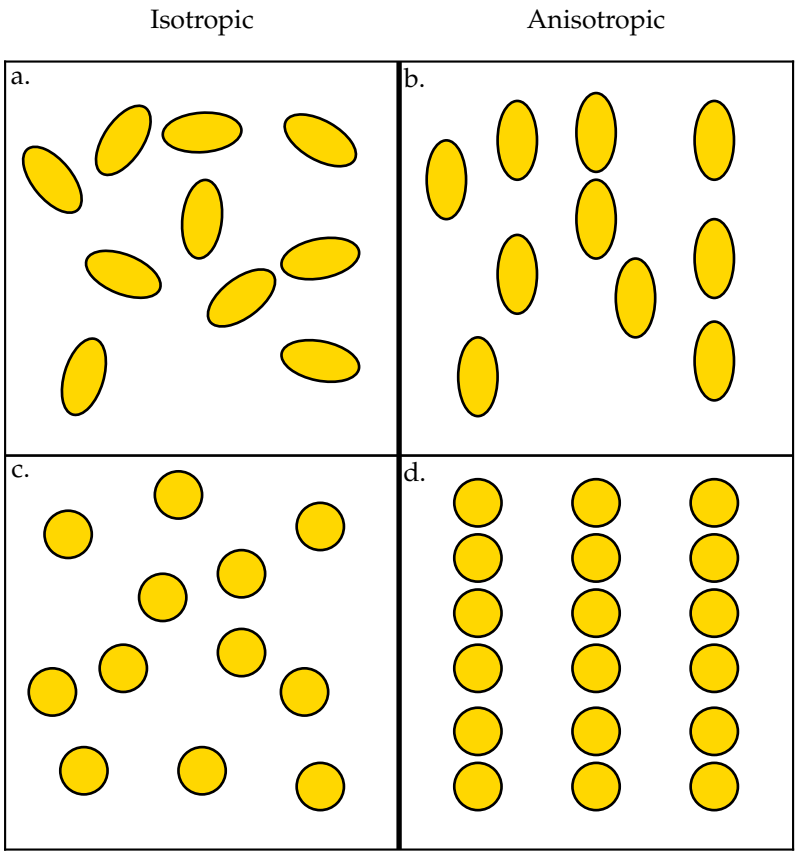

FIGURE 1.37: Diagram showing the difference between microscopic anisotropy and global anisotropy. a. shows randomly oriented ellipses which although each particle is anisotropic, the two resonance cannot be separated with polarised light. b. shows aligned ellipses which yields a globally anisotropic sample enabling the dissociation of each resonance using polarised light. c. shows a random arrangement of isotropic spheres which would only yield a signal LSPR peak. d. shows organised isotropic particles which would exhibit an anisotropic LSPR response.

• **Theoretical understanding of macroscopic anisotropy**

In order to achieve global anisotropy, the particles need to be aligned in a preferred orientation. Increasing the symmetry of the system therefore enables the measurement of the LSPR spectrum with a dependence on the polarisation. Alternatively, if isotropic particles are organised in an anisotropic pattern, for instance if rows of nanospheres are deposited on a surface, then the same type of anisotropy can be measured and be polarisation dependent. The argument is illustrated in the figure 1.37. On the left hand side of the diagram, a set of either ellipses (Fig. 1.37.a) or circles (Fig. 1.37.c) are randomly oriented and positioned in the plane, neither would lead to a globally anisotropic sample which could be decomposed in their x, and y components even though the former case would exhibit two maxima. On the other hand, when aligning the ellipses in the same direction (Fig. 1.37.b), or organising the circles in chains (Fig. 1.37.d), spectral anisotropy can be reached and separated with a polarised light. An in depth study of the fabrication techniques of anisotropic systems is discussed in chapter 3. Indeed, elaborating such samples is not an easy task and has been the focus of many research papers.

Anisotropic particles display the same type of spectral shift when the medium's refraction index is changed. That is both peaks undergo a red shift as the index increases. This is shown in figure 1.38.a. where the same ellipsoid particle, as earlier referenced, is calculated with $n = 1.33$ and $n = 1.36$. It is shown that for $\Delta n = 0.03$, as well as the increase in intensity, the silver particle undergoes a red shift of $\Delta\lambda = 6nm$.

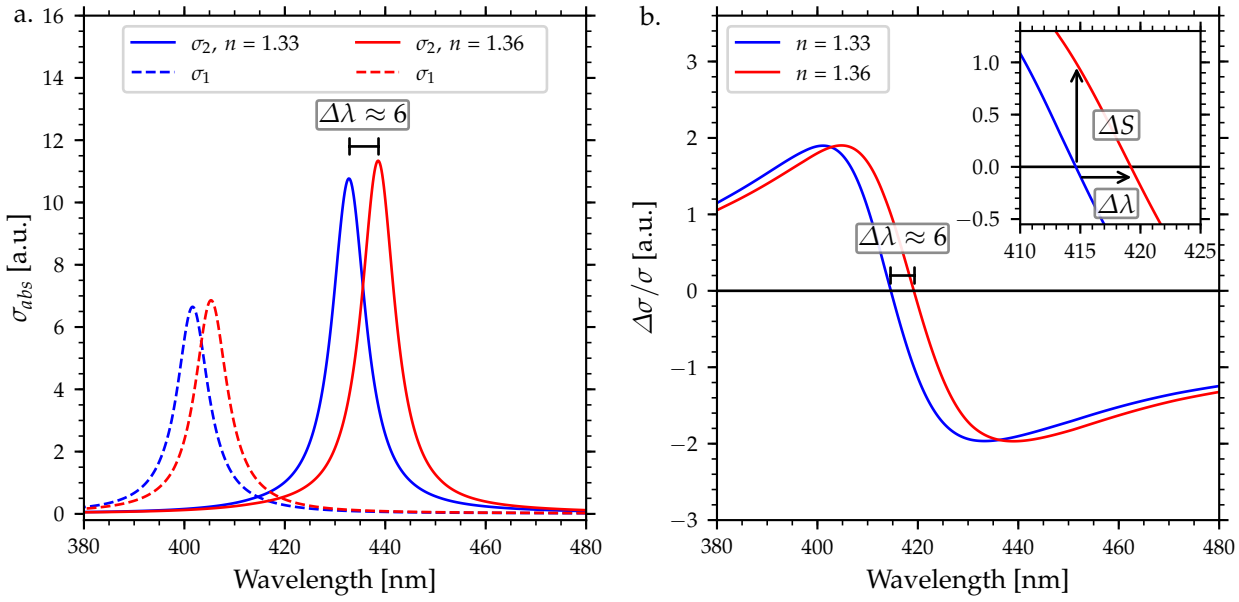

FIGURE 1.38: a. shows the calculated optical response of a silver ellipsoid with both orthogonal polarisation separated. The calculation is done with two different refractive indices for the medium 1.33 and 1.36 which would be equivalent to water and ethanol respectively. The increase in the medium's refractive index leads to a $6nm$ red shift of both LSPR peaks. b. shows the differential spectrum calculated from a. in both media. the same shift is observed. The inset shows a zoom in where the spectra crosses the zero line around $415nm$ to illustrate the difference between the spectral shift $\Delta\lambda$ and the signal shift ΔS.

• **Measurement of optical anisotropy: RAS and TAS**

An anisotropic system enables increase in the resolution of a LSPR spectral shift since it enables the measurement of a differential spectrum. Indeed, transmission or reflection anisotropy spectroscopy (TAS

or RAS) enable the measurement of the difference between both orthogonal polarisations (cf chapter 2 for more details on the experimental set up). It enables to spectrally measure the quantities

$$\frac{\Delta r}{r} = 2 \times \frac{r_x - r_y}{r_x + r_y} \quad \text{for RAS} \tag{1.81a}$$

$$\frac{\Delta t}{t} = 2 \times \frac{t_x - t_y}{t_x + t_y} \quad \text{for TAS} \tag{1.81b}$$

where $r_{x,y}$ and $t_{x,y}$ are the reflection and transmission in amplitude respectively. x and y are the main orthogonal axes of the system. These measurements therefore display a differential normalised spectrum. Let's apply eq. 1.81 to the ellipsoid spectrum from figure 1.38.a. For simplicity, we consider $\Delta\sigma/\sigma$ which yields the same behaviour as if the actual transmission or reflection were calculated. Figure 1.38.b. shows a maximum and a minimum for both polarisation and passes through zero when both absolute spectra cross one another. The increase in the refractive index leads to the same spectral shift of $\Delta\lambda = 6nm$ as for σ_1 and σ_2. The main advantage of this method is that due to the differential and normalised nature of the measure, the intensity, peak to peak, of the spectrum is unchanged when a spectral shift is induced. This reveals a clear advantage with using this method which is that it is in now possible to monitor the spectral shift by only measuring the change in intensity at a single wavelength. This is illustrated in the insert of figure 1.38.b which zooms in near where the spectra cross the zero line. As well as making non spectral measurement possible, the intensity of the signal is increased as a small shift in wavelength can induce a large change in intensity. In other words, the steeper the slope, the higher the change in signal to be measured. Furthermore, since the differential spectrum is normalised to the average signal, it cancels any outside fluctuations should it be due to mechanical vibrations, change in the light intensity or even ambient light which would interfere with UV-Vis spectrum. It could be thought that, with conventional absolute spectra, it would also possible to monitor the shift at a single wavelength by measuring on the slope of the LSPR. However, the reproducibility of the measurement would need to be extremely stable as changes in intensity of the spectrum would lead to false positives. The stability and sensitivity of this anisotropic differential measurement, performed at a fixed wavelength, represent the crucial improvement of the present technique.

• Use of anisotropic spectroscopy in the literature

The only example of this method being applied for preliminary work in sensing applications were published by Verre et al. in 2016 [i57]. They used a colloidal lithographic method to synthesis the sample (cf chapter 3 for more details), this yielded Au nanocylinders of about $100nm$ in diameter on a glass surface as shown in figure 1.39.a. Considering an isolated nanocylinder by itself, it is isotropic. However, the fact that they are paired in dimers leads to a coupling in the long axis. Moreover, as all the dimers are oriented in the same direction, the sample is globally anisotropic. This is confirmed by the UV-Vis spectra which, depending of the light polarisation (parallel or perpendicular to the alignment), yields a single LSPR maximum but at different wavelengths as shown in figure 1.39.b. They used the TAS method to measure the differential signal, shown in figure 1.39.b., in terms of rotation of the polarisation as given by the following equation

$$\theta + i\zeta = \frac{\pi d i}{\lambda} \frac{\left(\varepsilon_x - \varepsilon_y\right)}{1 + \sqrt{\varepsilon_{sub}}} \tag{1.82}$$

where ε_x and ε_y are the effective dielectric functions of the material along both orthogonal x and y is the rotation axes, λ is the wavelength, ε_{sub} is the dielectric function of the substrate, d is the thickness of the nanoparticle film layer. This equation therefore relates the rotation θ and the ellipticity ζ to the imaginary part and real part of the anisotropy of the sample respectively. This is analogous to the equation presented in eq. 1.81b since it is this rotation that leads to a change in transmission of the sample.

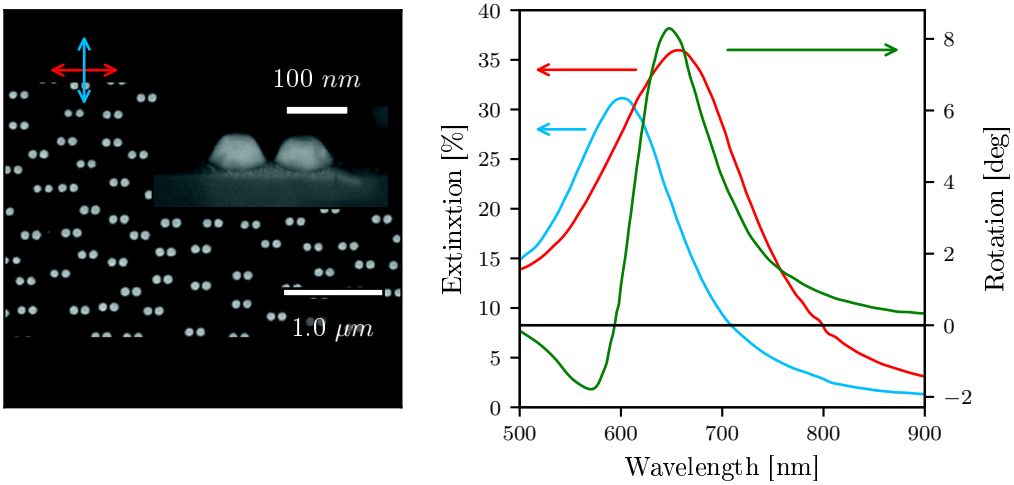

FIGURE 1.39: On the left hand side is an SEM image of the Au nanodimers fabricated by hole-mask colloidal lithography. The main image is a top view of the particles and the inset shows a side view of a single dimer. On the right hand side, the excitation spectra for both polarisations, corresponding to the coloured arrows on the SEM image, are shown. In green is the differential spectrum using the rotation of the circular polarisation. These figures were taken from ref. [i57].

They varied the refraction index of the medium by measuring the TAS spectrum of the sample in water at different concentrations of ethylene glycol. They demonstrated that the rotation of the polarisation is shifted, leading to a reduction on the maxima of the LSPR spectrum as shown in figure 1.40. They could follow this change by monitoring the spectra a single wavelength (marked as $\lambda^\star$). They also used this example to measure the change in optical response of their sample when exposed to the protein neutravidin. Prior to the experiment, they coated their nanoparticles with Biotylinated bovine serum albumin (bBSA) which selectively bonds to the analyte. This common molecular couple is often used for testing protein adsorption of biochemical sensors. Using this indirect method, they showed how the TAS method can be used for such analysis, as the sample displayed a large response to small concentrations around $10^{-2} g \cdot L^{-1}$.

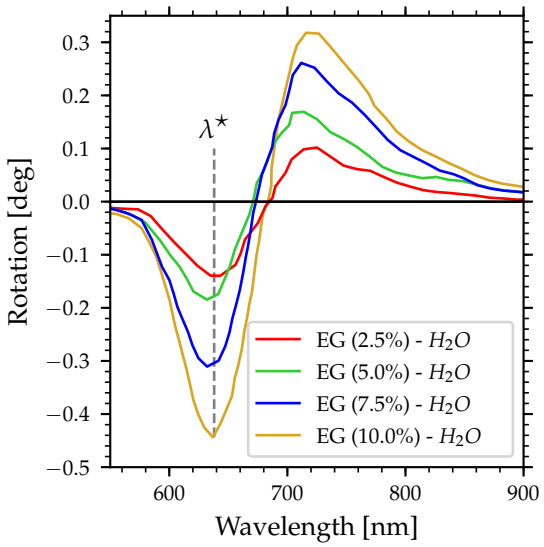

FIGURE 1.40: Differential spectra of the Au dimer sample presented in figure 1.39 when exposed at different concentrations of ethylene glycol in water. Figure taken from ref. [i57].

• Amount of anisotropy required

Nanorods or ellipsoid are the perfect academic example of anisotropic nanoparticles exhibiting multiple maxima, especially in the case of Ag. However, we have discussed that the crucial parameter for TAS is the slope of the spectrum which needs to be as steep as possible which is reached if the two LSPR peaks are not too far apart, this therefore means that the global anisotropy must not be too large.

Let's consider a silver ellipsoid and vary the depolarisation factor L_1 and L_2 with $L_3 = 1 - (L_1 + L_2)$. We have fixed $L_2 = 0.095$ and varied $L_1 = 0.115$, 0.16 and 0.26 which are drawn in figure 1.41.a.b and c. respectively. The figure shows the absolute absorption cross-section for both axes in blue and the TA spectrum, i.e. $\Delta\sigma/\sigma$ in green. What can be seen on the spectra is that when decreasing the value of L_1, the LSPR for σ_1 is red shifted towards that of σ_2. The TA spectrum is also red shifted, and the slope between the two peaks clearly increases as the system's anisotropy is reduced. The last point is very important as the steepness of the slope directly influences the quality of the spectrum for sensing applications. It is therefore not as advantageous to synthesis very anisotropic nanoparticles for such application rather a small anisotropy is required. However, too small and the overall amplitude of the TA spectrum starts to drop as shown in figure 1.41.c. With this in mind, the method of fabrication is a crucial point as arrays of aligned nanorods would not yield an as good spectrum as a slight anisotropic array of nanospheres

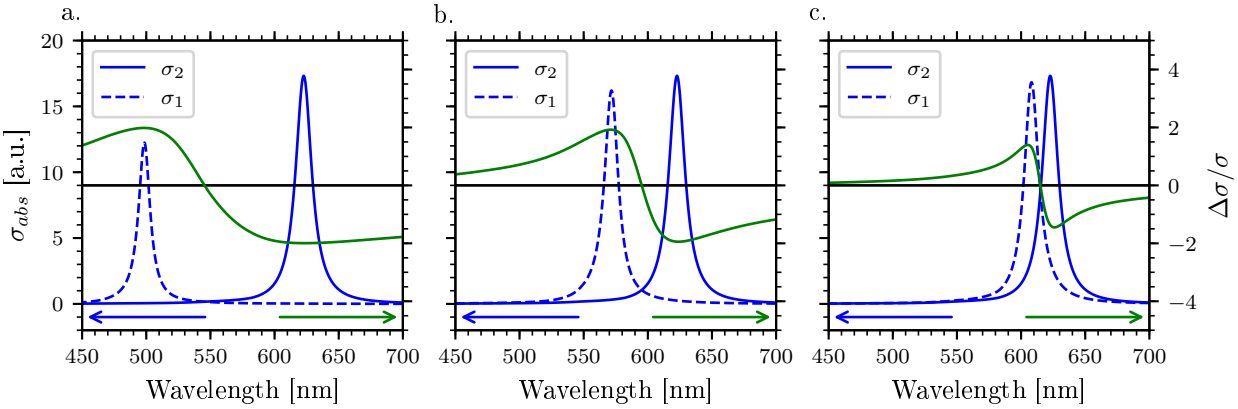

FIGURE 1.41: Absorption cross-section and differential cross-section calculated for an ellipsoid of different shape. The absorption cross-section are decoupled long both orthogonal axes of the ellipsoid. The aspect ratio of the ellipsoid is arbitrarily modified to illustrate the effect of the anisotropy on the differential spectrum. From a. to c. the anisotropy of the ellipsoid is decreased.

1.5 Summary and objectives of the research project

In this chapter we have defined the fundamentals of localised surface plasmon resonance (LSPR) for noble metals. LSPR is defined as the collective oscillation of the conduction electrons excited by an electromagnetic field. In the first part of the chapter, we have introduced the electrostatic models which explains the concept of polarisability enabling the calculation of the absorbance cross-section. The model is only applicable within the quasi-static approximation and is mainly used in with the dipolar approximation. The polarisability is based on the dielectric function of the particle, the refraction index of the surrounding medium, the particle's volume and its shape.

• The dielectric function of the metal represents its optical response. It is a consequence of the electronic transitions in the band structure and is thus element dependent. It is generally experimentally obtained. The Drude model enables to reproduce the intraband transitions based on multiple factors such as the electron density and the electron mean free path in the metal. With the Drude model plus interband transitions, it is possible to investigate the effects of each parameter on the metal's LSPR spectrum as well as account for confinement effects when considering small nanoparticles.

• The medium's dielectric function usually is taken as constant over the measured spectrum, however, in the case of nanoparticles deposited on a substrate, complexity arises. A simple solution is to consider an average effective dielectric function. It is nevertheless possible, using the dipolar approximation, to consider the image dipole generated by the particle in the substrate and thus calculate the dipole-dipole interaction. To go beyond the dipolar approximation for substrate consideration, one must account for multipolar resonances though, at the time of writing, the image multipole model has only been solved for spheroids with their revolution axes normal to the substrate's plane. In all cases, the effect of the substrate, with a refractive index higher than the medium, is to induce a red shift to the LSPR spectrum.

• The volume of the particle simply impacts on the intensity of the absorption cross-section. However, one needs to account for other effects. Indeed, the quasi-static approximation is only applicable for particles a lot smaller than the incident wavelength which therefore limits to particles a few dozen nanometres in width. On the other hand, when the particles become small, confinement effects now need to be considered within the particle's dielectric function which tend to broaden the resonance.

• The last factor in the polarisability, is the particle's shape. The analytical model is limited to ellipsoid variation. It may be argued that these idealised shapes cannot be experimentally fabricated as even colloidal nanospheres exhibit facets and are not perfect spheres. Nevertheless, the analytical methodology does reproduce the experimental results well which enable investigations of such effects as changes in the refraction index or charge transfers. Anisotropic shapes also exhibit multiple LSPR peaks depending on the direction of the electric field considered.

More complex systems such as particle-particle interaction or core-shell particles may also be calculated. For the former, it is still generally restricted to the dipolar approximation, which therefore does not account for multipolar interaction that may occur, such as hot spots generated in between the particles. Ellipsoid core-shell systems can also be calculated. There is however a small consequence of the model to consider which is that the thickness of the shell is not constant. Although a minor issue, it must still be accounted for to prevent aberrations. Indeed, the calculation of a core-shell particle's polarisability demands that both the core and shell are described by the dielectric functions of the respective materials, which is of course an issue for thin shells of one or a few atoms thick. On the other hand, to calculate the optical response of larger particles where the quasi-static approximation cannot apply, one may use Mie's theory which is suitable for such system. It accounts for multipolar resonance as well as scattering however is still limited to simple shapes.

A numerical approach is required for more complex systems. The method discussed in this chapter was discrete dipole approximation (DDA). This method considers an array of individual dipoles to reconstruct the particle's shape. With this method, the shape, composition and size of the particle system is not a limiting factor any more. However there are still limitations. The first one is the number of dipoles required to correctly reproduce the particle which, when large, increases the computation time. Too little dipoles, on the other hand, leads to numerical aberrations. The second main limitation is that DDA does not consider semi-finite elements such as substrates well. Nonetheless, it does greatly reproduce the enhanced electric field of the LSPR particle, particularly enabling the calculation of antenna effects which enhance the electric field on sharp features such as corners, or between multiple interacting particles.

In the second part of this chapter, we have discussed the use of LSPR for sensing applications. We have seen that there were two main types of sensing: indirect and direct sensing.

• Indirect sensing is when the plasmonic particles only play the role of the transducer and uses selective molecular sensors adsorbed in close vicinity to the nanoparticles to bond with the analyte which thus changes the refractive index in the transducer's enhanced field. The advantage of such system is the wide versatility in molecular sensors and thus target analytes, though it does usually require more complex sample fabrication.

• Direct sensing uses the LSPR particles both as the transducers and molecular sensors with the analyte directly interacting with them. It does limit the sensing possibilities especially when using Au, though it enables the study of the particle's chemistry which is of interest in such fields as catalysis.

The conventional method for LSPR sensing is to use a UV-Vis spectrometer to measure spectral shifts of the LSPR as it is exposed to the analyte. This however has intrinsic major limitations. The main one is the need for spectral measurements which thus require high reproducibility. Since the measurements are absolute, they are very sensitivity to external noise such as fluctuation in the light source, light pollution or mechanical vibrations. Furthermore, when measuring very small shifts in the LSPR, they also require a high resolution monochromator with small micrometer slits. This adds to the cost and bulkiness of the method as well as limits the amount of light reaching the detector hence leads to high noise. Alternatively, experiments

have been undertaken at a signal wavelength, though due to the absolute nature of the measurement, reproducibility is an unovercomable issue.

To enhance the sensitivity of this method, efforts have been put into the fabrication of nanoparticles exhibiting a high figure of merit which tend to be more difficult to synthesis and do not resolve the inherent issues of this spectroscopic method. Anisotropic particles in conjunction with transmission anisotropy spectroscopy (TAS) however offers an alternative which overcomes the issues stated above.

Anisotropic nanoparticles exhibit a polarisation dependent LSPR. However one must distinguish microscopic and macroscopic anisotropy. Indeed, only in the latter case, that is when the sample is globally anisotropic, can the two polarisation be decoupled with polarised light. This is possible by either orienting anisotropic particles in the same direction or by patterning isotropic particles anisotropically e.g. nanochains of spheres. Using TAS, it is possible to directly measure the normalised differential spectrum of such anisotropic sample which has the advantage of not being sensitive by nature to fluctuation in the light source, light pollution or mechanical vibrations. Furthermore, it is possible to monitor in real time the changes in anisotropy at a single wavelength since only a change in the LSPR will induce a spectral shift which is easily related to the change in intensity of the anisotropy thus bypassing the limitations of a monochromator.

In this thesis, the TAS method is used in conjunction with anisotropic LSPR samples to demonstrate the high sensitivity, reproducibility and stability of the method by investigating two case studies. The first on is the use of the direct sensing methodology to analyse the chemical mechanism of the dissociative adsorption of H_2 on Au nanoparticles which cannot be easily undertaken with conventional spectral measurement due to the very low effect the interaction has on the change in LSPR of the Au sample. The second case of study shows actual detection capabilities of the method by sensing very low partial pressures of H_2 both in an inert carrier gas and in air using a both direct (Pd nanoparticles) and indirect (Au/Pd nanoparticles) sensing approaches.

1.6 References

[i1] D. B. Harden and J. M. C. Toynbee, "VII.The Rothschild Lycurgus Cup", *Archaeologia*, vol. 97, no. December 1954, pp. 179–212, 1959.

[i2] F. E. Wagner, S. Haslbeck, L. Stievano, S. Calogero, Q. a. Pankhurst, and K. P. Martinek, "Before striking gold in gold-ruby glass", *Nature*, vol. 407, no. 6805, pp. 691–692, 2000.

[i3] R. C. Chirnside and P. M. C. Proffitt, "The Rothschild Lycurgus Cup: an analytical investigation", *Journal of Glass Studies*, vol. 5, pp. 18–23, 1963.

[i4] A. Ruivo, C. Gomes, A. Lima, M. L. Botelho, R. Melo, A. Belchior, and A. Pires de Matos, "Gold nanoparticles in ancient and contemporary ruby glass", *Journal of Cultural Heritage*, vol. 9, pp. 134–137, 2008.

[i5] M. Faraday, "The Bakerian Lecture: Experimental Relations of Gold (and Other Metals) to Light", *Philosophical Transactions of the Royal Society of London*, vol. 147, pp. 145–181, Jan. 1857.

[i6] G. Mie, "Beiträge zur Optik trüber Medien, speziell kolloidaler Metallösungen", *Annalen der Physik*, vol. 330, no. 3, pp. 377–445, 1908.

[i7] R. Gans, "ÜBER DIE FORM ULTRAMIKROSKOPISCHER SILBERTEILCHEN", *Annalen der Physik*, vol. 352, no. 10, pp. 270–284, 1915.

[i8] P. Drude, "Zur Elektronentheorie der Metalle", *Annalen der Physik*, vol. 306, no. 3, pp. 566–613, 1900.

[i9] ——, "Zur Elektronentheorie der Metalle II. Teil. Galvanomagnetische und thermomagnetische Effecte", *Annalen der Physik*, vol. 308, no. 11, pp. 369–402, 1900.

[i10] D. Pines and D. Bohm, "A Collective Description of Electron Interactions: II. Collective vs Individual Particle Aspects of the Interactions", *Physical Review*, vol. 85, no. 2, pp. 338–353, 1952.

[i11] R. Feynman, "There is plenty of room at the bottom (talk tanscript)", *Caltech Engineering and Science*, vol. 23:5, pp. 22–36, 1960.

[i12] F. Wooten, *Optical Properties of solids*. Academic press inc., 1972, ISBN: 9781483220765.

[i13] U. Kreibig and M. Vollmer, *Optical Properties of Metal Clusters*. Springer Berlin Heidelberg, 1995, ISBN: 978-3-642-08191-0.

[i14] J. D. Jackson, *Classical Electrodynamics*. New York ; London : John Wiley, 1999, ISBN: 0471431311.

[i15] C. F. Bohren and D. R. Huffman, *Adsorption and scattering of light by small particles*. New York ; London : John Wiley, 1983, ISBN: 047105772X.

[i16] F. Castro and B. Nabet, "Numerical computation of the complex dielectric permittivity using Hilbert transform and FFT techniques", *Journal of the Franklin Institute*, vol. 336, no. 1, pp. 53–64, 1999.

[i17] P.-O. Nilsson, "Determination of Optical Constants from Intensity Measurements at Normal Incidence", *Applied Optics*, vol. 7, no. 3, p. 435, 1968.

[i18] J. E. Nestell and R. W. Christy, "Optics of Thin Metal Films", *American Journal of Physics*, vol. 39, no. 3, pp. 313–320, 1971.

[i19] P. B. Johnson and R. W. Christy, "Optical Constants of the Noble Metals", *Physical Review B*, vol. 6, no. 12, pp. 4370–4379, 1972.

[i20] P. O. Nilsson, "Studies of AgIn and CuGe Alloys by Optical and Photoemission Techniques", *Physica Scripta*, vol. 1, no. 4, pp. 189–192, 1970.

[i21] G. P. Pells, "Measurement of the optical properties of alloys in ultra-high vacuum", *Journal of Scientific Instruments*, vol. 44, no. 12, pp. 997–1000, 1967.

[i22] J. E. Nestell and R. W. Christy, "Derivation of Optical Constants of Metals from Thin-Film Measurements at Oblique Incidence", *Applied Optics*, vol. 11, no. 3, p. 643, 1972.

[i23] V. M. Silkin, I. P. Chernov, P. M. Echenique, Y. M. Koroteev, and E. V. Chulkov, "Influence of hydrogen absorption on low-energy electronic collective excitations in palladium", *Physical Review B*, vol. 76, no. 24, p. 245 105, 2007.

[i24] V. M. Silkin, R. Díez Muiño, I. P. Chernov, E. V. Chulkov, and P. M. Echenique, "Tuning the plasmon energy of palladium–hydrogen systems by varying the hydrogen concentration", *Journal of Physics: Condensed Matter*, vol. 24, no. 10, p. 104 021, 2012.

[i25] C. Hogan, O. Pulci, P. Gori, F. Bechstedt, D. S. Martin, E. E. Barritt, A. Curcella, G. Prevot, and Y. Borensztein, "Optical properties of silicene, Si/Ag(111), and Si/Ag(110)", *Physical Review B*, vol. 97, no. 19, p. 195 407, 2018.

[i26] A. Marini, R. Del Sole, and G. Onida, "First-principles calculation of the plasmon resonance and of the reflectance spectrum of silver in the GW approximation", *Physical Review B*, vol. 66, no. 11, p. 115 101, 2002.

[i27] H. Ehrenreich and H. R. Philipp, "Optical Properties of Ag and Cu", *Physical Review*, vol. 128, no. 4, pp. 1622–1629, 1962.

[i28] B. R. Cooper, H. Ehrenreich, and H. R. Philipp, "Optical Properties of Noble Metals. II.", *Physical Review*, vol. 138, no. 2A, A494–A507, 1965.

[i29] H. S. Sehmi, W. Langbein, and E. A. Muljarov, "Optimizing the Drude-Lorentz model for material permittivity: Method, program, and examples for gold, silver, and copper", *Physical Review B*, vol. 95, no. 11, p. 115 444, 2017.

[i30] M. Valamanesh, Y. Borensztein, C. Langlois, and E. Lacaze, "Substrate Effect on the Plasmon Resonance of Supported Flat Silver Nanoparticles", *The Journal of Physical Chemistry C*, vol. 115, no. 7, pp. 2914–2922, 2011.

[i31] K. M. Mayer and J. H. Hafner, "Localized Surface Plasmon Resonance Sensors", *Chemical Reviews*, vol. 111, no. 6, pp. 3828–3857, 2011.

[i32] B. Luk'yanchuk, N. I. Zheludev, S. a. Maier, N. J. Halas, P. Nordlander, H. Giessen, and C. T. Chong, "The Fano resonance in plasmonic nanostructures and metamaterials", *Nature Materials*, vol. 9, no. 9, pp. 707–715, 2010.

[i33] R. Kuladeep, L. Jyothi, K. S. Alee, K. L. N. Deepak, and D. N. Rao, "Laser-assisted synthesis of Au-Ag alloy nanoparticles with tunable surface plasmon resonance frequency", *Optical Materials Express*, vol. 2, no. 2, p. 161, 2012.

[i34] L. Bossard-Giannesini, "Mesures et simulation du travail de sortie de nanoparticules d'or fonctionnalisées", PhD thesis, Sorbonne Université, 2018.

[i35] C. Goldmann, R. Lazzari, X. Paquez, C. Boissière, F. Ribot, C. Sanchez, C. Chanéac, and D. Portehault, "Charge Transfer at Hybrid Interfaces: Plasmonics of Aromatic Thiol-Capped Gold Nanoparticles", *ACS Nano*, vol. 9, no. 7, pp. 7572–7582, 2015.

[i36] P. Mulvaney, J. Pérez-Juste, M. Giersig, L. M. Liz-Marzán, and C. Pecharromán, "Drastic Surface Plasmon Mode Shifts in Gold Nanorods Due to Electron Charging", *Plasmonics*, vol. 1, no. 1, pp. 61–66, 2006.

[i37] B. G. Ershov, E. V. Abkhalimov, R. D. Solovov, and V. I. Roldughin, "Gold nanoparticles in aqueous solutions: influence of size and pH on hydrogen dissociative adsorption and Au(III) ion reduction", *Physical Chemistry Chemical Physics*, vol. 18, no. 19, pp. 13 459–13 466, 2016.

[i38] B. S. Hoener, H. Zhang, T. S. Heiderscheit, S. R. Kirchner, A. S. De Silva Indrasekara, R. Baiyasi, Y. Cai, P. Nordlander, S. Link, C. F. Landes, and W.-S. Chang, "Spectral Response of Plasmonic Gold Nanoparticles to Capacitive Charging: Morphology Effects", *The Journal of Physical Chemistry Letters*, vol. 8, no. 12, pp. 2681–2688, 2017.

[i39] A. H. Ali, R. J. Luther, C. A. Foss, and G. B. Chapman, "Optical Properties of Nanoscopic Gold Particles Adsorbed At Electrode Surfaces: the Effect of Applied Potential on Plasmon Resonance Absorption.", *Nanostructured Materials*, vol. 9, no. 5, pp. 559–562, 1997.

[i40] A. H. Ali and J. Colby, A. Foss, "Electrochemically Induced Shifts in the Plasmon Resonance Bands of Nanoscopic Gold Particles Adsorbed on Transparent Electrodes", *Journal of The Electrochemical Society*, vol. 146, no. 2, p. 628, 1999.

[i41] R. Chapman and P. Mulvaney, "Electro-optical shifts in silver nanoparticle films", *Chemical Physics Letters*, vol. 349, no. 5-6, pp. 358–362, 2001.

[i42] T. Miyazaki, R. Hasegawa, H. Yamaguchi, H. Oh-oka, H. Nagato, I. Amemiya, and S. Uchikoga, "Electrical Control of Plasmon Resonance of Gold Nanoparticles Using Electrochemical Oxidation", *The Journal of Physical Chemistry C*, vol. 113, no. 19, pp. 8484–8490, 2009.

[i43] M. Hu, D. P. Linder, M. Buongiorno Nardelli, and A. Striolo, "Hydrogen Adsorption on Platinum–Gold Bimetallic Nanoparticles: A Density Functional Theory Study", *The Journal of Physical Chemistry C*, vol. 117, no. 29, pp. 15 050–15 060, 2013.

[i44] B. T. Draine and P. J. Flatau, "Discrete-Dipole Approximation For Scattering Calculations", *Journal of the Optical Society of America A*, vol. 11, no. 4, p. 1491, 1994.

[i45] H. DeVoe, "Optical Properties of Molecular Aggregates. I. Classical Model of Electronic Absorption and Refraction", *The Journal of Chemical Physics*, vol. 41, no. 2, pp. 393–400, 1964.

[i46] E. M. Purcell and C. R. Pennypacker, "Scattering and Absorption of Light by Nonspherical Dielectric Grains", *The Astrophysical Journal*, vol. 186, p. 705, 1973.

[i47] S. B. Singham and G. C. Salzman, "Evaluation of the scattering matrix of an arbitrary particle using the coupled dipole approximation", *The Journal of Chemical Physics*, vol. 84, no. 5, pp. 2658–2667, 1986.

[i48] S. B. Singham and C. F. Bohren, "Light scattering by an arbitrary particle: a physical reformulation of the coupled dipole method", *Optics Letters*, vol. 12, no. 1, p. 10, 1987.

[i49] K. A. Willets and R. P. Van Duyne, "Localized Surface Plasmon Resonance Spectroscopy and Sensing", *Annual Review of Physical Chemistry*, vol. 58, no. 1, pp. 267–297, 2007.

[i50] J. N. Anker, W. P. Hall, O. Lyandres, N. C. Shah, J. Zhao, and R. P. Van Duyne, "Biosensing with plasmonic nanosensors", *Nature Materials*, vol. 7, no. 6, pp. 442–453, 2008.

[i51] K. Saha, S. S. Agasti, C. Kim, X. Li, and V. M. Rotello, "Gold Nanoparticles in Chemical and Biological Sensing", *Chemical Reviews*, vol. 112, no. 5, pp. 2739–2779, 2012.

[i52] D. Wild, *The Immunoassay Handbook*, Elsevier, Ed. 2005, ISBN: 0080445268.

[i53] J. Satija, N. Punjabi, D. Mishra, and S. Mukherji, "Plasmonic-ELISA: expanding horizons", *RSC Advances*, vol. 6, no. 88, pp. 85 440–85 456, 2016.

[i54] H. Chen, X. Kou, Z. Yang, W. Ni, and J. Wang, "Shape- and Size-Dependent Refractive Index Sensitivity of Gold Nanoparticles", *Langmuir*, vol. 24, no. 10, pp. 5233–5237, 2008.

[i55] B. Rožič, J. Fresnais, C. Molinaro, J. Calixte, S. Umadevi, S. Lau-Truong, N. Felidj, T. Kraus, F. Charra, V. Dupuis, T. Hegmann, C. Fiorini-Debuisschert, B. Gallas, and E. Lacaze, "Oriented Gold Nanorods and Gold Nanorod Chains within Smectic Liquid Crystal Topological Defects", *ACS Nano*, vol. 11, no. 7, pp. 6728–6738, 2017.

[i56] The Editors of Encyclopaedia Britannica, *Anisotropy*.

[i57] R. Verre, N. Maccaferri, K. Fleischer, M. Svedendahl, N. Odebo Länk, A. Dmitriev, P. Vavassori, I. V. Shvets, and M. Käll, "Polarization conversion-based molecular sensing using anisotropic plasmonic metasurfaces", *Nanoscale*, vol. 8, no. 20, pp. 10 576–10 581, 2016.

Chapter 2

Experimental techniques and set-up

Abstract

This chapter is dedicated to the description of the different techniques used throughout this work. The first part of this chapter dives into the reflection and transmission anisotropy spectroscopy (RAS & TAS) which is the main apparatus used in this work. Other characterisation techniques are described in the second part of this chapter. Lastly, details on the consumables used are listed as a reference for the rest of this thesis.

2.1 Reflection and transmission anisotropy spectroscopy (RAS, TAS)

2.1.1 Principles and instrumentation

Transmission anisotropy spectroscopy (TAS) was greatly inspired by Apsnes' design of the reflection anisotropy spectroscopy (RAS) [ii1]. "RAS is a non-destructive optical probe of surface that is capable of operation within a wide range of environments". It is a method analogous to ellipsometry though at normal incidence. This method measures either the difference in reflectance Δr or in transmittance Δt at a normal incidence plane-polarised light between two orthogonal directions in the x, y surface plane, normalised to the mean reflectance r, or transmittance t, given by eq. 2.1a and eq. 2.1b, respectively. The use of this apparatus enables the cancellation of isotropic signals such as that of the substrate or any isotropic mirrors put into the light pathway.

$$\frac{\Delta r}{r} = 2 \times \frac{r_x - r_y}{r_x + r_y} \quad \text{for RAS} \tag{2.1a}$$

$$\frac{\Delta t}{t} = 2 \times \frac{t_x - t_y}{t_x + t_y} \quad \text{for TAS} \tag{2.1b}$$

Initially, the RAS was designed in order to investigate small anisotropy at the surfaces of crystals. Indeed, even in the case of isotropic crystal, surface reconstruction can generate anisotropy at the surface of the material.Conventional absolute non differential methods such as UV-VIS spectroscopy are not sensitive enough to greatly investigate such weak signals [ii1].

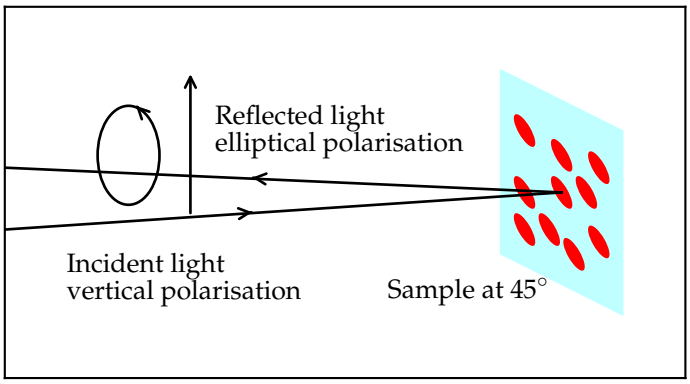

FIGURE 2.1: Diagram of the sample at 45° with respect to the incidence vertical linear polarisation. The sample reflects the light - with or without a mirror - and generates an elliptical polarisation.

The home-made apparatus, schematised in figure 2.2 and photographed in figure 2.3, comprises of a xenon discharge light source which has a broad wavelength from 200 to 1000nm. The light passes through a first linear polariser which imposes a vertical polarisation to the light beam. The light is reaches the sample at normal incidence. The sample is oriented such as the main anisotropy direction is at a 45° angle relative to the polariser. The anisotropy of the sample leads to an elliptical polarisation of the returning light as shown in figure 2.1. In the case of reflective samples such as Si crystal, the light is reflected to the apparatus, however when measuring transparent samples such as a thin metal film on glass, an isotropic mirror is placed behind the sample. For localised surface plasmon resonance (LSPR) sensing application, we will see that it is best to have the light beam pass twice into the sample as it doubles the sensitivity of the measurement. Following this same approach, it is also possible to add a third mirror in front of the sample to multiply the number of passes which significantly increases the measured optical anisotropy at the cost of decreasing the light intensity. However, this approach was not used in the rest of this work due to difficulty in implementing such a system with the gas cell system which is discussed in a later section.

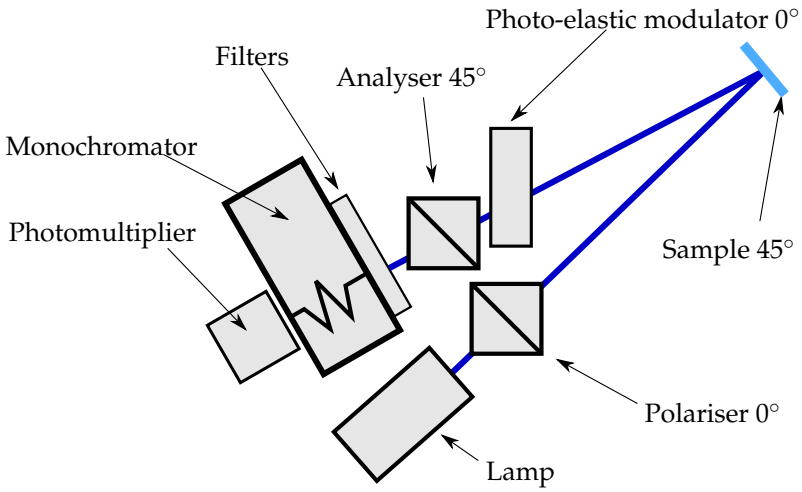

FIGURE 2.2: Schematic of the TAS system used anisotropic measurement of LSPR. As per Aspnes' design [ii1], the orientation of the sample and the analyser are rotated by 45° with respect to the polariser and photo elastic modulator. The sample is placed approximately one metre from the polariser as to have a quasi normal incident light with respect to the sample.

The light beam passes through a photo elastic modulator (PEM) which modulates the compression of a silica slab at 100kHz, this induces a phase difference between the two components of the electric field parallel to its optical axes. The orientation of the PEM is set so its optical axes are parallel to the initial polariser. The consequence of this orientation is that vertical polarisation of the light reflected from an isotropic surface is not affect by the PEM, whereas the elliptic polarisation induced by the anisotropic sample is imposed a phase difference modulated at the set frequency.

A second polariser is placed after the PEM at a 45° angle relative to the first polariser. This orientation leads to a change in intensity of the modulated elliptically polarised light reflected from or transmitted by the anisotropic sample. The oscillation of the intensity around a mean value is measured as $\Delta I/I_0$ from which can be calculated the change in transmittance of the sample $\Delta t/t$.

A set of filters is put after the analyser to prevent higher order harmonics before being focused into a monochromator. The use of the monochromator is to make it possible to undertake spectral measurements but its second application is to follow the change of anisotropy at a single wavelength as is discussed in a later section. The light intensity is measured with a photomultiplier and plugged to the electronic system.

The electric signal is measured with a voltmeter which gives the reference value I_0. Simultaneously, the signal is processed with a lock-in amplifier which is synchronised to the modulating frequency of the PEM. The change in intensity, $\Delta I/I_0$ is recorded. This method enables the measurement of a signal to noise ratio of about 10^{+5}. It thus overcomes any ambient noise should it be ambient light, mechanical vibrations or even fluctuations in the xenon light source.

In the case of measurements in a gas cell, one has to note that a fused silica window is placed in the light path. Intrinsic stress in this window from the fabrication process could introduce unwanted anisotropy in the signal path. However, by carefully inducing an opposite stress when attaching the window to the gas cell, the anisotropy can be greatly reduced and aligned at a 0° with respect to the first polariser which would thus lessen its effect on the signal.

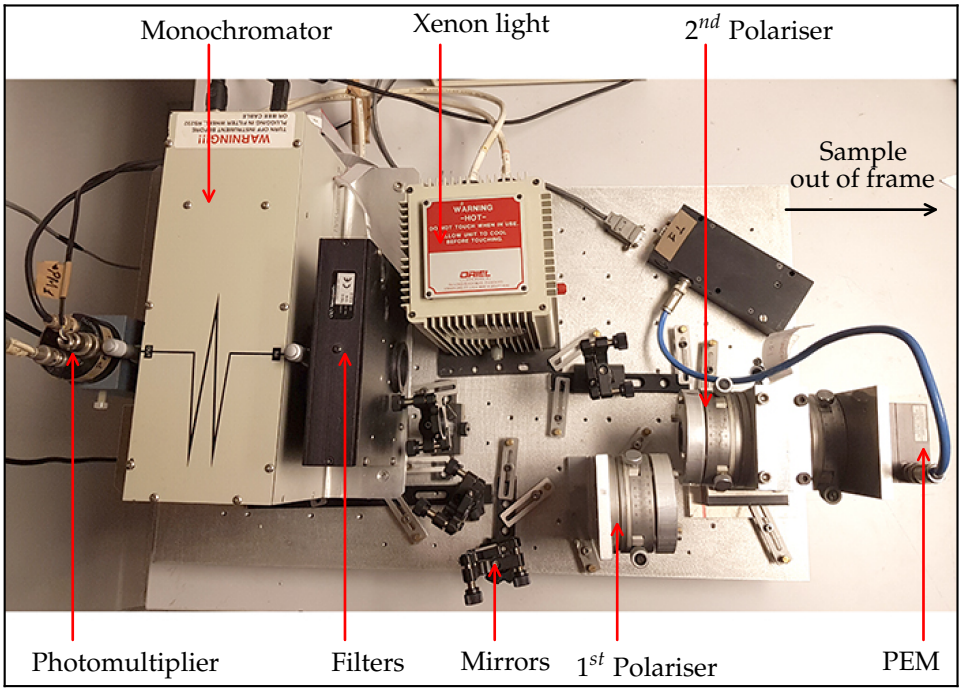

FIGURE 2.3: Photography of the RAS system with the different components indicated. The sample is placed on the far right of the system out of the frame.

The model references for the home made TAS is as follows. The photo elastic modulator was a PEM-90 from Hinds instruments. The polarisers were Glan Taylor types. The monochromator was a 1/8 m Cornerstone 130 from Newport and a 1200 lines per millimetre holographic grating, whose nominal wavelength resolution is around 4 to $6nm$ with 0.5 to $1mm$ I/O slits. The photomultiplier was a R758-10 from Hamamatsu. The lock-in amplifier was from EG& G Princeton applied research model 5209.

For sake of demonstration, let's focus on the TAS system that is the measurement of the change in transmittance $\Delta t/t$. The first order time dependence change in intensity $\Delta I/I_0$ is related to $\Delta t/t$ by:

$$\begin{aligned}\frac{\Delta I(t)}{I} = 2\left[-Im\left(\frac{\Delta t}{t}\right) + \delta_1 cos(2\theta_1) + \delta_2 cos(2\theta_2)\right] \\ \times J_1(\delta_c)\, sin(\omega t) + 2\left[Re\left(\frac{\Delta t}{t}\right) + 2\Delta \boldsymbol{P} + 2\Delta \boldsymbol{C}\right] \\ \times J_2(\delta_c)\, cos(2\omega t)\end{aligned} \tag{2.2}$$

where ω is the angular frequency of the PME. J_1 and J_2 are Bessel functions. δ_1, δ_2 and δ_c are the retardations due to the incident-ray window strain, the reflected-ray windows strain, and the compensator (modulator), respectively. The angles θ_1 and θ_2 are the incident-ray window strain and reflected-ray window strain, respectively. $(-\pi/4 + \Delta \boldsymbol{P})$ and $(+\pi/4 + \Delta \boldsymbol{C})$ are the first polariser and compensator angles, the Δ accounting for deviation to the ideal angle.

This equation shows that the imaginary or real part of the change in transmittance are selected by synchronising the lock-in amplifier to either ω or 2ω, respectively. Furthermore, the deviation from the angle of the polariser or compensator only affect the real part whereas the window strain only affects the imaginary part. For measurement of the anisotropic LSPR, we focus on the measurement of the real part.

The calibration of the TAS apparatus was done by using eq. 2.2 and fixing a given angle $\Delta \boldsymbol{P} + \Delta \boldsymbol{C}$ different from zero. It was verified by measuring the RAS of a Si(110) substrate which exhibits structural anisotropy. The experimental reference spectrum is provided by Aspnes et al. [ii2] for naturally oxidised Si(110) substrate as well as previously calibrated spectra from the laboratory. The spectrum is plotted in figure 2.4.

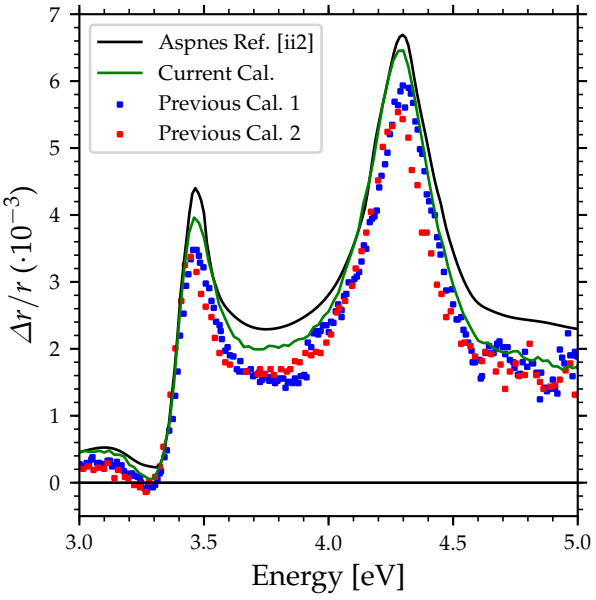

FIGURE 2.4: RAS spectrum of naturally oxidised Si(110) wafer used for calibration of the instrument. In black is the values taken from ref. [ii2]. The dots are previous measurements taken in the lab. In green is the calibration used in this work.

The orientation of the first polariser P must be adjusted with the compensator C oriented vertically in order to get a null signal when measuring an isotropic mirror such as a Si(100) clean wafer. The second polariser is oriented at a 45° relative angle.

2.2 UV-Vis-NIR spectroscopy

Measuring the localised surface plasmon resonance (LSPR) response of a sample can usually be done using the basic UV-Vis-NIR spectroscopic technique. In the case of this work, two different spectrometers were used. The first one was a commercial UV-Vis-NIR spectrometer "Cary 5000". This apparatus can measure optical transmission from $200nm$ to $3000nm$ with a spectral resolution of $0.05nm$ in the UV-Vis range and $0.2nm$ in the NIR range. The spectra are measured with a polariser before the sample. The reference beam is left empty and thus the blank spectrum is first measured on a blank glass substrate before measuring the sample. A difficulty with the Cary is to measure reflection spectra as the system in place easily scratch and damage the samples. Thus, for quick absolute spectra, a second spectrometer based on a Maya 2000 Pro from Ocean Optics Cie. was employed. It uses optical fibres to measure the transmission or reflection of the sample. The lamp is a deuterium and quartz-halogen source and the detector is Si-based providing a working spectral range from $200nm$ to $1100nm$. With this system, the spectra are obtained quicker than with the Cary and thus was employed when IR information was not required.

These spectrometers measure the ratio of the light intensity I of the sample and with the reference, I_0. The transmission or reflection is thus equal to this ratio. In the case of nanoparticles smaller than about $50nm$ in diameter , which is the case with the samples presented in the next chapter, the scattering can be negligible. In this case the absorption of the sample can be related to the transmission by Bear Lambert's law written as

$$A \approx -log\left(\frac{I}{I_0}\right) = -log(T) \tag{2.3}$$

$$\tag{2.4}$$

2.3 Microscopy techniques

The first step to properly characterise the samples is to use microscopic technique to determine the overall size and shape of the metallic nanoparticles. A wide variety of microscopic technique exist, however, due to the size of the sample (cf chapter 3) only two were used that is atomic force microscopy (AFM) and scanning electron microscopy (SEM). The next sections discuss in details the working of these methods as well as their intrinsic limitations.

2.3.1 Atomic force microscopy (AFM)

The invention of the AFM can be attributed to G. Bining et al. in 1986 [ii3]. An AFM is made of four elements shown in figure 2.6. The first element is the probing cantilever tip. It is a silicon substrate on which a microscopic tip is etched. Microscopic images of the tip are shown in figure 2.5. The second element is a ceramic piezoelectric motor which enable movement of the cantilever tip on the z axis as well as in the x, y plane. A laser is shone on the tip and reflected on a 2×2 photo diode grid which records the movement of the laser induced by the movement of the cantilever. In practice, two mirrors are placed after the laser, and before the photo diode for fine-tuning.

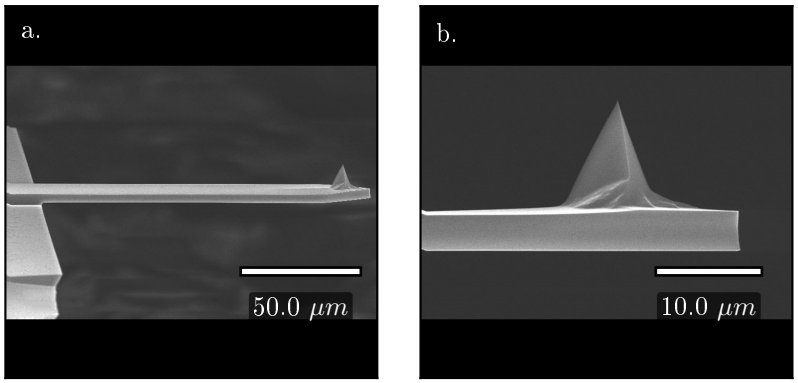

FIGURE 2.5: SEM image of the AFM tip used for the measurements in this work. The reference of the tip is *RESTPA-300*. The images were taken from the Bruker's website.

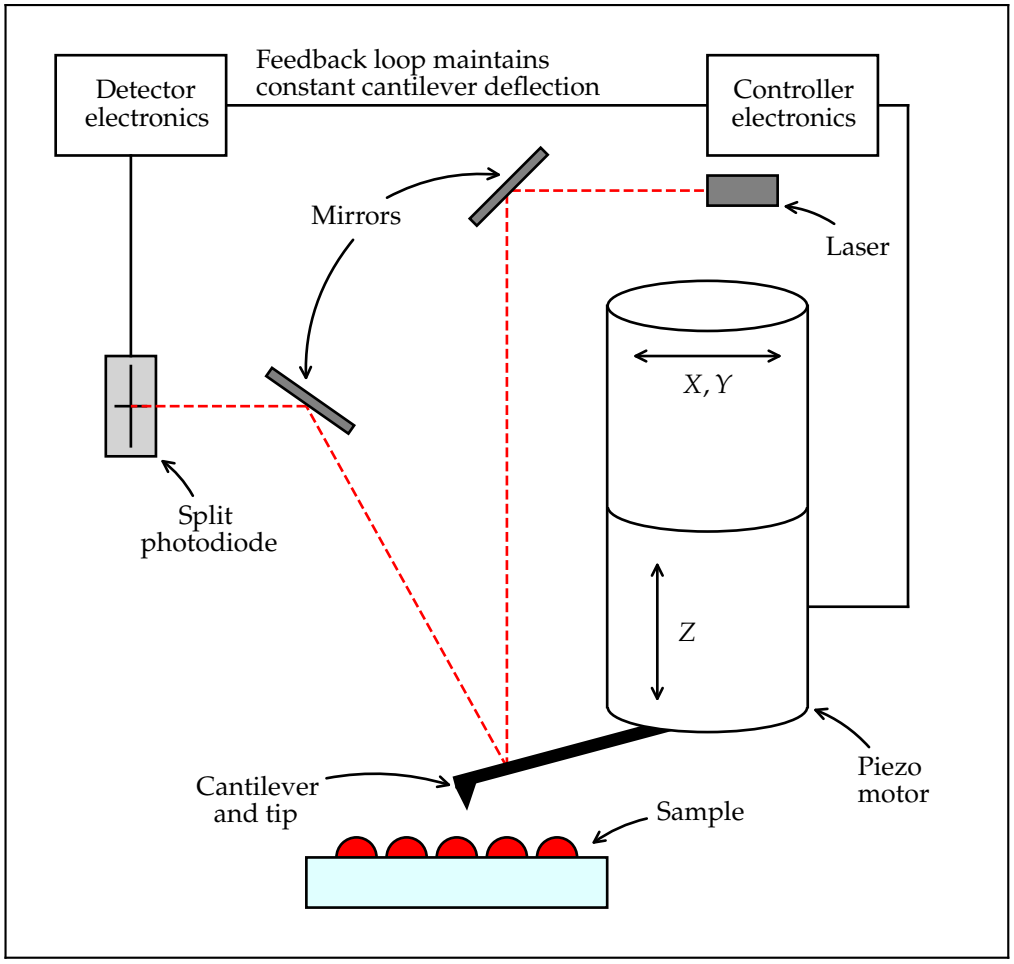

FIGURE 2.6: Diagram illustrating the operation of an AFM

There exist two main modes for AFM which are *contact mode* and *tapping mode*. In this section we shall only focus on the latter as it is the one used throughout this writing. This mode works as follows. Using the modulating piezoelectric mechanism, the cantilever is imposed an oscillation in the z axis at its resonating frequency at constant amplitude. For the tips used in this work it is around $300kHz$. As the oscillating cantilever is brought near the surface, weak attracting forces e.g. Van der Waals interaction, and repulsive forces e.g. Coulomb interaction, modify the amplitude of the cantilever oscillation. The force response curve perceived by the tip exhibits a minimum potential well as shown in figure 2.7. This feedback loop is thus used to determine the variation in height of the tip. The topographic image is generated by recording the change in height of the cantilever. The tip is scanned across an area to generate a 3D image of the surface. The variation in the phase can also be used to determine the hardness of the surface. Due to the nature of the forces at play, the cantilever never comes into contact with the surface hence why this mode is also known as non contact.

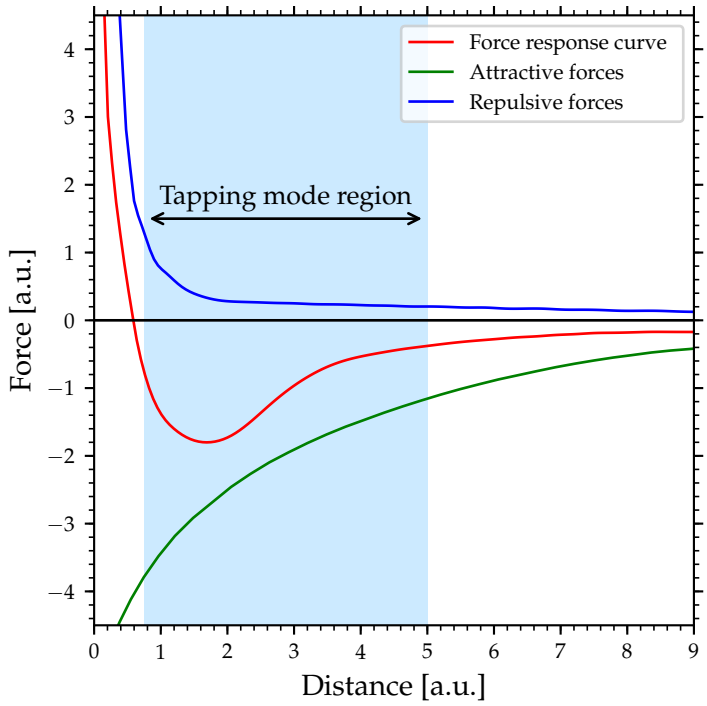

FIGURE 2.7: Graph illustrating the force response of an AFM tip when interacting with a surface. In tapping mode, the working region is shown in blue.

The benefit of AFM is that it enable the measurement of the topography of nearly any kind of surface even in liquid. Moreover, no preliminary treatments of the surface are required, making this method non destructive especially in tapping mode as the time of near contact at a specific point is very short hence reduces any risks of damaging or deforming the surface. Moreover, the technology has progressed to the point were the resolution in height is in the order of $\approx 30pm$ with a depth of field in the order of $10\mu m$. However the resolution of the lateral size is not directly defined by the performance of the piezoelectric motor which can be down to a few dozen picometers, but is limited by the shape of the tip. Indeed, a considerable drawback is the aberration due to the convolution of the tip and the surface topography. As the tip scans the surface, the lateral shape of the topography is dictated by the shape of the tip as schematised in figure 2.8. This leads to an increase in the perceived lateral size of the features covering the surface. For instance a cube etched on a surface would be recorded as hemisphere with an AFM. This phenomenon is mainly why, distribution in diameter of nanoparticles deposited on a surface cannot be well determined in

AFM. In the case of closely packed particles, the width of the tip could prevent it from reaching the space in-between particles and thus would show particles touching when in reality they are clearly separated. The reason for emphasising this already known and well understood phenomena is because it is still common place to find erroneous interpretation in the literature.

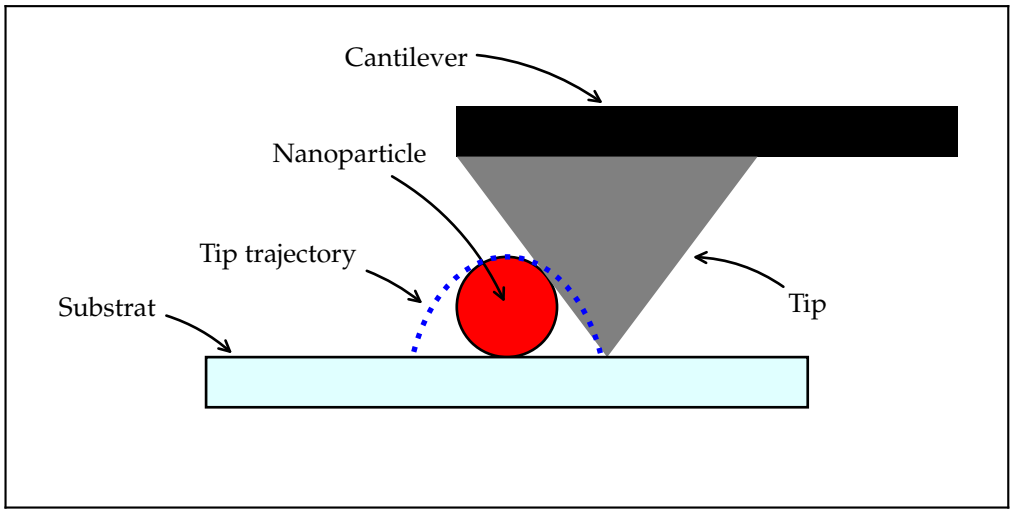

FIGURE 2.8: Diagram illustration the convolution between the tip and a nanoparticle. Although the nanoparticle is spherical, the tip will measure a hemisphere since it cannot contour the nanoparticle leading to deformation that one needs to account for in the resulting image.

More interestingly, understanding the convolution of the tip with features of the surface has enabled Rodriguez et al. to determine the actual shape of nanoparticles [ii4]. They recorded with AFM hematite ($\alpha-Fe_2O_3$) crystals which are chemically and thermodynamically stable, mono disperse and with a unique regular rhombohedral shape of $40nm$ in size. From the the measurements cross-sections, they were able to determine the radius of the AFM tip they have used which was around $7nm$.

The measurement of the sample's morphology in this work were undertaken in tapping mode on a *Digital Instruments dimension 3100*. The tips were *RESTPA-300* silicon n-doped with antimony with an oscillation frequency around $300kHz$.

2.3.2 Scanning electron microscopy (SEM)

There are two main types of electron microscope which enable morphological information acquirement of a nanoscopic sample. The first one, which is the method discussed in this section is known as scanning electron microscope (SEM). The second method is transmission electron microscope (TEM). Both methods operate by using electrons to analysis a sample, SEM working with *reflected* electrons and TEM working in transmission. Only SEM is discussed in further details within this section as it is the method used in later chapters. Indeed, the way the sample were prepared made it difficult to use TEM (see chapter 3 for more details on the sample fabrication).

SEM works analogous to an optical microscope set in reflection. A simplified diagram is shown in figure 2.9. A beam of electrons is fired towards a sample by means of an anode. A set of multiple electromagnets correct and focus the beam towards the sample, analogous to optical lens. The electrons interact with the sample through different electronic processes and are deflected back towards the detectors. Different types of detectors can be used depending on the information the user wishes to acquire. In the schematic

shown in figure 2.9, only the secondary electron and backscattering electron detectors are drawn. The sample usually needs to be conductive and connected to ground, otherwise accumulation of charge will deteriorate the quality of the image. Nonetheless, it is possible to make decent images of insulating materials as discussed in a later paragraph.

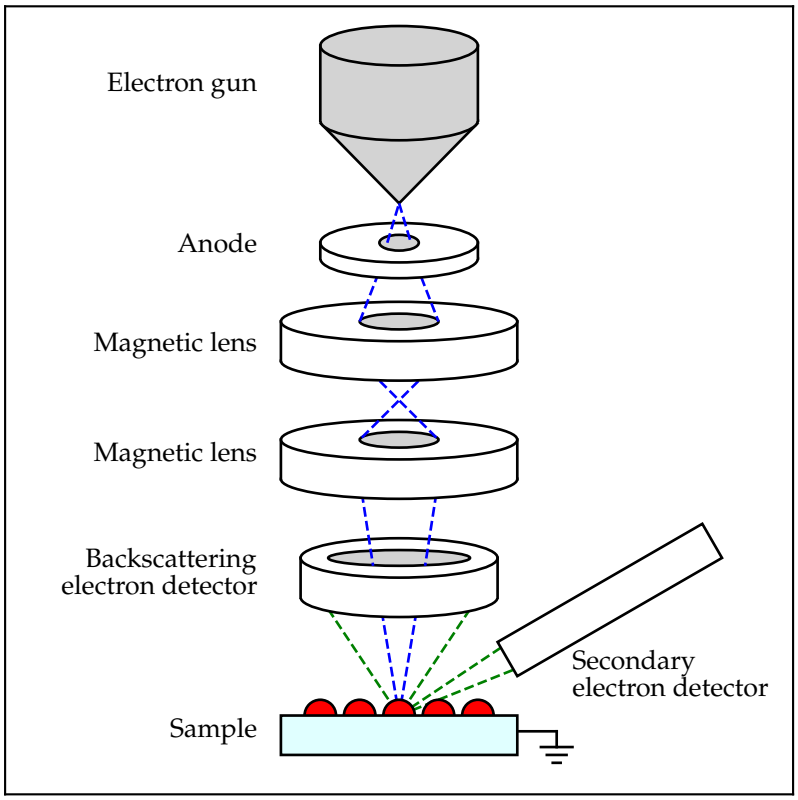

FIGURE 2.9: Digram illustrating the operation of a SEM.

The electrons deflected from the sample can come from different processes of interaction with the sample. A selection of processes are shown in figure 2.10. Some processes occur at the surface of the sample, whereas others do occur in the subsurface. When an electron beam hits a surface atom layer, the atoms might undergo Auger electron emission. This occurs as the high energy electron ionises another electron within the inner shell of the atom. The vacancy left induces a higher energy electron within the atom to fill in the vacancy an transfer the energy to an outer shell electron still within the atom. The outer electron, known as the Auger electron is ejected from the atom and captured by a detector. Its energy reveals information about the atom's orbital energy it was emitted from.

The second source of electron emission is the secondary electrons which give topographical information on the surface. This is the mode used to analyse the morphology of the sample. It simply consists in ejecting an electron from the outer shell of the surface atoms. The energy of the secondary electron can also give insight into the weight of the material emitting the atoms as heavier metals will emit more electrons than lighter atoms. This is translated to a color scale which can give qualitative information on the sample composition.

Two other modes are drawn in figure 2.10. Backscattering is similar to secondary electrons in terms of information that can be acquired that is topographical information. However, it can also give insight on

the atomic number of the emitting atoms. The source of emitted electrons comes the backscattering of the electron beam due to the nuclei of the surface atoms.

The last method which was not used in this work but worth mentioning is characteristic X-ray, also known as energy-dispersive X-ray spectroscopy (EDX or EDS). This method works by analysing the X-ray emission from the subsurface atoms of a sample due to the atoms' ionisation. Indeed, unlike Auger electrons which are emitted due to a electron relaxation, in EDX, the relaxation yields the emission of a photo in the X-ray range. The energy of the photon carries information on the element it comes from, thus EDX can generate composition maps of a sample and, contrary to Auger electrons, goes deeper under the surface of the sample down to about $1\mu m$.

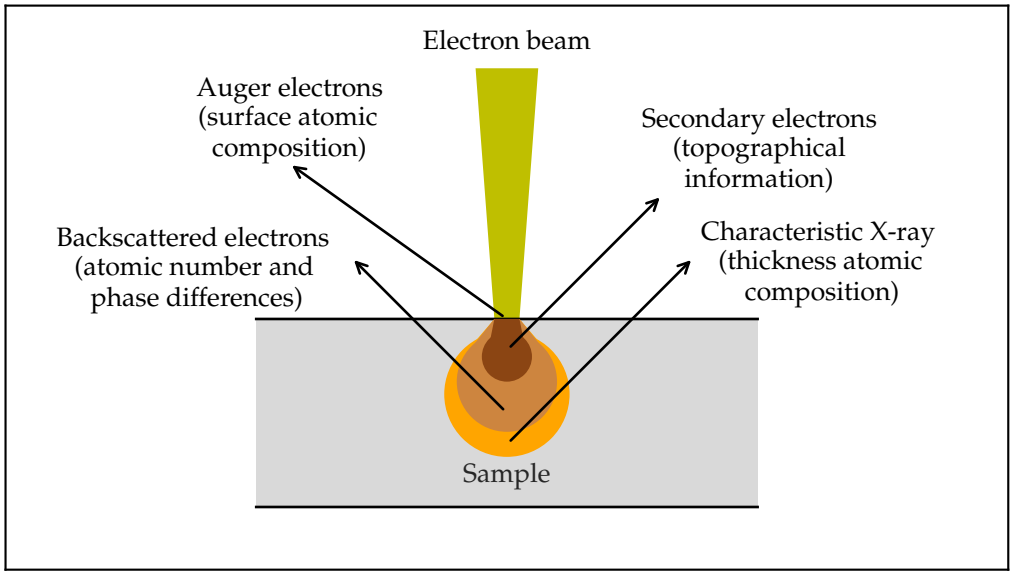

FIGURE 2.10: Diagram illustrating the different radiation types that can be emitted from a sample when hit with an electron beam. Each radiation type carries different information and thus give insight into different characteristic of the sample. Each radiation needs a special detector to be recorded.

SEM can therefore be used to gather a lot of information on a surface, its lateral resolution, in the best conditions can go below $1nm$, however, the sample needs to be perfectly conductive. In order to achieve conductivity even on non conductive samples, it is customary to cover the sample with a conductive layer, should it be gold or carbon. Indeed, if the sample is completely non conductive charging occurs which is a consequence of electron accumulation on the sample. An example of such a charging is shown in figure 2.11. The image shows a layer of metal-oxide framework deposited on a glass substrate, more specifically zeolitic Imidazolate Framework (ZIF-8) which is an isolator [ii5]. A crystal can be seen on the right hand side of the image. The dark patch on the left hand side is due to charging of the material. This image was recorded with the SEM set with an aperture of $7\mu m$ and the electron potential set at $7kV$ and a working distance of $3.4mm$. It is possible to reduce charging by working at a lower potential and by having a small working distance, that is the distance between the surface and the detector. Moreover, using conductive tape near the region of interests may help the charge to dissipate.This helps the evacuation of the electron charges but will reduce the maximum resolution of the image.

The SEM used in in this work was a Ziess Supra 40 with the electron potential set between 3 to $10kV$ with a working distance between 3 and $5mm$ with an aperture set at $7\mu m$.

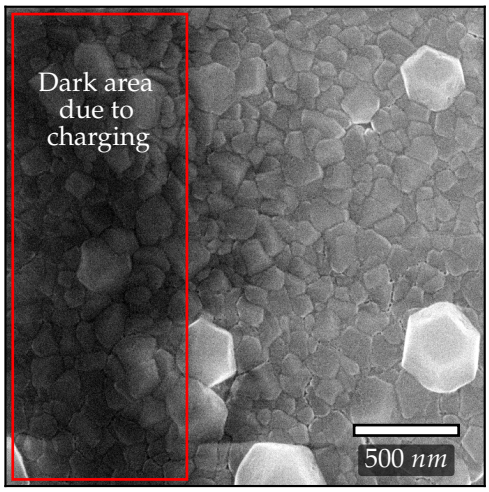

FIGURE 2.11: SEM image of a metal oxide framework (ZIF-8) deposited on a thin Pd layer evaporated on a non conductive glass substrate. Outlined in red is an illustration of the effect of charging due to the non conductive nature of the substrate.

2.4 Technical details of the gas systems

The samples are loaded in a gas cell equipped with a silica window enabling the TAS measurements during gas cycles. Figure 2.12 shows a diagram of the gas system. The sample is followed with a silicon (100) wafer which plays the role of an isotropic mirror. The light beam thus passes twice through the sample. The sample is put at a 45° in the cell. With this set up, the sample could be exposed to controlled atmospheric pressure.

Prior to experiments, the whole gas pipes are purged with Ar for several hours and cycled through Ar to eliminate any gas contaminants, mainly water and oxygen. The gas flow were around 1000$sccm$. This high gas flow was used to rapidly purge the pipes and the cell chamber as slower gas flows would induce artefacts in the measurements.

In order to make mixtures of different gas, such as Ar and H_2 an additional bottle was used in order to expose the sample to different partial pressures of the mixture. The preparation consists in pumping the bottle whilst heated to $3 \cdot 10^{-3} mbar$ for 24h. It can then be filled with different partial pressures of the wanted gases. For instance, in order to get 63% H_2 in Ar, it is then filled with 2.5bar of H_2 and completed to 4bar with the carrier gas. The bottle is then emptied to atmospheric pressure and refilled to 4bar with the carrier gas. By using this procedure several times, accurate proportions of H_2 down to a few ppm can be obtained.

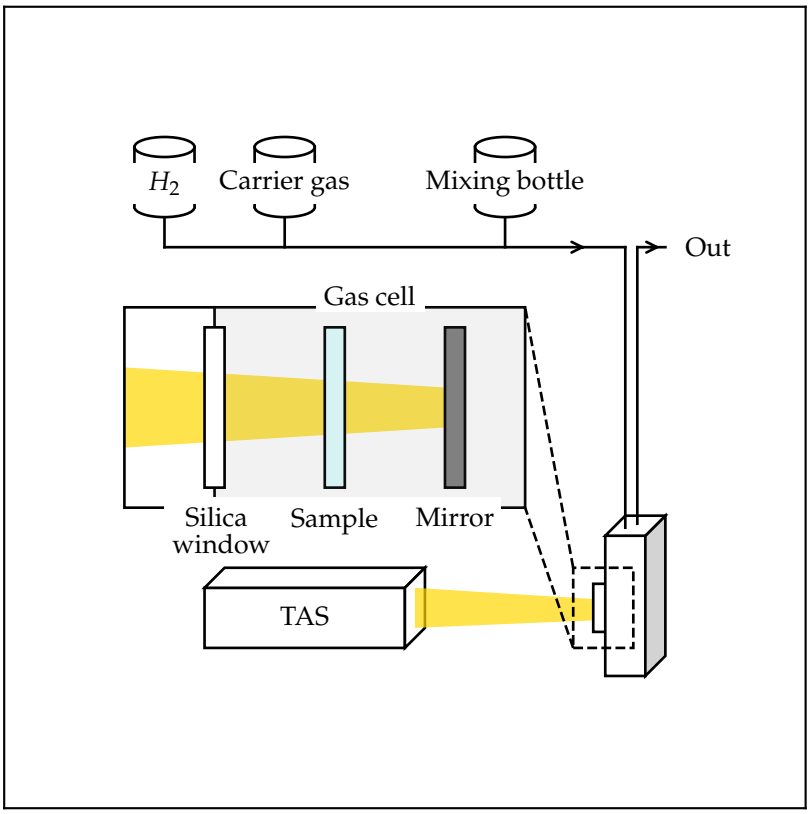

FIGURE 2.12: Diagram illustrating the gas flow system used. The flow were controlled using Swagelok metering valves, in stainless steel pipes. The sample is placed at a 45° angle with respect to the direction of evaporation and the polarisation. The mirror used was a $Si(100)$ wafer. The H_2 was generated by electrolysis whilst the other gases were taken from pressurised bottles.

The Ar, N_2 and O_2 gas bottles used were Air liquid alpha gas. The containments of the Ar and N_2 bottles were $< 3ppm$ of water, $< 0.5ppm$ of hydrocarbons, and $< 2ppm$ of O_2. The O_2 bottle has the same specifications for water and hydrocarbons as the inert gases. The H_2 was provided by a hydrogen generator model PGH_2 160 from FDBS. It provided a dry H_2 at 99.999% purity at pressures up to $7bar$.

2.5 References

[ii1] D. E. Aspnes, J. P. Harbison, A. A. Studna, and L. T. Florez, "Reflectance-difference spectroscopy system for real-time measurements of crystal growth", *Applied Physics Letters*, vol. 52, no. 12, pp. 957–959, 1988.

[ii2] D. E. Aspnes and A. A. Studna, "Anisotropies in the Above—Band-Gap Optical Spectra of Cubic Semiconductors", *Physical Review Letters*, vol. 54, no. 17, pp. 1956–1959, 1985.

[ii3] G. Binnig and C. F. Quate, "Atomic Force Microscope", *Physical Review Letters*, vol. 56, no. 9, pp. 930–933, 1986.

[ii4] R. D. Rodriguez, E. Lacaze, and J. Jupille, "Probing the probe: AFM tip-profiling via nanotemplates to determine Hamaker constants from phase–distance curves", *Ultramicroscopy*, vol. 121, pp. 25–30, 2012.

[ii5] M. R. Ryder, Z. Zeng, K. Titov, Y. Sun, E. M. Mahdi, I. Flyagina, T. D. Bennett, B. Civalleri, C. S. Kelley, M. D. Frogley, G. Cinque, and J.-C. Tan, "Dielectric Properties of Zeolitic Imidazolate Frameworks in the Broad-Band Infrared Regime", *The Journal of Physical Chemistry Letters*, vol. 9, no. 10, pp. 2678–2684, 2018.

Chapter 3

Sample elaboration

Abstract

Elaborating nanoparticles exhibiting localised surface plasmon resonance (LSPR) has been done for a long time as discussed in the main introduction. However, value is present in being capable of manipulating, organising and tailoring the nanoparticles to take advantage of interactions and morphological effects e.g. anisotropy.
In this chapter, we will take a look at different techniques used in the literature to fabricate anisotropic LSPR samples. After which, oblique angle deposition (OAD) will be described as it is the method chosen for to fabricate the samples used in this thesis. The reasoning goes that it offers the best performance ratio in terms of ease of fabrication and optical properties. Finally demonstrations on how to theoretically model the experimental samples are discussed which enables to better understand the origin of the optical anisotropy within the sample.

3.1 Introduction on the synthesis of anisotropic LSPR samples

There are two main paths for tailoring particles at the nanoscale: top-down and bottom-up. The first approach can be considered as sculpting or carving matter out of a solid block to reach nanometre dimensions. This powerful method has enabled the fabrication of integrated electronics using the infamous method known as lithography which can be either optical of electronical. Despite its great capabilities, its limits are quickly reached as optical lithography is intrinsically limited by the wavelength of light, which in turn limits the fabrication of features around the $50nm$ barrier at best. Electron beam lithography can reach the single digit, its main limiting factor, apart from the cost, is the overall size of the sample as a grid of $100 \times 100\mu m$ takes a long time to fabricate which therefore limits the scalability of the technique.

The second approach, that is bottom-up, consists in using very small building blocks, should it be nanoparticles or even molecules, and to assemble them into nanoscale features for instance through means of colloidal deposition or chemical synthesis. This breaks the limit of scalability and quantity which refrains top-down methods, and chemical processes have been able to generate large quantities of well controlled shapes of a wide variety of geometries. The limiting factor however is now the organisation of these particles. Indeed, isotropic system, through isotropic particles e.g nanospheres, or through randomly oriented anisotropic particles e.g. nanorods, are easy to fabricate, but a lot of efforts is still put into trying to macroscopically orient and organise such particles with various degrees of success.

These two categories are of course not strictly separated and some methods do employ both strategies as we will discuss below.

3.1.1 Top-down: Lithography

When wanting to manufacture controlled nanopatterns on a surface, the first method of choice is to use lithography [iii1]. The principle consist in using a beam of either light of electrons to print a pattern onto a photo sensitive surface and then to use chemical etching to reveal the pattern. In the case of photolithography, a photo sensitive polymer is coated on a surface, then a mask is placed in front which contains the pattern. Using high energy light, usually in the UV range, the photo sensitive polymer is exposed only where the mask lets the light through [iii2].

The resolution is pretty low as patterns of $100nm$ in dimension are usually the order of magnitude of the features. This is mainly due to the diffraction limit of UV light. Smaller features around $20nm$ can be achieved but require high resolution masks and extreme UV light ($\lambda \approx 13nm$) [iii3].

For smaller feature, electron beam lithography is an alternative. It works similarly, that is an "electron" sensitive polymer is deposited on a surface, however this time the electron beam directly *draws* the pattern on the surface instead of using a mask. Due to the fact that electrons do not have the diffracting behaviour as light does in this range of size, feature of $< 50nm$ are easily made and the lower limit is around a few nanometres. Indeed, Manfrinato et al. have demonstrated the fabrication of features below $4nm$ with such a technique [iii4]. However, the scanning method thus limits the total area which can be made. It is possible to extend this surface with multiple steps and by physically displacing the sample though it is a tedious process. The fact that the patterns can be precisely fabricated allowed authors such as Wallace et al. to preciselly control the shape of the LSPR spectrum [iii5]. Indeed they were capable of fabricating an array of Au nanoflacks as shown in figure 3.1.a. which exhibits two LSPR maxima in the IR. Moreover, they have shown a small dichroism with orthogonal polarisations as shown in the spectra in figure 3.1.b.

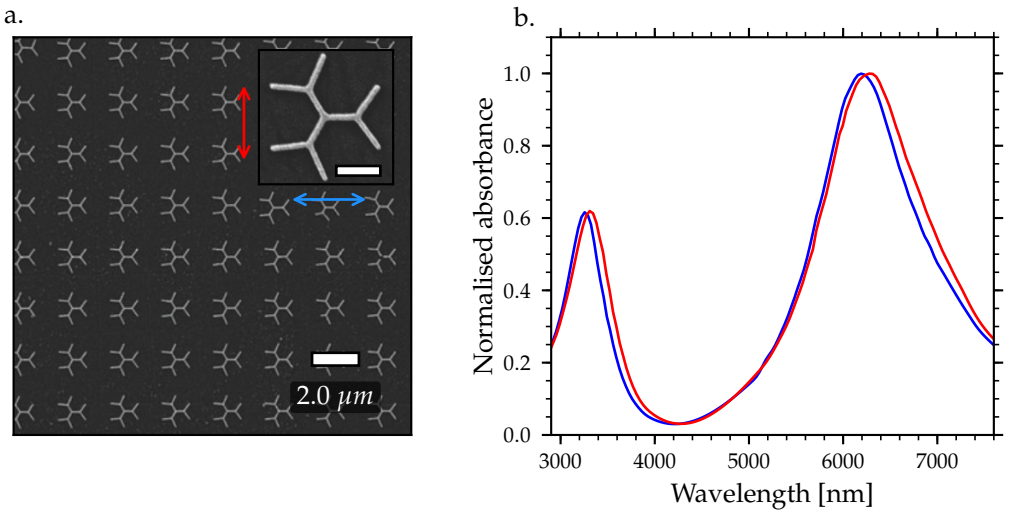

FIGURE 3.1: a. SEM image of the nanoflacks elaborated by electron beam lithography on a CaF_2 substrate with a $3nm$ titanium adhesion layer. The scale bar on the insert is $500nm$. b. UV-Vis absorbance spectra of the nanoflacks at orthogonal polarisation. The orientation of the polarisation is indicated by the coloured arrows on the inset of a. The images were taken from ref. [iii5].

In order to decrease the size of the nanoparticles as well as increase the surface area covered, hole-mask lithography was developed [iii6]. It has the advantage of enabling LSPR spectra in the visible range. The approach consists in organising nanobeads on a surface, the closed packed arrangement yields small holes in-between the beads where metal can be evaporated at different angles. The process is depicted in figure 3.2 which shows different ways of obtaining different nanoparticle geometries. The beads thus play the role of a mask and quite small features can be patterned on a large area [iii7], [iii8]. This method has been used to fabricate anisotropic LSPR systems as shown by Verre et al. for fabricating globally anisotropic samples as discussed in section 1.4.2 [iii9].

An alternative method for depositing patterns at the nanoscale is to use nanoimprint. This method consists in fabricating a nanometric stamps which can transfer its topography to a substrate. The fabrication of the initial pattern is the crucial step. It can be done by electron beam lithography, which although a heavy step, is only done once and the stamp can be replicated multiple times. Other fabrication techniques have

been used such as interference lithography which uses laser interference to print a pattern on a photosensitive media [iii10] , or even wrinkling which consists in generating wrinkles in a polymer surface which can then be used as a stamp [iii11]. The stamp is then pressed into a malleable material such as a resin which is then cured with the new pattern. Metal can then be evaporated and reveal patterns of nanoparticles. This method has been demonstrated as early as 1996 with Chou whom has demonstrated the possibility of stamping polymethyl methacrylate (PMMA) into nanodisk of around 25nm in diameter or nanostrips of about 30nm in width [iii12]. Further work has been accomplished by various different research teams to fabricate a wide variaty of patterns with various optical properties [iii13]–[iii16].

Although good results have been produced with these various types of lithographic techniques, they usually have the issue of producing either relatively large features, or small features but on a small area, as well as being difficult to scale, and require heavy equipment. For information a mask made for a CPU may cost in the vicinity of hundreds of millions of euros, which can only be profitable at the scale the units are sold.

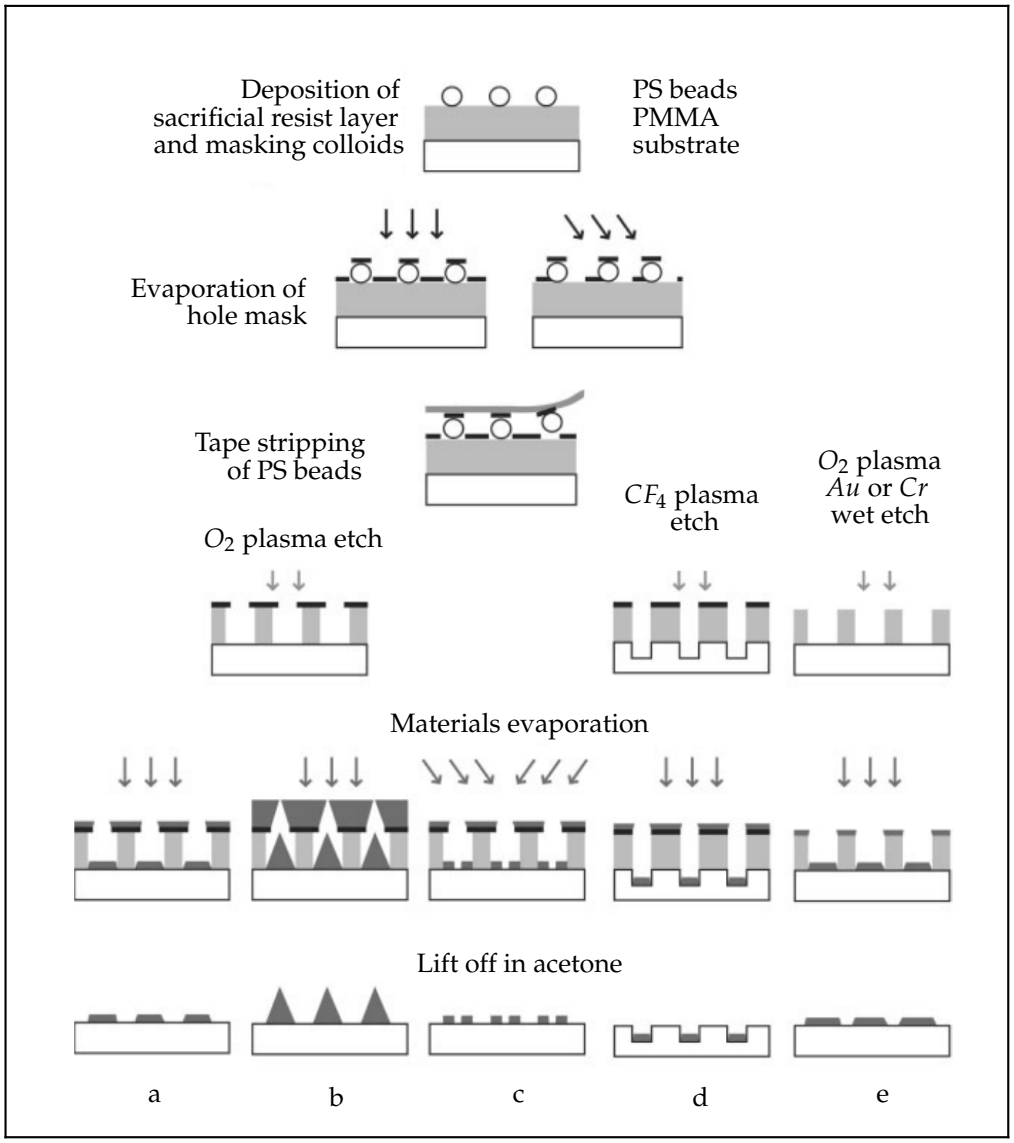

FIGURE 3.2: Diagram illustrating the basic steps and resulting structures produced with hole-mask colloidal lithographie. The resulting structures are a. arrays of nanodiscs and oriented elliptical nanostructures, b. nanocone arrays, c. binary arrays of nanodisc pairs, d. embedded nanodiscs, and e. discs with fine tunable diameters. The diagram was taken from ref. [iii7].

3.1.2 Bottom-up: chemical synthesis

The chemical synthesis of gold nanoparticles dates back to Faraday as presented in the introduction. In 1951, Turkevich proposed a very simple method of synthesising small ($\geqslant 5nm$ in radius) nanoparticles of gold by reacting gold salts with a reducing agent [iii17]. The method has been more generalised and it is now possible to craft a wide variaty of nanoparticle shapes with a quite narrow size distribution [iii18]. This has been extensively studied for LSPR applications with the shape of the particle enabling the design of the LSPR spectra (cf. section 1.4.1) [iii19]–[iii22]. However, the chemical process of these nanoparticles relies on the presence of surfactants at their surface, in order to stabilise the colloidal particle and prevent aggregation. This obviously is a problem when dealing with plasmonic sensing.

Yet a difficulty arises from aligning these particles over an extensive range to make a globally anisotropic sample. Indeed, obtaining long chains of nanorods is a difficult process to do. Nie et al. were capable of making chains of gold nanorods a few particles long by modifing the chemical surfactant on the ends of the nanorods (Fig. 3.3.a) [iii23]. Although a chemical feat, only small chains were obtained and it is not a usable process for LSPR sensing applications. A similar approach was also done by Correa-Duarte et al. whom have attached gold nanorods to carbon nanotubes (Fig. 3.3.b.) [iii24], [iii25]. This allowed the fabrication of long chains ; yet, the same problem arises as it is now an issue of aligning the carbon nanotubes.

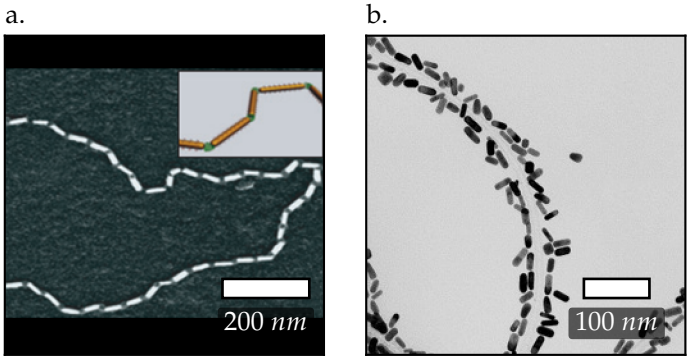

FIGURE 3.3: a. SEM images of the self assembled Au nanorod structures in the dimethyl formamide/water mixture from ref. [iii23]. The inset shows a diagram of the nanorods coated with polystyrene on the ends enabling the aligning of the nanoparticles. b. TEM image of the Au nanorods assembled on carbon nanotubes (MWNT) from ref. [iii24].

An interesting method prosed by Lacaze et al. was to use liquid crystals which can trap nanoparticles in their defects. The anisotropic nature of liquid crystals enables the alignement of nanospheres and nanorods [iii26], [iii27]. The aim could thus be to be able to orient the nanoparticles by modifying the orientation of the liquid crystals. However this poses an issue in terms of sensing applications as the nanoparticles are not exposed to the atmosphere and the particle density obtained in their experiments are quite low.

The same problem arises with polymer stretch methods which consists in embedding anisotropic nanoparticles such as nanorods in a flexible polymer matrix. The stretching of the matrix leads to a partial alignment of the nanorods and thus gives rise to a dichroic LSPR response [iii21], [iii28]–[iii31].

Alternatively, the use of nanostructured surfaces can be employed to align nanosphere and nanorods. The principle is to induce wrinkling in a surface, usually polydimethylsiloxane (PDMS) by stretching and releasing [iii32], [iii33]. This leads to parallel wrinkles of a few nanometres in depth and a few micrometres

apart. Using dip-coating it is possible to fill the wrinkles with nanoparticles which align in the same orientation [iii34]. Carefull control on the width and depth of the wrinkles even enables Tebbe et al. to fabricate rows of chemically synthesised single nanorods with quite a large density [iii35].

For LSPR application, nanoimprint can be further used, as instead of printing a pattern on a surface, the stamp can be used to deposit nanoparticles on a second surface [iii36]–[iii38]. The principle, schematised in figure 3.4 is to coat the stamp with nanoparticle, usually through the evaporation of a colloidal solution. When stamped, only the organised particles are transferred to the substrate.

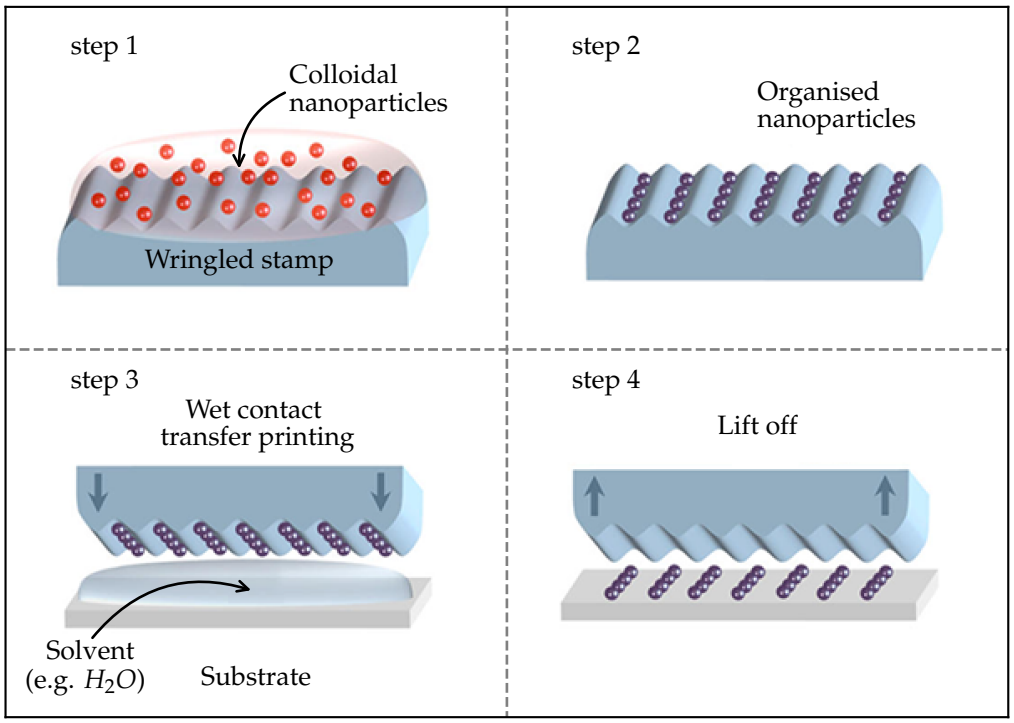

FIGURE 3.4: Diagram of a typical nanoimprint process. a. the colloidal nanoparticle solution is deposited on a structured stamp substrate and left to evaporate. b. the evaporation leads to an organisation of the nanoparticles on the stamp. c. a solvent (e.g. water) is deposited on a substrate and the nanoparticles are transferred by printing. d. the lift off leads to the particles sticking on the substrate whilst keeping their original organisation pattern.

This has been used by Hanske et al. to fabricate thin metal stripes on a large surface area as shown in figure 3.5 where they used this method to align Au nanoparticles of about $80nm$ in diameter [iii37]. As shown in the figure, they were able to make either single or multi particle chains which mainly depends on the size of the wrinkles.

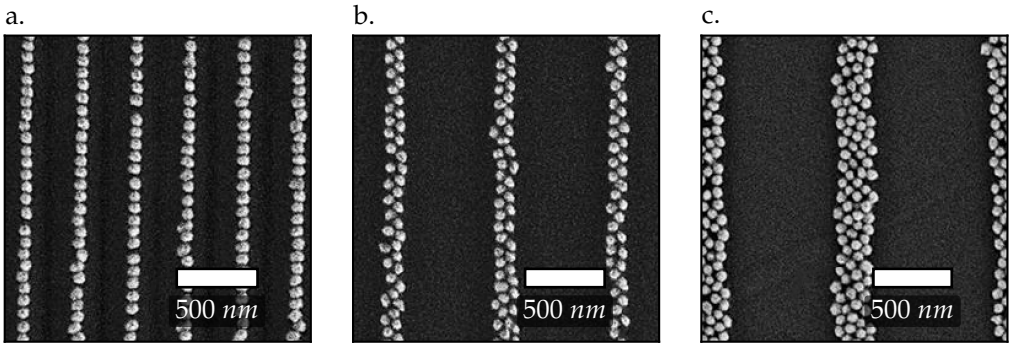

FIGURE 3.5: SEM images of nanoparticles deposited on a flat quartz substrates by nanoimprint. The difference in width of the nanoparticle chains is due to the size of the wrinkles on the stamp (a. smallest and c. largest). The images were taken from ref. [iii37].

3.1.3 Oblique angle deposition

Oblique angle deposition (OAD) has been a niche method used to easily fabricate anisotropic nanoparticles.It does not have the same control as the method proposed earlier ; nevertheless, it is possible to fabricate small nanoparticles for LSPR applications. One of the main advantage is the fact that the obtained particles are not chemically synthesised thus they do not have a surfactant layer which would interfere with the chemical reactivity of the metal towards its environment in the case of direct sensing.

The method consists in evaporating the plasmonic metal at an angle on a structured substrate. This method has been used by Anghinolfi et al. to fabricate dichroic Au samples [iii39], [iii40]. They used a ridge valley structure obtained on LiF crystals which spontaneously form upon homo epitaxial deposition at the (110) surface. The schematic of the process and the experimental results from Anghinolfi et al. are plotted in figure 3.6. The AFM image (Fig. 3.6.b.) shows ridges of about $40nm$ in width. The evaporation of Au at a grazing angle leads to the formation of nanowires as schematised in figure 3.6.c. Annealing the sample at $670K$ leads to the formation of droplets and thus an array of nanoparticle chains of narrowly distributed size (Fig. 3.6.d.e). This structuring leads to a LSPR spectrum in the visible range (Fig. 3.6.f) dependent on whether the polarisation is perpendicular or parallel to the ridges.

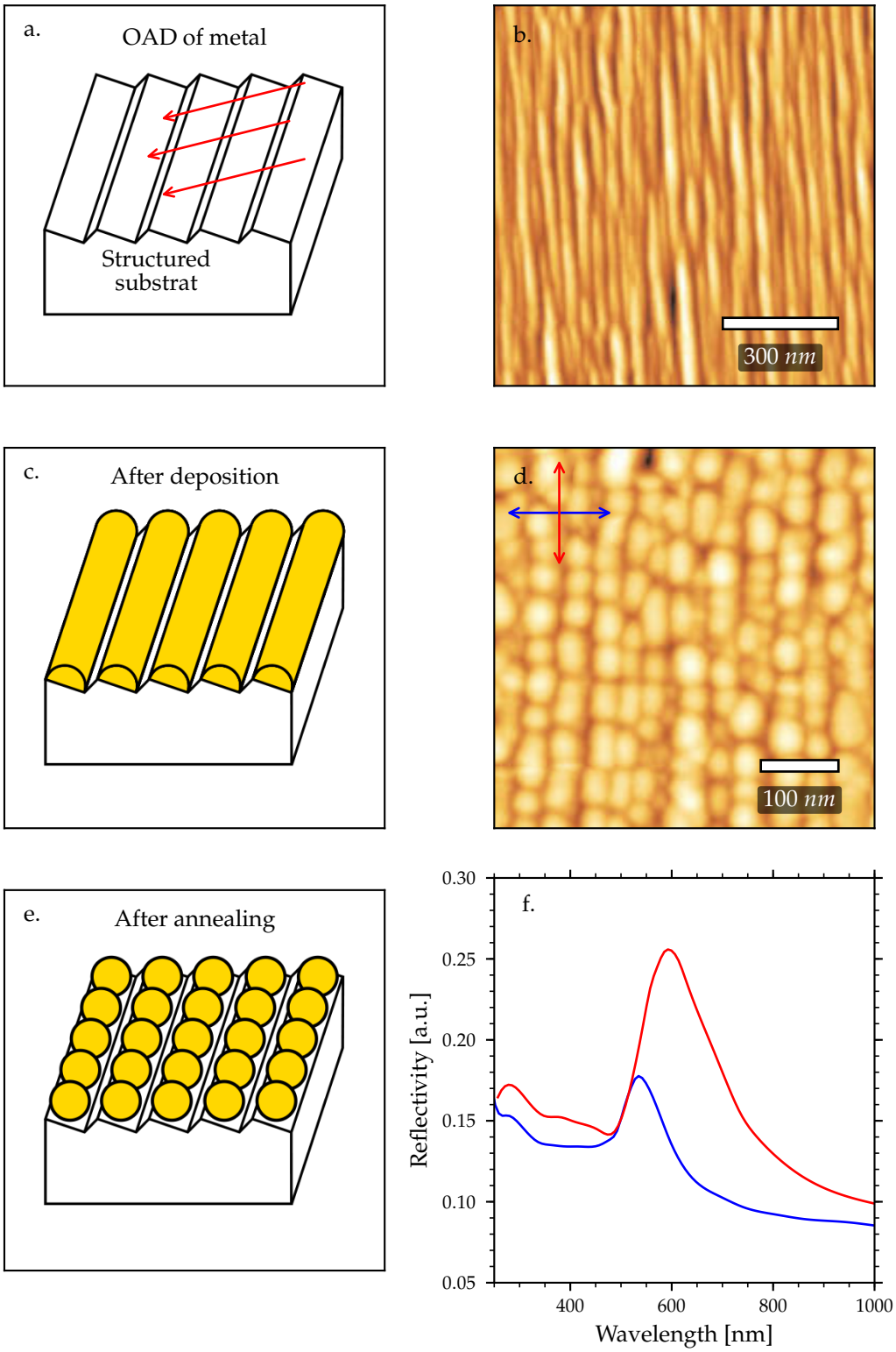

FIGURE 3.6: Oblique angle deposition process on a structured substrate. a. diagram of the evaporation at an oblique angle on the substrate. b. AFM images of a LiF strucutred substrate. c. diagram showing the Au after evaporation which shows lines of metal oriented perpendicular to the direction of evaporation. d. and e. show the AFM image of the substrate and a diagram of the nanoparticles, respectively, after annealing. f. shows the reflectivity spectrum using orthogonal polarised light of the sample showed in d. with the polarisation colour code given by the arrows of figure d. The experimental images are taken from ref. [iii39].

A similar method was used by Verre et al. though using a different structured substrate [iii41]–[iii43]. In their case, they used a sapphire crystal, more specifically the $\alpha-$plane Al_2O_3 miscut 6° along the $[1\bar{2}10]$. When annealing this substrate between 1500 to 1700K in atmosphere for 24h, an ordered terrace and stepped structure is formed. The terrace are about 150nm in length with steps of about 20nm as shown in the side view SEM image in figure 3.7.a. Evaporation of Ag at a grazing angle thus leads to aligned nanoparticles (Fig. 3.7.b.) with dichroic LSPR.

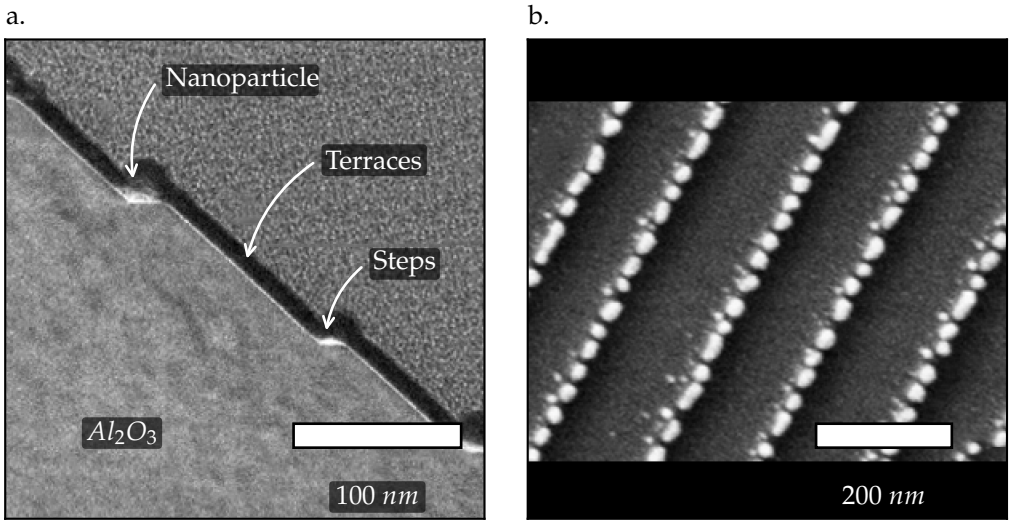

FIGURE 3.7: a. TEM image of a section of the alumina crystal showing the step and terrace formation. The nanoparticles form on the steps. b. SEM top view image of the structured alumina crystal on which the nanoparticles are deposited. The images are taken from ref. [iii42].

The issue with these inorganic nanostructured substrates is either the cost of manufacturing or the stability of the material used. Indeed sapphire crystals which must be precisely cut and heated above a 1500K are not a scalable process, the same way the LiF substrate, being a salt, is soluble in water making it impractical.

On the other hand, it has been shown that the wetting properties of Ag and Au, leads to the formation of small nanoparticles when evaporated on flat glass [iii44]–[iii47]. When adding an angle to the substrate during evaporation as shown in figure 3.8.a., the particles grow as nanorods on the substrate as shown in figure 3.8.b. [iii48], [iii49].

It has been shown by Fu et al. that evaporating a small amount of Ag at an angle leads to the formation of nanoparticles with a dichroic LSPR spectrum [iii50]. The advantage of this method is that it yields easily reproducible samples which can be of various size. Furthermore, the stability of glass makes its convenient for sensing applications as it will not interfere with neither the measurement nor the environment.

In the next section we will discuss the parameters which influence the LSPR spectrum of OAD prepared samples using glass substrates. The investigated parameters were the angle of deposition, the metal's mass thickness as well as the annealing.

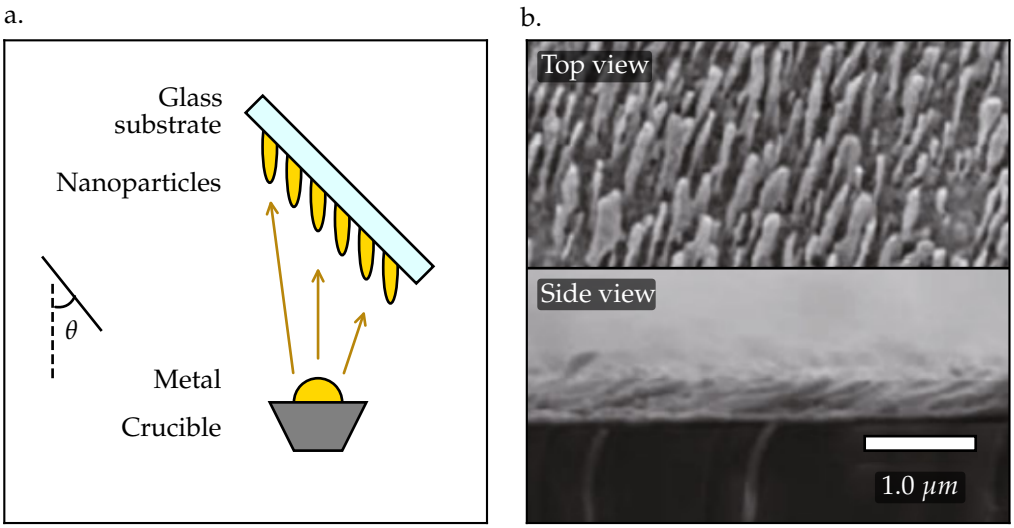

FIGURE 3.8: a. Diagram of the OAD process with θ being the angle between the verticle evaporation direction and the plane of the substrate. b. top and side view SEM images of Ag nanoparticles evaporated by OAD. The angle was $\theta = 4°$ and the mass thickness measured by the quartz micro balance i.e. normal to the direction of evaporation, was $2\mu m$. The SEM images were taken from ref. [iii48].

3.2 Use of oblique angle deposition (OAD)

3.2.1 Fabrication of Au samples: investigation of elaboration parameters

• Basic protocol of OAD used in this work

The protocol was to evaporate Au under a $3 \cdot 10^{-6} mbar$ vacuum on glass substrates, prepared from microscope slides cleaned with ethanol. The evaporation was carried out from a crucible heated by direct current with the samples positioned at a grazing angle relative to the crucible (Fig 3.8.a.). The evaporation rate was set at $\approx 0.2nm \cdot s^{-1}$ for all evaporations. The mass thickness was controlled using a calibrated quartz micro balance. To investigate the effect of the angle, mass thickness and annealing on the optical properties, multiple samples were made. The samples were evaporated at six different angles and with three different mass thicknesses as summarised in table 3.1. The samples were analysed by SEM to determine the particle morphologies and by AFM to determine their average heights.

TABLE 3.1: Table summarising the sample fabrication conditions. Fifteen samples were fabricated at five different angles denoted by the series number and at three different quantities of evaporated gold denoted A, B and C. The values under these columns correspond to the calculated mass thickness which accounts for the angle of deposition. The quartz mass thickness is the reference of the amount of metal evaporated at normal incidence. The mass thickness relative to series #1 are given in the last column.

Quartz mass thickness [nm]		10	13	17	Relative
Series	Angle [°]	A	B	C	mass thickness
#1	12	2.3	3.0	4.0	1.0
#2	16	3.0	3.9	5.2	1.3
#3	24	4.1	5.4	7.2	1.8
#4	26	4.3	5.7	7.6	1.9
#5	33	4.9	6.4	8.6	2.1

The method of elaboration yielded two different morphologies as shown in figure 3.9. On the one hand, some samples, such as #1A, exhibit individual nanoparticles which can be seen in the SEM image. This usually correlates to a low amount of evaporated metal and to a small angle. On the other hand, when a large amount is evaporated with a large angle, the Au forms strip structures separated by gaps as shown for sample #5C. In both images the direction of evaporation is from bottom to top. The AFM measurement showed that the height of both samples are 7.5nm and 11.8nm, even though the mass thickness (Tab. 3.1) were calculated to be 2.3nm and 8.6nm, respectively. The discrepancies between the AFM heights and the calculated mass thicknesses come from the formation of the nanostructures which are higher than if the Au had deposited in a continuous thin film.

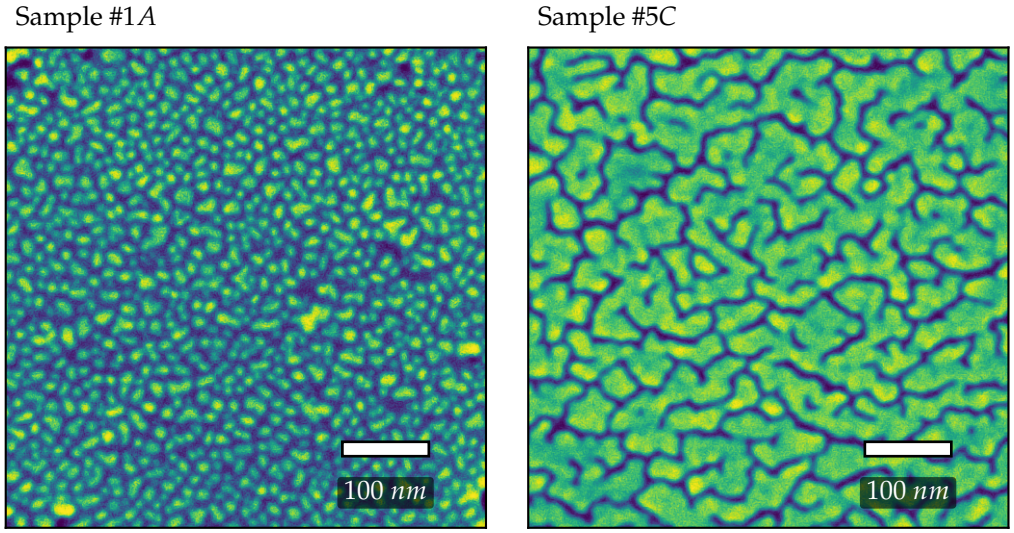

FIGURE 3.9: SEM images of #1A and #5C Au samples. The sample fabrication characteristics are given in table 3.1.

The two samples' transmissions were measured using UV-Vis spectroscopy with light orthogonally polarised relative to the direction of evaporation [1] (from bottom to top on Fig. 3.9). A polariser was placed in the light path and was oriented with respect to the direction of evaporation i.e. 0° is parallel to the direction of evaporation and 90° is normal to the direction of evaporation. The results are showed in figure 3.10. It can be seen for sample #1A (Fig. 3.10.a.), that it exhibits a dichroic spectra with two transmission minima at $\approx 575nm$ for parallel polarisation and $\approx 650nm$ for normal polarisation. On the other hand, sample #5C (Fig. 3.10.b.), only exhibits a minimum in transmission for parallel polarisation at about 700nm whilst the orthogonal polarisation shows a continuous decrease in transmission going to the IR. This comes from the rather large elongated nanostructures in the normal direction relative to the evaporation direction which leads to a red shift of the LSPR. It nevertheless also exhibits dichroic spectra. These two examples show that the OAD method does yield a polarisation dependent LSPR, which is dependent on the parameters set for the evaporation.

Thanks to this polarisation dependent optical response, it is possible to use transmission anisotropy spectroscopy (TAS) to measure the differential spectrum $\Delta T/T$ as described in section 2.1.1. The spectra for both samples are plotted in figure 3.10.c. and d. Looking at the first TAS spectrum from sample #1A, we can see a maximum at 520nm and a minimum 710nm. The spectrum crosses zero as both orthogonal

[1] Due to initial technical difficulties in the UV-Vis measurements which were solved afterwards, the spectra displayed are actually those of the samples after annealing at 140°C. They are very close to the spectra measured before annealing. More details are given in appendix A.2

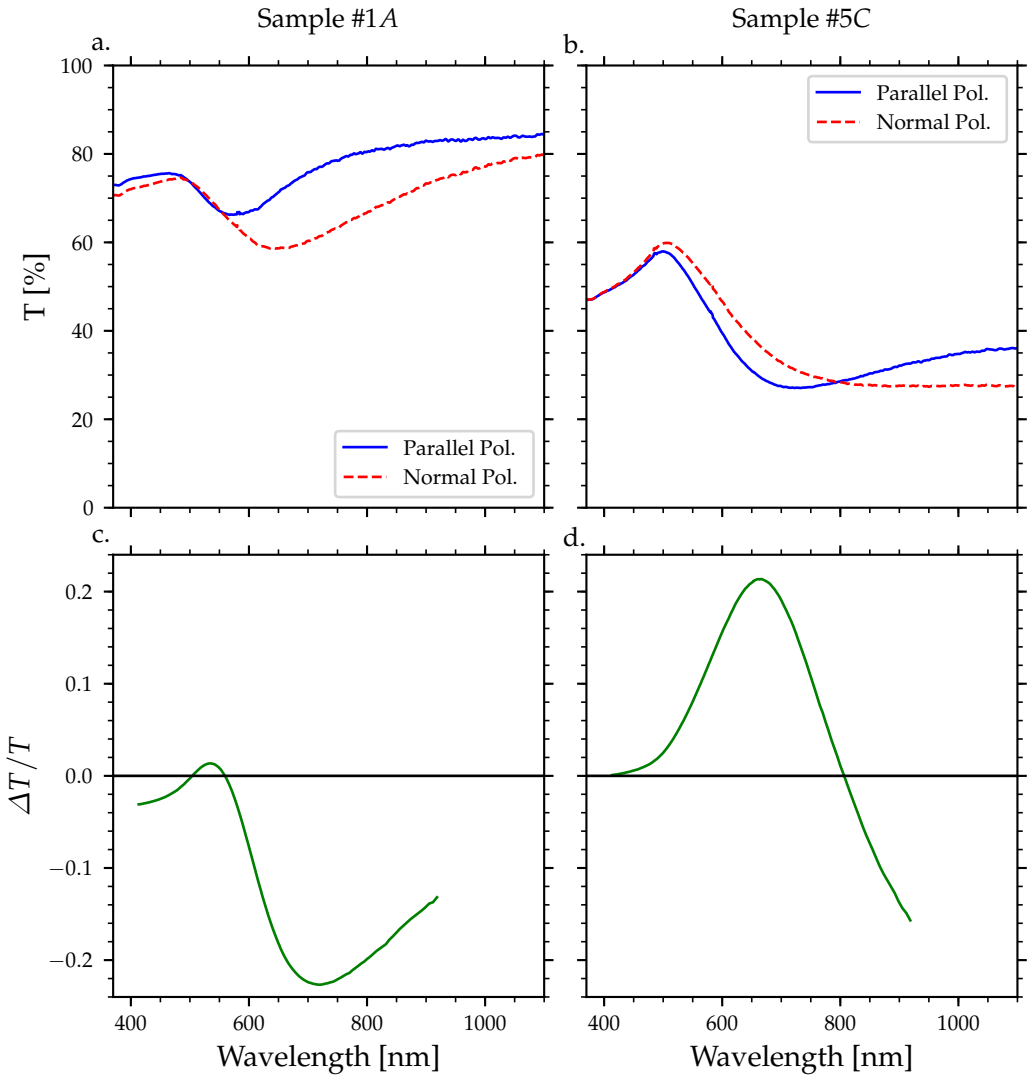

FIGURE 3.10: a-b. UV-Vis transmission spectra of samples #1A and #5C. Both orthogonal polarisations were measured parallel and normal to the direction of evaporation using a polariser. c-d. show the respective TAS spectra for each sample respectively. These TA spectra were measured by going twice through the sample.

transmission spectra cross each other. On the other hand, the TAS spectrum for sample #5C only shows a maximum at $700nm$ which comes from the fact that only the parallel polarisation exhibits a transmission minimum in the investigated wavelength range (Fig. 3.10.b.).

• Influence of the angle

To investigate the effect of the angle of evaporation on the particle morphologies and shape of the LSPR spectra, we can look at the couples #2B *vs.* #3A and #2C *vs.* #3B. Indeed the number "#2" in the nomenclature corresponds to an angle of incidence of 16° and "#3" to an angle of 24° with respect to the crucible (Tab. 3.1). Both couples have a mass thickness of $\approx 4nm$ and $\approx 5nm$, respectively. These couples therefore show the effect of the angle of incidence whilst keeping the mass thickness constant. The SEM images are shown in figure 3.11. Both the #2B and the #2C images exhibit relatively round individual nanoparticles of about $15nm$, whereas samples #3A and #3B exhibit aggregated islands where the individual nanoparticles have coalesced or aggregated into elongated nanostructures. Such structures are

contoured in red on the figures. From these images it can be seen that increasing the angle of evaporation leads to particles forming elongated islands. Furthermore, increasing the mass thickness, leads to slightly larger structures as can be seen when comparing both #2*B vs.* #2*C* and #3*A vs.* #3*B*. Looking at the UV-Vis spectra (Fig. 3.12.a. and b.), one can see that increasing the angle leads to a red shift of both resonances. Moreover, the resonance normal to the direction of evaporation is broaden as the angle increases. This has the effect of shifting the minimum of the TAS spectra (Fig. 3.12.c.d.) towards the red to the point where no minimum is measured.

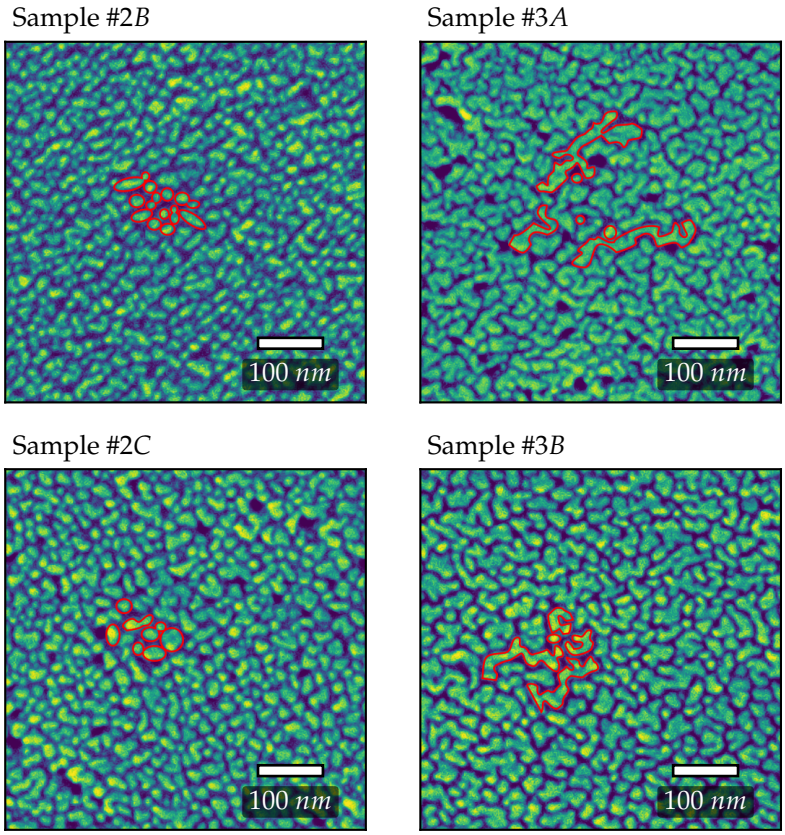

FIGURE 3.11: SEM images of each sample as labelled over the images. The sample were chosen to have a constant mass thickness between the two #2*B vs.* #3*A* and #2*C vs.* #3*B* pairs. In red are some nanoparticle formation contoured in order to better illustrate the difference between each sample with series #2 being mainly formed of individual nanoparticles whereas series #3 is formed of elongated aggregation of nanoparticles. The sample fabrication characteristics are given in table 3.1.

The difference in total mass thickness also has an effect on the TAS spectra. Indeed, in figure 3.12.c. increasing the angle leads to an increase in intensity of the spectra as well as a red shift. However, even though the anisotropy is increased, the increase in amplitude leads to a steeper slope, which is not the case in figure 3.12.d. where the slope at a higher angle is nearly unchanged if not decreased compared to the sample evaporated at a more grazing angle. This is a key concern as the steepness of the slope directly dictates the sensitivity of the single wavelength measurement as discussed in section 1.4.2.

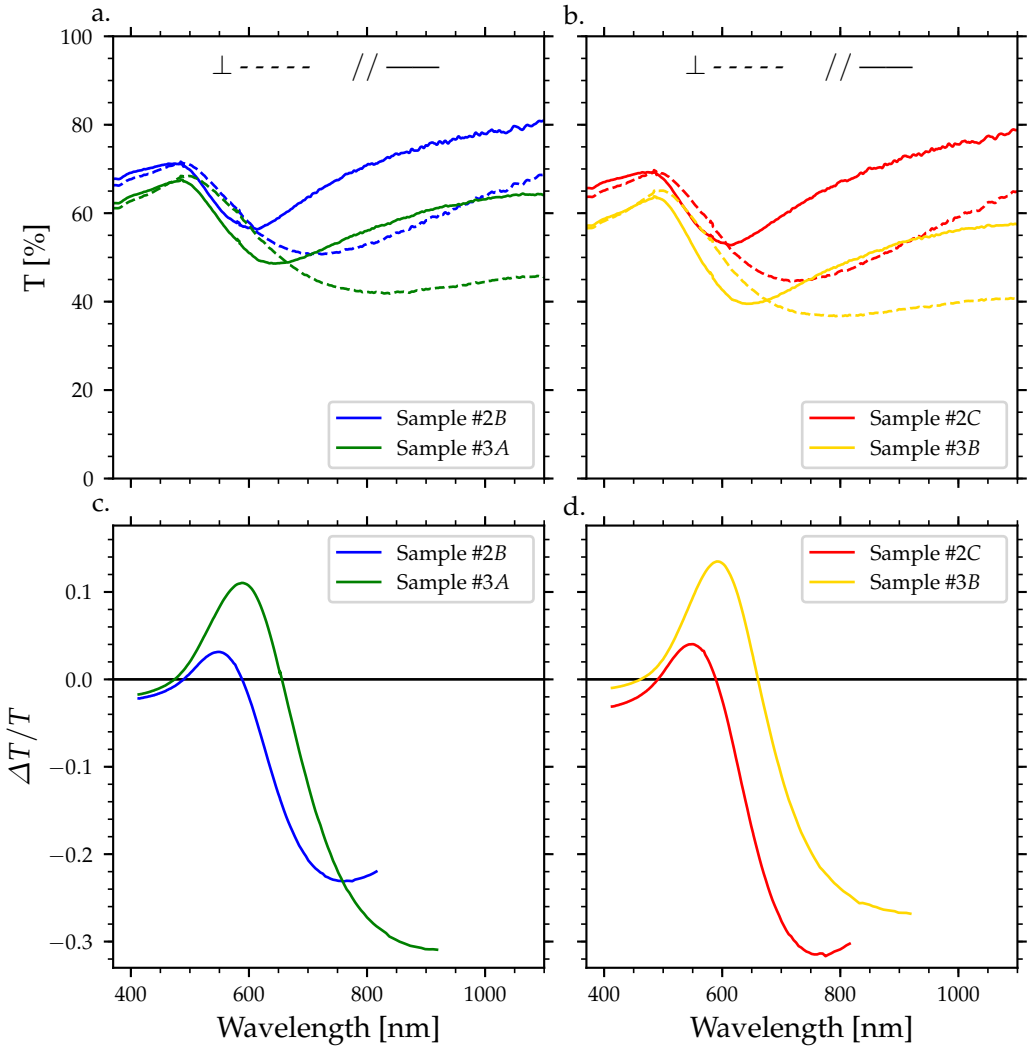

FIGURE 3.12: Optical characterisation of the samples presented in figure 3.11. a-b. UV-Vis transmission spectra of the different samples. Both orthogonal polarisations were measured parallel and normal to the direction of evaporation using a polariser. c-d. show the respective TAS spectra for each sample respectively. These spectra were measured by going twice through the sample.

• Influence of the mass thickness

The other parameter which influences the shape of the particles and hence the LSPR spectra, is the amount of metal evaporated. Figure 3.13.a.b. and c. shows the SEM images for samples #1A, #1B and #1C which were placed at a 12° angle. The difference in fabrication between these samples, as summarised in table 3.1, is the amount of Au evaporated. Indeed, the mass thicknesses for the samples are 2.3, 3.0 and 4.0nm, respectively. Increasing the quantity of evaporated metal clearly shows an increase in the particle size as can be seen in the SEM image. At this grazing angle, the metal forms individual nanoparticles even in the last sample (#1C) which only begins to show aggregation. Furthermore, the AFM measurements showed an increase in average particle height of 7.5, 8.2 to 11.1nm, respectively. It is interesting to note that even though the mass thickness doubles, the AFM height is only increased by a factor of 1.5, therefore hinting to an increase in particle width as well as in height. This is conformed on the SEM images (Fig. 3.13) which show that the main difference is the average particle lateral size.

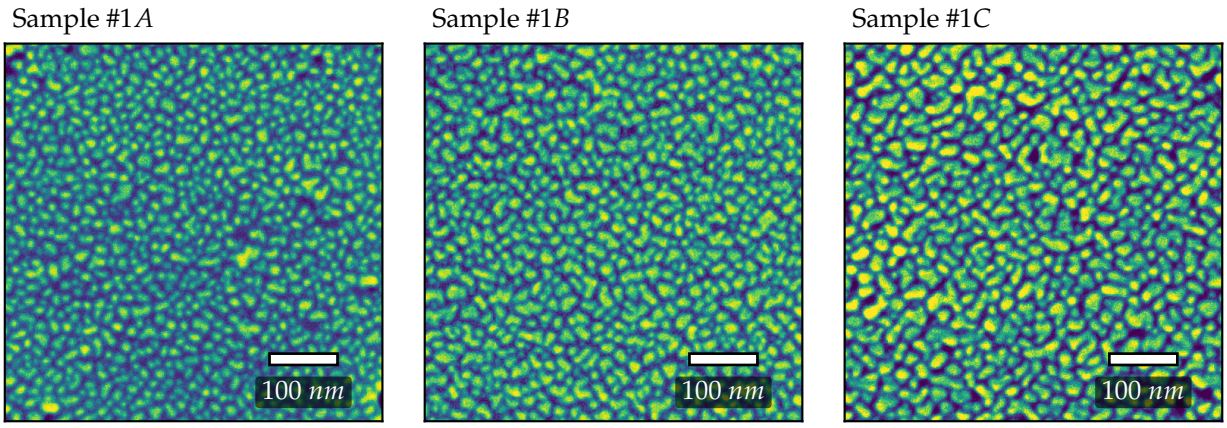

FIGURE 3.13: SEM images of series #1 samples which correspond to samples evaporated at 12° as described in table 3.1.

To determine the effect of the amount of evaporated metal on the LSPR, the UV-Vis and TAS are measured and plotted in figure 3.14.a. and b. respectively. The UV-Vis spectra show a clear dichroism for each sample with the polarisation normal to the evaporation direction being red shifted compared to the parallel polarisation. Every sample displays a LSPR minimum in both orthogonal polarisations. Increasing the amount of evaporated metal clearly induces a red shift of the LSPR for both polarisations. Measuring the TA spectrum also shows a modification due to the increased amount of evaporated Au. The effect shows an increase in the amplitude as well as a red shift of the anisotropic spectrum. The increase in amplitude therefore induces an increase in the slope of the curve between both peaks.

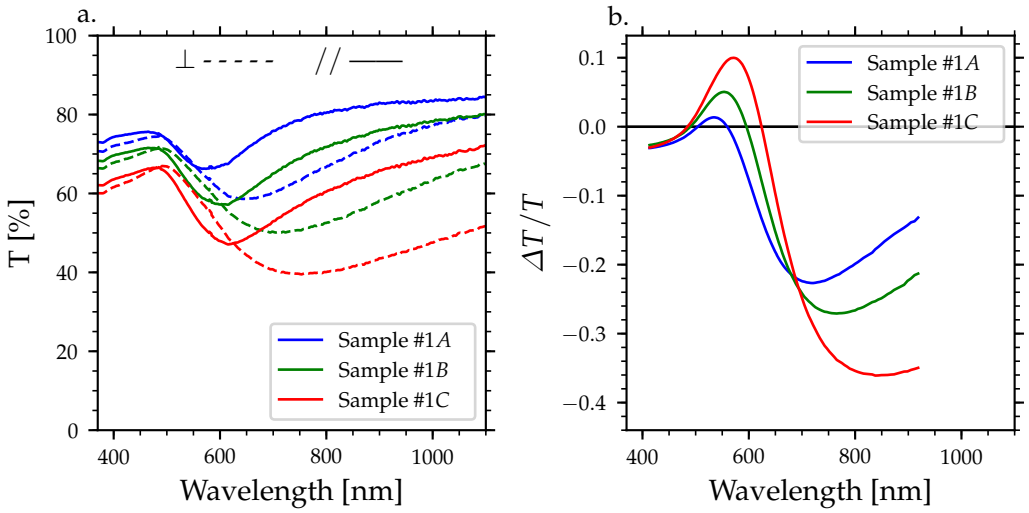

FIGURE 3.14: Optical characterisation of the samples presented in figure 3.13. a. UV-Vis transmission spectra using both orthogonal polarised light with respect to the direction of evaporation. b. TA spectra for each sample in a.

• **Influence of annealing**

Annealing the Au nanoparticles was done at 110°, 140°, 180° and 220°C for 10min in air. Annealing is known to modify the structure of the nanoparticles as well as increase their stability with time and during gas exposure. Without going into much details, it leads to small particles disappearing and large particles growing through physical processes such as coalescence and Ostwald ripening.Furthermore, in the case of Au, again due to its wetting properties on glass, the particles tend to grow in height and round up as to minimise their surface tensions. Annealing the samples also tends to stabilise the particles which get closer to equilibrium in terms of particle morphology.

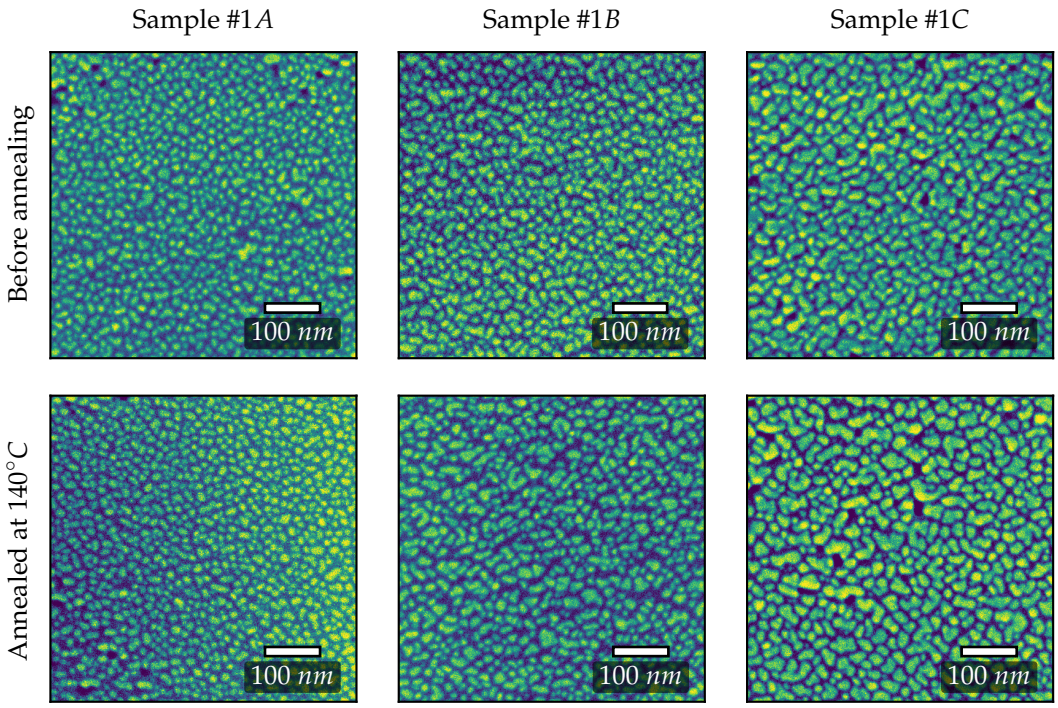

FIGURE 3.15: SEM images of series #1 before and after annealing at 140°C.

Let's focus on series #1. The SEM images of the three samples before and after annealing at 140°C are shown in figure 3.15. It is difficult to see on sample #1A, but is clearer on sample #1B and #1C that after annealing, the particles have grown in lateral size. Indeed, especially on the last sample, the gaps separating the nanoparticles and the particles themselves are larger. The coalescence has led to the formation of small aggregates which could not be seen before annealing. The UV-Vis and the TAS spectra were recorded for all temperatures and are shown in figure 3.16. Let's first focus on the UV-Vis spectra for each sample [2] (Fig 3.16.a.b.c.). The first characteristic to observe is that the annealing process, leads to a blue shift and a decrease in transmission intensity of both orthogonal LSPR. The higher the temperature, the more it shifts. Furthermore, the anisotropy, that is the difference in the transmission minima also decreases. This is most evident when looking at the TA spectrum (Fig. 3.16.d.e.f.). If we first compare the TA spectra at 140°, 180° and 220°C with the UV-Vis, we can confirm the blue shift. The TA spectra thus show that the amplitude is reduced with increasing temperature which leads to the slop between the maxima and minima to reduce. This time though, the spectra before annealing and at all other temperatures are plotted. The spectra before annealing and after 110°C, show that the process was not linear from the start. Indeed, for sample #1B and especially for sample #1C, the first annealing actually led to a red shift of the spectrum as well as an

[2]Only the spectra at 140°C onwards are plotted as the spectra at room temperature and 110°C were not recorded correctly or at all.

increase in amplitude. It is interesting to note though that when annealing at 140°C, the TAS spectra reverts back to the initial spectrum as seen when comparing the red and cyan TA spectra. It is only beyond this latter temperature that the spectrum starts to blue shift again. It can be proposed that the initial annealing led to the small particles being absorbed by the large particles hence slightly increasing the anisotropy and thus inducing a red shift of the spectrum as can be suggested by the SEM images. On the other hand, the second process, that is the rounding up of the particles which thus become less flat, results in a blue shift of the resonances.

For sample #1A, there is a clear change in the spectra beyond 180°C. Indeed, there is a jump in blue shift and a net decrease in amplitude. It can be proposed that above this temperature, the particles tend to homogenise and *lose* their anisotropy as they tend towards isotropic spheroidal shapes i.e. thermodynamic equilibrium.

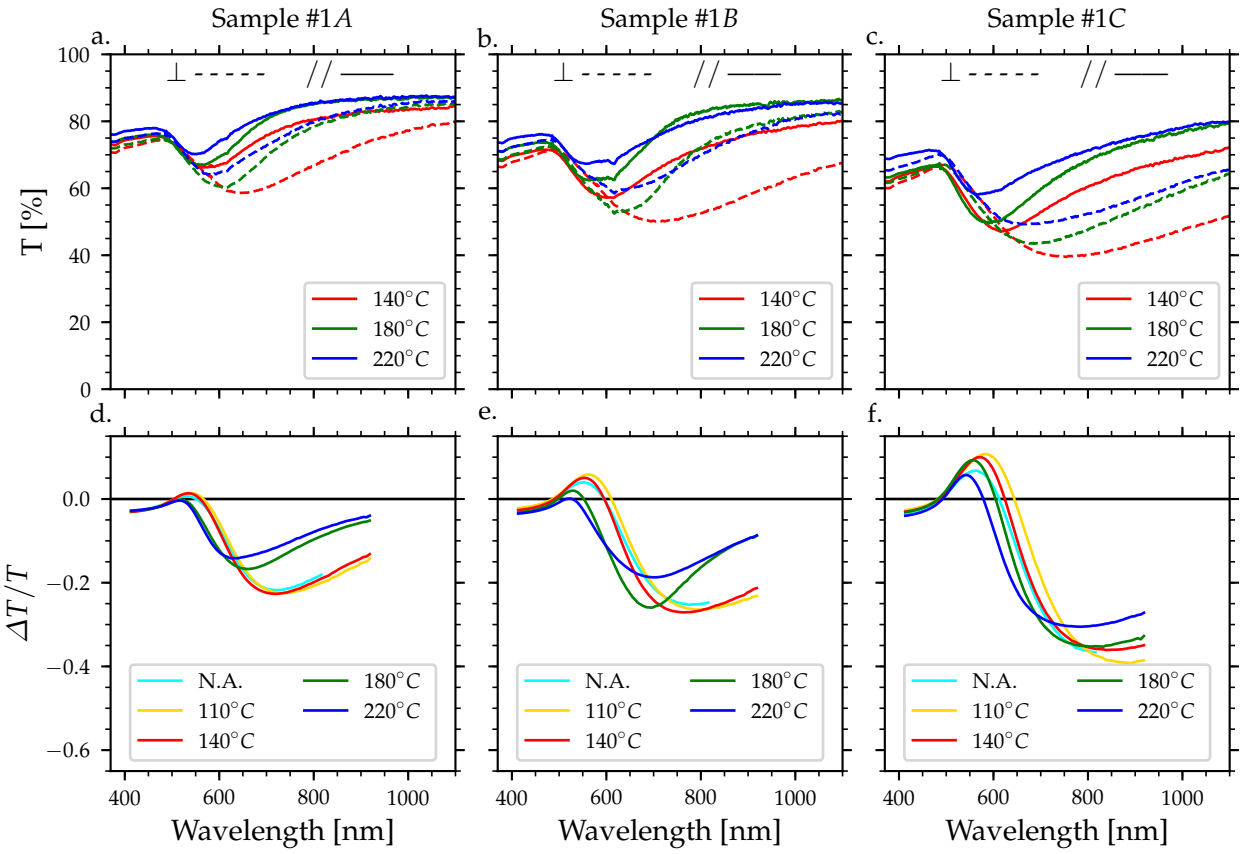

FIGURE 3.16: Optical characterisation of series #1 after different annealing temperatures. a-c. UV-Vis transmission spectra with orthogonal polarisation parallel and normal to the direction of evaporation of each sample after annealing at 140, 180 and 220°C for 10*min* in air. d-f. Respective TA spectra before and after annealing at 110, 140, 180 and 220°C for 10*min* in air. (N.A. = no annealing).

This phenomenological study of the effect of annealing is by no means exhaustive and only serves as an indication for the control in fabrication of the sample. Studying the actual growth process of metals on glass is out of the scope of this thesis. Nevertheless, it is interesting to see the flexibility of this fabrication method as anisotropic spectra can relatively be tailored to have the maximum slope at the wanted wavelength within the visible range with a relative variety in particle shapes. Furthermore, it is important to note that for surface reactivity study, it is more interesting to work with small particles as the total surface area is much greater that for large elongated slabs even though the TAS spectrum might be less intense.

3.2.2 Fabrication of Pd samples

The elaboration of the anisotropic Pd films was achieved in the same way as for Au by oblique angle deposition on glass substrates. The SEM image of a typical Pd film, with mass thickness approximately equal to 1.9nm evaporated at a 12° angle, is shown in figure 3.17.

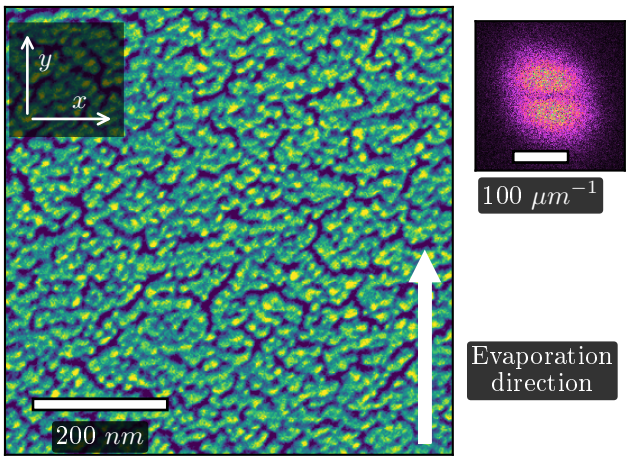

FIGURE 3.17: SEM image of the Pd sample fabricated by OAD. The direction of evaporation is shown by the white arrow. The x and y arrows represent the direction normal and parallel to the direction of evaporation for reference in figure 3.22. The upper right hand inset shows the FFT of the SEM image which shows the anisotropy. The sample rotation of the anisotropy seen on the FFT image with respect to the direction of evaporation is due to an artefact drift in the SEM measurement. The anisotropy is seen by considering the darker horizontal line between the two ellipses.

The difference in the wetting property between the two metals on the glass substrate is responsible for the difference in morphology of the Pd compared to the samples obtained with Au using similar fabrication parameters (sample #1A from Fig. 3.9). Indeed, the discontinuous nanostructured Pd film is made up of lines and islands, separated by large trenches. These islands appear to be formed by agglomerated nanoparticles of size around 10nm, separated by narrow gaps. They display a slight orientation close to the direction normal to the evaporation orientation, indicated by the arrow. The fast Fourier transformation (FFT), shown in the inset on the upper right hand corner, shows a clear anisotropy of the sample which aligned with the direction of evaporation (from bottom to top). The slight angle seen in the FFT is actually due to charging of the sample whilst the SEM image was recorded. The anisotropy is read by considering the darker separation between the two ellipses

The optical transmission of the sample was done using UV-Vis spectroscopy. Both parallel and perpendicular polarisations in relation to the sample's direction of evaporation were recorded and are plotted on figure 3.18.a. The spectra shows a clear dichroism. Indeed, the spectrum measured under parallel polarisation displays a broad resonance centred around 500nm, whereas the spectrum for perpendicular polarisation does not exhibit such a minimum. One must also note the small amplitude of the spectra as indicated on the y axis which hints to the low LSPR and optical anisotropy. Figure 3.18.b. shows a zoom in of the region of interest. This shows that although a dichroism is indeed present within this sample, it is small compared to other examples we have seen in the previous section with Au (cf. section 3.2.1).

The TAS spectrum of the sample is shown in figure 3.18.c. Although the spectrum does not display a maximum and minimum like the Au samples did, it still displays an anisotropy which can be used to monitor the change in optical properties of the Pd sample which is the subject of chapter 5.

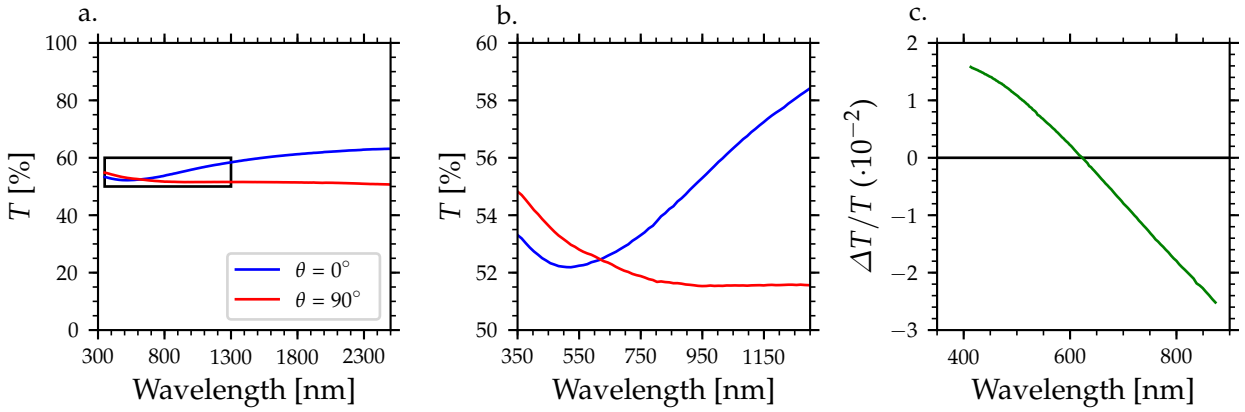

FIGURE 3.18: Optical characterisation of the Pd sample shown in figure 3.17. a. shows the transmission UV-Vis spectra with orthogonal polarisation parallel and normal to the direction of evaporation. b. shows a zoom in the region of interest of a. c. TA spectrum of the Pd sample.

3.3 Modelling the experimental results

In this section, we will take a brief look into how one can analytically model the optical properties of the obtained samples. The methodology consists in calculating the transmission through a layered system by considering a thin film of metal deposited on a glass substrate. We will demonstrate how to calculate the transmission through such system by representing the metal layer with an effective dielectric function. Determining the effective dielectric function is presented in the next sections for the two different types of nanoparticle films observed in the experimental results.

3.3.1 Calculating the transmission or reflection of a thin metal film on glass

Let's first discuss how to relate the calculated LSPR of the nanostructure to the absolute transmission as is measured in the experimental work. In this section, the mathematical approach is taken from Born et al.'s book, "Principles of optics" [iii51]. Every sample is fabricated with glass as a substrate of $1mm$ thickness, which is important to note as light loses coherence over such distance which must be accounted for in the equations. The first and last layers are air, whilst the second and third layers are the metal film of thickness h_2 and the glass substrate, respectively. The system is schematised in figure 3.19.

Each layer has its specified refraction index n_j, where j is the number of the layer as shown in figure 3.19. Let's first consider system (1) consisting of a the three layer with $j = 1, 2$ and 3. At the first interface, the reflection and transmission coefficients for normal incidence can be expressed as:

$$r_{1,2} = \frac{n_1 - n_2}{n_1 + \tilde{n}_2} \tag{3.1a}$$

$$t_{1,2} = \frac{2n_1}{n_1 + \tilde{n}_2} \tag{3.1b}$$

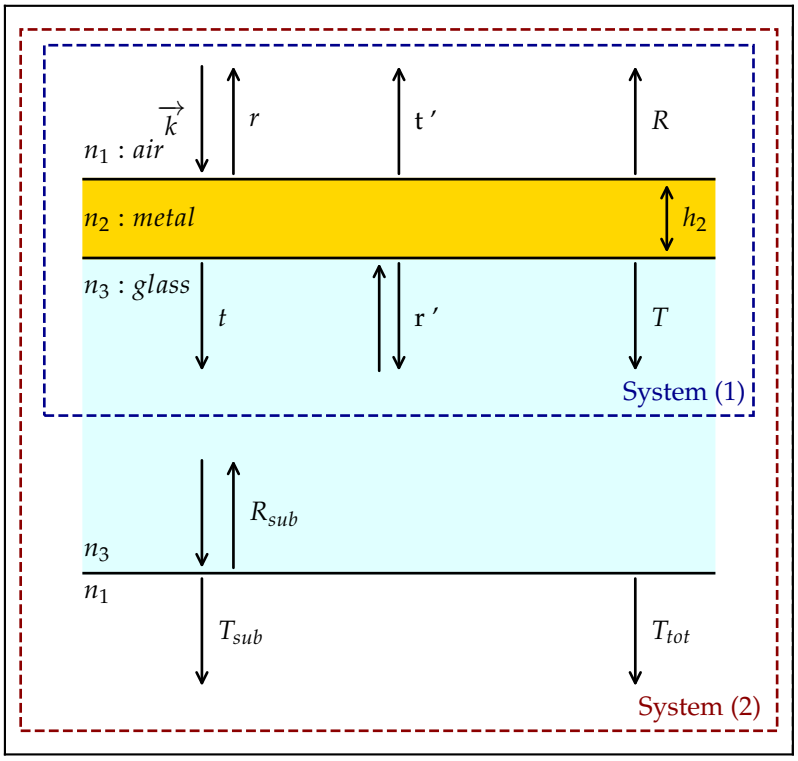

FIGURE 3.19: Diagram of the multilayer system considered for calculating the transmission of a metal layer on a glass substrate. System (1) only considers three layers with a semi-finite glass substrate. System (2) considers a four layer system which accounts for the finite glass substrate. The figure is not to scale as the metal layer is a few nanometres thick whereas the glass substrate used in the experiment is around $1mm$.

At the second interface the coefficients are similarly written

$$r_{2,3} = \frac{\tilde{n}_2 - n_3}{n_3 + \tilde{n}_2} \tag{3.2a}$$

$$t_{2,3} = \frac{2\tilde{n}_2}{n_3 + \tilde{n}_2} \tag{3.2b}$$

There, the formulae for r, r', t and t', corresponding to the transmission and reflection through and from the metal film, can be derived from those above as

$$r_{1,2,3} = \frac{r_{1,2} + r_{2,3}\, e^{2i\beta}}{1 + r_{1,2}\, r_{2,3}\, e^{2i\beta}} = r \tag{3.3a}$$

$$t_{1,2,3} = \frac{t_{1,2}\, t_{2,3}\, e^{i\beta}}{1 + r_{1,2}\, r_{2,3}\, e^{2i\beta}} = t \tag{3.3b}$$

$$r_{3,2,1} = \frac{r_{3,2} + r_{2,1}\, e^{2i\beta}}{1 + r_{3,2}\, r_{2,1}\, e^{2i\beta}} = r' \tag{3.3c}$$

$$t_{3,2,1} = \frac{t_{3,2}\, t_{2,1}\, e^{i\beta}}{1 + r_{3,2}\, r_{2,1}\, e^{2i\beta}} = t' \tag{3.3d}$$

where $\beta = \frac{2\pi}{\lambda}\tilde{n}_2 h_2$. h_2 is the thickness of the metal film. For the plasmonic metal film, we set an effective dielectric function so $\sqrt{\varepsilon_{eff}} = \tilde{n}_2$. The transmissivity and reflectivity through and from the metal layer are thus written as

$$R = \mid r \mid^2 \quad \neq \quad R' = \mid r' \mid^2 \tag{3.4a}$$

$$T = \frac{n_3}{n_1} \mid t \mid^2 \quad = \quad T' = \frac{n_1}{n_3} \mid t' \mid^2 \tag{3.4b}$$

Taking into account the multiple reflections within the glass substrate, with the reflection and transmission equal to R_{sub} and T_{sub}, respectively, the total transmissivity through the sample is given as

$$T_{tot} = \frac{T \times T_{sub}}{1 - R' R_{sub}} \tag{3.5}$$

With these equations it can be seen that T_{tot} is dependent on the effective dielectric function of the metal layer used. There are different ways of accounting for the LSPR of the metal layer. In the following, we will consider two examples which we apply to the experimental results obtained earlier.

3.3.2 Analytical calculation of the effective dielectric function to represent the metal layer

The key difficulty is now to determine the effective dielectric function which will represent the metal film. Looking at the samples, two different morphologies can be seen. Indeed, some samples such as the Au with a small amount of evaporated metal exhibit small separated nanoparticles of similar size. On the other hand, when more Au is evaporated, or in the case of Pd, the structure more resembles islands of aggregated particles separated by narrow gaps (cf. Fig. 3.9).

It is pretty challenging to model the exact optical response of these systems as it requires much more information that the characterisation techniques used would give. Indeed, one would need to know the exact morphology of the particles. Unfortunately, neither SEM nor AFM can yield sufficiently high resolution images due to the nature of the method as well as the glass substrate. Furthermore, to account for the particle - particle interaction, one would need to precisely know the distribution of the particles. Lastly, the particles interaction with the substrate needs to be accounted for as it does influence the LSPR of the system. It is important to note though, that even with all this knowledge, there are not theoretical model which could exactly determine the optical response of such films. Indeed, analytical equations cannot account for arbitrary shaped particles and are basically limited to ellipsoids. Numerical methods such as discrete dipole approximation (DDA) could be used, however, as discussed in the first chapter (cf. section 1.3.3), DDA is limited for processing large systems especially the substrate. Approximations can however be used to simplify the systems which does help to understand the origin of the LSPR and to go further than a simple phenomenological point of view.

• Ensemble of flat ellipsoids

For the first scenario of individual nanoparticles (Fig. 3.10.a.), one can consider a square lattice of ellipsoids. In this case, the dipolar approximation within the quasi-static approximation can be used and

the particle particle interaction is accounted for. Let us consider a Au nanoparticle as a flat ellipsoidal shape, close to the spheroid but with a slight anisotropy, with half-axes a_1, a_2 and a_3. The interaction between multiple ellipsoids are accounted for by considering the square lattice of ellipsoids deposited on glass. Such image model cannot, however, correctly account for the effect of the substrate, especially for flat particles. In consequence, we used a simplified method which describes the main effect i.e. the red shift induced by the substrate (cf. section 1.3.2). The effect of the substrate was described by considering an effective embedding medium with an effective refraction index equal to the average of the refractive indices of glass $n = 1.5$ and of air $n = 1$, squared [iii52]. The polarisability, α_j for an ellipsoid is reminded as

$$\alpha_j = \frac{4}{3}\pi a_1 a_2 a_3 \frac{(\varepsilon - \varepsilon_m)}{\varepsilon_m + L_j(\varepsilon - \varepsilon_m)} \tag{3.6}$$

where j is the axis 1, 2, or 3 of the particle. L_j is the depolarisation factor (cf section 1.3.2 for more details). ε the dielectric function of Au. ε_m the dielectric function of the medium, in this case the average dielectric function to account for the substrate.

The confinement effect due to the small size of the particle is taken into account by calculating a modified dielectric function using the equation sets from section 1.2.4. The effective radius of the particle was calculated as $a_{eff} = \sqrt[3]{a_1 a_2 a_3}$. To calculate the effective dielectric function of a square lattice of ellipsoids, we can use the following equations sets from ref. [iii53].

$$\varepsilon_j^{eff} = 1 + \frac{2f\alpha_j / (4\pi a_1 a_2 a_3)}{1 - \frac{1}{2}\alpha_j / (4\pi a_1 a_2 a_3)\, \xi_0 \left(\frac{f}{\pi}\right)^{3/2}} \tag{3.7a}$$

$$with \quad f = \pi \frac{a_1 a_2}{K^2} \tag{3.7b}$$

where f is the 2D filling factor and K the lattice constant. $\xi_0 = 9.0336$ is the geometry factor for a square lattice. Using the eq. 3.7a to set the effective refraction index $\tilde{n}_2$ of the metal layer, we can use eq. 3.5 to calculate the transmission of the layer on a substrate of glass.

For the sake of an example, let's calculate the transmission of sample #1A shown in figure 3.10.a. The half-axes are taken as $a_1 = 5nm$, $a_2 = 6.2nm$ and $a_3 = 1.2nm$ which are in the same range as the average values determined by AFM and MEB. The lattice constant, that is the distances center to center between the ellipsoids was taken as $16nm$ which is in the same order of magnitude as the distance separating the particles in the SEM image. Figure 3.20.a.b. show the calculated a,d experimental transmission parallel and perpendicular to the direction of evaporation, respectively. Just as the experimental, the calculated spectra exhibit a dichroism due to the anisotropy of the particle set. The calculated resonances are located around $600nm$ along the a_1 direction (the short axis of the ellipsoids parallel to the surface) and shifted to $700nm$ along the a_2 direction (the long axis). This is in agreement with the experiment shown in figure 3.20.b.

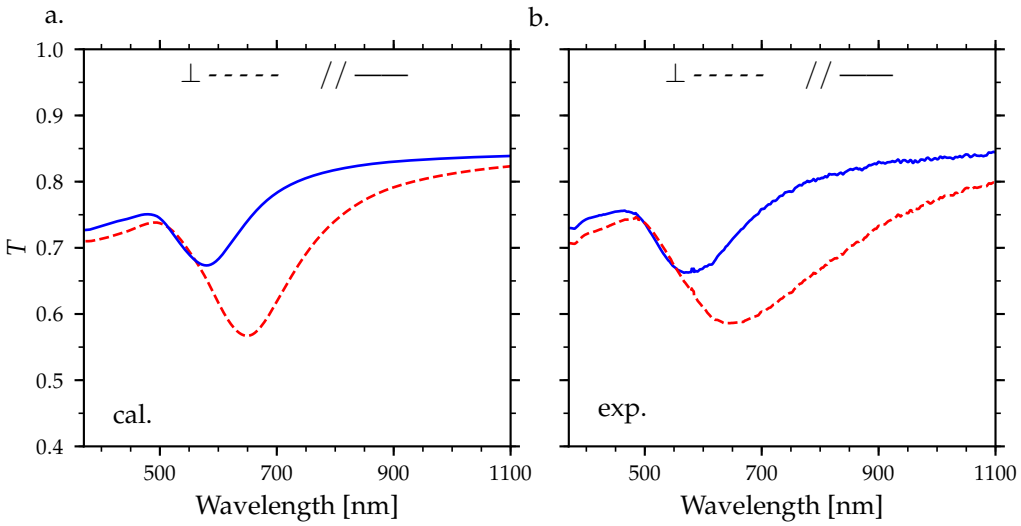

FIGURE 3.20: Comparison of the calculated transmission of the Au metal layer using the square lattice model compared to the experimental transmission spectra. Transmission of the sample for polarisation of light parallel (solid line) and perpendicular (dashed line) to the direction of evaporation. a. shows the calculated results and b. shows the transmission of sample #1*A* taken from figure 3.10.

The aim of the calculation here was not to perfectly reproduce the experiment but to demonstrate that the measured sizes of the nanoparticles could explain the observed positions of the LSPR. For a better agreement, several leads could be followed. For instance, taking into account the distribution of size and of shape of the particles would enlarge the resonances. This effect is known as the extrinsic broadening [iii52]. Though, one must still consider the limitation of the model as over fitting would not yield meaningful physical parameters, hence why it was not undertaken for this demonstration.

• Aspnes effective medium theory for nanostrips

Plasmonic absorptions have been previously observed for metals such as Ag, Au or Al in porous films and in films formed by agglomerated nanoparticles. The origin of the effect have been ascribed to LSPR located in between nanoparticles in close interaction and/or in the voids within porous and granular films [iii54]–[iii57]. Indeed, Abeles et al. have shown the prescence of LSPR on discountinuous thin films and rough surfaces of Ag [iii58]. Jebari et al. reported the LSPR observed in Cu and Al films, due to the empty cavities inside of porous metal films. They used an effective medium theory to model the porous films and well reproduce the experimental results [iii59]. More recently, Teperik et al. have proposed a different model for calculating "the light absorption spectra of planar metal structures containing a two-dimensional lattice of spherical nanocavities" [iii60]. They have shown that the voids in the metallic layer exhibit resonant absorption properties equivalent to LSPR.

To reproduce the optical response of the nanostriped structure seen in either Au (Fig. 3.9.#5C) or in Pd (Fig. 3.17), one can use the effective medium theory approach as described by Aspnes [iii61]. Two effective dielectric functions are thus obtained to describe the film's optical response in the two directions parallel,

ε_x and perpendicular ε_y to the direction of evaporation:

$$\varepsilon_x(\omega) = f\varepsilon(\omega) + (1-f)\varepsilon_m \tag{3.8a}$$

$$\varepsilon_y(\omega)^{-1} = f\varepsilon(\omega)^{-1} + (1-f)\varepsilon_m^{-1} \tag{3.8b}$$

where $\varepsilon(\omega)$ is the dielectric function of bulk metal and ε_m the dielectric function of the empty gaps, i.e. 1 for gas. $0 < f < 1$ is the fraction of metal in the film. The islands forming the nanostructured porous metal film are represented by elongated metal blocks separated by gaps as indicated in the schematic drawn in figure 3.21. From these equations, one can see that no resonance can be obtained for parallel polarisation, whereas, for perpendicular polarisation, LSPR localised in the gaps are obtained for values of ε given by the pole of ε_y, that is, when $\varepsilon_m = 1$:

$$\varepsilon = \frac{-f}{1-f} \tag{3.9}$$

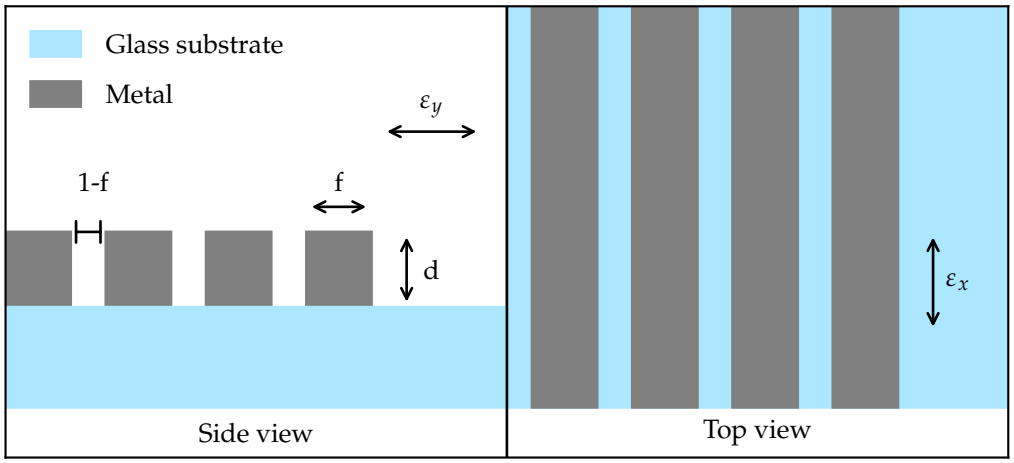

FIGURE 3.21: Diagram showing the semi-finite metal stripes illustrating eq. 3.8a and 3.8b. The figure on the left hand side shows a side view and on the right hand side it shows a top view.

• Model of the Au sample

Let's apply these equations on a Au sample exhibiting such stripes such as that of figure 3.10.b. By considering a value of $\geqslant 0.95$ and a mass thickness $h = 11nm$, we can calculate the transmission spectrum shown in figure 3.22.a. Comparing the calculated results with the experimental results shown in figure 3.22.b. shows that the model well reproduces the behaviour of the LSPR. Indeed, the LSPR at $700nm$ is reproduced as well as the continuous decrease in transmission in the orthogonal polarisation. The intensity is relatively reproduced though the mass thickness is overestimated compared to the experimental measurement. Lastly, the width of the parallel spectra is not as broad for the calculated spectrum compared to the experiment. Just as stated before, this could be also accounted for by considering a distribution in size of the slabs and gaps as we will see in the next section.

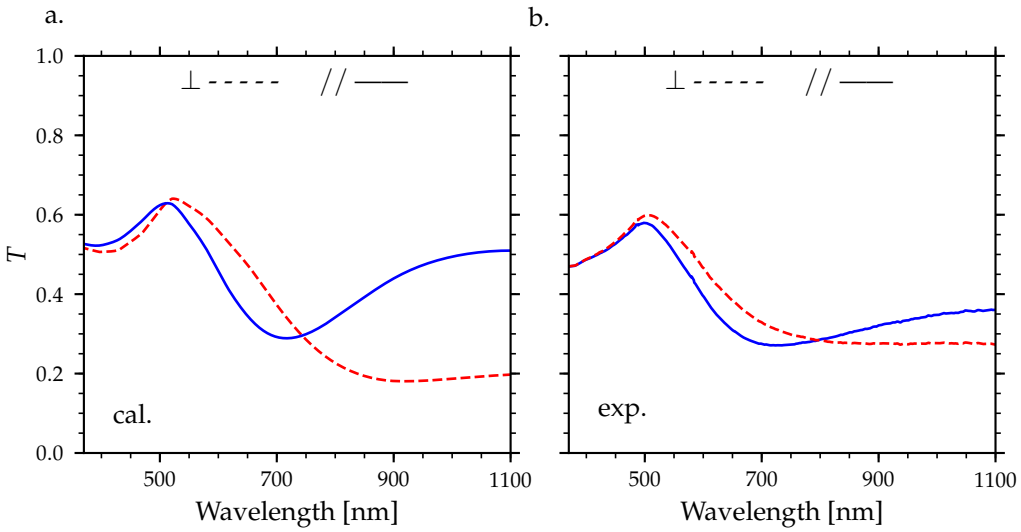

FIGURE 3.22: Comparison of the transmission calculated using Aspnes effective medium theory compared to the experimental results for Au. a. shows the calculated transmission with both parallel and normal polarisations. b. shows the experimental transmission spectra for both orthogonal polarisations taken from figure 3.10.

• **Model of the Pd sample**

To reproduce the experimental results for Pd, let us consider the experimental dielectric function for bulk determined by Johnson and Christy [iii62] (Fig 3.23.a.) The pole for eq. 3.8b is reached for negative values of $Re\left(\varepsilon_{Pd}\left(\omega\right)\right)$ which are indeed within the working spectral range shown in the dielectric function of Pd (Fig. 3.23.a.). The LSPR is located in the visible and IR range for values of $f > 0.9$. For instance, with a value of $f = 0.95$, the observed maximum at $500nm$ is reproduced though is much narrower than the experimental curve (Fig. 3.23.b.).

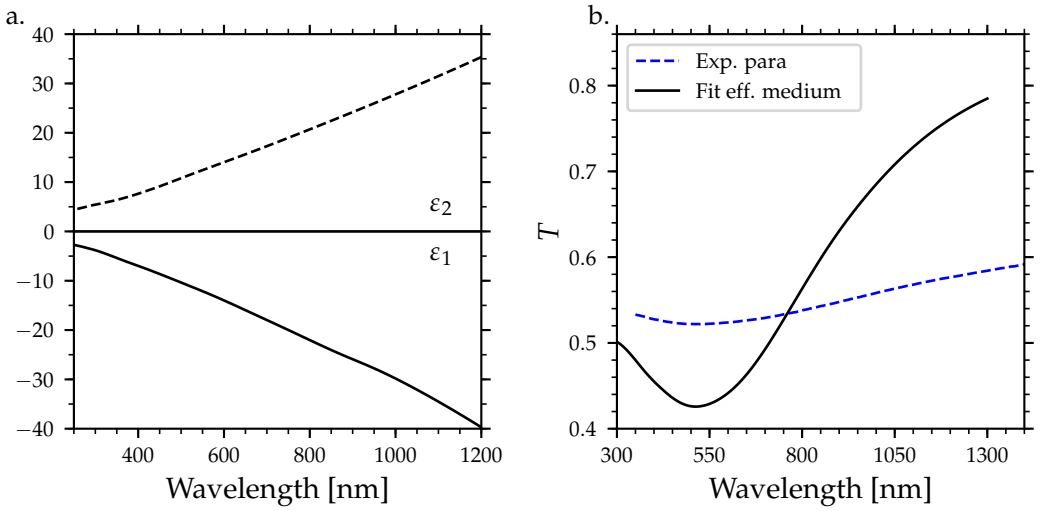

FIGURE 3.23: a. dielectric function for bulk Pd experimentally determined by Johnson and Christy [iii62]. b. Experimental (dashed) transmission spectra for light polarised parallel to the direction of evaporation and the calculated (solid) transmission using ε_x without considering a distribution in f.

The broadness on the experimental spectrum likely comes from the distribution in size and shape of the nanostructure. To reproduce the observed broadening of the LSPR, the actual disordered nanostructure of the sample is taken into account by considering a Gaussian distribution of f ranging from about 0.85 to 1 (Fig. 3.24.a.). Using the dielectric function experimentally obtained for Pd allows one to nicely reproduce the experimental transmission, as shown in 3.24.b. where the calculated transmissions in both directions are drawn in continuous lines. The mass thickness of the film is also obtained and found to be $1.4nm$, close to the value estimated from the quartz balance. The minimum of transmission around $500nm$ corresponds to polarisation of light normal to the gaps.

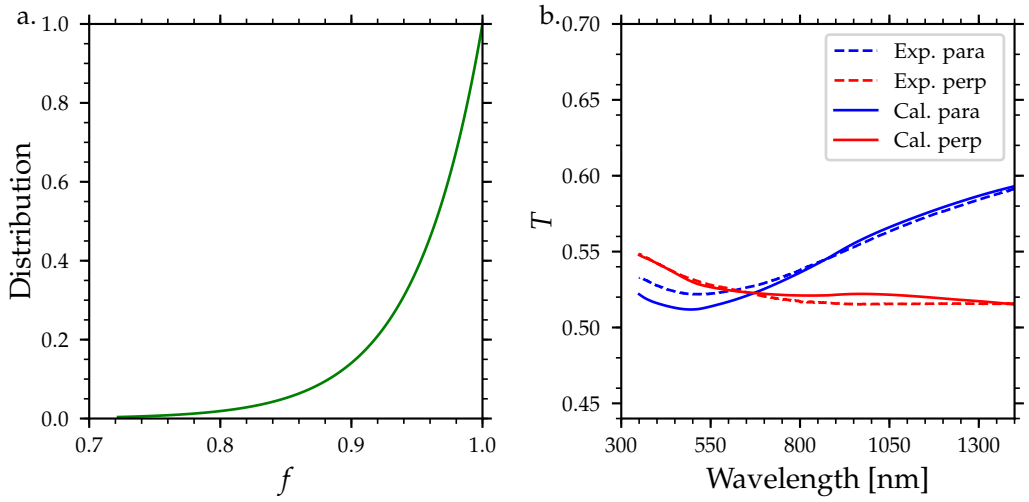

FIGURE 3.24: a. distribution in f to account for the disorder in the experimental sample. b. Experimental (dashed) and calculated (solid) transmission spectra for orthogonal polarisation parallel and perpendicular to the direction of evaporation. In this figure, the distribution from a. is considered.

It is worth noting that both this and Pd films could have been modelled in a different way: the islands formed by the small agglomerated nanoparticles could be considered as being larger elongated spheroidal nanoparticles. Indeed, figure 3.25 shows the calculated transmission for Pd flat ellipsoids with an aspect ratio equal to 0.05. It exhibits a similar shape to the calculation using the parallel slabs model with $f = 0.95$.

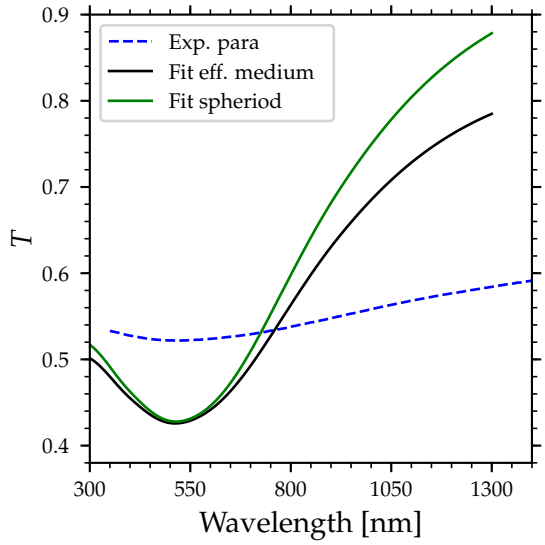

FIGURE 3.25: Dashed: experimental transmission spectrum for light polarised parallel to the direction of evaporation. Solid: calculated transmission considering ε_x using Aspnes effective medium (black) and considering elongated flat ellipsoids with aspect ratio equal to 0.05 (black).

3.4 Summary and conclusion

In this chapter, we have seen the vast variety of possible methods for fabricating LSPR samples. However, the requirements we were looking for were

- The samples need to be globally anisotropic.
- The samples need to cover a large area on the substrate for scalable industrial applications (e.g. at least a few millimetres squared)
- The metals need to be stable when exposed to the environment, but must not be covered with a surfactant which would inhibit its reactivity for direct sensing.
- The particles need to be small as to increase the surface area.
- The particles need to be deposited on a substrate which must be isotropic, and preferably transparent as well as chemically inert.
- The particles need to be exposed to the environment, or, for indirect sensing, the molecular sensors need to be exposed to the environment whilst be in close vicinity to the LSPR metal.

With these requirements in mind, the method chosen was oblique angle deposition on glass. It consists in evaporating the LSPR metal under vacuum at a grazing angle relative to the substrate's plane. This method yielded globally anisotropic samples which exhibit a polarisation dependent LSPR. The investigated metals were Au and Pd. Indeed, due to the wetting properties of Au on glass, individual nanoparticles of about $10nm$ in width could be fabricated. By adjusting the angle of deposition, the amount of evaporated metal and the annealing of the sample, the particle morphologies could be changed from individual particles to elongated nanostripes. This led to the possibility to tailor the LSPR spectrum within the visible range. Using the TAS method, anisotropic spectra could be recorded which will enable the monitoring of the LSPR at a signal wavelength. Using Pd, it was also possible to fabricate LSPR anisotropic samples, though, due to the difference in wetting properties of this metal on glass, the nanostructures obtained were thin discontinuous films which still exhibit polarisation dependent LSPR.

Using simple analytical theoretical models, it was possible to reproduce the experimental spectra for all systems and thus better understand the origin of the LSPR. Furthermore, this would allow the understanding of the origins of changes induced in the resonance should it be due to changes in the refraction indices, or in the dielectric function of the LSPR metal.

Although these samples were sufficient for the investigation undertaken in the following chapters, other paths could be studied. An interesting aspect could be the use of a dielectric protective layer, such as silica, which would be deposited on the LSPR metal layer, on top of which molecular sensors would be adsorbed. This would enable indirect sensing with only the molecular sensors being exposed to the environment whilst the LSPR metal layer is protected against chemical contamination of physical evolution. Yet the difficulty lies is the thickness of the dielectric layer. Indeed, the LSPR particles are only sensitive to changes in the refraction index in their close vicinity, using small nanoparticles would require a few nanometre thick dielectric layer which becomes quite difficult to fabricate. Another interesting path would be to employ metal alloys or core-shell systems. For instance using silver and gold could give the advantage of the silver's LSPR which is much more intense than that of gold whilst using the gold to reduce the silver's reactivity as well as give even more flexibility on the wavelength LSPR position which would display between those of Au and Ag.

In the next chapter, Au LSPR samples fabricated using the method discussed in this chapter are used in conjunction with TAS to study the interaction of H_2 with Au.

3.5 References

[iii1] S. Tawfick, M. De Volder, D. Copic, S. J. Park, C. R. Oliver, E. S. Polsen, M. J. Roberts, and A. J. Hart, "Engineering of Micro- and Nanostructured Surfaces with Anisotropic Geometries and Properties", *Advanced Materials*, vol. 24, no. 13, pp. 1628–1674, 2012.

[iii2] M. C. Traub, W. Longsine, and V. N. Truskett, "Advances in Nanoimprint Lithography", *Annual Review of Chemical and Biomolecular Engineering*, vol. 7, no. 1, pp. 583–604, 2016.

[iii3] B. J. Lin, "The ending of optical lithography and the prospects of its successors", *Microelectronic Engineering*, vol. 83, no. 4-9, pp. 604–613, 2006.

[iii4] V. R. Manfrinato, L. Zhang, D. Su, H. Duan, R. G. Hobbs, E. A. Stach, and K. K. Berggren, "Resolution Limits of Electron-Beam Lithography toward the Atomic Scale", *Nano Letters*, vol. 13, no. 4, pp. 1555–1558, 2013.

[iii5] G. Q. Wallace, S. T. Read, D. M. McRae, S. M. Rosendahl, and F. Lagugné-Labarthet, "Exploiting Anisotropy of Plasmonic Nanostructures with Polarization Modulation Infrared Linear Dichroism Microscopy (μPM-IRLD)", *Advanced Optical Materials*, vol. 6, no. 6, p. 1 701 336, 2018.

[iii6] J. Boneberg, F. Burmeister, C. Schäfle, P. Leiderer, D. Reim, A. Fery, and S. Herminghaus, "The Formation of Nano-Dot and Nano-Ring Structures in Colloidal Monolayer Lithography †", *Langmuir*, vol. 13, no. 26, pp. 7080–7084, 1997.

[iii7] H. Fredriksson, Y. Alaverdyan, A. Dmitriev, C. Langhammer, D. S. Sutherland, M. Zäch, and B. Kasemo, "Hole–Mask Colloidal Lithography", *Advanced Materials*, vol. 19, no. 23, pp. 4297–4302, 2007.

[iii8] Z. Tang and A. Wei, "Fabrication of Anisotropic Metal Nanostructures Using Innovations in Template-Assisted Lithography", *ACS Nano*, vol. 6, no. 2, pp. 998–1003, 2012.

[iii9] R. Verre, N. Maccaferri, K. Fleischer, M. Svedendahl, N. Odebo Länk, A. Dmitriev, P. Vavassori, I. V. Shvets, and M. Käll, "Polarization conversion-based molecular sensing using anisotropic plasmonic metasurfaces", *Nanoscale*, vol. 8, no. 20, pp. 10 576–10 581, 2016.

[iii10] S.-W. Lee, K.-S. Lee, J. Ahn, J.-j. Lee, M.-g. Kim, and Y.-B. Shin, "Highly Sensitive Biosensing Using Arrays of Plasmonic Au Nanodisks Realized by Nanoimprint Lithography", *ACS Nano*, vol. 5, no. 2, pp. 897–904, 2011.

[iii11] S. Park and A. Böker, "Ceramic nanowrinkles via a facile replication process", *Journal of Materials Chemistry*, vol. 21, no. 32, p. 11 734, 2011.

[iii12] S. Y. Chou, "Nanoimprint lithography", *Journal of Vacuum Science & Technology B: Microelectronics and Nanometer Structures*, vol. 14, no. 6, p. 4129, 1996.

[iii13] S. J. Barcelo, W. Wu, X. Li, Z. Li, and R. S. Williams, "Nanoimprint lithography of plasmonic platforms for SERS applications", *Applied Physics A*, vol. 121, no. 2, pp. 443–449, 2015.

[iii14] Y. Yao, H. Liu, Y. Wang, Y. Li, B. Song, A. Bratkovsk, S.-Y. Wang, and W. Wu, "Nanoimprint lithography: an enabling technology for nanophotonics", *Applied Physics A*, vol. 121, no. 2, pp. 327–333, 2015.

[iii15] N. Alayo, A. Conde-Rubio, J. Bausells, X. Borrisé, A. Labarta, X. Batlle, and F. Pérez-Murano, "Nanoparticles with tunable shape and composition fabricated by nanoimprint lithography", *Nanotechnology*, vol. 26, no. 44, p. 445 302, 2015.

[iii16] T. Tomioka, S. Kubo, K. Nagase, M. Hoga, and M. Nakagawa, "Fabrication of Au nanorod and nanogap split-ring structures by reactive-monolayer-assisted thermal nanoimprint lithography involving electrodeposition", *Journal of Vacuum Science & Technology B, Nanotechnology and Microelectronics: Materials, Processing, Measurement, and Phenomena*, vol. 30, no. 6, 06FB02, 2012.

[iii17] J. Turkevich, P. C. Stevenson, and J. Hillier, "A study of the nucleation and growth processes in the synthesis of colloidal gold", *Discussions of the Faraday Society*, vol. 11, no. c, p. 55, 1951.

[iii18] M. Grzelczak, J. Pérez-Juste, P. Mulvaney, and L. M. Liz-Marzán, "Shape control in gold nanoparticle synthesis", *Chemical Society Reviews*, vol. 37, no. 9, p. 1783, 2008.

[iii19] R. Sardar, A. M. Funston, P. Mulvaney, and R. W. Murray, "Gold Nanoparticles: Past, Present, and Future", *Langmuir*, vol. 25, no. 24, pp. 13 840–13 851, 2009.

[iii20] M. C. M. Daniel and D. Astruc, "Gold nanoparticles: Assembly, supramolecular chemistry, quantum-size related properties and applications toward biology, catalysis and nanotechnology", *Chemical Reviews*, vol. 104, pp. 293–346, 2004.

[iii21] J. Pérez-Juste, B. Rodríguez-González, P. Mulvaney, and L. M. Liz-Marzán, "Optical Control and Patterning of Gold-Nanorod-Poly(vinyl alcohol) Nanocomposite Films", *Advanced Functional Materials*, vol. 15, no. 7, pp. 1065–1071, 2005.

[iii22] E. Boisselier and D. Astruc, "Gold nanoparticles in nanomedicine: preparations, imaging, diagnostics, therapies and toxicity", *Chemical Society Reviews*, vol. 38, no. 6, p. 1759, 2009.

[iii23] Z. Nie, D. Fava, E. Kumacheva, S. Zou, G. C. Walker, and M. Rubinstein, "Self-assembly of metal–polymer analogues of amphiphilic triblock copolymers", *Nature Materials*, vol. 6, no. 8, pp. 609–614, 2007.

[iii24] M. a. Correa-Duarte, J. Pérez-Juste, A. Sánchez-Iglesias, M. Giersig, and L. M. Liz-Marzán, "Aligning Au Nanorods by Using Carbon Nanotubes as Templates", *Angewandte Chemie International Edition*, vol. 44, no. 28, pp. 4375–4378, 2005.

[iii25] M. A. Correa-Duarte, N. Sobal, L. M. Liz-Marzán, and M. Giersig, "Linear Assemblies of Silica-Coated Gold Nanoparticles Using Carbon Nanotubes as Templates", *Advanced Materials*, vol. 16, no. 23-24, pp. 2179–2184, 2004.

[iii26] E. Lacaze, O. Merchiers, Y. Borensztein, and D. Coursault, "Trapping of gold nanoparticles within arrays of topological defects: evolution of the LSPR anisotropy", *Rendiconti Lincei*, vol. 26, no. S2, pp. 183–191, 2015.

[iii27] D. Coursault, J. Grand, B. Zappone, H. Ayeb, G. Lévi, N. Félidj, and E. Lacaze, "Linear Self-Assembly of Nanoparticles Within Liquid Crystal Defect Arrays", *Advanced Materials*, vol. 24, no. 11, pp. 1461–1465, 2012.

[iii28] J. H. Park and Y. L. Joo, "Tailoring nanorod alignment in a polymer matrix by elongational flow under confinement: simulation, experiments, and surface enhanced Raman scattering application", *Soft Matter*, vol. 10, no. 19, p. 3494, 2014.

[iii29] G.-W. Hsieh, J. Wang, K. Ogata, J. Robertson, S. Hofmann, and W. I. Milne, "Stretched Contact Printing of One-Dimensional Nanostructures for Hybrid Inorganic–Organic Field Effect Transistors", *The Journal of Physical Chemistry C*, vol. 116, no. 12, pp. 7118–7125, 2012.

[iii30] J. Li, S. Liu, Y. Liu, F. Zhou, and Z.-y. Li, "Anisotropic and enhanced absorptive nonlinearities in a macroscopic film induced by aligned gold nanorods", *Applied Physics Letters*, vol. 96, no. 26, p. 263 103, 2010.

[iii31] C. J. Murphy and C. J. Orendorff, "Alignment of Gold Nanorods in Polymer Composites and on Polymer Surfaces", *Advanced Materials*, vol. 17, no. 18, pp. 2173–2177, 2005.

[iii32] J. Y. Chung, A. J. Nolte, and C. M. Stafford, "Surface Wrinkling: A Versatile Platform for Measuring Thin-Film Properties", *Advanced Materials*, vol. 23, no. 3, pp. 349–368, 2011.

[iii33] A. Schweikart, A. Horn, A. Böker, and A. Fery, "Controlled Wrinkling as a Novel Method for the Fabrication of Patterned Surfaces", in *Advances in Polymer Science*, 2012, 2009, pp. 75–99, ISBN: 9781118056776.

[iii34] A. Horn, H. G. Schoberth, S. Hiltl, A. Chiche, Q. Wang, A. Schweikart, A. Fery, and A. Böker, "Nanostructured wrinkled surfaces for templating bionanoparticles—controlling and quantifying the degree of order", *Faraday Discussions*, vol. 143, p. 143, 2009.

[iii35] M. Tebbe, M. Mayer, B. a. Glatz, C. Hanske, P. T. Probst, M. B. Müller, M. Karg, M. Chanana, T. A. F. König, C. Kuttner, and A. Fery, "Optically anisotropic substrates via wrinkle-assisted convective assembly of gold nanorods on macroscopic areas", *Faraday Discussions*, vol. 181, no. 0, pp. 243–260, 2015.

[iii36] C. Hanske, M. B. Müller, V. Bieber, M. Tebbe, S. Jessl, A. Wittemann, and A. Fery, "The Role of Substrate Wettability in Nanoparticle Transfer from Wrinkled Elastomers: Fundamentals and Application toward Hierarchical Patterning", *Langmuir*, vol. 28, no. 49, pp. 16 745–16 750, 2012.

[iii37] C. Hanske, M. Tebbe, C. Kuttner, V. Bieber, V. V. Tsukruk, M. Chanana, T. A. F. König, and A. Fery, "Strongly Coupled Plasmonic Modes on Macroscopic Areas via Template-Assisted Colloidal Self-Assembly", *Nano Letters*, vol. 14, no. 12, pp. 6863–6871, 2014.

[iii38] M. Mueller, M. Tebbe, D. V. Andreeva, M. Karg, R. A. Alvarez Puebla, N. Pazos Perez, and A. Fery, "Large-Area Organization of pNIPAM-Coated Nanostars as SERS Platforms for Polycyclic Aromatic Hydrocarbons Sensing in Gas Phase", *Langmuir*, vol. 28, no. 24, pp. 9168–9173, 2012.

[iii39] L. Anghinolfi, R. Moroni, L. Mattera, M. Canepa, and F. Bisio, "Flexible Tuning of Shape and Arrangement of Au Nanoparticles in 2-Dimensional Self-Organized Arrays: Morphology and Plasmonic Response", *The Journal of Physical Chemistry C*, vol. 115, no. 29, pp. 14 036–14 043, 2011.

[iii40] L. Anghinolfi, L. Mattera, M. Canepa, and F. Bisio, "Plasmon dispersion in self-organized Au nanoparticle arrays", *Physical Review B*, vol. 85, no. 23, p. 235 426, 2012.

[iii41] R. Verre, K. Fleischer, O. Ualibek, and I. V. Shvets, "Self-assembled broadband plasmonic nanoparticle arrays for sensing applications", *Applied Physics Letters*, vol. 100, no. 3, 2012.

[iii42] R. Verre, K. Fleischer, J. F. McGilp, D. Fox, G. Behan, H. Zhang, and I. V. Shvets, "Controlled in situ growth of tunable plasmonic self-assembled nanoparticle arrays", *Nanotechnology*, vol. 23, no. 3, p. 035 606, 2012.

[iii43] R. Verre, K. Fleischer, R. G. S. Sofin, N. McAlinden, J. F. McGilp, and I. V. Shvets, "In situ characterization of one-dimensional plasmonic ag nanocluster arrays", *Physical Review B - Condensed Matter and Materials Physics*, vol. 83, no. 12, p. 125 432, 2011.

[iii44] N. Semaltianos and E. Wilson, "Investigation of the surface morphology of thermally evaporated thin gold films on mica, glass, silicon and calcium fluoride substrates by scanning tunneling microscopy", *Thin Solid Films*, vol. 366, no. 1-2, pp. 111–116, 2000.

[iii45] H. Sun, M. Yu, X. Sun, G. Wang, and J. Lian, "Effective Temperature Sensing by Irreversible Morphology Evolution of Ultrathin Gold Island Films", *The Journal of Physical Chemistry C*, vol. 117, no. 7, pp. 3366–3373, 2013.

[iii46] A. Schaub, P. Slepička, I. Kašpárková, P. Malinský, A. Macková, and V. Švorčík, "Gold nanolayer and nanocluster coatings induced by heat treatment and evaporation technique", *Nanoscale Research Letters*, vol. 8, no. 1, p. 249, 2013.

[iii47] R. Gupta, M. J. Dyer, and W. A. Weimer, "Preparation and characterization of surface plasmon resonance tunable gold and silver films", *Journal of Applied Physics*, vol. 92, no. 9, pp. 5264–5271, 2002.

[iii48] Y. He, J. Fu, and Y. Zhao, "Oblique angle deposition and its applications in plasmonics", *Frontiers of Physics*, vol. 9, no. 1, pp. 47–59, 2014.

[iii49] T.-C. Peng, W.-C. Lin, C.-W. Chen, D. P. Tsai, and H.-P. Chiang, "Enhanced Sensitivity of Surface Plasmon Resonance Phase-Interrogation Biosensor by Using Silver Nanoparticles", *Plasmonics*, vol. 6, no. 1, pp. 29–34, 2011.

[iii50] J.-X. Fu, A. Collins, and Y.-P. Zhao, "Optical Properties and Biosensor Application of Ultrathin Silver Films Prepared by Oblique Angle Deposition", *The Journal of Physical Chemistry C*, vol. 112, no. 43, pp. 16 784–16 791, 2008.

[iii51] M. Born and E. Wolf, "A homogeneous dielectric film", in *Principles of Optics*, P. Press, Ed., 3rd, 1965, pp. 60–63.

[iii52] U. Kreibig and M. Vollmer, *Optical Properties of Metal Clusters*. Springer Berlin Heidelberg, 1995, ISBN: 978-3-642-08191-0.

[iii53] R. G. Barrera, M. del Castillo-Mussot, G. Monsivais, P. Villaseor, and W. L. Mochán, "Optical properties of two-dimensional disordered systems on a substrate", *Physical Review B*, vol. 43, no. 17, pp. 13 819–13 826, 1991.

[iii54] S. Grésillon, L. Aigouy, A. C. Boccara, J. C. Rivoal, X. Quelin, C. Desmarest, P. Gadenne, V. A. Shubin, A. K. Sarychev, and V. M. Shalaev, "Experimental Observation of Localized Optical Excitations in Random Metal-Dielectric Films", *Physical Review Letters*, vol. 82, no. 22, pp. 4520–4523, 1999.

[iii55] B. Lamprecht, G. Schider, R. T. Lechner, H. Ditlbacher, J. R. Krenn, A. Leitner, and F. R. Aussenegg, "Metal Nanoparticle Gratings: Influence of Dipolar Particle Interaction on the Plasmon Resonance", *Physical Review Letters*, vol. 84, no. 20, pp. 4721–4724, 2000.

[iii56] M. O. Stetsenko, L. S. Maksimenko, S. P. Rudenko, I. M. Krishchenko, A. A. Korchovyi, S. B. Kryvyi, E. B. Kaganovich, and B. K. Serdega, "Surface Plasmon's Dispersion Properties of Porous Gold Films", *Nanoscale Research Letters*, vol. 11, no. 1, p. 116, 2016.

[iii57] R. Esteban, R. W. Taylor, J. J. Baumberg, and J. Aizpurua, "How Chain Plasmons Govern the Optical Response in Strongly Interacting Self-Assembled Metallic Clusters of Nanoparticles", *Langmuir*, vol. 28, no. 24, pp. 8881–8890, 2012.

[iii58] F. Abelès, Y. Borensztein, and T. López-Rios, "Optical properties of discontinuous thin films and rough surfaces of silver", in *Advances in Solid State Physics*, vol. 125, Springer Berlin Heidelberg, 1984, pp. 93–117.

[iii59] M. Jebari, Y. Borensztein, and G. Vuye, "Anomalous optical absorption in porous metal films", *Physica A: Statistical Mechanics and its Applications*, vol. 157, no. 1, pp. 371–376, 1989.

[iii60] T. V. Teperik, V. V. Popov, and F. J. García de Abajo, "Void plasmons and total absorption of light in nanoporous metallic films", *Physical Review B*, vol. 71, no. 8, p. 085 408, 2005.

[iii61] D. Aspnes, "Optical properties of thin films", *Thin Solid Films*, vol. 89, no. 3, pp. 249–262, 1982.

[iii62] P. Johnson and R. Christy, "Optical constants of transition metals: Ti, V, Cr, Mn, Fe, Co, Ni, and Pd", *Physical Review B*, vol. 9, no. 12, pp. 5056–5070, 1974.

Chapter 4

Probing the interaction of dihydrogen on gold nanoparticles

Abstract

This chapter discusses results which have been published in the Royal Society of Chemistry journal, Physical Chemistry Chemical Physics (PCCP) [iv1]. The focus of this work is to take advantage of the sensitivity of transmission anisotropic spectroscopy to analyse the change in localised surface plasmon resonance of Au nanoparticles obtained by oblique angle deposition as they are exposed to cycles of Ar and H_2 in Ar at different partial pressures.
Through this procedure, it is possible to probe the chemical interaction between the Au and H_2. The results demonstrate that H_2 does indeed interact with Au nanoparticles as apparent from the literature. However, results have shown that, contrary to conventional knowledge, dissociated H diffuse on the (100) surface of Au nanoparticles inducing a measurable charge transfer.
The chapter is constructed as follows: a general overview of the literature is given before describing and characterising the gold samples after which follow the results, discussion and conclusion.

4.1 Introduction

"Why Gold is the noblest of all the metals"
- 1995

B. Hammer & J.K. Nørskov

GOLD HAS ALWAYS PEAKED THE INTEREST OF RESEARCHER and its reactivity reveals to be more interesting when working at the nanoscale. Understanding its chemical and physical properties at this scale has revealed possibilities not yet imagined. At the same time, hydrogen has been under the spot lights as to be a great candidate for the future fuel economy as well as the already rich hydrogen chemistry in organic, inorganic and thus catalytic chemistry. The reactivity of H_2 with Au has been studied for the last 50 years. The general consensus has been that hydrogen does not react with extended gold surface, but does with lower coordinated gold atoms such that of the corners and edges. Many experiments have shown this reactivity at the nano-scale and specifically the capability of H_2 to dissociate on the edges of nanoparticles. This dissociative adsorption therefore leads to a chemisorption of H adatoms on the Au. Yet the literature could not indicate whether the H is stationary on the edges, or whether a spill over onto the facets is to be expected. This afore mentioned chemisorption should obviously lead to a charge transfer as the adatom bonds to the metal atoms, though discrepancies in the literature made this point less than clear with different articles referring to positive charge transfers, that is from the metal to the hydrogen, negative charge transfer i.e. from the hydrogen to the metal, or no charge transfers. All these claims are discussed in the next section.

The approach undertaken in this chapter is to investigate these features using localised surface plasmon resonance as it is an optical method ideal for probing surface reactivity with a high sensitivity to the surfaces of plasmonic metals. The Au nanoparticles were prepared by oblique angle deposition on glass which led to the formation of Au nanoparticles of size around $10nm$. The samples were characterised using atomic force microscopy to determine the height of the nanoparticle films and scanning electron microscope to determine the shape, and thus the effective diameter of the nanoparticles. The optical properties of the sample were investigating using UV-Vis spectroscopy in conjunction with anisotropic spectroscopy. The results clearly showed a dichroism characteristics of anisotropic plasmonic systems. The key to the sensitivity of the system is the possibility to measure, at a single wavelength the change in the anisotropy directly dictated by the LSPR of nanoparticles.

4.1.1 Background of gold reactivity

In their article entitled "Why gold is the noblest of all the metals", Hammer et al. have discussed the interaction and dissociation of H_2 on (111) surfaces of Au, Cu, Ni and Pt [iv2]. Their theoretical approach consisted in using density functional theory (DFT) to calculate the activation barriers and chemisorption energies for the above-mentioned reaction. As the H_2 molecule approaches the metallic surface, the energy is either increased or decreased depending on which metal is chosen. Their results are plotted in figure 4.1.a. On this graph the energy between the H_2 and the metal surface is calculated as the $H_2 - \text{surface}$ separation is decreased. Two behaviours are observed. For the case of Pt and Ni, the energy drops when the H_2 gets $\approx$ 3Å away from the surface. The minimum energy is reached at about 1Å distance before rising again. On the other hand, for Au and Cu, the energy starts rising at $\approx$ 3Å and reaches a maximum around 1.5Å before dropping. These calculation thus clearly demonstrate the occurrence of an energy barrier for Cu and Au but not for Ni nor Pt. The second observation, as the authors of the paper write, is that "Au stands out as having both the highest barrier for dissociation and the least stable chemisorption state". This describes the lack of reactivity on the behalf of Au compared to the other metals.

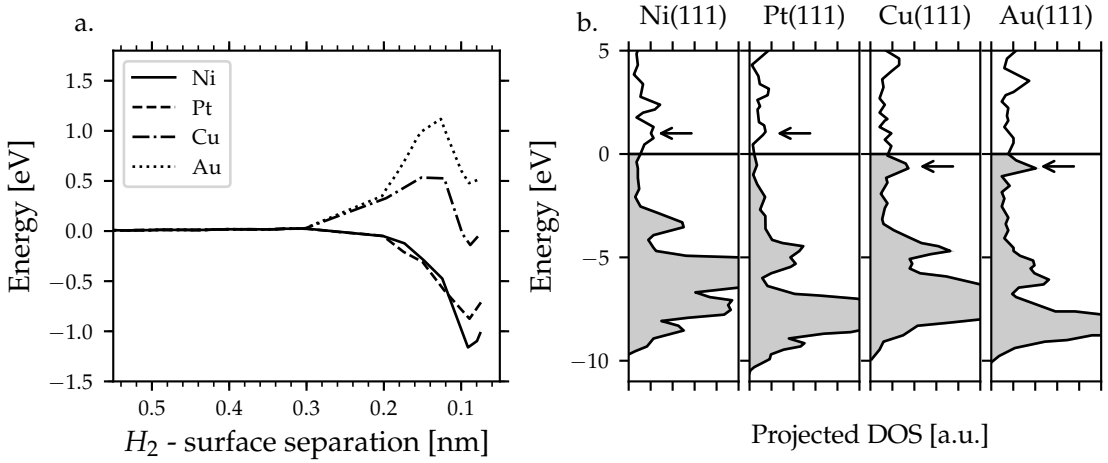

FIGURE 4.1: a. Calculated energy along the minimum energy reaction path for H_2 dissociation on the (111) surfaces of Ni, Cu, Pt, and Au. b. Density of one-electron states (DOS) for H atomically chemisorbed on the (111) surface of Ni, Cu, Pt, and Au. These figures were reproduced from ref [iv2].

The calculations of the molecular orbital between a H atom and the metal (111) surface further differentiate Ni and Pt from Cu and Au. This is reproduced in figure 4.1.b. where the density of one-electron state (DOS) for H atomically chemisorbed on the surface is drawn. For the case of Cu and Au, the anti-bonding molecular orbital is filled (arrow on the figure beneath the Fermi level) which is not the case for Ni nor Pt. This result explains why $H - Au$ and $H - Cu$ are not favoured. The difference in reactivity between Cu and Au comes from the fact that the energy between the adsorbate and the Au 5d state is considerably larger than for the Cu 3d state [iv2], [iv3]. Further theoretical studies agree with this conclusion such as L. Barrio et al. and A. Corma et al. whom have studied the chemisorption of H_2 on Au(100) and Au(111) facets[iv4], [iv5]. The method consisted in calculating the energy of a H_2 on the surface of the bulk Au. The results showed that the H_2 molecule preferentially sits at $\approx$ 4Å off the surface, with a $H - H$ bond length equal to that obtained for isolated H_2 (0.75Å) , thus further acknowledging that Au surfaces are non-reactive towards H_2 chemisorption. [iv4], [iv5]. Experimental work also display similar results. Indeed, L. Stobiński et al. have shown that on thin Au films, H_2 does not adsorb at room temperature but does when the sample is brought down to 78K [iv6]. A. G. Sault et al. have shown that H atoms can adsorb on Au(110) when H_2

is dissociated with a hot filament at 150K, but not at room temperature nor with the absence of the filament [iv7].

However, these results only apply to extended metallic surfaces. In the case of Au nanoparticles, the reduction in size induces low coordinated atoms which are known to have increase reactivity compared to bulk metal. Barrio et al. have numerically studied the dissociation of H_2 on Au_{29} clusters equivalent to nanoparticles of $1.2nm$. The mechanism they propose is a spontaneous dissociation of H_2 on the top of the Au cluster which consist of four Au atoms, arranged in a square plane, each with a coordination of six leading to a bridged bonding of dissociated H_2 (Fig. 4.2) [iv4]. The investigation undertaken by A. Corma et al., have shown that H_2 can dissociate on low coordinated Au atoms irrespective of whether these are located at the nanoparticles' edges or belonging to an extended line defect. Additionally, they have shown that this dissociation barrier, of $0.09eV$ is very low further agreeing that this is a spontaneous reaction [iv5]. Experimental results do confirm the adsorption sites as shown by Stobiński et al. They have found that H_2 does chemisorbs on unsintered Au films formed of isolated Au islands. Although their experiments were undertaken at 78K, they have concluded that chemisorption occurs on low coordinated Au atoms as well [iv6].

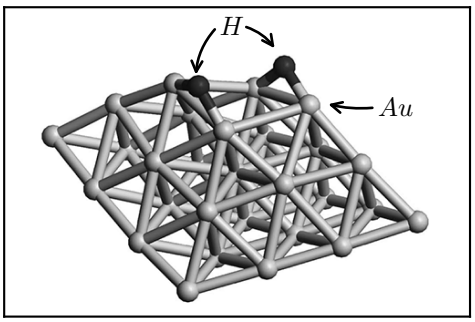

FIGURE 4.2: Au_{29} cluster with hydrogen atoms adsorbed on the top, low coordinated Au atoms. This figure was reproduced from [iv4].

These phenomena are of great interest in the field of catalysis which has brought authors such as M. Haruta to publish a detailed review rightly entitled "When gold is not noble: catalysis by nanoparticles" [iv8]. His overview shows how Au becomes *surprisingly* active towards catalytic reactions such as CO oxidation when formed of small nanoparticles deposited on metal oxides such as TiO_2 or ZrO_2, &c... Figure 4.3 shows the rate of CO oxidation as a function of the Au nanoparticle mean diameter when supported on TiO_2. The data shows that below $\approx 5nm$, the reactivity increases suddenly at room temperature ($273K$).

The conclusion of these research however sheds light on a new parameter, that is the role of the substrate in the reactivity of the metal. Indeed, the oxide used has a direct impact on the reaction yield as it takes part in the reaction mechanism. For instance, in the particular case of CO oxidation, it is proposed that the reaction takes places on the interface of Au and TiO_2 [iv8], [iv9].

Furthermore, Au has also been investigated for use in hydrogenation reactions. As a matter of fact, Au is capable of catalysing the synthesis of nitro groups, for instance in the Henri condensation reaction of carbonyl compounds with nitromethane [iv10]. Many hydrogenation reactions have been studied with Au nanoparticles supported on various types of substrates[iv11]. Understanding the mechanism of H_2 adsorption and the attributes of the substrate were studied via various characterisation techniques. For instance E. Bus et al. have studied the chemisorption of H_2 on Al_2O_3-supported Au nanoparticles using X-ray absorption spectroscopy (XAS). Their results show that the adsorption sites are the edge and corner positions of Au

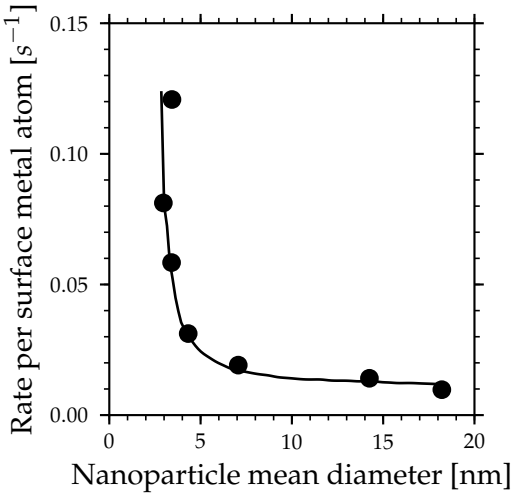

FIGURE 4.3: Turnover frequency for CO oxidation over Au/TiO_2 as a function of the mean diameter of Au particles. This figure was reproduced from [iv8].

where H_2 dissociates. More characterisation such as Fourier-transform infra-red spectroscopy (FTIR) done by M. Manzoli et al. has shown evidence of the formation of $Au-H$ species as well as indicating that H_2 dissociates at room temperature on the edge and corner sites independently from the nature of the support. They have also shown that H migrate on the TiO_2 substrate but not on CeO_2 nor on ZrO_2 demonstrating that dissociation does occur regardless of the substrate, though the reaction mechanism differs [iv12].

Proving the dissociation of H_2 on Au was achieved by using the isotope D_2. S. Mukherjee et al. have first studied Au nanoparticles of about 5 to 30*nm* in diameter supported on TiO_2 [iv13]. Although their main motivation was to investigate photo-induced dissociation of H_2, they also have recorded a small formation of HD at ambient temperature without illumination thus showing that Au nanoparticles are capable of spontaneously dissociate H_2. Furthermore, they have also observed that increasing the temperature 5°C, led to a slight increase in the HD formation thus also indicating that the mechanism may be thermo-induced. In a later paper, they repeated the same protocol but this time using SiO_2 as a supporting material, thus determining the influence of the substrate in the reaction. The results are similar to the experiments done on TiO_2 with the formation of $H-D$ confirming that the splitting catalitic reaction is independent of the substrate, further reinforcing that the reaction occurs from the surface of the particles [iv14]. They have summerised their work in the review [iv15].

The general experimental and theoretical consensus is that the active sites are the low-coordinated atoms located on the corners and/or edges of Au nanoparticles and that the substrate has not such a strong role in the hydrogenation reaction compared to other catalytic processes. Nevertheless, the fundamental mechanism of H_2 dissociation and especially the fate of the H atoms are still not entirely understood. Indeed, discrepancies exist regarding which atoms of the nanoparticle are specifically the most reactive, whether there is a charge transfer between Au and H, whether the dissociation is spontaneous, almost spontaneous or activated or whether the H atoms are mobile on the Au nanoparticles. Furthermore, in spite of the numerous studies undertaken in this field, to the writer's knowledge the issue of diffusion and recombination of H atoms after H_2 dissociation has not been investigated so far. A comprehensive investigation of these latter issues is therefore still essential for a deep understanding of H adsorption and hydrogenation reactions on the Au nanoparticles.

4.1.2 Objectives, hypothesis and methodology: advantages of LSPR

The objective of this work is to gain insight on the mechanisms at play when H_2 interacts on Au nanoparticles. As H_2 adsorbs, a charge redistribution with the nanoparticle should induce a shift of the LSPR spectrum. The direction of the shift depends on the direction of the charge transfer i.e. whether it goes from the H to the nanoparticle or the other way round. Moreover, the intensity of the shift should correlate with the amount of charge transferred which in turn should be related to the amount of H_2 adsorbed on the particle. This latter point could thus indicate which sites the H atoms interact with and if diffusion occurs.

The interaction between Au and H_2 is very weak hence the transferred charge is expected to be small, thus the shift difficult to measure if one were to rely on conventional UV-Vis spectroscopy. Thus the method undertaken was to take full advantage of the sensitivity of anisotropic spectroscopy. The system studied were Au nanoparticles deposited on a glass substrate following the method described in chapter 3. The samples were fully characterised using AFM, SEM, and both UV-Vis and transmission anisotropic spectroscopies. This enabled to take advantage of the sensitivity of the TAS and do real time *in situ* monitoring of the change in optical anisotropy of the sample as cycled through with Ar and H_2.

The chapter is decomposed in three main sections. First of all, a full characterisation of the studied samples and the presentation of the real time monitoring of the change in optical response of the sample when exposed to cycles of H_2 and Ar. A theoretical model is proposed and used to interpret the experimental results. After which the kinetic mechanism is analysed. Finally, the charge transfer is estimated by corroborating the experimental observations with data from the literature.

4.2 Sample elaboration and characterisation

4.2.1 Sample preparation

The Au samples were prepared by oblique angle deposition (OAD)[1] on glass substrates under a vacuum. The sample was positioned at a 12° grazing angle to the crucible and the evaporation rate was set to $0.02nm \cdot s^{-1}$ to control the evaporation in a reproducible manner. The mass thickness was controlled using a calibrated quartz balance and corrected to account for the angle of evaporation. The characterisation of the samples was carried out by optical measurements, scanning electron microscopy (SEM) and atomic force microscopy (AFM). Several samples were elaborated with different mass thicknesses ranging from $0.5nm$ to $3nm$ and investigated towards H_2 reaction.

4.2.2 AFM Characterisation: Limitations due to tip convolution

Attempting to characterise the samples with AFM was the first step undertaken to determine the shape and size of the Au nanoparticles. A typical cliché[2] is presented in figure 4.4. Particles with an apparent spherical shape can be seen on the topological image. The average height on the particle is in the order of $10nm$. However, this image clearly shows the limitations of the AFM. Indeed, the tip convolution is responsible for the appearance of large Au nanoparticles touching one another. Moreover, the apparent shape of the particle is directly dictated by the convolution of the shape of the AFM tip and the shape of the nanoparticles. These two issues limit the interpretation of the image and thus the characterisation of

[1] For more details on the fabrication method, please refer to chapter 3.

[2] The sample showed in this AFM image is not the sample refereed to in the previous paragraph but illustrates the limitation of the AFM. Such an image of the actual sample was not recorded as too little useful information could be extracted from AFM images.

the nanoparticles. It can nevertheless be seen that the OAD method of fabrication leads to the formation of nanoparticle on glass. This is due to the wetting properties of Au on glass substrate [iv16].

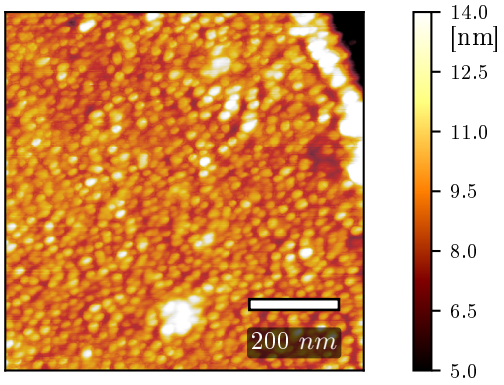

FIGURE 4.4: AFM image of Au evaporated on glass using OAD. The particles show an average height of 10nm. However, no information can be extracted from this image regarding the average width of the particles. Indeed, due to tip convolution, the particles appear larger than they really are. Moreover, the apparent shape of the particle being strongly dependent on the tip morphology, it is not possible to determine an overall orientation of the particles.

On the other hand, AFM can be used to determine the overall thickness of the nanoparticle film deposited on the substrate. Figure 4.5 shows an example of the boundary between the substrate covered with nanoparticles and the bare substrate. This was obtained by scratching the sample, with a plastic tweezers to reveal the substrate. The nanoparticles are seen in bright yellow whilst the substrate is in dark red. The profile shows a step of about 8nm for this particular sample. Although a higher thickness can be seen for x between 2μm and 3.5μm, it is due to aggregation of matter when the scratch to discover the substrate was made. The thickness must be considered for x between 0 and 2μm as it is where the sample is unchanged. It is important to note that AFM displays the height of the highest particles. Hence the value measured does not indicate the average height of the particles. The height of the samples are recapitulated in table 4.1 For further characterisation of the particle's morphologies, SEM was used to determine the average lateral size of the particles and to confirm whether the nanoparticles are indeed in contact or not.

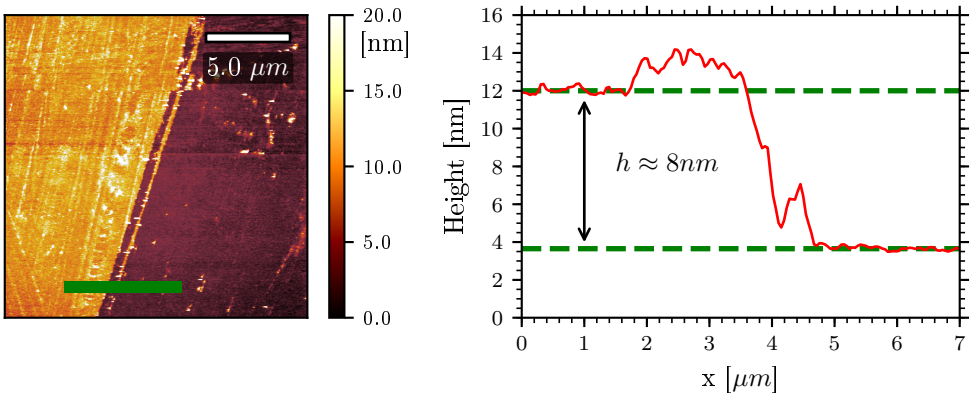

FIGURE 4.5: Example AFM image on a scratch made on a sample of Au evaporated on glass to determine the average height of the nanoparticles evaporated. The profile is taken over the green line and shows an average height of 8nm

4.2.3 SEM Characterisation: Challenges of non conductive substrates

Scanning electron microscopy has a much higher definition than AFM for lateral features. It was used to determine the overall shape and morphology of the nanoparticles but lacks information on height. The SEM was set between $3kV$ and $6kV$ depending on the sample analysed. The working distance was around $4mm$ with an aperture opened at $7\mu m$. The substrate being insulating glass, efforts were made to add conductive copper tape near the region of interest to evacuate the electronic charge. This difficulty however limited the maximum electron high tension applied and therefore, the overall definition of the images. Figure 4.6.a shows the SEM image of the Au sample chosen for this study. The image shows Au nanoparticles deposited on the substrate. The direction of evaporation is from bottom to top.

It is clear that the particles are not touching each other as one could have established from the AFM images. The sample does not display a clear anisotropy ; the particles do seem to display irregular shapes, though, due to the charging of the sample during the SEM measurements, the resolution of the smaller nanoparticles is limited. It is likely that these apparent irregularities are rather formed by agglomeration of a few or more regular and smaller nanoparticles. Nevertheless, chains of nanoparticles are visible, with orientations ranging between approximately $+30^\circ$ and -20° with respect to the horizontal axes, hence normal to the direction of evaporation. Examples of such alignments are indicated by the white arrows. To characterise the particles, the effective diameter, d_{eff} was measured and defined as $d_{eff} = 2\sqrt{A/\pi}$ where A is the projected area of the particles observed by SEM. The histogram drawn in figure 4.6.c indicates the effective diameter distribution of the particles which is from $5nm$ to over $20nm$. The average effective diameter is calculated to be $\approx 12nm$. The height measured for this sample is $7.8nm$,. It should thus be compared to the larger particles which are $\approx 20nm$ wide on the SEM. The aspect ratio of the larger particles, and most likely of most of them, is therefore around 0.4. The other samples' effective dimensions are written in table 4.1. It is interesting to note that the ratio determined above is constant over all the samples which would indicate that the sample growth is constant over all samples. The AFM and SEM images of all the sample are plotted in appendix A.5. This observation clearly illustrates the overestimation tip convolution introduces in AFM images. The 2D Fourier transform shown in Fig 4.6.b does indeed reveal a small anisotropy. Yet, the anisotropy has to be, for the purposes of this research, optically significant.

TABLE 4.1: Table summarising six samples with different amount of Au evaporated. The height was determined by AFM and the average diameter using SEM images. The sample #3 and in bold is the sample discussed in the optical characterisation below.

Sample number	Fig. 4.9	*Height* [nm]	d_{eff} [nm]	d_{max} [nm]	$Height/d_{max}$
#1	d.	9.66	16.45	27	0.4
#2	e.	12.34	18.67	34	0.4
#3	**a.**	**7.80**	**12.12**	**21**	**0.4**
#4	f.	8.15	13.81	23	0.4
#5	b.	10.00	16.68	28	0.4
#6	c.	8.09	12.54	22	0.4

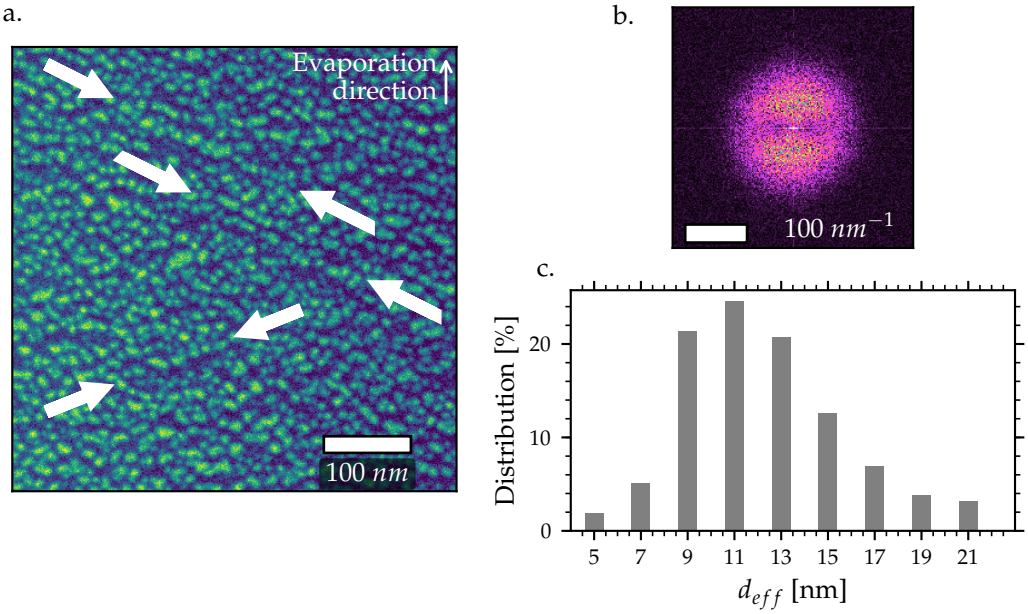

FIGURE 4.6: (a) Image obtained by SEM of Au on glass. (b) Fourier Transform of the SEM image. (c) Histogram giving the frequency as a function of the lateral size of the NPs. The sample was prepared by oblique angle evaporation of Au on glass. The direction of evaporation was aligned to the vertical axis of the image from bottom to top.

4.2.4 Optical properties: UV-Vis and TAS characterisation of the Au samples

The optical transmittance of the sample, for polarisations perpendicular ($T_\perp$) and parallel ($T_\parallel$) to the direction of deposition is shown in figure 4.7.a. It displays an important dichroism, with sharp LSPR given by the minimum of the spectra and centred at 700nm for $T_\perp$ and at 600nm for $T_\parallel$. The behaviour of the experimental spectra can be modelled with a flat Au nanoparticle of aspect ratio (height/lateral size) around 0.37 in agreement with the estimations from the SEM measurements and a small overall anisotropy, caused by the slight anisotropic shape of the nanoparticles and/or interaction between the nanoparticles along the chains. This is shown in figure 4.7.b. which also exhibits a dichroism dependent on the light polarisation. The aim of the calculation was not to perfectly reproduce the experiment but to demonstrate that the measured sizes of the nanoparticles could explain the observed positions of the LSPR. As discussed in chapter 3, accounting for the distribution of sizes and shapes of the nanoparticles would of course allow for better reproduction of the experimental results as it would broaden the calculated spectra. More details on the calculations are discussed in chapter 3 which deals with the fabrication method and ways to model the optical responses of the samples.

Figure 4.8 shows the TAS spectrum of the sample. One can see a maximum at 547nm and a minimum at 745nm. The spectrum crosses through zero at about 600nm which is the same wavelength read on figure 4.7.a. where both orthogonal polarisation cross each other. Measuring the sample under H_2 leads to an imperceptible red shift of the spectrum as seen in the insert. As discussed in chapter 1, the shift in the spectrum can be measured in terms of the change in intensity ΔS at a single wavelength instead of measuring the spectral shift $\Delta\lambda$.

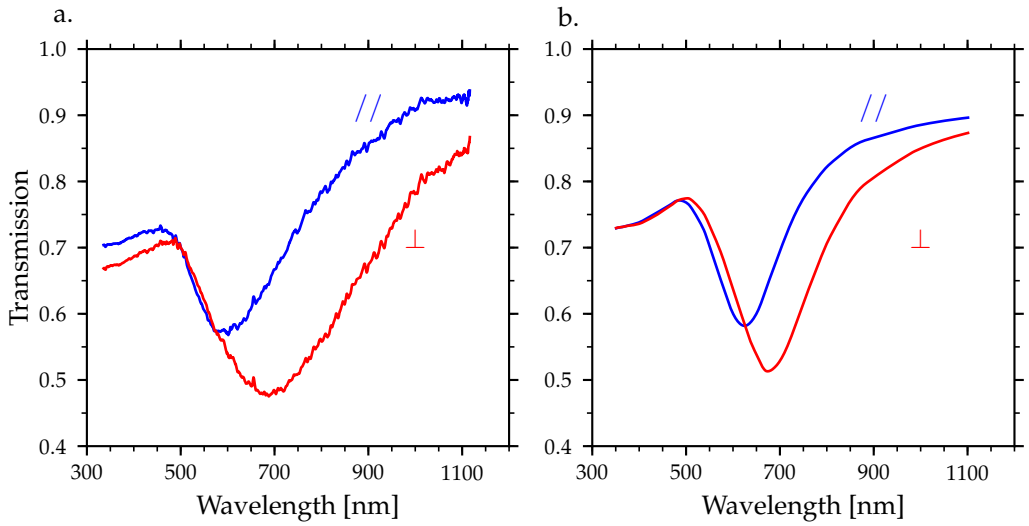

FIGURE 4.7: Transmission of the sample (normalised to the glass transmittance) for polarisation of light parallel (blue) and perpendicular (red) to the direction of evaporation. a. experiment, b. calculation

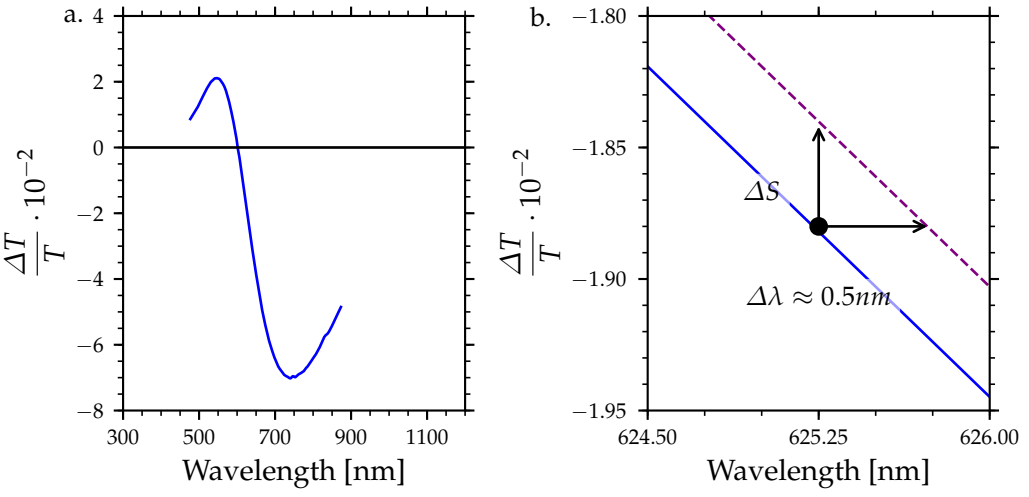

FIGURE 4.8: Square of the transmittance of the sample (a. Transmission anisotropy spectrum (TAS) of the same sample as in figure 4.7 under Ar. b. Schematic zoom around 613 nm. The solid blue line shows the spectrum under Ar and the dashed violet line under H_2. The exposure to H_2 leads to a small but clear red shift of about $\approx 0.5nm$.

4.3 Single wavelength monitoring of exposure to dihydrogen

4.3.1 Experimental results

The first step was to purge the cell initially with Ar, and then with H_2, whilst following the evolution of the signal at 613nm. Cycles were undertaken until the signal behaves in a reproducible manner. After accurate purging of the cell and stabilisation of the signal, the change in intensity of the TA measured at 613nm, is monitored as a function of time as the sample was exposed to cycles of pure Ar and H_2 at atmospheric pressure. The gas flow was shifted between Ar and H_2 every 100s at atmospheric pressure. The result is shown in figure 4.9 for several successive cycles for the six different samples (cf Table 4.1). This figure also shows the associated TAS spectrum for each sample. The figures framed in green are the sample corresponding to the SEM image and spectra discussed in the previous section. In order to work with the most sensitive range of the lock-in amplifier, a slight rotation of the first polariser was made to adjust the TA signal around 0 for the wavelength 613nm.

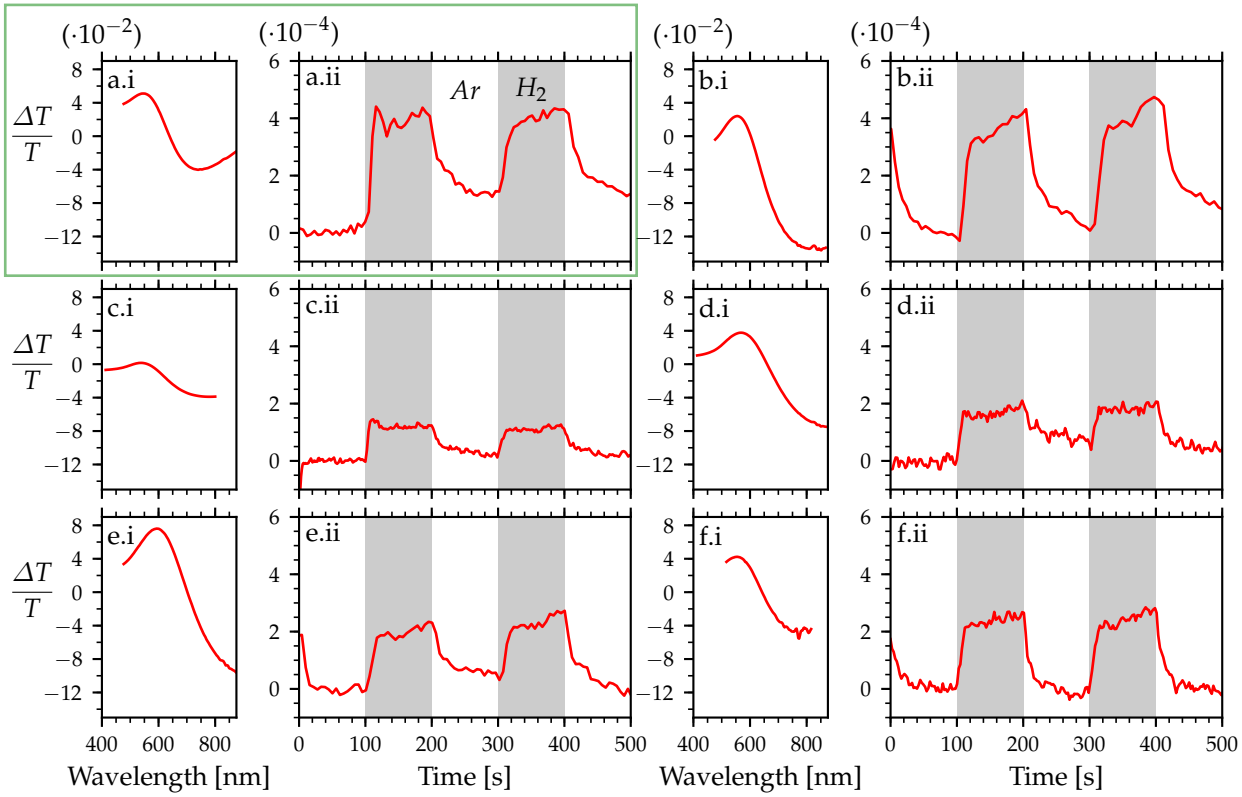

FIGURE 4.9: Series of TAS spectrum (i.) for all six samples referred in table 4.1. (ii.) shows the respective cycles of H_2 and Ar for each sample which all exhibit a red shift, though the amplitude is different for each sample. The average TA value has been shifted to a value close to 0 to enable better sensitivity on the lock-in amplifier (cf 2). The spectrum and cycles graph set framed in green represent the sample discussed in details in the next section.

When shifting from Ar to H_2, a clear increase in TA is observed. This is equivalent to a red shift of the TA spectra (Fig.4.8). The signal change upon gas shifting takes about 10s. This duration corresponds mainly to the time needed to purge the cell and tubes with the new gas. Shifting back to Ar reverts the signal back thus showing the reversibility of the mechanism. Yet, the fact that the signal does not completely recover

(in the case of 4.9a.ii, c.ii or d.ii) might come from the residual H_2 absorbed in the cell and tube walls as well as the fact that a limit of 100s was set.

Let's focus on the specific sample discussed in section 4.2.4. The cycles are repeated six times in figure 4.10. The important point here is that the initial exposure to H_2 gives a positive increase of the TA signal of $(4.0 \pm 0.2) \cdot 10^{-4}$, which corresponds to a red shift of the LSPR, equal to $\Delta\lambda = 0.50 \pm 0.02nm$ calculated by measuring the slope of the TA spectrum at 613nm.

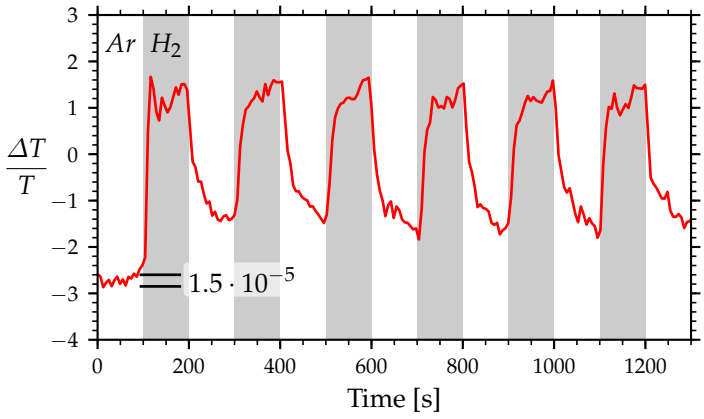

FIGURE 4.10: Change in intensity of the TA signal monitored at 613nm over 100s Ar/H_2 cycles at room temperature. The exposure to H_2 is due to a red shift of the LSPR. Moreover, the signal is reversible as can be seen in the periodicity of the measurement. The average TA value has been shifted to a value close to 0, with respect to figure 4.8.

The observation of this red shift upon exposing the Au nanoparticles to H_2 clearly confirms that, at room temperature, H_2 does interact with Au nanoparticles of lateral sizes ranging from 5 to 20nm, even supported on a non-reactive substrate such as glass. This adsorption is supposedly followed by dissociative chemisorption, as previously discussed.

4.3.2 Presentation of the model and interpretation of the results

In order to determine the impact of this adsorption, one must consider the charge redistribution within the particle and how this influences its dielectric function. In chapter 1, we have discussed how the dielectric function of a metal could be described by the sum of the Drude contribution and the interband contribution. Furthermore, we have discussed that the Drude contribution is dependent on the plasma frequency Ω_p (cf eq. 1.28) which is in turn dependent on the conduction electron density N (cf eq. 1.29). Therefore, varying the electron density, N in a plasmonic particle will directly influence the dielectric function of the metal. Lastly, we have discussed that the relative shift in energy of the LSPR spectrum, ω_{LSPR} can be related to the variation in the conduction electron density ΔN such as:

$$\frac{\Delta\lambda_{LSPR}}{\lambda_{LSPR}} = -\frac{\Delta\omega_{LSPR}}{\omega_{LSPR}} \approx -\frac{\Delta\Omega_p}{\Omega_p} = -\frac{1}{2}\frac{\Delta N}{N} \tag{4.1}$$

Thus as H_2 adsorbs on the Au nanoparticles, the electron redistribution leads to a decrease of the overall electron density within the particle as the weak $H - Au$ bond mobilises electrons on the surface of the nanoparticles. As a matter of fact, when considering chemisorption on metal surfaces, the bonding

between the chemisorbed entities and the metal atoms mobilises electrons, which are both donated by the adsorbate and back-donated by the metal [iv17]. The accumulation of electrons donated both by the H atoms and, though weaker, by the Au atoms, within the $Au-H$ molecular orbital induces a significant charge redistribution. This, in turn leads to an overall red-shift of the LSPR spectrum as the mobilised electron density may not contribute to the LSPR. Moreover, the amplitude of this shift should consequently give information on the total amount of the negative charge back-donated by the Au nanoparticle to the $Au-H$ bonds on its surface.

The influence of H_2 on the LSPR spectrum of Au nanoparticles has previously been studied in a couple investigations, though the results are contradictory. Collins et al. have studied the dark field scattering of Au nanorods of $13 \times 40nm$ deposited on glass substrate [iv18]. These rods were synthesised through the reduction of a solution of gold chloride ($HAuCl_4$), which inevitably left surfactants on the Au nanoparticles. They did not report any shift in the spectra upon exposure cycles to 100% N_2 and H_2. This point is however not in contradiction with the results presented in this thesis as the amplitude of the shift would reside within their noise - which is of $0.5nm$ - measured in the referred article, hence explaining why they could not observe any shift. Moreover, the difference in chemical composition of the Au surface might also influence their reactivity towards H_2.

On the other hand, Sil et al. have studied the modification of the LSPR spectrum of particles grown by vacuum evaporation on glass [iv19]. They reported a particle diameter ranging from 10 to $50nm$ though, having been determined by AFM, the size might have been overestimated as discussed above. Upon exposure to 10% H_2 in N_2, they recorded a decrease in transmittance (of $\approx 1\%$) of the spectrum as well as a $\approx 3nm$ blue shift. This in total contradiction with our present observations as well as in contradiction with what Collins et al. reported. Furthermore, they concluded that the change in transmittance of the sample was due to hot electrons generated by the Au LSPR. This is also questionned by Mukherjee et al. whom have demonstrated that no hot electrons were formed at low light intensities, but that a high power laser ($0.5W \cdot cm^{-2}$) was needed [iv14]. They demonstrated this by shining a super-continuum laser on small Au nanoparticles deposited either on TiO_2 or SiO_2 [iv13]–[iv15]. They have exposed the sample to a mixture of 50% H_2 and D_2 and recorded the formation of HD. The experiment showed that increasing the light intensity on the nanoparticle linearly increased the turn over frequency of HD formation. They further demonstrated that the rate of formation of HD was correlated to the wavelength used which was proportional to the LSPR spectrum of the Au nanoparticles. They thus convincingly attributed this phenomenon to a photo-induced generation of hot electrons induced by LSPR on the surface of the nanoparticle which would dissociate the adsorbed hydrogen molecules. On the other hand, Sil et al. used an incandescent light source which according to the demonstration discussed above, would not have enough energy to generate hot electrons. The fact that they observed a shift six times larger and in the opposite direction compared to the results reported here might come from artefacts, such as the purity of the gases they used and/or from the time over which the system was purged from air prior to the experiments which is necessary to remove contaminates, mainly H_2O and O_2.

Nevertheless, we have verified whether the observed adsorption of H_2 reported in this current work is photo-induced by the impinging light. In the present experiments, the illumination intensity was about $0.01W \cdot cm^{-2}$ which should be too low to induce any additional dissociation according to Mukherjee et al. [iv14], [iv15]. Several cycles of H_2/Ar were performed with illumination intensities varying from 10^{-2} to $2 \cdot 10^{-4} W \cdot cm^{-2}$ as shown in figure 4.11. This was achieved by adding a supplementary polariser after the main light source and rotating it in relationship to the second polariser. The graph shows that regardless of the intensity of the light, the signal amplitude during the gas cycles is identical. The only noticeable difference is the expected lower signal/noise ratio for smaller light intensities. This demonstrates that the

chemisorption and dissociation of H_2 by the Au nanoparticles observed in the present experiments is not induced by the incident light, i.e. not photo-induced, thus invalidating the observations done in ref [iv19].

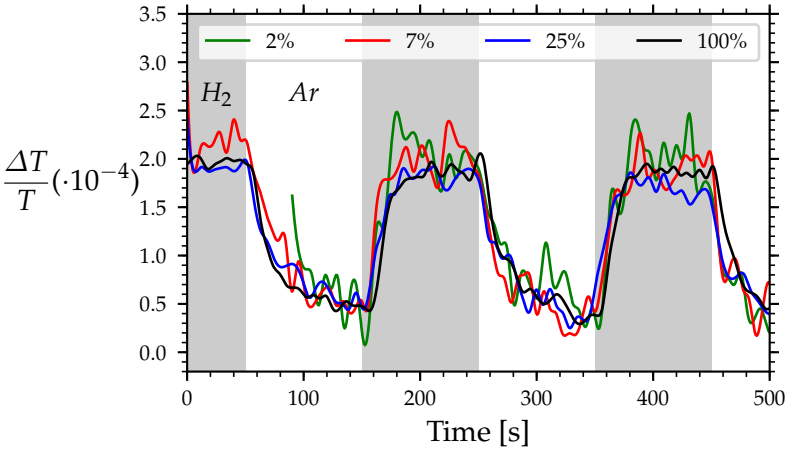

FIGURE 4.11: H_2/Ar cycles for a Au sample with various intensities of impinging light. Black: 100% intensity (about $0.01W \cdot cm^{-2}$), blue: 25%, red: 7%, green: 2%. Although the signal to noise ratio decreases when the light intensity decreases, it is clear that the amplitude of the shift is not related to the light intensity as the amplitude of all cycles are identical, meaning that the process is not photo-activated.

4.3.3 Adsorption, diffusion and desorption of hydrogen: what is the full mechanism?

So far, the interaction of H_2 with Au is confirmed from the experiments presented in the previous section. The red shift observed is justified by a charge redistribution within the particle. However, apart from the edges and corners i.e. the low coordinated sites where H_2 adsorb and dissociates, the becoming of the dissociated H atoms is still an unknown. The general hypothesis is that the surfaces and bulk of Au are not reactive as discussed in the introduction (section 4.1.1). Bus et al. experimentally showed that the adsorption sites are the edge and corner positions on Au where H_2 dissociates [iv20].

In order to verify this observation, several samples with different quantities of evaporated Au (c.f. Table 4.1) have been investigated. The hypothesis is that since the total length of the edges is directly proportional to the diameter of the nanoparticles, one should observe a proportional relationship between the variation in the density of conduction electron, ΔN and the average diameter, $\overline{d}$ of the nanoparticles. However, if H_2 interacts with the facets of the nanoparticles, the proportionality should be observed with the average surface area of the nanoparticles. If H_2 were to interact with the volume of the nanoparticles, the proportionality should be observed with the diameter cubed. Though H_2 being unable to absorb in Au, the latter statement is only proposed as to cover all three scenarios. In order to discriminate which of the nanoparticle's feature (the edges, facets or bulk) is determinant in the interaction taking place between H_2 and Au, ΔN must follow a linear proportionality with the feature's growth. The hypothesis is therefore that ΔN should vary proportionally with the diameter $\overline{d}$ if H accumulates on the edges of the nanoparticles.

To verify this hypothesis, the change in TA, for each sample, has been measured and compared to the average size of the nanoparticles. The nanoparticles were approximated to simple spheroid shapes, with the effective volume determined by measuring the average lateral size of the particles from the SEM images and the average height from the AFM 4.2. Therefore the average effective diameter was calculated by taking the cube root of the volume. The average diameter was defined as $\overline{d}$, the average surface as $\overline{d^2}$, and volume as $\overline{d^3}$. By measuring the slope of the TA spectrum at the measured wavelength and the change

in signal intensity, one can calculate the spectral shift, $\Delta\lambda$ for each sample when cycling through Ar and H_2 at ambient pressure. Thus the corresponding total variation in the conduction electron density ΔN can be calculated using eq. 4.1.

The evolution of ΔN with $\overline{d}$, $\overline{d^2}$ and $\overline{d^3}$ are drawn in figure 4.12.a, b. and c. respectively. The experimental points were fitted using both a linear regression in the form $y = ax + b$ (coloured) and $y = ax$ (dashed). The r^2 values for each fit is indicated on the respective graphs.

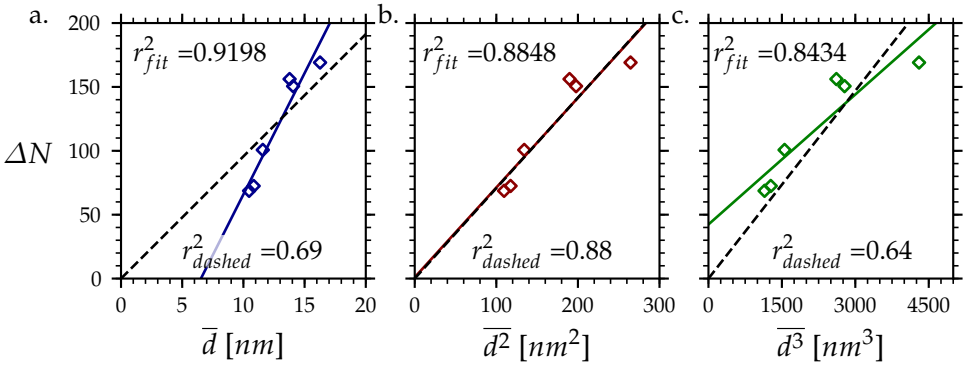

FIGURE 4.12: Graphs representing the change in conduction electron density as a function of the a. average diameter b. average surface area and c. average volume of the Au samples presented in table 4.1. The dash line show a fit of the data following an equation in the form $ax = y$. The coloured line show a fit of the experimental data with an equation in the form $ax + b = y$.

The reading of the graph suggests that the variation in the density of conduction electrons is not proportional to the average diameters of the nanoparticles, figure 4.12.a nor is it to the average volume (Fig. 4.12.c.). On the other hand, when plotting ΔN as a function of the average surface area of the nanoparticles (fig 4.12.b.), it can be seen that a proportionality is met. Since the average length of the edges grows linearly with the diameter of the particles, whereas the surface of the facets grows as the diameter square, it suggests that the facets do play a role in the interaction of H_2 with Au nanoparticles. This, at first sight, surprising dependence contradicts the hypothesis proposing that H_2 only interacts with the edges of the Au particles. It can however be explained by considering that the adsorbed H atoms can migrate towards the Au facets after dissociation at the edges and remain on the facets.

From the literature, one can find the binding energy of H on dense Au surfaces as well as the surface diffusion barrier which have been calculated using DFT by considering hopping between different sites. The values are shown in Table 4.2. These energy values must be compared to the bond energy of H_2 (g) which, according to Ferrin et al., is $4.57eV$ (calculated) and $4.52eV$ (experimental) [iv21]. The bond energy for H_2 accounts for the energy of two hydrogen atoms whereas table 4.2 only accounts for the binding energy between one H and the Au surface. The binding energy for a single H atom in an isolated H_2 molecule is thus $2.29eV$ and $2.26eV$ respectively.

On the $Au(111)$ surface, the calculations considered H adatoms located on the fcc, top, hcp and bridge sites and for the $Au(100)$ the locations were the hollow, top and bridge sites. The diffusion paths are determined by calculating the energy for multiple sites along the pathway which determines the diffusion energy barrier to overcome in order for a H to diffuse from one site to another. The different sites and diffusion pathways are drawn on Figure 4.13 for both $Au(100)$ and $Au(111)$.

From table 4.2, the binding energies of H on the $Au(111)$ surface are indeed above the bond energy of H_2, the most stable site being the fcc with an energy of $-2.18eV$ [iv21]. Thus, even if the diffusion barrier

TABLE 4.2: Table listing DFT calculated binding energies between Au and H adatoms and energy barriers of diffusing H through different paths taken from the literature. Site notations for $Au(111)$: F: fcc, H: hcp, T:top, B: bridge ; $Au(100)$: H: hollow, T:top, B: bridge. [a]This value is unstable, it is at a local maximum. [b]These values are relative to the binding energy of gaseous H_2, the values were calculated using the calculated value for one H atom ($\approx 2.29eV$) [iv21]. [c]This value is unusually low and is overlooked in the discussion. It can be wondered if an error was not made in the reference as all the other values for this column are $1eV$ higher.

		Au(111)							
		binding energy				diffusion energy			
		FCC	H	B	T	F B H	F T H	F T F	H T H
ref	[iv22]	-2.12	-2.12	-2.07^a	-1.91	0.06	0.24	0.24	0.24
	[iv23]	-	-1.96^b	-	-1.76^b	-	-	0.1	-
	[iv21]	-2.18	-	-	-	-	-	-	-
	[iv24]	-2.18	-2.14	-	-1.87	0.15	-	-	-

		Au(100)					
		binding energy			diffusion energy		
		H	B	T	B H B	H T H	B T B
ref	[iv22]	-1.87	-2.16	-1.88	0.29	0.06	0.29
	[iv25]	-	-3.27^c	-2.87	-	-	0.4
	[iv21]	-	-2.27	-	-	-	-
	[iv26]	-	-2.26^b	-1.95^b	-	-	-

on the (111) facet, between $0.24eV$ to $0.06eV$, is low, it is unlikely that H would remain on this surface as it is more favourable to form the $H-H$ bond, thus the adatoms would recombine and desorb. On the other hand, when considering the binding energies of H on the $Au(100)$ facets, the literature shows that for certain sites such as the bridge sites, the binding energy is around $-2.27eV$, close to the calculated dissociation energy for H_2 $-2.29eV$ [iv21]. When considering that the thermal energy kT at room temperature is around $0.03eV$, the diffusion path on the $Au(100)$ becomes as favourable as the desorption path. Furthermore, the pathway BTB has a relatively small energy barrier of $0.29eV$, and the diffusion rate was calculated to be $\approx 1.1 \cdot 10^7 s^{-1}$ [iv25], thus can lead to a very fast diffusion on the Au surfaces. It is therefore reasonable to anticipate that H atoms issued from the Au nanoparticle's edges can migrate to the (100) facets and stay a sufficient time before recombining and desorbing to give rise to additional charge transfers and therefore to the observable red shift of the LSPR.

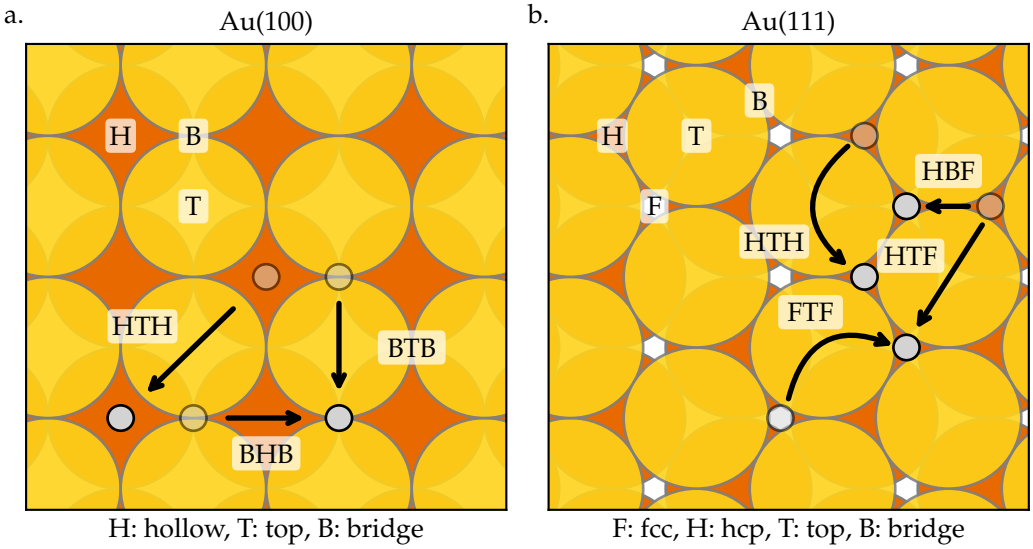

FIGURE 4.13: Schematic of the a. Au(100) and b. Au(111) facets with the different positions and pathways drawn. The yellow atoms are the surface atoms and orange are the sub-surface atoms. The grey circles represent hydrogen atoms.

From these energies, the equilibrium equation between the coverages of H on the (100), $\theta_{(100)}$ and on (111) facets, $\theta_{(111)}$, can be written as:

$$\theta_{(100)} e^{\frac{E_{(100)}}{k_B T}} = \theta_{(111)} e^{\frac{E_{(111)}}{k_B T}} \tag{4.2}$$

If one takes $E_{(100)} = -2.27eV$ and $E_{(111)} = -2.18eV$ [iv21], one can calculate the ratio $\theta_{(111)}/\theta_{(100)} = 0.025$ meaning that the coverage of the (100) facets is about forty times higher than for the (111) facets. However, one might argue that both facets do not have the same total area. Therefore to determine whether this coverage ratio is significant, one must calculate the surface area ratio of both facets. Determining the shape of nanoparticles is, nonetheless pretty challenging. Indeed, the samples, as prepared in this work cannot be easily studied using high resolution transmission electron microscopy (HRTEM). From the literature, it can be found that the equilibrium shape for Au nanoparticles is a truncated octahedron (Fig 4.14.a.b.) [iv27]–[iv29]. Experimental work has shown that epitaxial growth of Au on metal oxide such as MgO yields a section of truncated octahedron with (100) and (111) facets at room temperature even if the equilibrium shape is not reached [iv30]. Although Au nanoparticles cannot display epitaxial orientation on amorphous substrates such as glass, they are still expected to also display well-defined facets at room temperature. As the surface ratio between the (111) and (100) facets on a Au nanoparticle with the Wulff equilibrium shape is ≈ 3.5, this indicates that the number of sites occupied by H on the (111) facet remains quite smaller than those occupied on the (100) facets, i.e. of the order of 9%. In the following discussion, it will consequently be neglected.

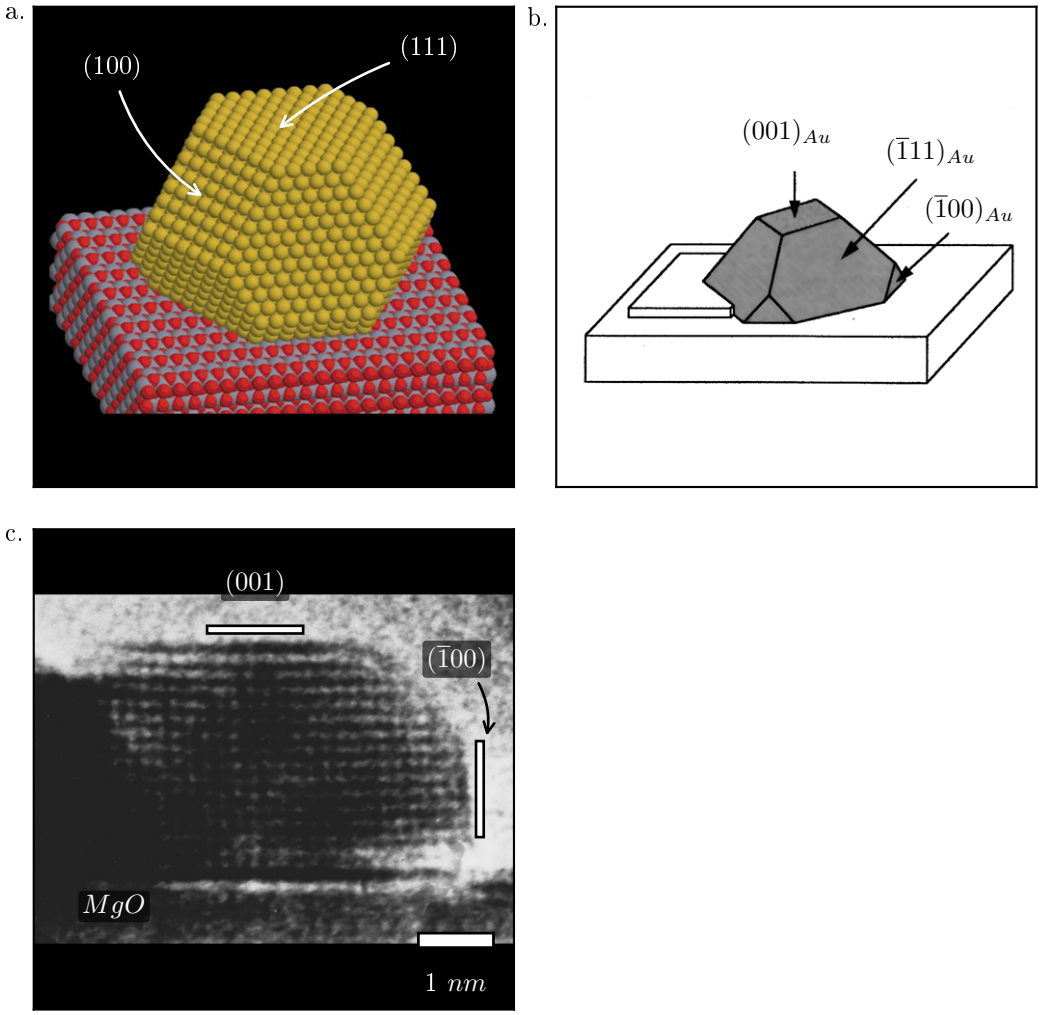

FIGURE 4.14: a. shows a schematic of a Au particle on TiO_2 substrate with (111) and (100) facets [iv31]. b. shows the same type of particle on a MgO substrate [iv30]. c. shows a TEM image of Au grown at room temperature on MgO and shows the different facets [iv30].

4.3.4 Kinetics of diffusing hydrogen on the (100) surface: determining the coverage of the gold nanoparticles

The experimental results have shown that H_2, when it reacts with Au, dissociates on the edges and diffuse mainly on the (100) facet whilst the amount of H_2 on the (111) facets is negligible. In order to investigate the kinetic mechanisms in play, experiments have been performed with varying flows of incident H_2 molecules. The amount of H on the (100) facets should increase with increasing flow, leading to a larger charge transfer, thus a larger red shift.

The experimental protocol is as follows: the flow of incident H_2 has been varied by changing the partial H_2 pressure, p in the H_2/Ar mixture within the cell, maintained at atmospheric pressure, from 67% to 1%. Figure 4.15 gives the spectral shift, $\Delta\lambda$ of the measured red shift for a given sample as a function of the H_2 partial pressure. The red shift strongly decreases for decreasing H_2 partial pressure.

The kinetics of dissociative adsorption and associative desorption of molecules has been long-time investigated [iv32], [iv33]. In the present case, one can consider that the adsorption occurs on the edges of

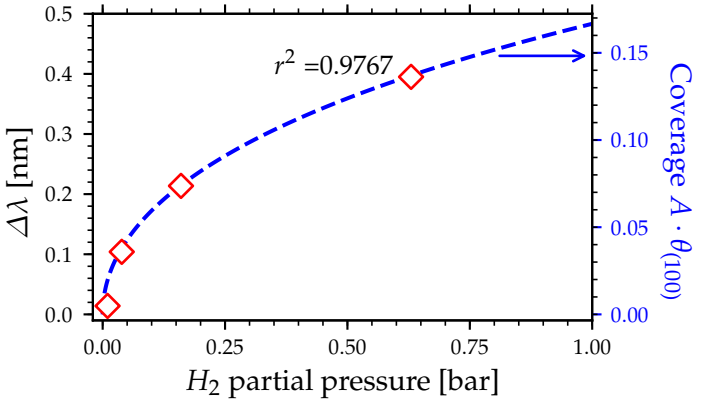

FIGURE 4.15: Red lozenges: experimental red shift of the LSPR upon H_2 adsorption (left scale); blue continuous line: H coverage θ of the nanoparticle facets, obtained from eq. 4.6 (right scale). The height of the lozenges corresponds to the error bar.

the nanoparticles, where the molecules dissociate, with a H coverage θ_{edge}. Then the H atoms either desorb back to the gas phase or can migrate to the facets. On the (100) facets, they can either stay a finite time and diffuse with coverage $\theta_{(100)}$, recombine and desorb back to the gas phase, or migrate back to the edges. The diffusion rate on the (100) facets being very fast, the coverage $\theta_{(100)}$ can be taken as homogeneous. Applying the stationary state approximation for the edges and facets, the corresponding kinetic equations at equilibrium can be written as:

$$\frac{d\theta_{edge}}{dt} = 0 = r_a(\theta_{edge}) - r'_d(\theta_{edge}) - r_{mig}(\theta_{(100)}, \theta_{edge}) + r'_{mig}(\theta_{(100)}, \theta_{edge}) \tag{4.3a}$$

$$\frac{d\theta_{(100)}}{dt} = 0 = r_{mig}(\theta_{(100)}, \theta_{edge}) - r'_{mig}(\theta_{(100)}, \theta_{edge}) - r_d(\theta_{(100)}) \tag{4.3b}$$

where $r_a(\theta_{edge})$ is the adsorption rate at the edges, $r'_d(\theta_{edge})$ and $r_d(\theta_{edge})$ are the desorption rates from the edges and the (100) facets, $r_{mig}(\theta_{(100)}, \theta_{edge})$ and $r'_{mig}(\theta_{(100)}, \theta_{edge})$ are the migration rates from the edges to the facets and from the facets to the edges, respectively. The desorption and adsorption rates, in the case of non-interacting adsorbed atoms without considering the precursor state, have the following second-order Langmuirian expressions, dependent on the coverages [iv32], [iv33]:

$$r_a(\theta_{edge}) = k_a(T) \times (1 - \theta_{edge})^2 \Phi \tag{4.4a}$$

$$r'_d(\theta_{edge}) = k'_d(T) \times \theta^2_{edge} \tag{4.4b}$$

$$r_d(\theta_{(100)}) = k_d(T) \times \theta^2_{(100)} \tag{4.4c}$$

where $k_a(T)$, $k'_d(T)$ and $k_d(T)$ are the rate coefficients of dissociative adsorption on the edges and associative desorption from the edges and facets, respectively, which are dependent on the temperature T. Φ is the flow of impinging molecules from the gas phase given by $p/(2\pi m k_B T)^{1/2}$. Calculating the

difference between eq. 4.3a and 4.3b thus leads to the suppression of the unknown migration rates, and yields the following expression:

$$0 = k_a(T) \times (1 - \theta_{edge})^2 \Phi - k'_d(T) \times \theta^2_{edge} - k_d(T) \times \theta^2_{(100)} \tag{4.5}$$

In order to determine the ratio between $\theta_{(100)}$ and θ_{edge}, the adsorption energies on the edge and on the facet should be calculated within the same theoretical model. To the writer's knowledge, such a comparison had not been performed. Consequently, the ratio $\frac{\theta_{edge}}{\theta_{(100)}}$ was taken in the following as a constant A, which is likely close to or larger than 1. After normalising the flow by using $F = k_a(T)/k'_d(T)\Phi$, the coverage $\theta_{(100)}$ can be written:

$$A\theta_{(100)} = \frac{F^{1/2}}{F^{1/2} + \left(1 + \frac{k_d}{A^2 k'_d}\right)^{1/2}} \tag{4.6}$$

This expression, with only one parameter $\left(1 + \frac{k_d}{A^2 k'_d}\right)$ allows one to reproduce the experimental points of figure 4.15 very well. Within this approach, the H coverage on the (100) facets can be obtained (with the factor A), and its value read on the right hand side scale of figure 4.15 as $A\theta_{(100)} = 0.16 \pm 0.05$ at atmospheric pressure. This large uncertainty is due to the fact that the evolution of the experimental points in Figure 4.15. can be reproduced correctly within the error bars, for a range of values of $\left(1 + \frac{k_d}{A^2 k'_d}\right)$, each one modifying the right scale.

However, as the ratio A between θ_{edge} and θ_{100} is unknown, it is not easy to know the actual H coverage on the (100) facets. Due to the fact that the adsorption sites on the edges [iv5] and on the (100) facets [iv24] are similar bridge sites, we can consider this ratio A to be close to 1. This will be used in section 4.4 for the charge transfer determination.

4.3.5 Effect of temperature

The mechanism for the adsorption, dissociation and diffusion processes is temperature dependent as discussed in ref [iv13]. In order to verify this statement, the cycles of alternating Ar and $\mathrm{H_2}$ at atmospheric pressure were repeated at different increasing temperatures from $295K$ to $390K$. The LSPR shift during the Ar / $\mathrm{H_2}$ cycles strongly decreases with increasing temperature which appear at first sight in contradiction with Mukherjee et al. whom have shown an increase of HD formation [iv13]. The present observation can be explained by a reduced time for the recombination of H atoms chemisorbed on the Au nanoparticles at high temperatures, leading to a faster desorption of $\mathrm{H_2}$ molecules, and therefore a smaller H coverage on the Au nanoparticles. This reduced time can be related to a faster diffusion on the facets and to an easier overcoming of the possible activation barrier for $\mathrm{H_2}$ recombination. However, a simple behaviour involving only one activation energy, following either an Arrhenius law or eq. 4.6, could not be determined from the present temperature dependence of the LSPR shift. Figure 4.16 shows that when plotting the natural logarithm of the shift in wavelength against the inverse of temperature, it does not show a linear relationship. Nonetheless, such an increase in the $\mathrm{H_2}$ recombination explains both the decrease of the LSPR shift measured herein and, in contrast, the increase of the $\mathrm{H-D}$ formation with higher temperatures during

the H/D exchange experiment observed by Mukherjee et al., which actually corresponds to an increase of the turn-over-frequency, related to the increase of both the dissociation rate and recombination rate [iv13].

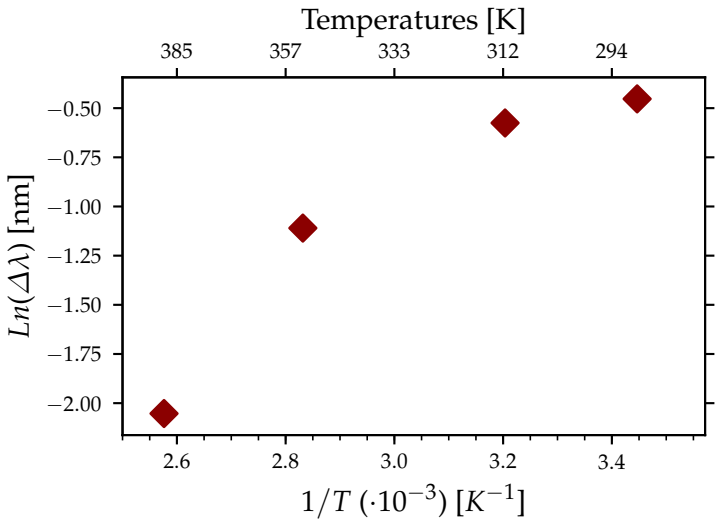

FIGURE 4.16: LSPR shift measured as a function of the sample's temperature.

4.4 Charge transfer between gold and hydrogen: experimental determination

The charge transfer ΔN induced by H adsorption can now be calculated from eq. 4.1. This gives, for the results presented in Figure 4.10, $\Delta N/N = -1.5 \cdot 10^{-3}$. In order to relate this value to the charge transfer per H adatom, the number of adsorbed H atoms in the permanent regime has to be estimated.

For simplicity, let us consider all particles having the shape of the upper part of a truncated octahedron, with either a (111) or a (100) facet in contact with the substrate. We also consider that only the (100) facets are covered by H. The average area of (100) facets for nanoparticles of lateral size equal to $12nm$ and height equal to $4.5nm$ is about $50nm^2$, which contains 600 atoms (of which 150 are on the edges). The average volume of these nanoparticles is about $400nm^3$, which contains 24 000 Au atoms. Exposed to pure H_2, the negative charge transfer is therefore $\Delta N = -35$ yielding an average charge transfer equal to $-0.06e$ per (100) surface Au atom with the ratio A taken close to 1. Figure 4.15 indicates that the coverage under atmospheric pressure of H_2 is about $\theta_{(100)} = 0.16 \pm 0.05$, which would correspond to 96 ± 30 H atoms on the (100) facets. Therefore, one can estimate that an amount 0.2 ± 0.05 electrons are back-donated from Au to each $Au - H$ bond.

Comparing this result with theoretical results is not straightforward. Indeed, the main limitation with theoretical calculation is their limitation in the number of atoms they can consider which is in the order of a few hundreds. Whereas experimental nanoparticles tend to have thousands if not more. Nevertheless, a few investigations of the charge transfer between H and Au nanoparticles have been performed, but they are somewhat contradictory. For instance, Kuang et al. found a small negative charge of about $-0.1e$ in the Au_n part of Au_nH_2 clusters with dissociated H_2 [iv34], whilst Lyalin et al. found no or smaller charge transfer for Au clusters, either isolated or supported [iv35]. In contrast, Zhao et al. calculated a positive charge equal to $0.25e$ and $0.3e$ in the Au parts of Au_4H and Au_5H clusters [iv36]. Similarly, Libisch et al.

calculated an electron transfer from Au to an adsorbed H_2 molecule, corresponding to a partial occupation of the σ^* antibonding orbital of H_2, reaching the value $-0.8e$ at the top of the barrier, which favoured the dissociation [iv37]. Finally, Hu et al., for Au_{85} clusters, showed that H adsorption leads to a significant reorganisation of the charge distribution, with a depletion of electrons, both in the Au atoms in the vicinity of the adsorbed H and on the H atom, explained by the back-donation and the donation of electrons, from Au and H atoms, respectively [iv38].

Consequently, in spite of the approximations used to estimate the charge transfer, the results found herein, showing a decrease of the electron population in the Au nanoparticle upon H adsorption and thus a positive charge transfer, appear in line with these three latter theoretical results.

4.5 Summary and conclusion

In this work, transmission anisotropic spectroscopy (TAS) was used to study the interaction of H_2 with plasmonic Au nanoparticles. The sensitivity of this method enabled the measurement of minute shifts as the Au samples were exposed to cycles of Ar and H_2 at atmospheric pressure. This made it possible to probe the interaction between Au and H_2 and allowed us to propose a mechanism on what is the becoming of adsorbed H_2 after its dissociation on the edges of the Au nanoparticles.

The samples were prepared by oblique angle evaporation. The characterisation of the samples was undertaken by AFM and SEM to determine the average morphology of the nanoparticles. UV-Vis spectroscopy displayed a dichroism for both orthogonal polarisations with respect to the direction of evaporation. Indeed, the polarisation parallel to the direction exhibited a spectrum blue shifted compared to that measured with a polarisation perpendicular to the direction of evaporation. The TAS spectrum displayed the anisotropy of the sample which could be used to measure the shift of the spectrum by monitoring the change in intensity of the spectrum at a single wavelength.

Cycles of H_2 in Ar were undertaken on several samples made of different size particles. Upon exposure to H_2 the change in signal was equivalent to a red shift of the LSPR spectrum. When switching back to Ar, the transmission anisotropy (TA) showed a reversibility of the signal as it reverted near to its initial state. It was therefore possible to relate the intensity of the spectral shift to the variation in conduction electron density within the particle. The observation showed that upon adsorption of H_2 on the particle, the density of conduction electrons was reduced. By quantitatively measuring this change in density for every sample, it was possible to show that it was proportional to the average surface area of the particles. This observation thus led to the conclusion that the H_2 not only does dissociate on the edges of the Au particles as proposed by the literature, but also diffuses on the surface of the nanoparticles. By determining the different binding energies of H adatoms on different surfaces of Au from the literature and correlating these energies with the probable shape of the particles, the proposed mechanism is that H_2 adsorbs and dissociates on the edges of the Au nanoparticles and then diffuses preferably on the Au(100) facets on the particles before desorbing.

Kinetic analysis of the signal shifts upon exposure to different partial pressures of H_2 made it possible to determine the charge transfer between the adsorbed H and the Au. This latter result revealed that, at atmospheric pressure of H_2, the average negative charge transfer from every surface Au atom to H is about $-0.06e$, and the back-donated charge localised on every Au − H bond is estimated to be around $-0.2e$ which is not in contradiction with the literature.

Results at different light intensities showed no correlation between the power of the incident light and the amplitude of the shift, meaning that the mechanism observed is not photo-induced. However, a correlation was showed with temperature, with a decrease in amplitude of the signal as the temperature was increase, though it does not follow an Arrhenius mechanism. It could nevertheless be explained by a reduction in transit time of the H adatoms on the (100) facets and an increase in the kinetics of desorption. This would lead to less H adatoms on the Au surfaces at a given time, thus less charge transfer occurring therefore a smaller spectral shift.

4.6 References

[iv1] W. L. Watkins and Y. Borensztein, "Mechanism of hydrogen adsorption on gold nanoparticles and charge transfer probed by anisotropic surface plasmon resonance", *Phys. Chem. Chem. Phys.*, vol. 19, no. 40, 2017.

[iv2] B. Hammer and J. K. Norskov, "Why gold is the noblest of all the metals", *Nature*, vol. 376, no. 6537, pp. 238–240, 1995.

[iv3] B. Hammer and J. Norskov, "Theoretical surface science and catalysis — calculations and concepts", *Advances in Catalysis*, vol. 45, pp. 71–129, 2000.

[iv4] L. Barrio, P. Liu, J. A. Rodríguez, J. M. Campos-Martín, and J. L. G. Fierro, "A density functional theory study of the dissociation of h_2 on gold clusters: Importance of fluxionality and ensemble effects", *Journal of Chemical Physics*, vol. 125, no. 16, pp. 12–16, 2006.

[iv5] A. Corma, M. Boronat, S. González, and F. Illas, "On the activation of molecular hydrogen by gold: A theoretical approximation to the nature of potential active sites.", *Chemical communications (Cambridge, England)*, no. 32, pp. 3371–3373, 2007.

[iv6] L. Stobiński, L. Zommer, and R. Duś, "Molecular hydrogen interactions with discontinuous and continuous thin gold films", *Applied Surface Science*, vol. 141, no. 3-4, pp. 319–325, 1999.

[iv7] A. G. Sault, R. J. Madix, and C. T. Campbell, "Adsorption of oxygen and hydrogen on au(110)-(1x2)", *Surface Science*, vol. 169, no. 2-3, pp. 347–356, 1986.

[iv8] M. Haruta, "When gold is not noble: Catalysis by nanoparticles", *Chemical Record*, vol. 3, no. 2, pp. 75–87, 2003.

[iv9] T. Fujitani, I. Nakamura, T. Akita, M. Okumura, and M. Haruta, "Hydrogen dissociation by gold clusters", *Angewandte Chemie - International Edition*, vol. 48, no. 50, pp. 9515–9518, 2009.

[iv10] A. Corma and H. Garcia, "Supported gold nanoparticles as catalysts for organic reactions", *Chemical Society Reviews*, vol. 37, no. 9, pp. 2096–2126, 2008.

[iv11] G. C. Bond, "Hydrogenation by gold catalysts: An unexpected discovery and a current assessment", *Gold Bulletin*, vol. 49, no. 3-4, pp. 53–61, 2016.

[iv12] M. Manzoli, A. Chiorino, F. Vindigni, and F. Boccuzzi, "Hydrogen interaction with gold nanoparticles and clusters supported on different oxides: A ftir study", *Catalysis Today*, vol. 181, no. 1, pp. 62–67, 2012.

[iv13] S. Mukherjee, F. Libisch, N. Large, O. Neumann, L. V. Brown, J. Cheng, J. B. Lassiter, E. A. Carter, P. Nordlander, and N. J. Halas, "Hot electrons do the impossible: Plasmon-induced dissociation of h_2 on au", *Nano Letters*, vol. 13, no. 1, pp. 240–247, 2013.

[iv14] S. Mukherjee, L. Zhou, A. M. Goodman, N. Large, C. Ayala-Orozco, Y. Zhang, P. Nordlander, and N. J. Halas, "Hot-electron-induced dissociation of h_2 on gold nanoparticles supported on sio_2", *Journal of the American Chemical Society*, vol. 136, no. 1, pp. 64–67, 2014.

[iv15] M. L. Brongersma, N. J. Halas, and P. Nordlander, "Plasmon-induced hot carrier science and technology", *Nature Nanotechnology*, vol. 10, no. 1, pp. 25–34, 2015.

[iv16] L. Leandro, R. Malureanu, N. Rozlosnik, and A. Lavrinenko, "Ultrathin, Ultrasmooth Gold Layer on Dielectrics without the Use of Additional Metallic Adhesion Layers", *ACS Applied Materials and Interfaces*, vol. 7, no. 10, pp. 5797–5802, 2015.

[iv17] G. A. Somorjai, *Introduction to surface chemistry and catalysis.* Nov. 1994, p. 369, ISBN: 0-471-03192-5.

[iv18] S. S. E. Collins, M. Cittadini, C. Pecharromán, A. Martucci, and P. Mulvaney, "Hydrogen spillover between single gold nanorods and metal oxide supports: A surface plasmon spectroscopy study", *ACS Nano*, vol. 9, no. 8, pp. 7846–7856, 2015.

[iv19] D. Sil, K. D. Gilroy, A. Niaux, A. Boulesbaa, S. Neretina, and E. Borguet, "Seeing is believing: Hot electron based gold nanoplasmonic optical hydrogen sensor", *ACS Nano*, vol. 8, no. 8, pp. 7755–7762, 2014.

[iv20] E. Bus, J. T. Miller, and J. A. Van Bokhoven, "Hydrogen chemisorption on Al2O3-supported gold catalysts", *Journal of Physical Chemistry B*, vol. 109, no. 30, pp. 14 581–14 587, 2005.

[iv21] P. Ferrin, S. Kandoi, A. U. Nilekar, and M. Mavrikakis, "Hydrogen adsorption, absorption and diffusion on and in transition metal surfaces: A dft study", *Surface Science*, vol. 606, no. 7-8, pp. 679–689, 2012.

[iv22] X. Shen, Y. Li, X. Liu, D. Zhang, J. Gao, and T. Liang, "Hydrogen diffusion into the subsurfaces of model metal catalysts from first principles", *Phys. Chem. Chem. Phys. Phys. Chem. Chem. Phys*, vol. 19, no. 19, pp. 3557–3564, 2017.

[iv23] L. Kristinsdóttir and E. Skúlason, "A systematic dft study of hydrogen diffusion on transition metal surfaces", *Surface Science*, vol. 606, pp. 1400–1404, 2012.

[iv24] Y. Santiago-Rodríguez, J. A. Herron, M. C. Curet-Arana, and M. Mavrikakis, "Atomic and molecular adsorption on au(111)", *Surface Science*, vol. 627, no. 2, pp. 57–69, 2014.

[iv25] E. Del, V. Gómez, S. Amaya-Roncancio, L. B. Avalle, D. H. Linares, and M. Cecilia Gimenez, "Dft study of adsorption and diffusion of atomic hydrogen on metal surfaces", *Applied Surface Science*, vol. 420, pp. 1–8, 2017.

[iv26] M. N 'dollo, P. S. Moussounda, T. Dintzer, and F. Garin, "A density functional theory study of methoxy and atomic hydrogen chemisorption on au(100) surface", *Journal of Modern Physics*, vol. 4, pp. 409–417, 2013.

[iv27] A. S. Barnard and Y. Chen, "Kinetic modelling of the shape-dependent evolution of faceted gold nanoparticles", *Journal of Materials Chemistry*, vol. 21, no. 33, p. 12 239, 2011.

[iv28] G. D. Barmparis and I. N. Remediakis, "First-principles atomistic Wulff constructions for gold nanoparticles", Nov. 2011. arXiv: 1111.4667.

[iv29] G. D. Barmparis, K. Honkala, and I. N. Remediakis, "Thiolate adsorption on Au(hkl) and equilibrium shape of large thiolate-covered gold nanoparticles", *The Journal of Chemical Physics*, vol. 138, no. 6, p. 064 702, 2013.

[iv30] T. Kizuka and N. Tanaka, "Atomic process of epitaxial growth of gold on magnesium oxide studied by cross-sectional time-resolved high-resolution electron microscopy", *Physical Review B - Condensed Matter and Materials Physics*, vol. 56, no. 16, pp. 10 079–10 088, 1997.

[iv31] S. Giorgio, M. Cabié, and C. R. Henry, "Dynamic observations of au catalysts by environmental electron microscopy", *Gold Bulletin*, vol. 41, no. 2, pp. 167–173, 2008.

[iv32] D. A. King and M. G. Wells, "Reaction mechanism in chemisorption kinetics: Nitrogen on the plane of tungsten", *Proceedings of the Royal Society A: Mathematical, Physical and Engineering Sciences*, vol. 339, no. 1617, pp. 245–269, 1974.

[iv33] H. C. Kang and W. H. Weinberg, "Dynamic monte carlo simulations of surface-rate processes", *Accounts of Chemical Research*, vol. 25, no. 6, pp. 253–259, 1992.

[iv34] X.-J. Kuang, X.-Q. Wand, and G.-B. Liu, "A comparative study between all-electron scalar relativistic calculation and all-electron calculation on the adsorption of hydrogen molecule onto small gold clusters", *Journal of Chemical Sciences*, vol. 125, no. 2, pp. 401–411, 2013.

[iv35] A. Lyalin and T. Taketsugu, "A computational investigation of h_2 adsorption and dissociation on au nanoparticles supported on tio_2 surface", *Faraday Discussions*, vol. 152, no. 0, p. 26, 2011, ISSN: 1359-6640.

[iv36] S. Zhao, Y. Ren, Y. Ren, J. Wang, and W. Yin, "Density functional study of hydrogen binding on gold and silver-gold clusters", *The Journal of Physical Chemistry A*, vol. 114, no. 14, pp. 4917–4923, 2010.

[iv37] F. Libisch, J. Cheng, and E. A. Carter, "Electron-transfer-induced dissociation of h_2 on gold nanoparticles: Excited-state potential energy surfaces via embedded correlated wavefunction theory", *Zeitschrift für Physikalische Chemie*, vol. 227, 2013.

[iv38] M. Hu, D. P. Linder, M. Buongiorno Nardelli, and A. Striolo, "Hydrogen Adsorption on Platinum–Gold Bimetallic Nanoparticles: A Density Functional Theory Study", *The Journal of Physical Chemistry C*, vol. 117, no. 29, pp. 15 050–15 060, 2013.

Chapter 5

Use of palladium for dihydrogen sensing: thermodynamics and kinetics limitations

Abstract

Anisotropic nanostructured porous Pd films were fabricated using oblique angle deposition in vacuum on a glass substrate. They display a dichroic response, due to localised surface plasmon resonances (LSPR) within the discontinuous film, and dependent on the incident light polarisation. Ultra sensitive hydrogen sensing was reached by using these films in conjunction with reflectance anisotropy spectroscopy. The evolution of the samples' optical responses was monitored during the formation of Pd hydride in either the dilute α-phase and the dense β-phase, whilst the samples were exposed to different concentration of H_2 in Ar (from 100% H_2 to a few ppm). The measurements were performed at a single wavelength in the visible range and at room temperature 22°C. The results showed that a quantitative measurement of the hydrogen concentration in a carrier gas could be measured throughout the concentration range. The limit of detection was $10ppm$ and the time for detecting the presence of H_2 in the carrying gas was below one second at concentration down to 0.25% of H_2 in Ar. Furthermore, the optical anisotropy of the samples and its evolution with exposure to H_2 were correctly reproduced with an effective medium theory. The thermodynamics and kinetics were studied to quantitatively determined the degree of hydrogenation as well as the reaction mechanism at play. Preliminary investigation in dry and humid air was also undertaken which revealed an issue of competition between the oxidation and hydrogenation of the Pd. A look into the use of metal oxide frameworks, in order to protect the metal film was done, though this investigation was not completed. This preliminary work was done in collaboration with Christian Serre, Antoine Tissot and Shan Dai from the materials institute of Paris ENS.

5.1 Introduction and context: hydrogen economy

"The third plasmonic sensing material"
- 2015

K. Sugawa et al.

THE ADVENT OF CLIMATE CHANGE induced by the heavy use of fossil fuels has triggered off alarms in both the scientific community as well as on the political scene. In 2016, the COP21 Paris agreement brought 116 countries to pledge to take action to slow global warming down by cutting off on CO_2 emissions and other greenhouse gases. To accommodate this goal, both industry and academia have invested a lot of resources in research and development for alternative cleaner and sustainable renewable energy sources [v1], [v2].

H_2 has many chemical properties making it a keen candidate for such a task [v3], [v4]. It has a low density and boiling point making it a lighter gas to transport than other natural gases. H_2 has many advantages as an energy source. It is one of the most abundant element on the Earth's crust. Moreover, it has a high heat of combustion and a wide flammability range ($4 - 70\%$). Table 5.1 shows a couple physical and chemical characteristics of H_2 compared to methane, propane and butane.

From these values it can be seen that H_2 does not produce as much energy per mole than natural gases however, its low molar mass makes it more energetic in terms of energy generated by weight. Furthermore its combustion reaction only produces water as a by-product whereas the heavier alkanes produce CO_2 in quantities proportional to the length of the hydrocarbon chain.

TABLE 5.1: Chemical and physical characteristics of H_2 against the methane, propane and butane.

	Hydrogen (H_2)	methane (CH_4)	Propane (C_3H_8)	Butane (C_4H_{10})
Density $[kg \cdot m^{-3}]$	$8.9 \cdot 10^{-2}$	$6.7 \cdot 10^{-1}$	2	2.5
Boiling point $[K]$	20	111	231	273
Combustion enthalpy $[kJ \cdot mol^{-1}]$	286	889	2220	2877
Heat of combustion $[kJ \cdot g^{-1}]$	142	55	50	49

$$C_nH_m + nO_2 \longrightarrow nCO_2 + \frac{m}{2}H_2O$$

$$2H_2 + O_2 \longrightarrow 2H_2O$$

Harvesting the energy from H_2 can be achieved by simple combustion. However, electricity can be directly produced by using a fuel cell which works by dissociating the H_2 on the anode, the electron passes through the output circuit and the formed cations pass through an electrolyte to the cathode where it recombines with O_2 to form H_2O (Fig. 5.1). This process yields an efficiency of about 60% to 70%, compared to gas turbins which yield up to 40% [v5], [v6].

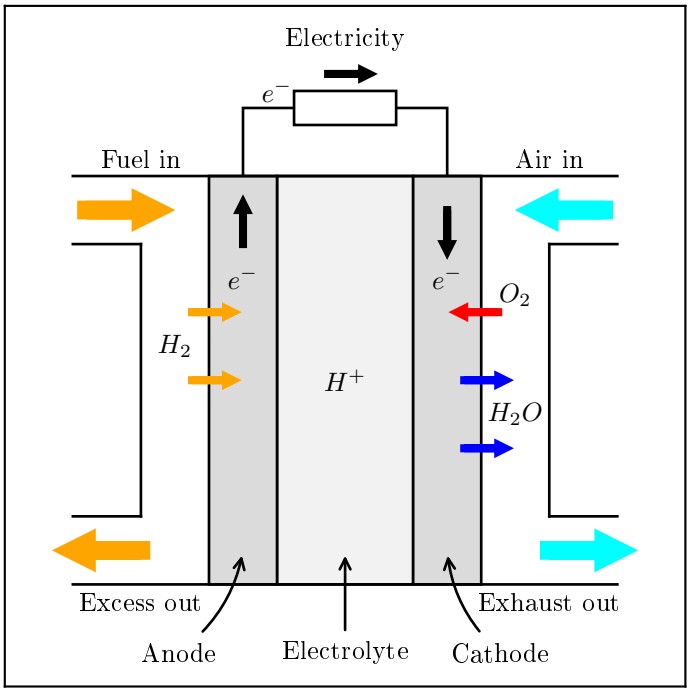

FIGURE 5.1: Schematic of a fuel cell design which uses H_2 as a fuel to generate an electrical current.

H_2 is colorless and orderless which means it cannot be detected by human senses. Moreover, its small size also means that issues of H_2 leakage are very high as it can permeate through different metals such as steal. The lower flammability mixture for H_2 in air at atmospheric pressure is around 4% [v7]. Attempts of adding odorant markers as it is commonly done with natural gas has proven difficult as shown by D. Imamura et al. Indeed, the addition of sulphur compounds lead to poisoning of the fuel cell reducing its electrical generation performance. They do propose sulphur-free alternatives which could be compatible

with the energy harvesting process of H_2 but do underline that the unknowns in terms of long term performance of fuel cells, degradation of H_2 storage materials and diffusion properties have to be further studied [v8]. The need for accurate, fast and quantitative H_2 sensor has only been increasing throughout the years. Many industries require such capabilities such as the chemical industry which requires H_2 monitoring in the synthesis of ammonium or methanol, in the hydration of hydrocarbons or even in the production of rocket fuels. Automotive industries are looking into substituting common petrol with H_2 thus changing from a relatively safe liquid fuel to a flammable gas. According to T. Hubert et al. the demands and requirements for H_2 sensors can be summarised as follows:

- Indication of H_2 in concentration range 0.001 - 10% for safety and 1-100% for fuel cells.
- Safe performance i.e. explosion proof sensor design and protecting housing.
- Reliable results of sufficient accuracy and sensitivity with an uncertainty below 5 to 10%.
- High signal to noise ratio.
- Robustness including low sensitivity to environmental parameters such as temperature, pressure, relative humidity, gas flow rate.
- Fast response and recovery time below 1 second.
- Low cross sensitivity e.g. hydrocarbons, CO, H_2S
- Life time above 5 years.
- Low power consumption.
- Small size.
- Simple operation and maintenance with long service interval.
- Simple system integration and interface.

In his review dated from 2011 [v9], he and his co-workers have listed different technologies for H_2 detection which can be categorised into two main groups: electronic and optic based. Electronic detectors regroups many different technologies based on the measurement of an electric signal from the sample. For instance a prominent methode is to use metal oxides and measure the change in electrical resistance of the oxide as it reacts to H_2 [v10], [v11]. Another approach is to use catalytic materials which ignite the present H_2 generating heat within the sensor, this heat can be measured and quantitatively determine the presence of H_2. Many different methods exist but an exhaustive review of all these different technologies is not in the scope of this thesis. Nevertheless, electronic methods have proven reliable and are very much in use, in spite of the inherent draw-backs of each specific methods [v9]. Yet, one of the main disadvantage in all these methods is that the sensor itself is an active component of the detector. This means that accessibility to the sensor is required with the use of electrical wires which thus means that electrical sparks are an intrinsic hazards especially in an explosive environment.

Optical methods work in a different way mainly by measuring the change in the optical response of a material when it reacts to H_2. Again, many different technologies have emerged with an interesting development of fibre optic based sensors [v12]–[v14]. Y. Zhang et al. in 2017 published a review accounting for recent advances in optical fibre hydrogen sensors[v15]. The basic principal is to strip the fibre's cladding and coat the glass with a reactant that will influence the light signal when it reacts with H_2. Other technique of course use common spectroscopy to detect the change in optical response of the sensor [v9]. Specifically the use of LSPR which has shown to be a promising method for the detection of low quantities of H_2 [v16]. In addition to the good sensitivity and fast response of such plasmonic sensors, the use of light as a probe

implies that the sample is a passive component of the system, which eliminates hazards such as electrical sparks associated with electronic systems. A common element used in these optical systems though and in many hydrogen technologies in general is palladium since its physical and chemical properties towards H_2 makes it a near ideal material [v1], [v16], [v17] .

5.1.1 Physical and chemical properties of Pd metal

• Formation of palladium hydride

A common denominator of most hydrogen technologies is the use of palladium. Pd exhibits a high affinity to H_2 as well as a high selectivity. Its latter caracteristic goes as far as making it a capable material for seperating hydrogen and deuterium as the two isotopes have different *solubilities* within the metal [v18]. When H_2 reacts with the Pd, it forms a metal hydride, however, thermodynamic studies show that depending on the partial pressure of H_2, different phases are formed.

Palladium hydride, PdH_x exhibits two phases depending on the partial pressure of H_2 $p(H_2)$ and temperature. In the case of bulk metal at ambient temperature, the dense phase known as the $\beta-$phase is formed for $p(H_2) > 10^{-2} bar$ which leads to PdH_x with $x \geqslant 0.6$. Therefore, at atmospheric pressure this phase is only formed when more than 1% of the ambient gas is composed of H_2. On the other hand, when $p(H_2) < 10^{-3} bar$, only the dilute $\alpha-$phase exists. This forms PdH_x with $x \leqslant 0.02$. At intermediate pressures, around $10^{-3} bar$, a hybrid $\alpha + \beta$ phase is obtained constituted of $\beta-$phase regions embedded in the $\alpha-$phase. Increasing the temperature makes it possible for the metal hydride to sustain higher pressures of H_2 in the $\alpha-$phase as well as reducing the range of the $\alpha + \beta$ phases. The phase diagram is illustrated in figure 5.2.a. For experimental results at room temperature figure 5.2.b. shows the phase diagram determined by Manchester et al. at different temperatures [v19].

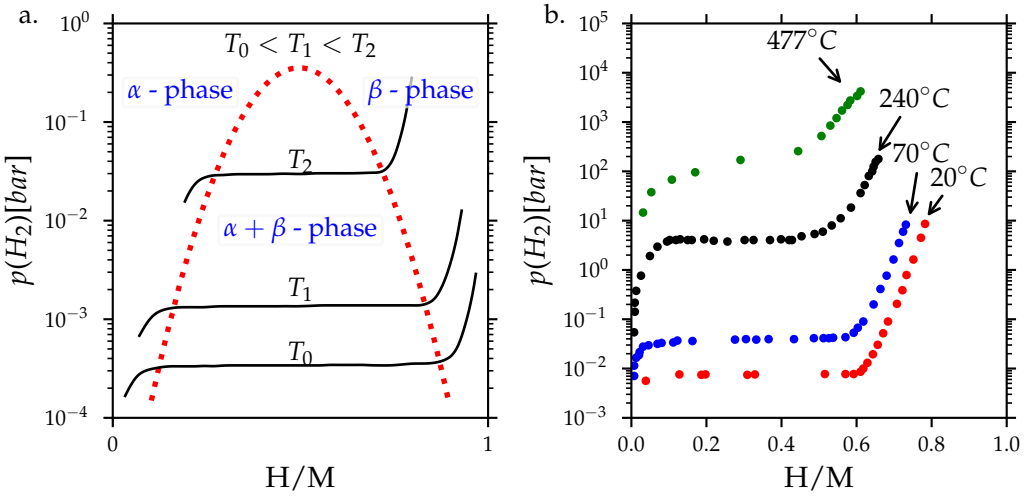

FIGURE 5.2: a. Diagram of phase diagram of palladium hydride b. Experimental phase diagram at different temperature for bulk palladium hydride taken from ref [v19].

• Optical property and LSPR of palladium nanoparticles

The dielectric function for bulk Pd was determined by Johnson and Christy and is plotted in wavelengths in figure 5.3.a. [v20]. Pd exhibits an approximative Drude like curve. Yet, using equation sets presented in chapter 1, no resonance is reached in the visible range for a 10nm nanosphere as shown in figure 5.3.b.

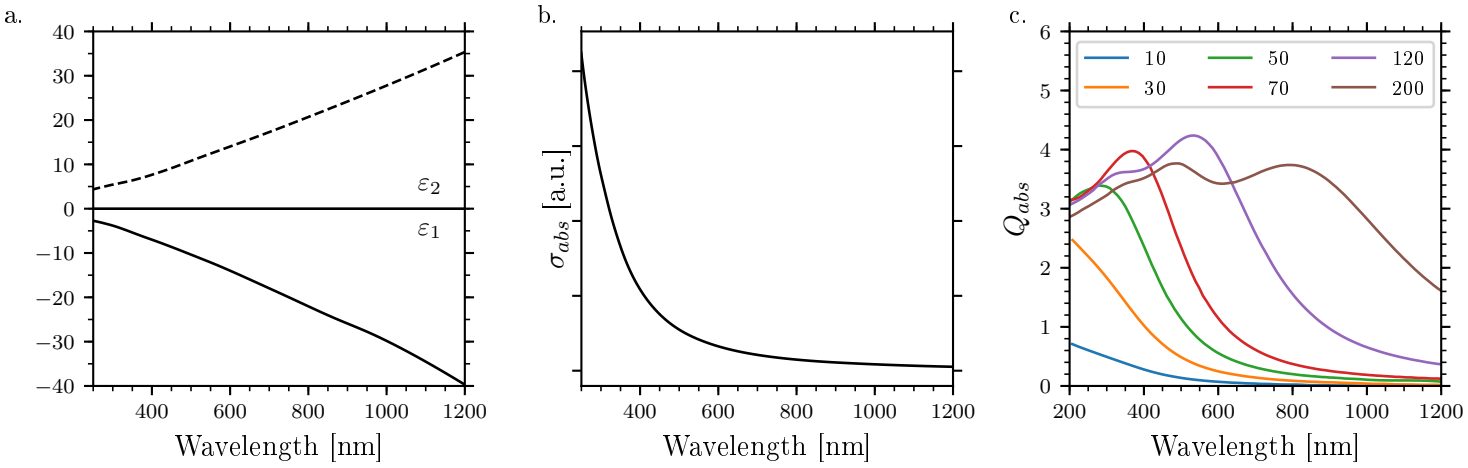

FIGURE 5.3: a. Dielectric function by Johnson and Christy of bulk Pd [v20]. b. Absorption cross section of a Pd nanosphere calculated using analytical equation from chapter 1. c. Mie calculation from ref [v21] for different sized palladium spheres from 10nm to 200nm.

Recently however, K. Sugawa et al. made the claim that Pd is the "third plasmonic sensing material" [v21]. Indeed, LSPR in the visible range were calculated using Mie's theory by considering large Pd spheres with diameters up to 200nm as is shown in figure 5.3.c. As the size of the particle increases, a LSPR peak appears in the UV and is shifted towards the visible range. The increase in size also leads to multi polar effects which are well visible at 120 and 200nm.

The key feature of Pd, for it to be a *sensing material* is its capability to have its optical properties changed by an adsorbate. Experimentally Zoric et al. have shown Pd nanodisk of size around 300nm (Fig 5.4.a) to display LSPR near the infra-red at $\approx$ 1000nm in vacuum as depicted in figure 5.4.b [v22]. When exposing the sample to H_2 at $p(H_2)$ = 500$mbar$, they have recorded a clear red shift of the spectrum due to the formation of palladium hydride (Fig 5.4.b). This experiment therefore shows the capability of LSPR to register the change in the dielectric function of Pd as it reacts to H_2.

A phenomenon that is not observed in the phase diagram of figure 5.2.b. is the existence of a hysteresis when cycles of hydriding and dehydriding are undertaken. Bardhan et al. have experimentally determined the isotherm at 22°C and 82°C for bulk Pd when looking at the normalised luminescence against the increase or decrease in pressure of H_2 against vacuum [v23]. Similar results where obtained by Zoric et al. for the 300nm nanodisks at 30, 55 and 80°C when they followed the maximum spectral shift, $\Delta\lambda_{max}$ against the pressure of H_2 [v22]. The isotherms are plotted in figure 5.5.a and b. respectively.

It can be seen, in both cases that, when the H_2 is increased from $10^{-3}bar$ to near ambient pressure, the measured entity follows the phase diagram, that is a low influence when raising the pressure to about 10^{-2} to $10^{-1}bar$, depending on the temperature, then a sharp jump in signal after this threshold which leads to a significant optical change of the Pd. However, when decreasing the pressure of H_2 back to $10^{-3}bar$, a

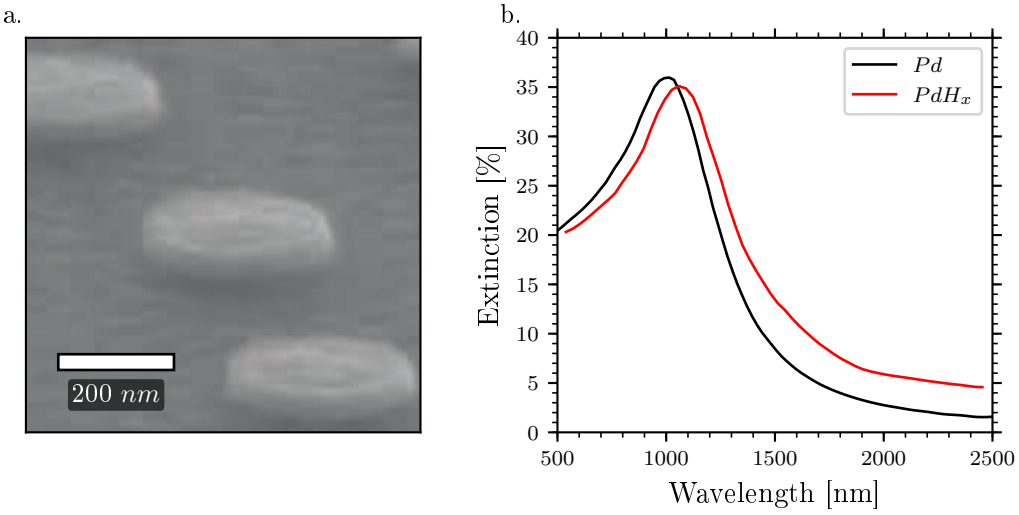

FIGURE 5.4: a. Nanodisk of Pd on fused silica substrate. b. Extinction spectra for the palladium nanodisk under vacuum (black) and with 500$mbar$ H_2 (red) taken from ref. [v22].

hysteresis is observed. Moreover, the increase in temperature shows that higher pressures are needed to reach the $\beta-$phase and a slight reduction in the hysteresis.

Despite this sensitivity to H_2 the thermodynamics of Pd hydride does impose an important limitation for hydrogen sensing applications. At atmospheric pressure, the flammability limit starts at 4% H_2 which is equivalent to $4 \cdot 10^{-2} bar$. It can be seen on 5.5.a. and b. that increasing the H_2 pressure to this limit, only the $\alpha-$phase is formed. Yet, the $alpha-$phase looks to have very small effect on the optical response of the Pd at room temperature whereas when the $\beta-$phase or the $\alpha + \beta$ phase are obtained, the optical change is much more significant. This leads to an important issue for plasmonic sensors as it is therefore mandatory that H_2 sensors be sensitive to the very initial $\alpha-$phase formation [v16].

To better understand the potential of Pd to be used in conjunction with LSPR methods, one must first understand the effect of the hydrogenation of the metal on its dielectric function.

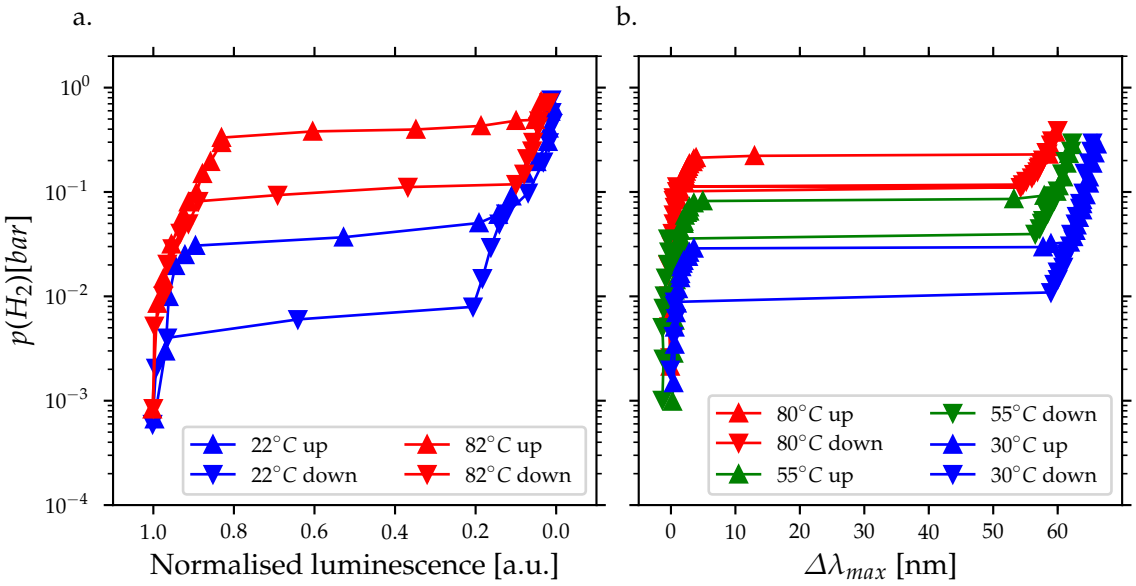

FIGURE 5.5: a. Isotherm of palladium bulk, from ref [v23]. b. Isotherm of palladium nanoparticles, from ref. [v22].

• LSPR shift induced by hydrogenation of palladium nanoparticles

Different sources are available in the literature for the dielectric function of Pd. The dielectric functions chosen for comparison were those of Johnson and Christy which are reputable experimental results [v20], Vargas et al. whom have provided experimental values for Pd as well as PdH [v24] and Silkin et al. whom have proposed a DFT determined dielectric function for Pd as well as for PdH_x, where x is the stoichiometry of the palladium hydride [v25].

Let's first focus on the results for Pd. Figure 5.6.a. shows the different dielectric functions for Pd mentioned above. As already discussed, the dielectric function of Pd have a Drude like curve. If we compare the experimental results from Johnson and Christy [v20] and Vargas et al. [v24], we can see an inconsistency between their results especially in the imaginary part (ε_2). This might come from the quality of the film especially as Vargas et al.'s films exhibit a granular surface as shown on their AFM measurements [v24].

Comparing the experimental with the theoretical results for pure metallic Pd, one can see that the experimental dielectric function is not perfectly reproduced by the calculation, although the main behaviour is correct. This discrepancy comes from the difficulty to theoretically reproduce the band diagram for different excited states as discussed in chapter 1. However, what is interesting here is to see how the dielectric function will be modified in the presence of H.

The experimental dielectric function determined by Vargas et al. for PdH is shown in figure 5.6.b. compared with that of pure Pd [v24]. The spectrum was measured by exposing a Pd film to $1atm$ of H_2. A clear red shift of the spectrum is seen in both the imaginary and real parts of the dielectric function. As stated above, experimentally determining the actual value of x in PdH_x is quite difficult. According to isotherm experimental analysis discussed above (cf figure 5.2) and band structure calculations undertaken by Silkin et al. [v25], the degree of hydrogenation of Pd at $1atm$ pressure of H_2 is estimated to have a stoichiometry of $PdH_{0.67}$, though, this value is expected to decrease to around $PdH_{0.3}$ for thin granular $10nm$ films or small nanoparticles (in the order of $10nm$ in diameter) [v26]–[v28].

Figure 5.6.c. shows Silkin et al.'s results for the dielectric function of Pd and PdH_x for different values of x using first principle methods. We can see that a red shift is indeed induced as the amount of H with the metal hydride is increased even though the spectra for $x = 0.5$ and $x = 0.67$ are very similar. The red shift effect of the hydrogenation on the dielectric function therefore explains the experimental red shift of the LSPR observed by Zoric et al. in figure 5.4 [v22] .

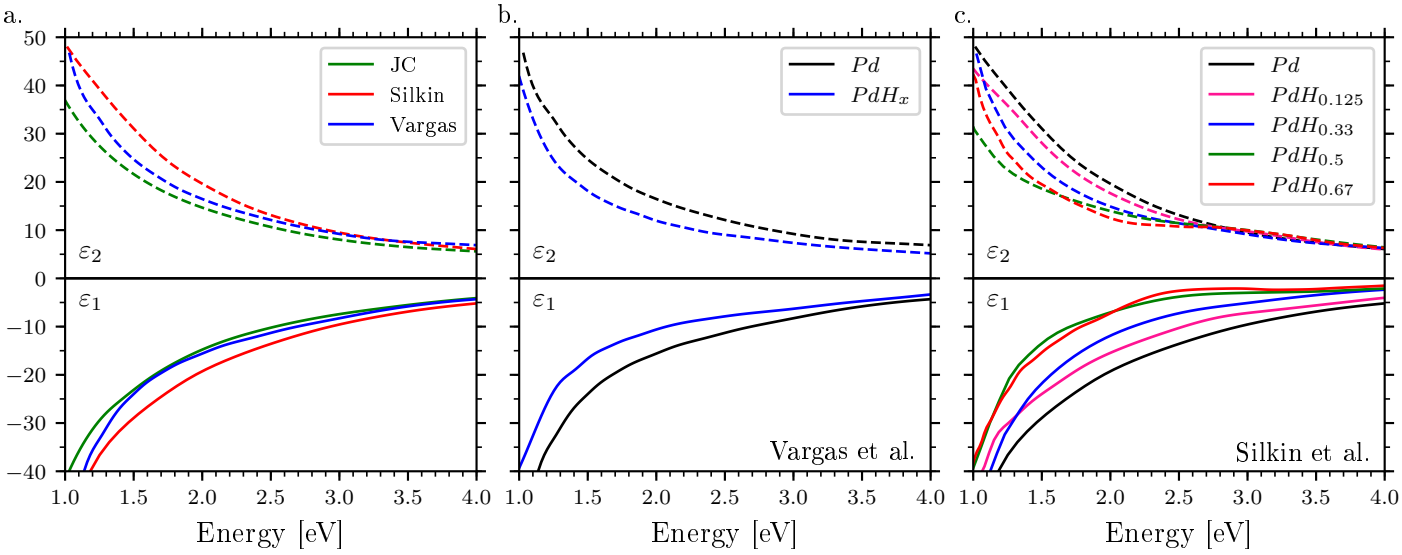

FIGURE 5.6: a. Experimental dielectric functions for bulk Pd by Johnson and Christy (green) [v20] and Vargas et al. (blue) [v24] and theoretical by Silkni et al. (red) [v25]. b. Experimental dielectric function for Pd and PdH_x at $1atm$ H_2 from Vargas et al. [v24]. c. Dielectric function determine by Silkin for Pd and PdH_x at different degrees of hydrogenation [v25].

5.1.2 Advances in LSPR-based systemes

In recent years, attempts have been made to develop plasmonic sensors, using LSPR excited by light in $metal - Pd$ or pure Pd nanoparticles based on the change in optical response of Pd when forming hydrides. However, we have seen in chapter 4 that Au by itself interacts very weakly with H_2 making it unusable for direct sensing. Hence why a lot of efforts have been proposed for hybrid systems using indirect sensing as a basic model [v29]. Indeed, these systems are based on the principal where the Au LSPR particles play the role of plasmonic transducers and the Pd nanoparticles, the molecular sensors. By interacting with H_2, the Pd nanoparticles placed in the vicinity to the transducer lead to a change in the refractive index in the vicinity of the Au leading to a shift in its LSPR spectrum.

In their review dealing with this topic, Wadell et al. have presented different indirected sensors based on Pd reactivity towards H_2 and Au [v16]. They demonstrate that the use of Au as a LSPR transducer coupled with Pd nanoparticles have better performance than Pd alone. The initial system, the same team has proposed in 2010, is to use Au nanodisks protected with a dielectric coating, in this case SiO_2 on which nanoparticles of Pd are deposited [v30]. Through the principle of enhanced field discussed in the first chapter (cf chapter 1), the formation of palladium hydride in the vicinity of the Au leads to a shift in its LSPR. They have exposed the sample to different pressures of pure H_2 starting at $10^{-3}bar$ up to atmospheric pressure. However, this experiment was not undertaking with a carrier gas should it be an inert gas such as Ar or N_2 or a reactive gas such as air.

The use of transducers have shown encouraging potential such as the work undertaken by Liu et al. where they have used lithographic techniques to fabricate a triangular prism pointing towards a nanodisk (Fig. 5.7). With this method, the high electric field generated by the LSPR of the gold prism is *focused* on the nanodisk of Pd. They have shown that thanks to this antenna enhanced system, the sensitivity of the scattering spectra is amplified [v31].

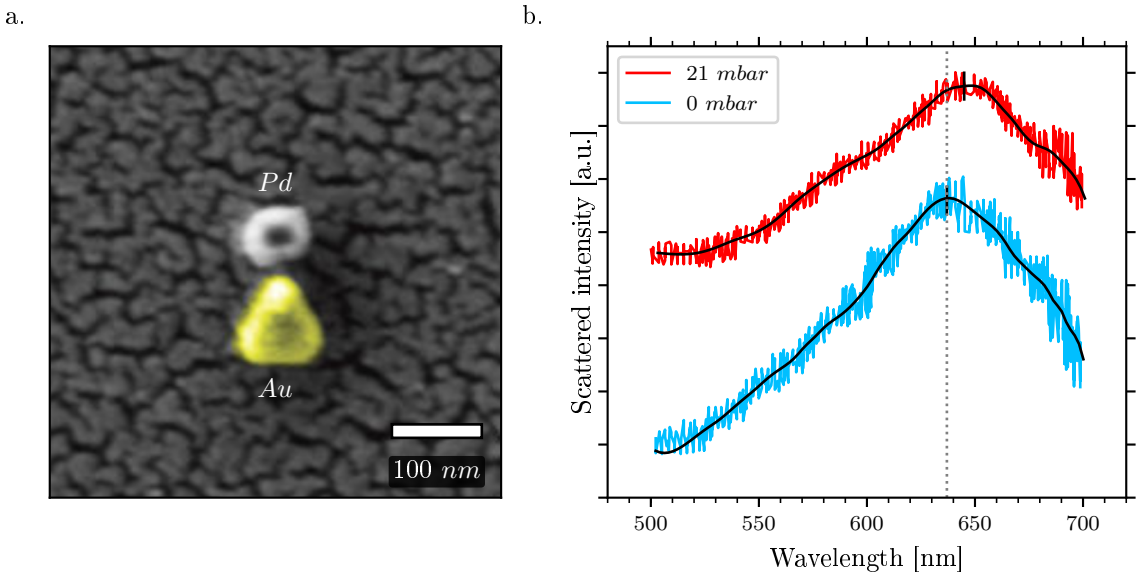

FIGURE 5.7: a. SEM image from ref [v31]. b. Scattering spectrum of system a. under vacuum and under 21*mbar* of H_2 from the same reference.

Many other systems have been studied. For instance Jiang et al. have used core shells Au/Pd nanorods of $115 \times 43nm$ and Au nanorods coated with small irregular nanospheres of Pd [v32]. In both systems they observed a red shift of the LSPR when exposed to H_2. In the first core-shell system, they observed a red shift of about 55*nm* and in the second system a red shift of 15*nm* when exposing the nanoparticles with 4% H_2 in N_2. The detection limit they have reached was about 0.2%.

Using AuPd nanodisk alloys of about 200*nm*, Wadell et al. were capable of reducing the effect on the hysterisis as they exposed their samples to vacuum and increasing pressures of H_2 from 1*mbar* to 1*bar* [v33]. In their experiments they recorded the change in extinction spectra as the pressure of H_2 increased for a sample made of pure Pd and a sample with 25% Au, their values are reproduced in figure 5.8.a. When the difference in extinction is normalised (Fig. 5.8.a.) it looks as if the hysteresis effect is reduced. Which one could interpret as a continuous transition between the $\alpha-$phase to the $\beta-$phase. However, when looking at the non-normalised values (Fig. 5.8.b.), it can be seen that the effect of the Au actually reduces the overall change in extinction. Meaning that even though the hysteresis is greatly reduced, this method also reduces the overall sensitivity of the system.

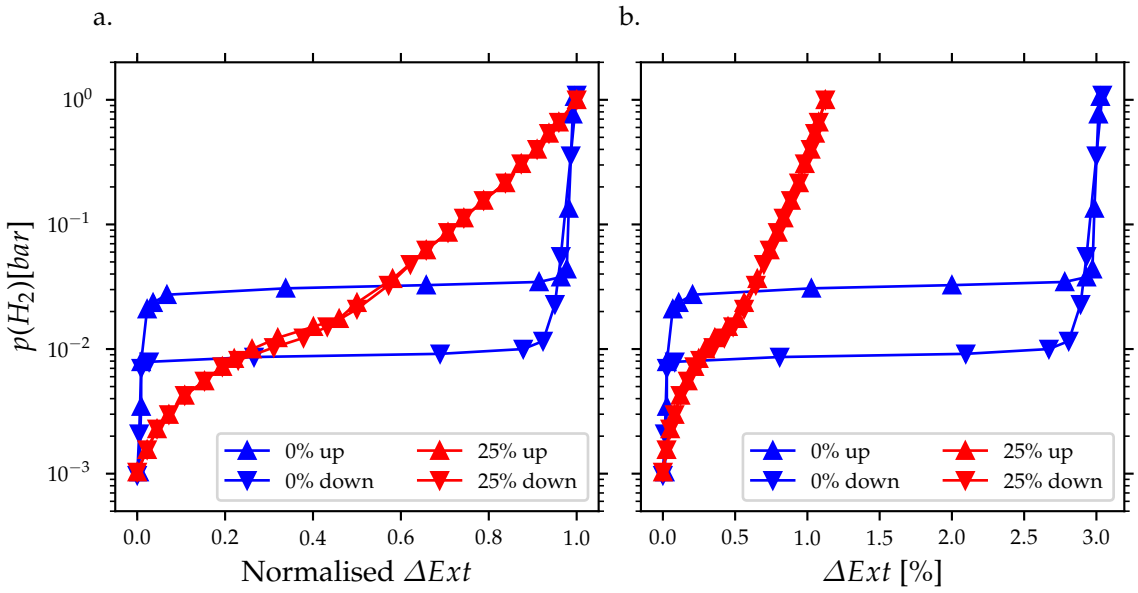

FIGURE 5.8: a. Phase diagram from ref. [v33] with pure palladium nanodisk and Pd with 25% Au normalised b. Same data as a. but with the change in extinction not normalised.

Yang et al. have studied what they call *hetero-oligomer* nanoparticle arrays [v34]. As far as the writer's opinion is concerned, the term is not appropriate to describe the system. Nevertheless, this does not diminish the elegance of the system they proposed. Using photo-lithography, they fabricated pyramidal hole arrays in Si in which different metals, specifically Au, Pd and Pt, are deposited at different angles. This led to the coverage of the facets within the holes with nanoparticles of different composition as shown in figure 5.9.

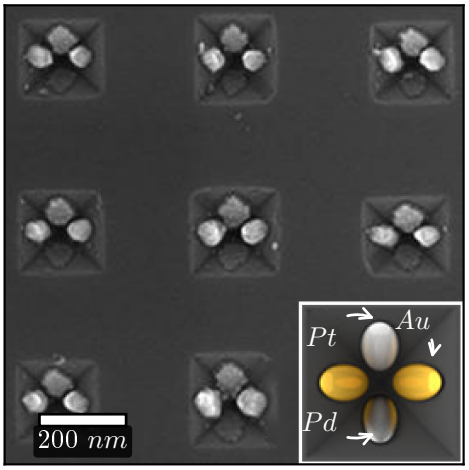

FIGURE 5.9: SEM image of the system from ref. [v34].

Through different combinations of metals, they were able to measure a shift in resonance of the LSPR spectrum as the sample was exposed to cycles of pure H_2 and N_2. With two Au nanoparticles facing each other and one Pd particle, they were able to observes shifts in wavelength of at least $0.7nm$ when exposing

the sample to 2% H_2 in N_2[1] .

One aspect that has not yet been addressed in this section is that due to the fact that all the previously mentioned examples use UV-Vis spectroscopy, should it be by measuring the transmission or extinction of the samples, they all are absolute measurements. Therefore, an inherent problem associated with that is the fact that the sample naturally drifts with time and cycles. This can be due to fluctuation in the environment such as changes in temperature, fluctuations of the lamp intensity or simply due to the fact the sample evolves with time.

Wadel et al. have approached this problem by taking advantage of the polarisation dependency of LSPR [v35]. The system they used where Au nanodisks of about 120nm in diameter next to which a Pd nanoparticle of 40nm is deposited. The trick for this method to work is for the sample to be global anisotropic, that is all the Pd nanoparticles have to be deposited on the same side for each Au nanodisk. The system is reproduced in figure 5.10.a. They achieved this by hole-mask colloidal lithography [v36]. In this system, the LSPR of the Au nanoparticle is only influenced by the Pd nanoparticle for one polarisation. This means that by measuring both polarisation at the same time, it is possible to isolate the change in the LSPR due to the formation of Pd hydride, from overall fluctuations of Au LSPR. This is shown in figure 5.10.b. As cycles of 4% H_2 in Ar and pure Ar are undertaken, the signal coming from the polarisation parallel to the nanoparticles exhibits a periodic shift of the LSPR peak, but also an overall drift of the signal. On the other hand the signal coming from the polarisation perpendicular only exhibits the overall drift and is not influenced by the cycles of H_2. Taking the difference between the two thus leads to the cancellation of the overall drift.

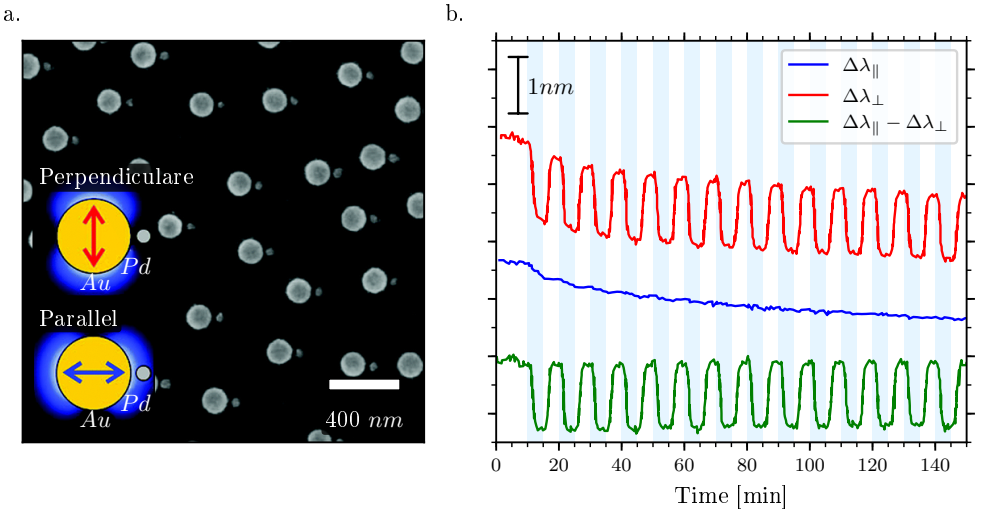

FIGURE 5.10: a. SEM image of Au and Pd nanodisk from ref. [v35]. b. Real time cycles between N_2 and H_2 in N_2 at 4% from same reference.

One of the main difficulties concerning the detection limit is, as we have discussed, the limitations in measuring small shifts in the LSPR accurately. Matuschek et al. have undertaken a different approach to conventional UV-Vis spectroscopy here by utilising circular dichroism [v37]. The objects in question they have studied are Au nanoparticle on which is deposited an helix shaped rode of Pd. They have accomplished this fabrication by evaporating Pd at a grazing angle whilst rotating the sample. When measuring the extinction spectrum of the sample as it is exposed to H_2 a small red shift and decrease in intensity is

[1]This value was read from their supplementary information, though since they did not let the sample recover completely, it is possible that the shift was actually larger.

observed (Fig. 5.11.a.). On the other hand when measuring the change in circular dichroism, they observed a flattening of the spectrum much more pronounced as shown in figure 5.11.a. Using this method they were able to detect down to 0.1% H_2 in N_2 as well as greatly increasing the signal to noise ratio.

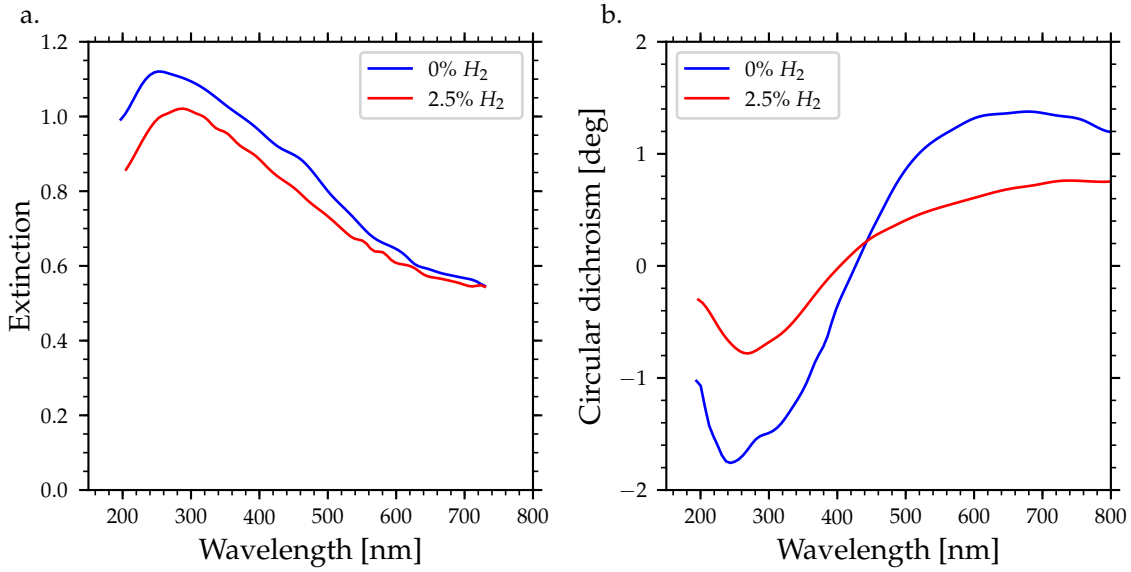

FIGURE 5.11: a. Extinction spectra for system of ref. [v37] with pure N_2 and 2.5% H_2 in N_2. b. Circular dichroism spectra with same gas exposure from the same reference.

All these example underline the fact the couple $Au - Pd$ is a promising combination for LSPR-based H_2. However, in terms of performance, that is the detection limit and response time as well as the application in real world conditions i.e. detection of H_2 in air, these methods tend to fall short due to the difficulty in detecting the small variation in the dielectric function of Pd induced by the formation of the $\alpha-$phase. Some results from the literature are presented in table 5.2 which lists the detection limit, the considered conditions and response time. It has to be noted though, as Hubert et al. put it "the response and recovery times of a sensor are difficult to measure experimentally without there being some component of the measured value that is due to the time taken for gas transport to the sensor face. This transport time varies from one experimental set up to another, which renders direct comparison of sensor response times difficult."

TABLE 5.2: Difference values from the literature showing the detection limit, carrier gas used and method of detection.

Reference	$\Delta\lambda$ [nm]	Entity measured	Detection limit	Carrier gas	Response time [s]
[v38]	1.5	Single partile scattering	15%	Ar	110
	5.5	Extinction	4%	Ar	50
[v39]	-	Reflectance intensity	0.50%	air	40
[v32]	8	Extinction	0.20%	N_2	-
[v34]	0.7	Transmission	2%	N_2	180
[v37]	-	Circular dichroism	0.1%	N_2	-
[v40]	10	Extinction	0.10%	N_2	-

5.1.3 Objective and methodology

The main limitation with the different techniques discussed so far is first of all that the fabrication of the sample usually tends towards using lithographic techniques which inherently adds complexity to the manufacturing process of the sample and limits the scalability of the methods (cf. chapter 3). Second of all, the use of a monochromator and the measurement of a spectral shift, leads to limitations due to the resolution of the apparatus as already discussed. Yet, sensitivity below 0.1% of H_2 in a carrier gas is desirable, for safety consideration but also for analysis of impurities in several industrial processes. In the present investigation, we address the sensitivity issue due to the resolution limitation of the monochromator, by using the transmittance anisotropy spectroscopy. We address the issue of sample fabrication by initially elaborating indirect Au/Pd samples as well as pure Pd films, grown by oblique angle deposition as discussed in chapter 3. This elaboration method provides anisotropic nanostructured films formed by nanoparticles a few nanometers large, where the LSPR excited by the impinging light strongly depends on the polarisation of light, leading to dichroic properties suitable for TAS. We demonstrate that the Au samples coated with a Pd layer indeed exhibit higher sensitivity than Au alone, to amounts of H_2 diluted in Ar as low as a few part per million (ppm) at room temperature. The results using only Pd samples give insight into using this metal for direct sensing. Indeed, these sample yield similar performance with a fast response in the range of seconds. Moreover, it also grants us the ability to determine the precise amount of small fractions of H_2 diluted in Pd, showing the quantitative potentiality of this technique. Preliminary experiments were also undertaken in dry and humid air (50% humidity) to determine perspectives in terms of selectivity and reactivity of the system in realistic conditions.

5.2 Initial investigation: Au/Pd indirect sensors

The initial investigation undertaken was to see whether evaporating a thin layer of Pd on a Au sample elaborated by oblique angle deposition (OAD) would increase the sample's sensitivity towards H_2. The expectation was that the thin layer would act as a molecular sensor and the Au as the LSPR transducer in order to increase the LSPR shift as it is exposed to H_2 (cf. section 1.4.1).

The Au was elaborated as discussed in chapter 3. The transmission anisotropy (TA) spectrum is plotted in figure 5.12.a. The spectrum exhibits the usual maximum and minimum due to its structural anisotropy. A $0.2nm$ Pd layer was then evaporated on the $1.6nm$ Au sample. The radius of a Pd atom is about $0.16nm$ which means that the quantity evaporated would have made a monoatomic thick layer. The TA spectrum was measured afterwards (shown in the same figure). The effect of the thin Pd layer was to induce a red shift of the minimum to the point where it cannot be seen in the working spectral range. Nonetheless, the new metal layer did not attenuate the anisotropic LSPR which still exhibits an amplitude nearly identical to Au prior the Pd deposition.

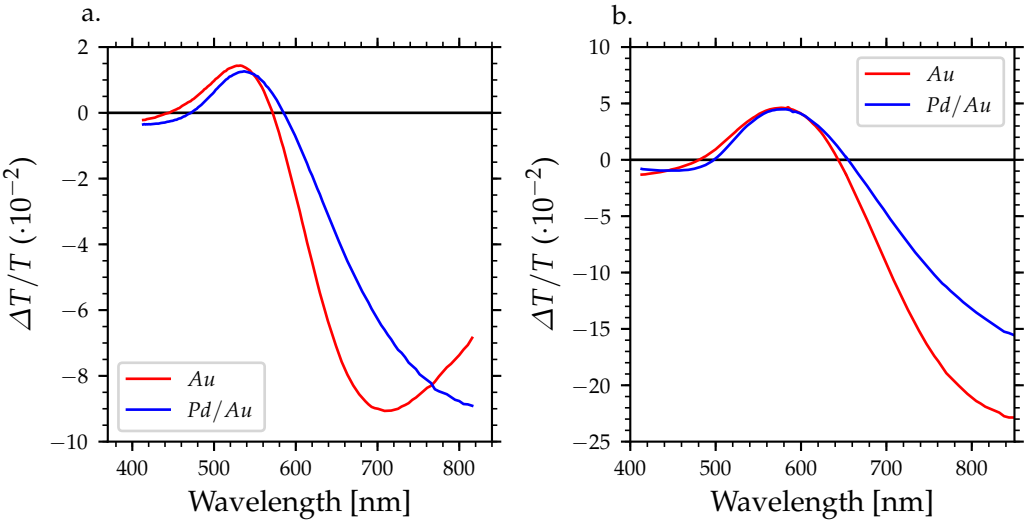

FIGURE 5.12: TA spectra of the Au before (red) and after (blue) evaporation of a Pd. a. corresponds to the first sample with a small amount ($\approx 0.2nm$) of evaporated Pd. b. correspond to the second sample with more Pd evaporated ($\approx 1nm$). Note the difference in vertical scale.

The sample was exposed to cycles of H_2 in Ar at decreasing partial pressures of H_2. The protocol was the same as in section 4.3. The aim was to determine whether the increase in TA, was reproduced with the Pd layer, if not enhanced. The results are plotted in figure 5.13 for partial pressures from 63% down to 0.004%. The experiment was done at room temperature ($\approx 22°C$), with a high gas flow to rapidly purge the gas cell. On each subgraphes, the signals for the pure Au sample are plotted in blue for comparison. In both cases, the signals were adjusted, by rotation of the polariser to have their baselines at 0, though, for visibility, the graph of Au was offset by 10. The signal was monitored at $670nm$. The initial cycle to H_2 at 63% in Ar (Fig. 5.13.a.) yields a rapid increase and decrease of the TA signal. This hence reproduces the behaviour observed with only Au, though the intensity is nearly doubled. Decreasing the amount of H_2 partial pressure led to a decrease in the amplitude of the signal increase, though at 1% (Fig. 5.13.d.) unlike for Au, the Pd/Au still exhibited an optical response to the analyte. The experiment was continued down to 0.004% which is equivalent to $40ppm$ of H_2 in Ar. Through each step, in spite of the noise, the increase in TA may still be observed, though even at 0.015%, we may say that we have reached the limit of detection as, at 0.004%, the signal is barely higher than the noise, though still distinguishable.

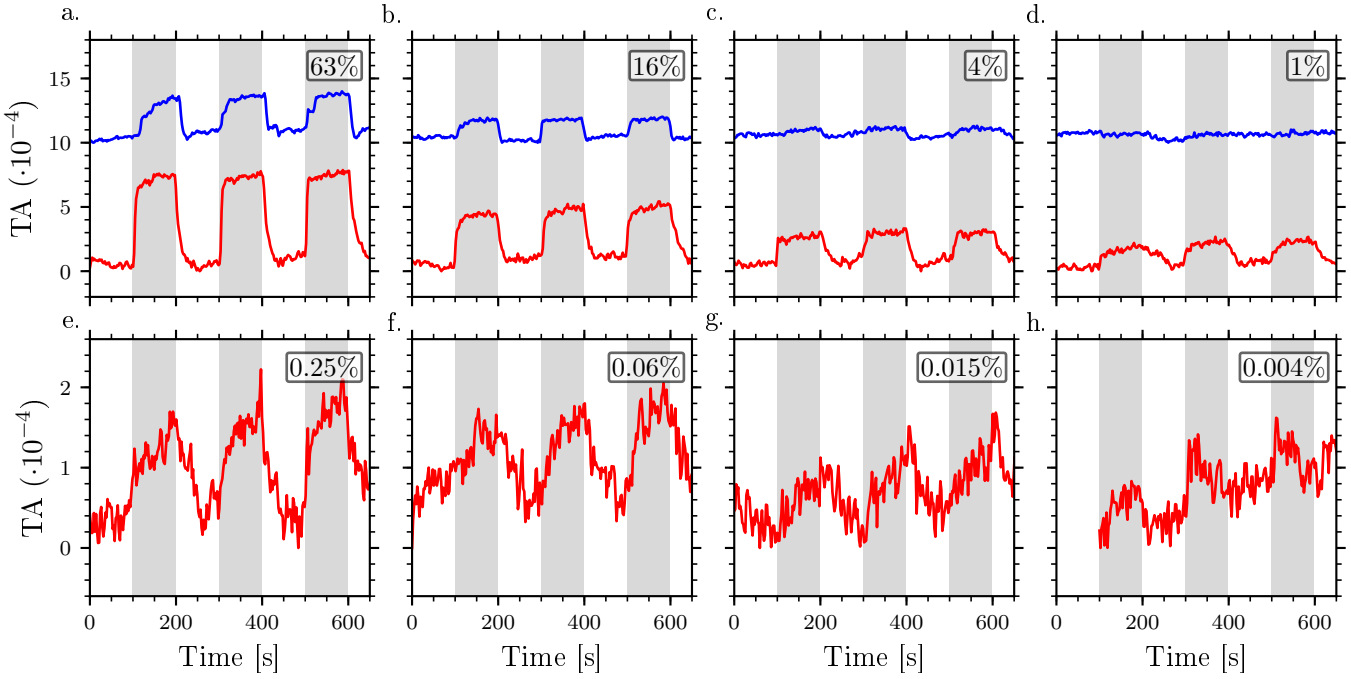

FIGURE 5.13: Real time monitoring of the TA signal ΔS at whilst cycling between different concentration of H_2 in Ar. In white is the Ar purge and in grey is the H_2/Ar exposure at the respective concentrations. In red is the Pd/Au sample discussed in figure 5.12.a. whilst in blue is the gold sample discussed in the previous chapter (cf Fig. 4.10) The red spectrum was monitored at 670nm whilst the blue was monitored at 613nm corresponding to where the slope was steepest.

This initial experiment demonstrates the enhanced sensing capability of the system when Pd is used as a molecular sensor. The change in signal is clearly improved compared to that of bare Au , with much lower partial pressures of H_2 being detected. This is explained by the formation of Pd hydride which has a different dielectric function than pure Pd (cf page 146). Hence, the dielectric surrounding of the Au nanoparticles is modified and leads to a shift of the LSPR.

However, the question that one may ask is whether increasing the amount of Pd would improve the signal response of the LSPR system. For this, another sample was prepared with a 1nm mass thickness Pd layer evaporated at the same grazing angle as for the initial 3.2nm mass thickness Au layer. The TA spectra of the sample before and after Pd evaporation are shown in figure 5.12.b. The initial Au spectrum only exhibits a maximum around 580nm, whilst the minimum is shifted to the near IR. After Pd evaporation, the maximum is barely shifted whilst the slope after 600nm is reduced indicating that the out of range minimum has red shifted. This is the same behaviour as for the previous sample.

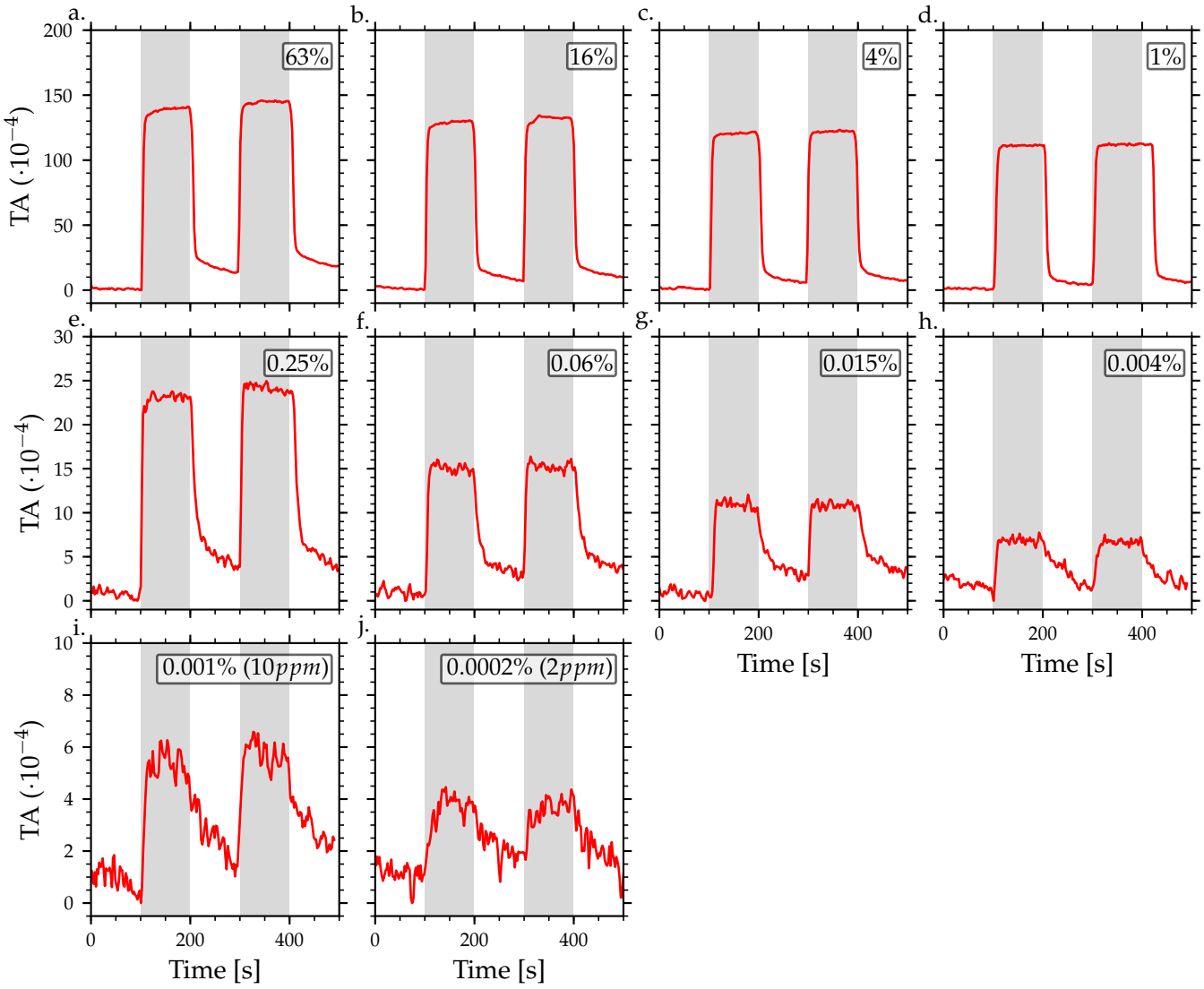

FIGURE 5.14: Real time monitoring of the TA signal at 775*nm* whilst cycling between Ar and H_2 in Ar at different partial pressures from 100% H_2 to 0.0002% H_2 in Ar. In white is the Ar purge and in grey is the H_2/Ar exposure at the respective concentrations. The wavelength was chosen as to have the highest change in signal from the Pd/Ar spectrum of figure 5.12.b. The graphs were adjusted to have the baseline close to zero. Note the difference in the vertical scale.

The anisotropy being still significant, the same gas cycle experiment was undertaken by exposing the sample to H_2 in Ar at decreasing partial pressures from 63% down to 0.0002%, equivalent to $2ppm$. The LSPR was monitored at $775nm$ and the results are plotted in figure 5.14. Throughout the experiment the TA signal is seen to increase rather rapidly when exposed to the H_2 mixture and decrease back to near its initial state when purged with pure Ar. However, the intensity of the TA shift is not the same throughout the gas range just as seen before. From 63% to 1%, the TA shift is rather large, and only decreases a small amount. Indeed at the larger H_2 partial pressure the TA signal is around 140 whilst at 1% it reaches around 110. Below this threshold, the signal intensity drops considerably as it barely reaches 25 when exposed to 0.25%. Lowering the partial pressure induces smaller and smaller intensities of the TA signal and at 0.0002% it reaches about 4. Although this is about 35 times smaller than the initial response at 63%, the effect of the H_2 is still measurable underlining the sensitivity of the measurement.

From these experiments it is clear that the Pd has increased the optical response of the sample towards H_2 exposure. To understand the origin of the sudden decrease in TA when the sample was exposed at 0.25% in figure 5.14, let's plot the amplitude of the cycles against the partial pressure of H_2. This is shown in figure 5.15, where the change in signal ΔS from both 5.13 and 5.14 are plotted against the partial pressure in log scale. Let's first focus on figure 5.15.a. which shows the raw data of both samples. At low partial pressures, below 1%, the signal only increase a little from the lowest pressure to 0.25%. However, at 1% and beyond, there is a considerable jump in signal intensity as observed in the real time experiments. Cycles at higher pressures only increase the signal a small amount. The shape of this data clearly reproduce the isotherm of palladium hydride as previously discussed in the introduction of this chapter. Indeed, if we compare the obtained data with that of figure 5.5 obtained by Bardhan et al., we see a resemblance in the jump around 1% H_2. We may therefore deduce that the change in hydride phase is responsible for this difference in optical response. The interpretation of the data is therefore that at low partial pressures of H_2 only the α-phase is formed with a small amount of diluted H. At higher partial pressures, it is the $\beta-$phase that is obtained within a much higher density in absorbed H. In between would be the hybrid $\alpha + \beta$ phase which is difficult to measure as it occurs at a narrow interval of partial pressures, around 1%. The difference in hydrogen density within the metal hydride has therefore a direct effect on the dielectric function of Pd and thus on the LSPR response of the Au sample. Yet this phenomena is not observed for the first sample which only shows a steady increase in ΔS as the H_2 pressure is increased. It would indeed seem that only the $\alpha-$phase is obtained. This is more clearly shown in figure 5.15.b. which shows a zoomed in view of figure 5.15.a. at low ΔS and figure 5.15.c. which shows the same data but with ΔS normalised to 1. In the case of the thin Pd/Au sample, the transition when increasing the partial pressure of H_2 is much more continuous than the other sample. A possible explanation for this behaviour is that actual thin Pd layer does not behave as bulk. Indeed, for the first sample only a monolayer was deposited which means that H cannot be absorbed but only adsorbed. In this particular case, one may not consider the phase diagram discussed in figure 5.2.a. as it is not applicable. Alternately, the Au nanoparticles may not be completely recovered by the Pd, in which case what is seen may be the interaction of the H_2 with both the surface Pd and Au atoms.

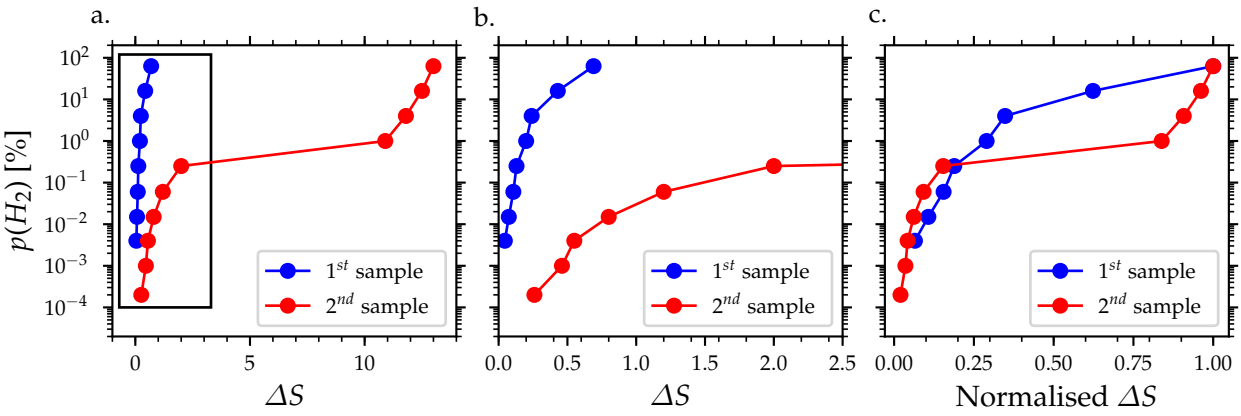

FIGURE 5.15: Graphs plotting the amplitude of the shift ΔS from figure 5.13 (1^{st} sample) and 5.14 (2^{nd} sample) against the partial pressure in log scale. a. shows the raw results whilst b. shows a zoomed in section at low ΔS. c. shows the same data normalised to the maximum ΔS. The data points are joined with a straight line for visibility but it does not mean the data can be interpolated.

The use of Pd has clearly enhanced the H_2 sensing capabilities of the samples. However, one can wonder whether the Au is strictly necessary. Indeed, Pd does exhibit LSPR, which thus could be used to measure its change in optical response as it is exposed to H_2. This has already been investigated in the litterature such as in ref. [v22] with isotropic nanodisk. Though using anisotropy, the sensitivity may be increased as Pd tends to have a very broad LSPR spectrum. This enables the use of direct sensing which simplifies the overall system as only one step is required in the sample fabrication. In the next section, we will thoroughly discuss the use of such system, that is Pd nanostructures for enhanced H_2 sensing, and discuss in more details the issues of thermodynamics and kinetics related to the formation of Pd hydrides.

5.3 Anisotropic Pd nanostructured film: Sample morphology and optical properties

The elaboration of the anisotropic Pd films was achieved by oblique angle deposition. More information on the fabrication process and characterisation is given in chapter 3. Nonetheless, a typical Pd sample is reproduced in figure 5.16. The figure shows a SEM image of the sample which exhibits a porous nanostructured thin Pd film made up of lines of islands, separated by trenches. These islands appear to be formed by agglomerated nanoparticles of size around $10nm$, separated by narrow gaps, and they are in majority oriented close to the direction normal to the evaporation orientation, indicated by the arrow. The 2D finite Fourier transform (FFT) image shown on the upper right hand corner of the figure confirms that the nanostructure exhibits a structural anisotropy.

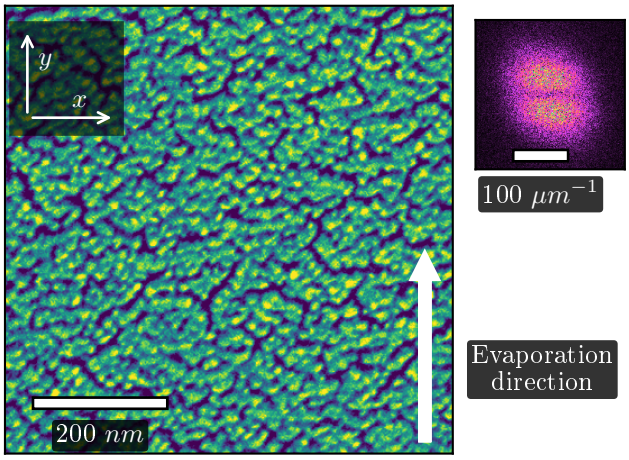

FIGURE 5.16: SEM image of a Pd nanostructured sample evaporated by oblique angle deposition on glass. The arrow shows the direction of evaporation and the upper right hand figure shows the FFT of the SEM image.

The optical characterisation of the sample was first done using UV-Vis spectroscopy. Both x and y polarisations in relation to the sample's direction of evaporation were recorded and are plotted on figure 5.17 (dashed lines). The absorbance is given in $-log(T)$, where T is the transmission of the sample. The spectra shows a clear dichroism. The spectrum measured under parallel (y) polarisation displays a broad resonance centred around $500nm$, whereas the spectrum for perpendicular (x) polarisation does not exhibit such a maximum. One must also note the small amplitude of the spectra as indicated by the ordinate. This shows that although a dichroism is indeed present within this sample, it remains small compared to other examples we have seen in the previous chapter.

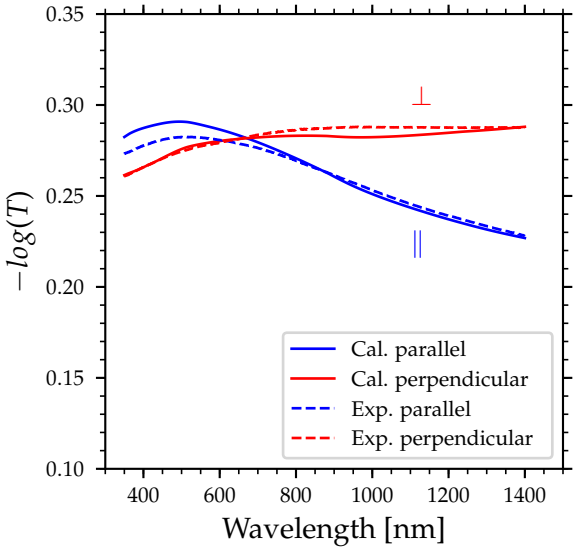

FIGURE 5.17: UV-Vis-NIR transmission spectra using polarised light with orthogonal polarisation parallel and perpendicular to the direction of evaporation. The spectra is plotted in $-log(T)$.

It is possible to model the optical response of this nanostructure by using Aspnes effective medium

theory [v41]. More details is given in chapter 3. The Pd nanostructure was models by considering a distribution of metal slabs and considering the dielectric function provided by Johnson and Christy The results reproduce the experimental results well as shown by the solid lines in figure 5.17.

This dichroism thus enables the use of TAS to measure the transmission anisotropy of the sample. The transmission anisotropy (TA) was measured after placing the sample in a gas cell and purging with Ar (Fig. 5.18.a.). The spectrum confirms the optical anisotropy shown in figure 5.17, for absorbance measurements in both polarisations. The TA goes through zero as the two spectra of figure 5.17 cross each other. When the sample is exposed to pure H_2 at atmospheric pressure, the TA spectrum also drawn in figure 5.18.a. is strongly modified and its intensity is reduced. After purging the reactor with Ar, the signal reverts back to its initial state, hence showing the reversibility of the phenomenon.

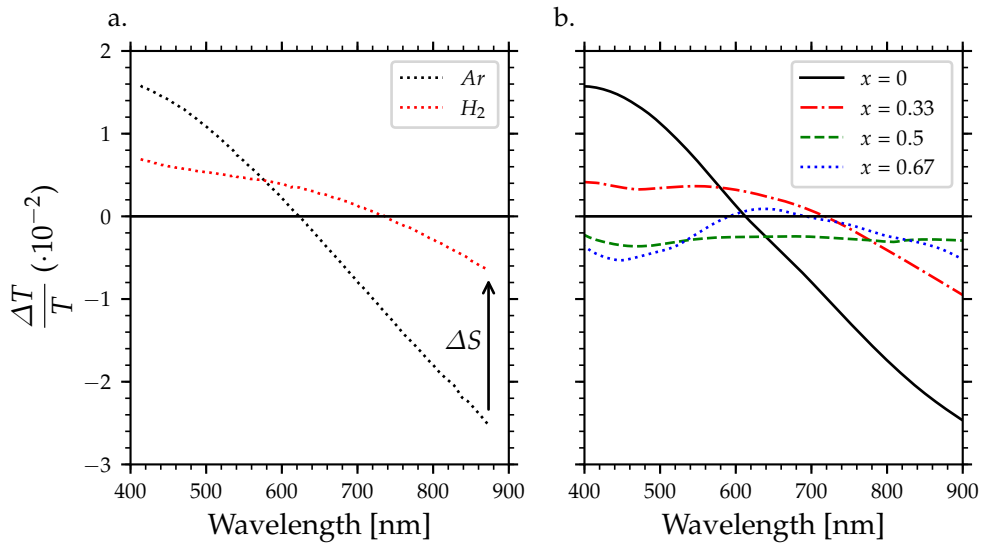

FIGURE 5.18: a. Experimental transmission anisotropy of the Pd nanostructure under pure Ar (black) and under H_2 (red). b. Calculation of the experimental spectra using Aspness effective medium theory with Silkin et al.'s dielectric functions for PdH_x with x = 0.33, 0.5 and 0.67 [v25]. For more information on the calculation cf chapter 3.

The effect of H_2 exposure can be ascribed to the absorption of hydrogen by the Pd nanoparticles, leading to the formation of the $\beta-$phase and, consequently, to a strong change in its dielectric function. This is confirmed when calculating the theoretical TA using the theoretical dielectric function determined by Silkin et al. for pure Pd and hydrogenated PdH_x with different values of x (Fig. 5.6.c.). The important aspect here is to show that the change in the dielectric function of the nanostructured Pd film, due to formation of hydride, does explain the experimental observation.

The TA spectrum measured under Ar (Fig. 5.18.a) is reproduced with a Pd anisotropic nanostructured film and Silkin et al.'s dielectric functions following analogous steps as shown in the chapter 3. The results given in figure 5.18.b are in good agreement with the experimental TA of figure 5.18.a. The obtained parameters, that is the distribution factor f and the thickness e, describing the nanostructured anisotropic film are very similar, although not identical, to those previously obtained for the fit shown in the UV-Vis-NIR spectra (Fig. 5.17). Indeed the distribution vary slightly but are very comparable as shown in figure 5.19. and the mass thickness determined from that fit are $e_{Johnson} = 1.4nm$ and $e_{Slikin} = 1.3nm$. This difference in calculated thickness comes from the difference in the theoretical and experimental dielectric functions. In the case of the UV-Vis-NIR calculation, it is correct to use the experimental dielectric function from Johnson and Christy as it best describes the optical properties of metallic Pd. However, the use of Silkin et al.'s

theoretical dielectric function is required to fit the TA spectra as they have provided dielectric functions for Pd and PdH_x with different values of x [v25]. This is indeed necessary if one wants to compare the effect of hydrogenation on the TA spectra.

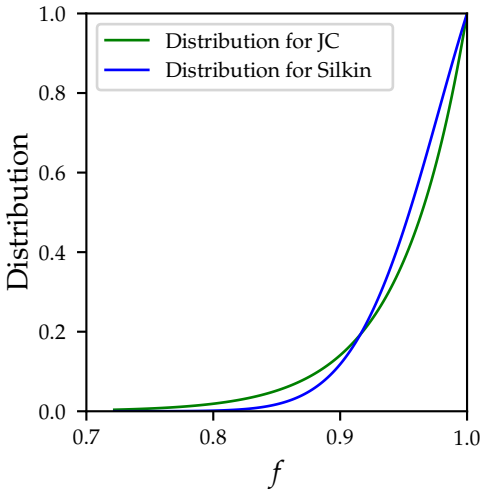

FIGURE 5.19: Graph plotting the distribution in size used to fit the UV-Vis spectra and TA spectra using the two dielectric functions from Johnson and Christy [v20] and Silkin et al. [v25].

Keeping the parameters determined with the theoretical dielectric function on the experimental TA spectrum measured in Ar and replacing the dielectric function of Pd with those of $PdH_{0.33}$, $PdH_{0.5}$ and $PdH_{0.67}$ leads to a strong decrease of the TA, as shown in figure 5.18.b. A very good agreement is found between the experimental TA spectrum under H_2 and the calculation for $PdH_{0.33}$, though the expected Pd hydride should be closer to $PdH_{0.5}$ or $PdH_{0.67}$ for bulk. This result is likely due to the fact that the actual H concentration is smaller than expected for bulk. It has been shown that H concentration within Pd, at a given H_2 pressure, is smaller for nanoparticles than for bulk. Indeed Bugaev et al. have demonstrated a method for determining the concentration of H in PdH by using quantitative XANES (X-ray absorption near edge structure) fitting [v27]. They have demonstrated that for the case of $10nm$ in effective diameter Pd nanoparticles, the $\beta-$phase is reached at $PdH_{0.35}$. This has also been demonstrated by Bardhan et al. whom have demonstrated the size dependance trends in the thermodynamics from measured absorption and desorption isotherms on nanocube ensembles [v23]. It is also possible that the difficulty in accurately determining the dielectric functions of crystals with *ab-initio* methods may induce further error in the fit.

Moreover, it can be wondered whether the known expansion of PdH_x with respect to pure Pd could explain this change of the TA. Indeed, the absorption of hydrogen within the Pd leads to a lattice expansion. This has been applied for H_2 sensors as the expansion of the metal induces cracks which in turn change the conductivity of palladium nanostructures. This method has been investigated by Zeng et al. whom have produced Pd nanowires of about $10nm$ in diameter. They have measured the change in resistance of the structured film and were able to measure H_2 at about 0.01% in N_2 [v42]. Determining the expansion is not possible with the current set up presented in this work. Nevertheless, Johnson and Christy have reported a theoretical expansion of 3.2% for $PdH_{0.75}$, which according to the same authors is in agreement with experimental results which reported between 3.3% and 3.5% [v20].

To determine the effect of the expansion on the TA spectra, the results from the calculations presented in figure 5.18.b. were modified by adding a 3.4% increase in thickness and in width of the slabs. The expansion coefficient is indeed proportional to the degree of hydrogenation of the Pd bulk. However, for

the sake of argument, a 3.4% expansion is used for PdH_x with $x = 0.3$, 0.5 and 0.7. For more accurate result the expansion would decrease with x, though these results do give an indication on whether the expansion of the Pd crystal is negligible in terms of its effect on the optical response of the Pd nanostructure, compared to the change in the dielectric function. (For more details on the calculations cf. chapter 3.) The results are plotted in figure 5.20. for three values of x in PdH_x. Each figure has the experimental spectrum of the sample under Ar and H_2 as well as the fit using the pure Pd dielectric function from Silkin et al. for reference. For each figure the calculation for PdH_x (solid line) and PdH_x with a 3.4% expansion (dashed line) are plotted. Overall the effect of the expansion is very small. Although, it induces an increase in the TA signal which, compared to the effect of the change in dielectric function of the metal hydride, seams negligible. It can thus be approximated that it has little effect on the LSPR of the Pd and thus is not considered in the rest of this analysis.

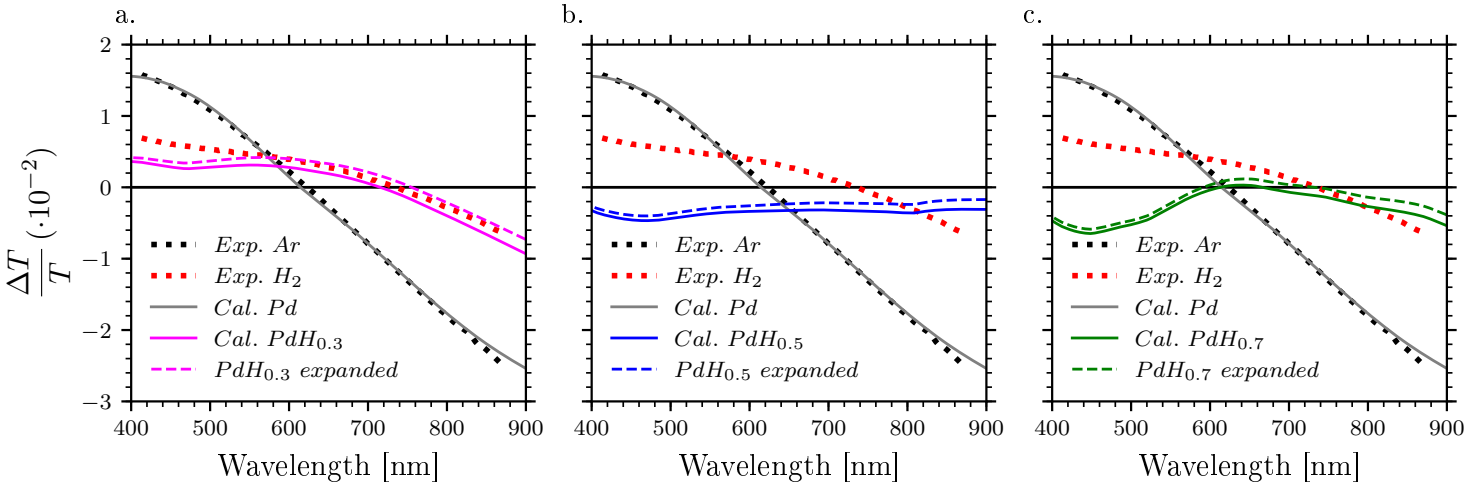

FIGURE 5.20: Spectra showing the effect of a 3.4% expansion on the calculated TA spectra. a. $PdH_{0.3}$, b. $PdH_{0.5}$ and c. $PdH_{0.7}$. Every spectra also shows the experimental spectra under Ar and H_2 as well as the fit for the pure Pd spectrum.

In conclusion, the above comparison does show that the observed change of the TA signal is indeed by the formation of Pd hydride, which modifies and reduces the LSPR of the Pd. This illustrates that the present nanostructured porous films are quite reactive to H_2 absorption and can be used for sensing H_2. Determining the detection limit of such a sensor is the topic of the next section where the Pd is exposed to low partial pressures of H_2 whilst the TA is followed in real time.

5.4 Quantitative detection of small amounts of H_2 in Ar: thermodynamic limitations

5.4.1 Ar and H_2 sensitivity of real time measurements

After purging of the cell with pure Ar for 24 hours in order to eliminate any possible contamination, the samples are exposed alternately to pure Ar and to various H_2/Ar mixtures at atmospheric pressure. For this purpose, different concentrations of H_2 in Ar are prepared in a dedicated bottle by the following procedure. The mixture bottle is pumped whilst heated to $3 \cdot 10^{-3} mbar$ for 24 hours. It is then filled with $2.5 bar$ of H_2 and completed to $4 bar$ with Ar. The bottle is then emptied to atmospheric pressure and refilled

to 4*bar* with Ar. By using this procedure several times, accurate proportions of H_2 in Ar down to a few ppm can be obtained. The experiments in the gas flow reactor are undertaken at atmospheric pressures and at 22°C, and the gas flows are fixed to 1000*sccm*. These large flows are used to rapidly switch from pure Ar to the chosen concentration, and vice-versa.

The real-time experiments consists in measuring the change of the TA signal, ΔS, as a function of time, at a given wavelength, during exposure cycles to pure Ar and H_2 in Ar with decreasing concentrations. The chosen working wavelength is where the largest change in TA within the investigated wavelength range is observed, therefore $\lambda = 885nm$ (see Fig. 5.18.a). An optical offset is added in order to have a TA value close to zero under Ar to increase the sensitivity of the measurements. The experiments are performed with reducing partial pressures from $1bar$ to $2 \cdot 10^{-6} bar$ of H_2 in Ar at atmospheric pressure, which corresponds to H_2 concentration in Ar varying from 100% to 0.0002% ($2ppm$). The results are drawn in figure 5.21.

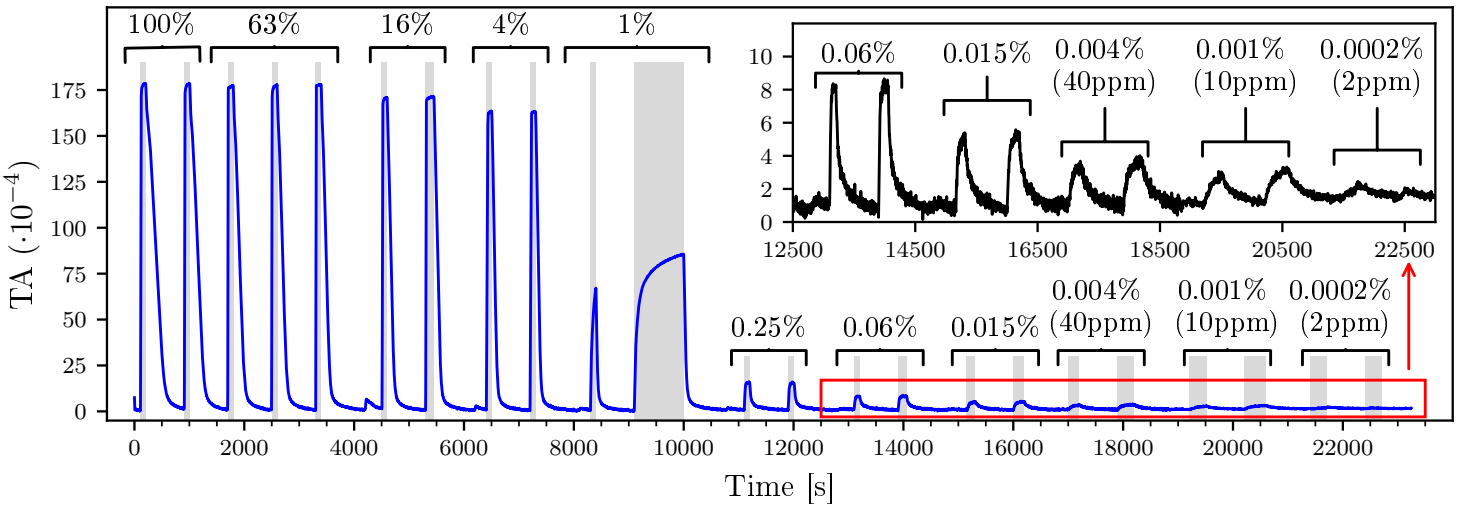

FIGURE 5.21: Graph showing the TA change of the Pd sample as cycles of Ar and H_2 in Ar at different partial pressures are undertaken from 100% H_2 to about $2ppm$ of H_2 in Ar. The insert shows a zoom of from 0.06% to $2ppm$.

When the gas is switched from Ar to H_2 in Ar, the shift ΔS is almost immediate and positive, as expected from figure 5.18.a. When exposed back to Ar, the signal reverts quickly, and eventually the sample regenerates to its initial state. The cycles show that the sample follows three different behaviours. At high concentrations of H_2 in Ar, between 100% to 4%, ΔS is large and quickly saturates within a few seconds or less, as shown in figure 5.25.a. ; its intensity is almost unchanged throughout the range. At low concentrations, 0.2% and below, the signal is about 10 to 100 times smaller. The intensity depends on the concentration of H_2, but saturation is also rather quickly reached. Figure 5.21 also shows that the detection limit in the present case is about 2 to $10ppm$. At 1% though, the signal behaves differently; the increase is also fast, but saturation is not reached, even after 1000*s* under H_2 in Ar. The intensity is also intermediate between the high and the low pressure regimes. These three behaviours correspond to the different Pd hydride phases. The region on the left hand side of figure 5.21 corresponding to H_2 percentages between 100% to 4% (1 to $0.04bar$) correlates to the formation of the dense $\beta-$phase. The region on the right hand side, corresponding to percentages from 0.2% ($0.002bar$) and lower, correlates to the formation of the dilute $\alpha-$phase. The experimental point at 1% corresponds to the co-existence of both phases, where the $\beta-$phase is progressively formed. This explains the slow saturation as only a small amount of H_2 would yield a high shift in the TA signal. The mechanism proposed is the nucleation of the $\beta-$phase which precipitates and

grows in the $\alpha-$phase. This leads to a transition in the phase diagram leading to the observed plateau utile the complete $\beta-$phase is reached [v44].

5.4.2 Quantitative reading of PdH degree of hydrogenation

The H_2 partial pressures as a function of the maximum signal change ΔS reached for every pressure is displayed in figure 5.22.a. It shows a shape perfectly analogous to the phase diagram in figure 5.2. The phase diagram for bulk Pd determined at 20°C by Manchester et al. [v19] is also drawn as a function of the H/Pd ratio x in the hydride (upper abscissa) on figure 5.22.a. Although Pd bulk and nanoparticles do not absorb the same amount of hydrogen, the scale of this latter axis has been chosen so the phase diagram obtained in our experiment is superimposed with the bulk phase diagram.

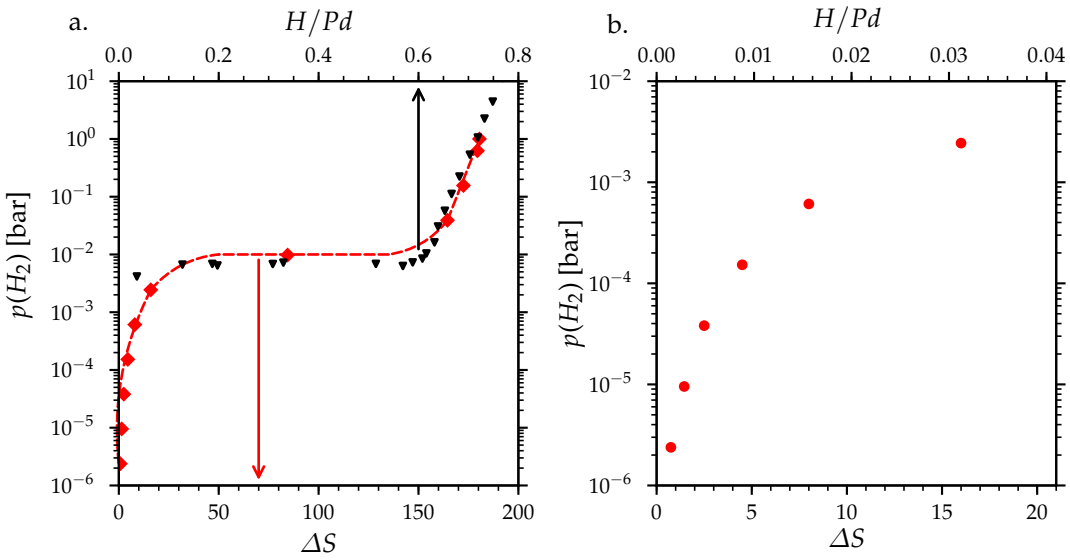

FIGURE 5.22: a. Graph plotting the change in TA (ΔS) against the partial pressure of H_2 in log scale (red dots) as well as the phase diagram of bulk Pd exposed to different pressures of H_2 at 20°C (black dots) from ref. [v19]. b. Zoom of (a.) at low H_2 pressures with bottom x axis showing the ΔS and the upper x axis showing the H/Pd ratio.

This demonstrates that the observed change in the TA signal can provide a measurement of the H concentration in the Pd film after calibration, although it cannot be inferred from this superposition that the H/Pd ratio x indicated on the upper abscissa does exactly correspond to our experimental results.

In order to quantitatively relate ΔS to the H/Pd ratio x for low pressures of H_2, one must consider the dielectric function of dilute PdH_x compounds calculated by Silkin et al. Although they did not present results for values smaller than $x = 0.125$, their dielectric functions for Pd and for $PdH_{0.125}$ are very close, hence it is reasonable to consider intermediate functions obtained by interpolation for $x \leqslant 0.125$. One can consider the following intermediate dielectric function for x between 0 and 0.125:

$$\varepsilon_{PdH_x}(\omega) = \varepsilon_{Pd}(\omega) + \frac{x}{0.125}\left[\varepsilon_{PdH_{0.125}}(\omega) - \varepsilon_{Pd}(\omega)\right] \tag{5.1}$$

The dielectric functions from Silkin et al. for Pd, and $PdH_{0.125}$ as well as the calculated $PdH_{0.04}$ are displayed in figure 5.23.a. [v45]. One can see that the dielectric function for $PdH_{0.04}$ is close to that of Pd

though with a small red shift. The effect on the TA spectrum of a small value of x, e.g. equal to 0.04 which is two times larger than the density limit of the $\alpha-$phase, is shown as an illustration in figure 5.23.b.

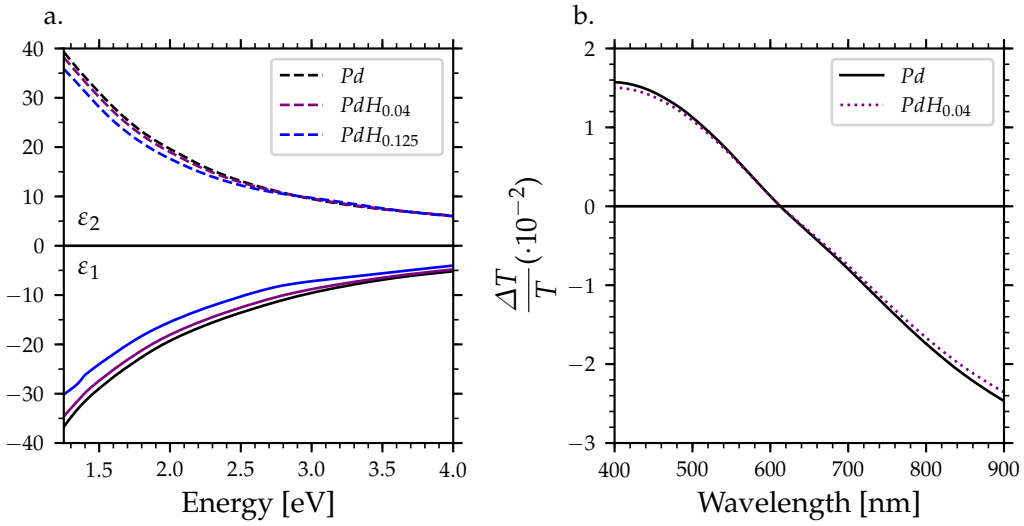

FIGURE 5.23: a. Dielectric function of Pd and PdH_x with $x = 0.125$ taken from ref. [v25] as well as the dielectric function determined for $PdH_{0.04}$ suing eq. 5.1. b. Calculated TA spectra using the pure Pd dielectric function from ref. [v25]. and the spectra determined for $PdH_{0.04}$.

This illustrates that the change of transmission signal for small amount of H in Pd is indeed weak, and that the present differential method based on the TAS is necessary to accurately measure such minute changes. By using the above procedure, one can determine the values of x from the measurement of ΔS for every H_2 partial pressures in the $\alpha-$phase which are listed in table 5.3.

TABLE 5.3: Values of ΔS an the H/Pd ratio at the corresponding partial pressures determined.

$p(H_2)$ [%]	ΔS	α
0.25	15.5	0.031
0.06	8.0	0.016
0.015	4.5	0.0087
0.004	2.5	0.0049
0.001	1.5	0.0028

The so-obtained values are drawn as abscissa in the upper part of figure 5.22.b. for pressures lower than $2 \cdot 10^{-3} bar$ (0.2%). For $p(H_2) = 6 \cdot 10^{-4} bar$, the H/Pd ratio obtained is 0.016. This almost corresponds to the complete $\alpha-$phase. For the higher pressure of $p(H_2) = 2 \cdot 10^{-3} bar$, the H/Pd ratio is 0.031. In this case, the $\alpha-$phase has saturated and the $\beta-$phase has started to form. From that point on, this procedure for determining x is thus no longer valid as the change of the dielectric function must now account for the development of the $\beta-$phase.

The partial pressure of H_2 against the so-determined H/Pd ratio x, in the $\alpha-$phase, is drawn in $log-log$ diagram in figure 5.24. It shows a linear relationship, with a slope equal to 2.36 up to $x = 0.016$. The deviation from the linear dependence, which begins from the value of $x = 0.031$, confirms that the $\beta-$phase is starting to form. The point determined by the same procedure, for $p(H_2) = 10^{-2} bar$, and which gives $x > 0.15$, is clearly out of the linear evolution, which was indeed expected as, for this pressure, the two phases are coexisting.

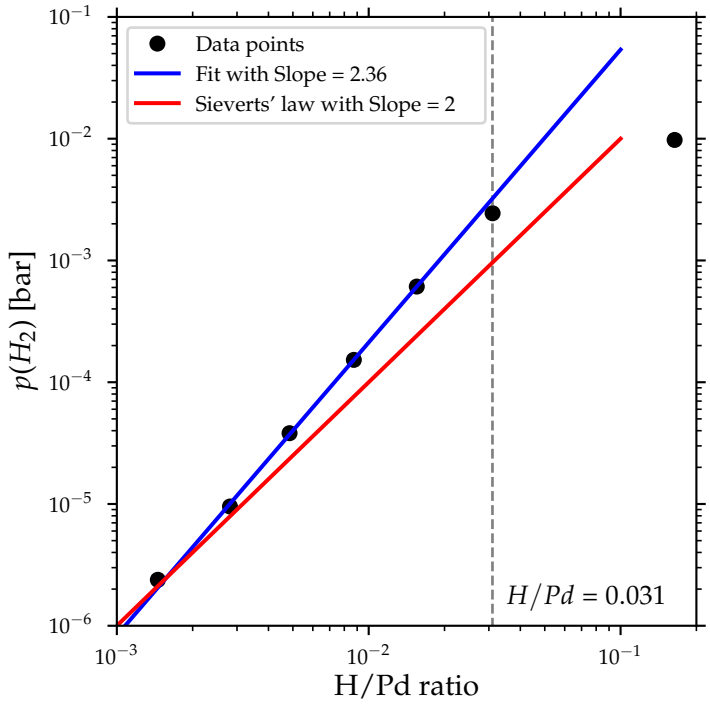

FIGURE 5.24: Log log plot of the experimentally determined H/Pd ratio against the partial pressure of H_2. (blue) fit of the first six experimental data point, (red) expected relation for Sieverts' law.

Coming back to the initial evolution, Sieverts' law states that "the solubility of a diatomic gas in a metal is proportional to the square root of its partial pressure in the gas in equilibrium with the metal" [v46]. This law is followed for diatomic molecules such as O_2, N_2 but also H_2[v19]. Therefore, the H/Pd ratio x should be proportional to the square root of the pressure, i.e. the points should be aligned with a slope of 2 (slope = $1/0.5$), which is drawn in figure 5.24 (red). The measured slope is thus in variance with the Sieverts' law. A detailed analysis of this process is out of the scope of the present work. Nevertheless, this deviation is most likely related to the complex dissociation process of H_2 molecules on the surface of the Pd nanoparticles. Indeed, whilst Sieverts' law corresponds to a second order, Langmuir-type, dissociation of H_2, i.e. that two empty sites are necessary for the reaction to take place, it has been shown that the dissociation on the (111) surface actually involves more than two empty sites and therefore that the reaction deviates from the expected Langmuir process [v47] [v48].

5.4.3 Response time: intrinsic limitations of Pd?

As well as the detection limit, a second important aspect regarding H_2 sensing is its response time. The response time can be considered in two ways. For qualitative measurements, which are crucial for safety consideration, one can define the time, t_{detect}, it takes for the sensor to provide a significant response, i.e. the time it takes to register the presence of H_2 in the atmosphere. On the other hand quantitative measurements conventionally consider the time, t_{90}, after which 90% of the signal is reached. According to European and US authorities, hydrogen sensors are required to have a response time of less than 1s for industrial applications [v9], [v49], [v50].

To measure these rapid variation in the TA signal, the programme used to measure the sample was modified to enable the number of measured points to be about 10 per second. More details are given in

chapter 2. In figure 5.25, the evolution of the TA signal measured as a function of time is shown in detail for three concentrations of H_2 in Ar: 63%, 4% and 0.25%. These correspond, in the two former cases, to the explosive concentration range which is composed of the $\beta-$phase, and in the latter case to the sub-flammable range which is mainly composed of the $\alpha-$phase.

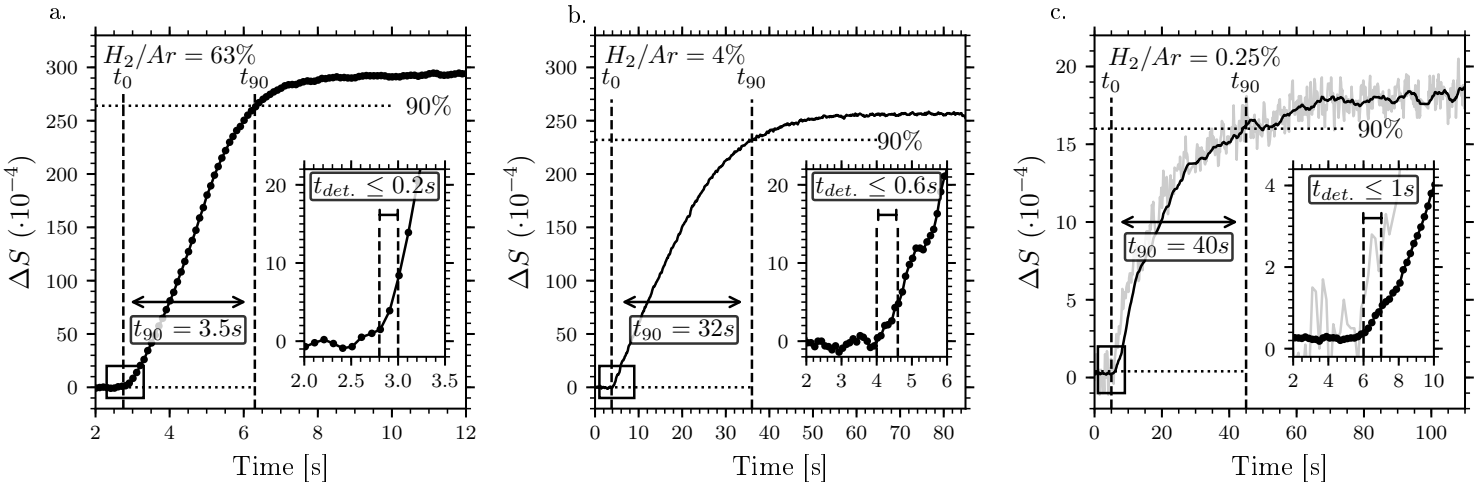

FIGURE 5.25: Response time of Pd when exposed to a. 63%, b. 4% and c. 0.25% H_2 in Ar. The inserts show a zoom in graph within a few seconds of exposure to the hydrogen mixture.

For 63% H_2 in Ar (Fig. 5.25.a.), t_{90} = 3.5s, and $t_{detect} < 0.2s$. The first acceleration seen between 2.75s and 4s is due to the time constant set on the lock in amplifier. Before reaching t_{90}, the trend seems to be quasi-linear after which the signal quickly saturates. For lower partial pressures of H_2, the reaction time is slower. Indeed at 4% (Fig. 5.25.b.) and 0.25% (Fig. 5.25.c.), t_{90} increases to 32s and 40s and t_{detect} to 0.6s and 1s, respectively. A two step process is seen in all cases with a linear increase before saturation is reached.

At 1% though, the saturation is not reached due to the fact that at this pressure, the $\alpha + \beta$ phase is formed. This is quite clear from figure 5.21, which shows that saturation is not reached at 1% of H_2, even after 1000s. This occurs at a very narrow pressure interval which has a strong effect on the optical response of the Pd as discussed in section 5.4.1. Nevertheless, the detection time, t_{detect}, is still below 1s at 1% thus within the requirements for hydrogen sensors. For smaller partial pressures, t_{detect} increases to about 10s at 0.06% to 50s at 10ppm, which is still an acceptable detection time for security and analytical applications. Table 5.4 summarises the values of t_{90} and t_{detect} determined for the two similar samples.

Comparing these results with the literature shows that the obtained values for the response time t_{90} at concentrations between 63% to 1% are of the same order or better to previously reported for Pd-based plasmonic sensing systems. Some values are given in table 5.4. Smaller response times (t_{90} = 1s) have been previously observed in plasmonic sensors using Pd, but not with H_2 in a carrying gas at atmospheric pressure; instead, the experiments were undertaken in vacuum, where the H_2 pressure was increased from 1 to 500$mbar$ [v30].

Understanding the exact mechanism taking place requires the complete knowledge of the adsorption and dissociation kinetics as well as the rate of diffusion within the Pd crystal. Furthermore, the kinetics at play will differ depending on which phase is forming within the metal hydride. Needless to say that such a study requires more information than could be provided by the here presented technique. It can nevertheless be proposed that this reduction in response time is due to the kinetics in the hydride formation which is proportional to the chemical potential of H_2. This is shown in figure 5.26 which plots the natural

TABLE 5.4: Response time values for t_{90} and t_{detect} for two different samples at different partial pressure of H_2 in Ar. The right hand side of the table shows values taken from the literature for t_{90} at different H_2 pressures.

H_2 in Ar [%]	Sample 1 (recorded at a rate of $0.5s^{-1}$)		Sample 2 (recorded at a rate of $10s^{-1}$)		Ref	Literature	
	t_{detect} [s]	t_{90} [s]	t_{detect} [s]	t_{90} [s]		H_2 [%]	t_{90} [s]
63	< 2	4	0.2	3.5	[v34]	100%	10
16	< 2	9	0.3	7.5	[v38]	4%	30
4	< 2	20	0.6	32			
1	< 2	-	1	-	[v35]	4%	60
0.25	< 5	30	1*	40			
0.06	7	35	10*	70	[v51]	100%	20
0.025	10	50	-	-		1%	60
0.004	30	105	-	-	[v32]	0.2%	90
0.001	50	185	-	-			

log of the partial pressure in H_2 as a function of the time t_{90} for the two different samples. An increase in t_{90} is seen as the partial pressure of H_2 is reduced. The measured response time t_{90} seems sample dependent, e.g. for 4% of H_2, from about 20 to 35s.

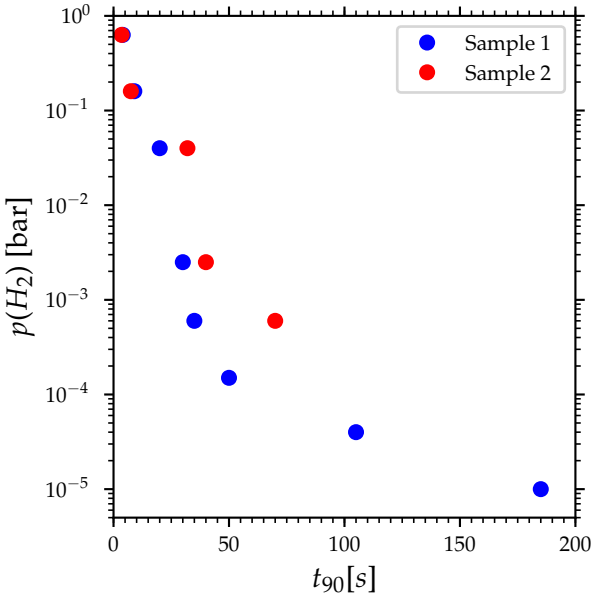

FIGURE 5.26: Graph plotting the time t_{90} against the partial pressure of H_2 in Ar in log scale.

The increase of t_{90} observed in the present experiments, from 3.5s at 63% to 20 or 32s at 4% is likely also due to the competition between physisorption of H_2 molecules at the nanoparticle surfaces, prior their dissociation [v52], and transient physisorption of Ar atoms. Indeed, in spite of the low reactivity of Ar with the Pd surface, it still undergoes physisorption which would for an instant prevent the adsorption of H_2 at a specific site. At low partial pressures of H_2, this competitive interaction could have a considerable repercussion on the kinetic of absorption of H_2 within the metal. This could explain why Wadell et al. would observe a smaller $t_{90} \leqslant 1s$ at 500$mbar$ with no carrier gas [v30]. This competition between H_2 molecules and atoms or molecules of the carrying gas and the kinetics in the formation of metal hydride appear to be an intrinsic limitation which seems difficult to overcome for a faster quantitative determination of H_2 concentration in a gas.

5.5 Absorption and desorption kinetics of the $\alpha-$phase

As well as the thermodynamic insight, the real time experiment discussed in the previous section (cf. section 5.4) also gives information on the kinetics of absorption and desorption. This is particularly true for the $\alpha-$phase as the time it takes for the signal to saturate is not limited by the time constant set on the lock-in amplifier ($TC = 1s$). Furthermore, it is the $\alpha-$phase that is of interest for sensing applications as a low detection time at low H_2 pressures is a key characteristic for such sensing technique.

5.5.1 Kinetics of the $\alpha-$phase: theoretical model

In this first section, we will define and describe the reaction model proposed and see in the following section how it fits the experimental data. The kinetic model was based on ref. [v53]. The reaction model for the reactivity between the Pd nanostructure and the H_2 gas is as follows

$$H_{2(g)} + 2S \underset{k_{des}}{\overset{k_{ads}}{\rightleftharpoons}} 2H - S \tag{5.2a}$$

$$H - S + V \underset{k_{emp}}{\overset{k_{abs}}{\rightleftharpoons}} H - V + S \tag{5.2b}$$

where S denotes the surface Pd adsorption sites and V the Pd volume sites. In this model we account for two sites needed to chemisorb a H_2 gas molecule, though this point is open to discussion (cf. section 5.4.2). We will however see, in the following discussion, that making this assumption fits the experimental observations.

It can nevertheless be proposed that the number of adsorption sites for the dissociation of H_2 should be close to 2 [v54]–[v56] . The mechanism thus consists of two reversible steps: the adsorption/desorption between the surface and the gas, and the absorption/emptying between the surface and the bulk. The term *emptying* is used to refer to the desorption from the bulk to the surface in order to avoid confusion with the desorption from the surface to the gas phase. To make the demonstration more clearer, we use the following notations.

- α corresponds to the ratio H/Pd of the absorbed hydrogen in the bulk as a function of time i.e. it represents the concentration $[H - V]$. It is given between $0 \leqslant \alpha \leqslant 1$.
- θ corresponds to the coverage of the Pd surface i.e. the concentration $[H - S]$. It is given between $0 \leqslant \theta \leqslant 1$.

The reaction rates can be written as

$$r_{ads} = k_{ads} p \left(1 - \theta\right)^2 \quad \text{with } k_{ads} p = k'_{ads} \Phi \tag{5.3a}$$

$$r_{des} = k_{des} \theta^2 \tag{5.3b}$$

$$r_{abs} = k_{abs} \theta \left(1 - \alpha\right) \tag{5.3c}$$

$$r_{emp} = k_{emp} \left(1 - \theta\right) \alpha \tag{5.3d}$$

where k are the reaction constants for each reaction steps from the reactions 5.2a and 5.2b. Φ is the flux given by $p/(2\pi m k_B T)^{1/2}$ where m is the molecule mass, p is the pressure and T the temperature (cf. section 4.3.4). The adsorption rate, k_{ads} is given in terms of the pressure times the free space left on the

surface squared $(1-\theta)^2$ as we consider two sites of adsorption being necessary to dissociatively chemisorb a H_2 molecule. The desorption rate is given as a simple second order reaction of associative desorption of H_2. The absorption rate is taken as proportional to the coverage of the Pd surface, θ, as the adsorbed H would act as a source of hydrogen which will absorb, and to the free space in the bulk, $1-\alpha$. Inversely, the emptying rate is proportional to the *space* left on the surface, $1-\theta$, and to the concentration in the bulk, α.From these reaction rates, we may determine the differential equations couple as below which accounts for the kinetics of the surface as well as that of the bulk.

$$\begin{cases} \frac{d\theta}{dt} &= r_{ads} - r_{des} - r_{abs} + r_{emp} \\ \frac{d\alpha}{dt} &= r_{abs} - r_{emp} \end{cases} \tag{5.4}$$

which when substituting the rates give

$$\frac{d\theta}{dt} = \left[k_{ads} p \left(1-\theta\right)^2\right] - \left[k_{des}\theta^2\right] - \left[k_{abs}\theta\left(1-\alpha\right)\right] + \left[k_{emp}\left(1-\theta\right)\alpha\right] \tag{5.5a}$$

$$\frac{d\alpha}{dt} = \left[k_{abs}\theta\left(1-\alpha\right)\right] - \left[k_{emp}\left(1-\theta\right)\alpha\right] \tag{5.5b}$$

This equation set should thus reproduce both the absorption kinetics, that is when the sample is exposed to H_2 as well as the desorption, that is when it is purged with Ar. Indeed, the main difference between the absorption and desorption kinetics is the absence of r_{ads} in the latter.

5.5.2 Fitting of the adsorption and desorption of the $\alpha-$phase

Before apply the model, let's first examine the behaviour of the two systems. From the discussion on the response time (cf. section 5.4.3), it is clear that the kinetic of adsorption is dependent on the partial pressure of H_2. The lower the partial pressure, the longer it takes for the saturation to be reached and the lower it is.

The desorption occurs when the partial pressure of H_2, to which the sample is exposed, drops to none. This leads to a disruption in the chemical potential equilibrium between the pressure of H_2 in the gas phase and the absorbed H. The desorption graphs in the α-phase for each partial pressures from 0.25% to 0.001% from figure 5.21 are considered. For comparison, the desorption were adjusted in time and are plotted in figure 5.27. What is immediately clear from this figure is that the desorption rates are the same regardless of the initial hydrogenation state of the Pd. Indeed, when the desorption occurs, the H/M ratio decreases. This can be interpreted by the fact that the state at which the metal hydride is at t_n is identical to what it would have been if it had started in this state at t_0. For instance, if we look at the 0.25% curve where it meets the 0.06% curve, they both are in the same state i.e. same H/M ratio. This is indeed helpful in terms of analysis, as only the desorption from 0.25% needs to be analysis to get insight on the mechanism within the $\alpha-$phase.

Lastly, an important point to remind is the fact that the TA experiment measure the change in optical response of the Pd bulk. In other words, the factor that most effects the change in signal is the change in concentration of H in the metal bulk and not the surface.

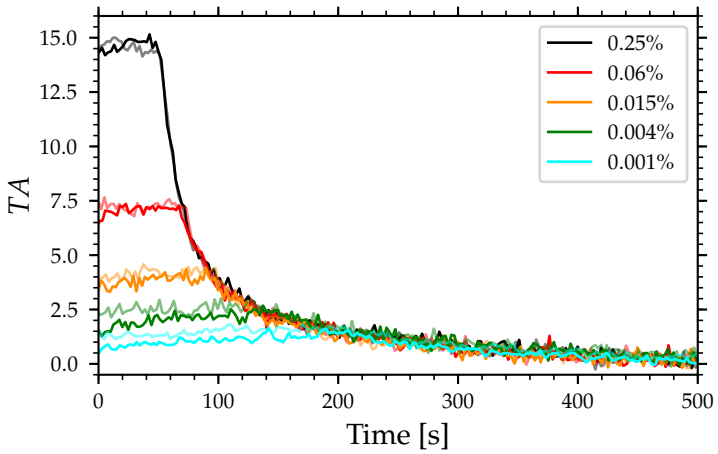

FIGURE 5.27: Graph showing the desorption of the Pd sample taken from figure 5.21 of the $\alpha-$phase. The graph were adjusted to start to have their kinetics super imposed. Each desorption were done twice.

To fit the model discussed in the previous section, we have plotted the desorption from 0.25%, and the adsorptions at the different partial pressures in figure 5.28. The differential equation set 5.5a and 5.5b were numerically solved using Mathematica. The rate constants k, were manually adjusted to fit both the adsorption and desorption data simultaneously.

The data does not fit perfectly, nevertheless, the model does reproduce the behaviour of the experiment. The values determined were $k_{ads} = 1.11 \cdot 10^{-2} mbar^{-1} \cdot s^{-1}$, $k_{abs} = 0.214 s^{-1}$, $k_{des} = 0.235 s^{-1}$ and $k_{emp} = 0.111 s^{-1}$. Every absorption data points were fitted by adjusting the pressure in $mbar$ (from $2.5 mbar$, down to $0.01 mbar$ which is equivalent to 0.25% to 0.001%, since the experiment was undertaken at atmospheric pressure). The model nevertheless accounts for the slowing down on the time constant when the partial pressure is decreased. Indeed, the lower the hydrogen partial pressure, the longer it takes to reach saturation. This effect is accounted for in the model, which therefore shows that the slowing down of the response time is inherent to the chemistry of Pd and H_2 and would be a difficult issue to overcome.

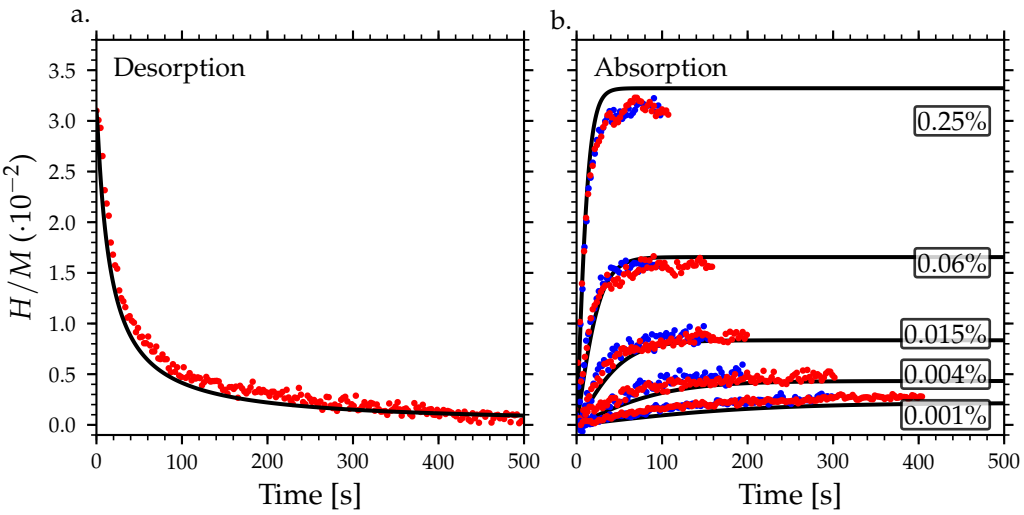

FIGURE 5.28: a. Desorption kinetics, taken from figure 5.21, from 0.25% initial partial pressure of H_2 adjusted so the y axis shows the H/M ratio determined from table 5.3. b. Absorption kinetics, taken from figure 5.21, for partial pressures from 0.25% down to 0.001% adjusted so their saturation reaches the H/M ratio determined from table 5.3. The red points shows the experimental data. In the case of b. the blue points show the second cycle at the same partial pressures. In black are the fit using the differential couple equation described in eq. 5.5a and 5.5b

Although this procedure allows to well reproduce the experimental data, it does not give a simple understanding of the phenomenon at play, in particular which, if any, mechanism is limiting. To determine if a mechanism in eq. 5.2a and/or 5.2b is limiting the kinetics should it be during the absorption or the desorption, we can look at the kinetic equations shown in eq. 5.5a and 5.5b and consider the boundary conditions.

If we consider the reaction at the surface being the limiting process, then the absorption in the bulk is more important. We can translate that by considering $kabs \to \infty$. Since $d\alpha/dt$ is finite, the term

$$\left[k_{abs}\theta(1-\alpha) - k_{emp}\alpha(1-\theta)\right] = 0 \tag{5.6}$$

If we denote $K_{ab} = k_{abs}/k_{emp}$, we can write

$$\theta = \frac{\alpha}{\alpha + K_{ab}} \quad or \quad \alpha = \frac{\theta K_{ab}}{1-\theta} \tag{5.7}$$

Now, we may replace θ from the above expression in eq. 5.5b, we obtain

$$\frac{d\alpha}{dt} = -k_{abs}\frac{\alpha^2}{\alpha + K_{ab}} \tag{5.8}$$

The rigorous resolution of this equation is

$$\alpha = \frac{K_{ab}}{W\left(K_{ab}e^{k_{abs}t+Cst}\right)} \tag{5.9}$$

where W is Lambert W function. However, since $\alpha \leqslant 0.031$ and K_{ab} was found to be around ≈ 2, we may write this first approximation

$$\frac{d\alpha}{dt} \approx -k_{abs}\frac{\alpha^2}{K_{ab}} = -k_{emp}\alpha^2 \tag{5.10a}$$

$$\text{giving} \quad \frac{1}{\alpha} = \frac{1}{\alpha_0} + k_{emp}t \tag{5.10b}$$

In this case, it can be seen that the reaction mechanism is second order. Figure 5.29 shows the desorption kinetics adjusted as follows: Figure 5.29.a. shows the raw data with the y axis adjusted to represent the H/M ratio. Figure 5.29.b. shows the data normalised to 1. Figure 5.29.c. shows the natural log of figure 5.29.b. Figure 5.29.d. shows the inverse of figure 5.29.b. What can be seen is that linearity is observed, from the beginning, in figure 5.29.d. indicating that the main process is, in fact, second order for the desorption and emptying processes, which is therefore limited by the reaction at the surface. However, one may also note the linearity beginning around $t = 200s$ in figure 5.29.c. which would indicate a second, first order, mechanism which is not accounted for in the model. This could come from the fact that when the desorption starts, the desorption from the surface is the limiting factor, as the surface sites are rapidly occupied by the hydrogen emptying from the bulk which means that the bottleneck occurs for the desorption process. However, as the concentration of H in the bulk decreases, it reaches a point were the bottleneck becomes the emptying of the bulk. This proposition needs further investigation to verify but would explain two different kinetics.

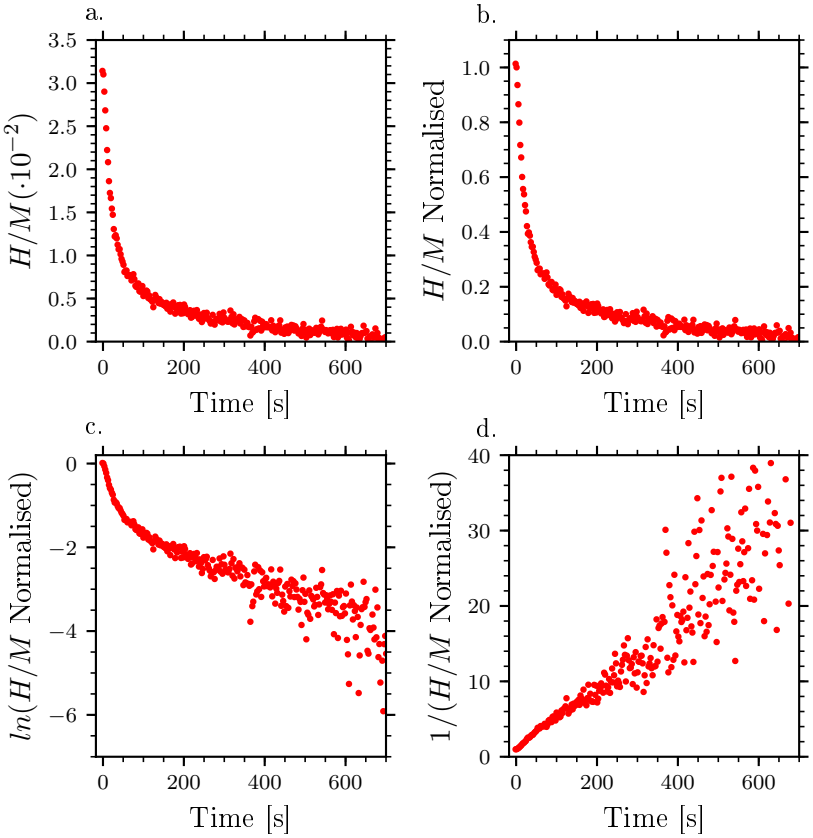

FIGURE 5.29: Desorption data points taken from 5.28.a. a. shows the raw data. b. shows the data normalised to 1. c. shows the natural log of the data plotted in b. c. shows the inverse of the data plotted in b.

The second boundary condition is when considering the absorption/emptying process is being limiting. In this case we consider $k_{ads} \to \infty$. If we sum eq. 5.5a and 5.5b we get

$$\frac{d\theta}{dt} + \frac{d\alpha}{dt} = k_{ads}\left[p(1-\theta)^2 - \frac{1}{K_{ad}}\theta\right] \quad \text{with} \quad K_{ad} = \frac{k_{ads}}{k_{des}} \tag{5.11}$$

Again, since the sum $\frac{d\theta}{dt} + \frac{d\alpha}{dt}$ is finite, then $\left[p(1-\theta)^2 - \frac{1}{K_{ad}}\theta\right] = 0$, which leads to the following relation

$$\theta = \frac{\sqrt{pK_{ad}}}{1+\sqrt{pK_{ad}}} \tag{5.12}$$

This infers that θ is dependent on the partial pressure of H_2, and, due to the fast rate the adsorption, we can consider θ to be constant against time. We may thus write

$$\frac{d\alpha}{dt} = -\alpha\left[k_{abs}\theta + k_{emp}(1-\theta)\right] + k_{abs}\theta \tag{5.13}$$

which integrates to

$$\alpha = \frac{k_{abs}\theta}{k_{abs}\theta + k_{emp}(1-\theta)}\left[1 - e^{\left[k_{abs}\theta + k_{emp}(1-\theta)\right]t}\right] \tag{5.14}$$

This kinetics therefore leads to a first order reaction process. Just as previously, the adjusted kinetics for the absorption at 0.25% are plotted in figure 5.30. Figure 5.30.a. shows the raw data with the y axis adjusted to represent the H/M ratio. Figure 5.30.b. shows the data normalised to 1. Figure 5.30.c. shows the natural log of figure 5.30.b. Figure 5.30.d. shows the inverse of figure 5.30.b. Contrary to the desorption kinetics discussed above, we now see a linearity only occuring on figure 5.30.c. which indicates that the main mechanism is first order as the model proposes, which shows that, for the absorption kinetics, the reaction in the bulk is the limiting process.

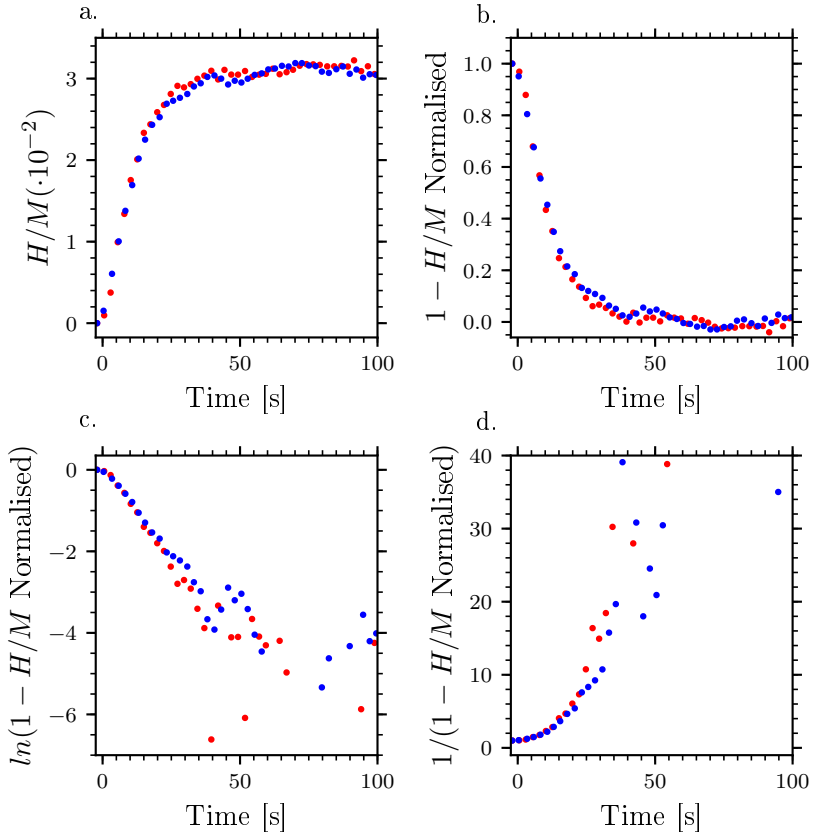

FIGURE 5.30: Absorption data points at 0.25% taken from 5.28.b. a. shows the raw data. b. shows the data normalised to 1. c. shows the natural log of the data plotted in b. c. shows the inverse of the data plotted in b.

The experiments were not repeated at different temperatures, and thus no information was gathered concerning whether the kinetics follows an Arrhenius behaviour. We, nevertheless, may propose that, on the one hand, adsorption processes are generally exothermic i.e. the difference in enthalpy ΔH_{ads} is negative [v55]. According to the Arrhenius equation, we would expect

$$k_{ads} = k_0\, e^{-\frac{\Delta_{H_{ads}}}{RT}} \tag{5.15}$$

This translates in a decrease in adsorption with elevated temperatures. According to the model (eq. 5.5b), a decrease in k_{ads} only impacts the absorption kinetics (Fig. 5.28.a.) leading to a decrease in the intensity reached and slowing down of the absorption.

On the other hand, the absorption process in an activated reaction which therefore means that the rate would increase with temperature. It is thus unclear how the kinetics is influenced with a change in temperatures. This would require further investigation.

5.6 Preliminary work: Detection of H_2 in the presence of oxygen and water

In this section we will briefly introduce the preliminary work done regarding the effect of dry and humid air on the sensing capability of the LSPR Pd system.

Selectivity of a gas sensor to the analytes against other possible reactants of the medium is an important point for practical applications. The average composition of dry air is summarised in table 5.5 [v57] with N_2 and O_2 being the main constituents. N_2 is in essence considered to be an inert gas as the $N{\equiv}N$ triple bond is one of the strongest in chemistry with a bond energy of $946 kJ \cdot mol^{-1}$. On the other hand O_2 may oxidise various metals. It is thus important to understand the effect of O_2 on Pd for application in air of such metal-based sensors. Moreover, water and hydrocarbons are also known to react with the Pd surface which inhibits its sensing abilities [v58].

TABLE 5.5: Average composition of dry air taken from ref. [v57]

Compound	Mole percent [%]
N_2	78
O_2	21
Ar	0.93
CO_2	0.035
Ne	0.0018
He	0.00052
CH_4	0.00017
Kr	0.00011
H_2	0.000053
N_2O	0.000031
Xe	0.0000087
O_3*	trace to 0.0008
CO	trace to 0.000025
SO_2	trace to 0.00001
NO_2	trace to 0.000002
NH_4	trace to 0.0000003

A lot of research regarding the reactivity of O_2 with Pd have been undertaken as Pd and PdO play a vital role in catalytic processes for oxidation and hydrocarbons such as applications in motorcar exhausts systems [v59].

5.6.1 Reactivity of Pd towards O_2

On bulk metal, O_2 chemisorbs and diffuses within the metal structure as brought forwards by Flanagan et al. whom have experimentally determine the diffusion constant [v60]. The oxidation mechanism of

different Pd facets has been readily studied using various techniques in ultra high vacuum (UHV) environment [v61]–[v66]. Although comparing the behaviour of single crystal surfaces in UHV and nanoparticles at atmospheric pressure is quite a stretch, information on the mechanisms at play can still shed light on the behaviour of the metal towards oxidation. The oxidation of Pd usually follows three steps: O_2 chemisorbs of Pd surfaces, followed by the formation of a surface layer of metal oxide which then forms into bulk PdO seeds that can grow to form metal oxide.

When looking at Pd nanoparticles supported on $\gamma - Al_2O_3$, Baylet et al. have shown that for nanoparticles smaller than $5nm$, oxidation under a O_2/N_2 atmosphere and reduction under H_2/N_2 atmosphere occurs at ambient temperature, whereas, for larger particles, temperature above $373K$ for reduction and $573K$ for oxidation are required [v59].

The dielectric function of PdO was determined by Nilsson[v67], and is shown in figure 5.31 against the dielectric function of Pd determined by Johnson and Christy [v20]. The difference in the optical properties is considerable mainly due to the fact that PdO losses its metallic property. It is therefore conceivable that the oxidation of the LSPR sample will *kill* the TA signal.

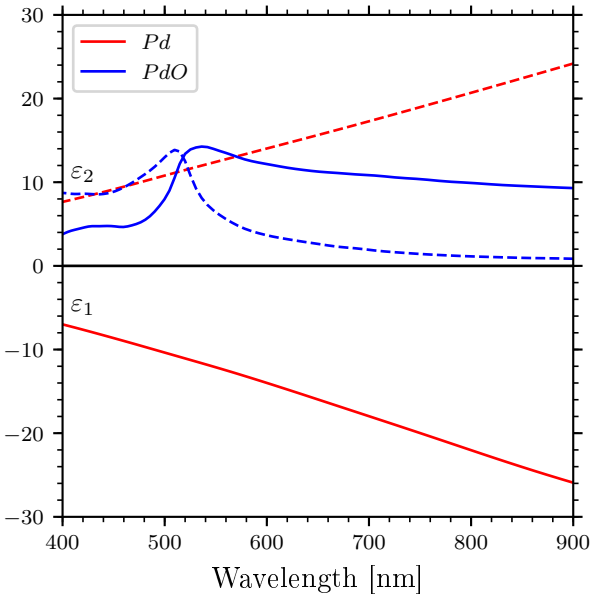

FIGURE 5.31: Dielectric fuction of bulk Pd (red) from Johnson and Christy [v20] and for PdO from [v67].

Using Pd samples similar to those used in the previous section, we have exposed the sample to cycles of O_2 and Ar at atmospheric pressure to verify the immediate effect of the oxidation on the TA signal. Figure 5.32 shows cycles between pure Ar and O_2 after an initial exposition to H_2 to make sure the sample was activated. After the initial decrease in TA whilst purging with Ar, the sample is exposed to a pure flow of O_2. The signal is seen to increase rapidly and then stop for around $200s$ before increasing again linearly. The sample was exposed again to Ar and the signal is seen to decrease without reaching its initial state. The second O_2 exposure leads to a rapid increase in the TA, much higher than the first time, though the signal reaches saturation and stays constant. These cycles are repeated and the behaviour is the same with a rapid increase in TA under O_2 and a slow decrease without complete regeneration of the sample un Ar. The amplitude of the signal increase is much lower than when the sample is exposed to pure H_2. Indeed, the initial exposure to H_2, in the above mentioned figure, was $TA \approx 400 \cdot 10^{-4}$, compared to the amplitude when exposed to O_2 which is $TA \approx 3 \cdot 10^{-4}$.

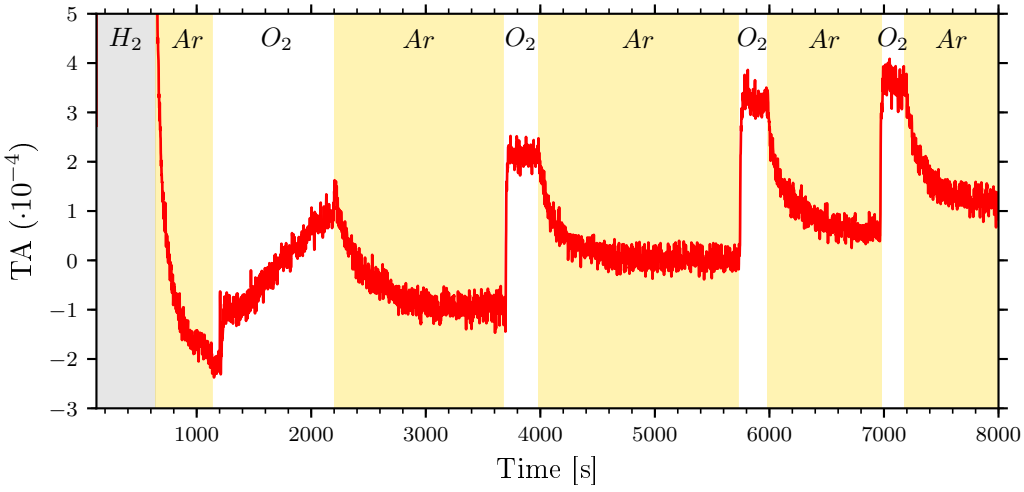

FIGURE 5.32: Real time cycles on the Pd sample when exposed to cycles of pure Ar and O_2 after an initial cycle of pure H_2.

The increase in signal is due to the oxidation of the Pd nanoparticles. The difference between the first exposure to O_2 and the others has not been investigated. It can be proposed that the initial exposure leads to the formation of an oxygen species which was not desorbed when exposed to Ar. A similar effect should thus also be seen when exposing the sample to air. Figure 5.33.a. shows the Pd sample under two cycles of Ar and 0.25% H_2 in Ar after which the sample was exposed to dry air for about 40*min*. The H_2 cycles were done to verify the activity of the sample which did react as expected. When the air was introduced at t = 1600*s*, the initial reaction of the TA signal was to decrease for about 100*s* before slowly increasing passed the intensity of the previous H_2/Ar cycles. This initial decrease can be distinguished after the first exposure to O_2 in figure 5.32. It can be proposed that, after the initial exposure to H_2, a small amount of metal hydride was still present when the sample was exposed to air. This led to the O_2 desorbing the last absorbed or adsorbed H before oxidising the metal. When the sample was eventually exposed to Ar again, it spontaneously reduces to near its initial state. This hypothesis may explain the initial behaviour of the sample when cycling between Ar and O_2 in figure 5.32. Indeed, the initial slow increase might have been a reaction to the H present in the metal which was absent after the first cycle with oxygen. Furthermore, a similar initial decrease is seen just after the first exposure to O_2 though the signal quickly increases again. This might come from the fact that the sample was exposed to 100% O_2 in the first case, whereas, in figure 5.33.a., the air only contained 20% O_2, which would lead to a slower kinetic.

This hypothetical mechanism is reinforced in figure 5.33.b. Indeed, at t = 400*s*, the sample was exposed to 0.25% H_2 in air after being purge with air for about one hour. The initial reaction of the TA signal was a small decrease before it started increasing again and saturating after $\approx$ 75*s*. At $t \approx$ 600*s*, the sample was re-exposed to air which led to a rapid decrease of the signal before a slow increase. According to the hypothesis proposed above, at t = 400*s*, the oxidised Pd is reduced to metallic Pd before it hydrogenise. At $t \approx$ 600*s*, the opposite effect occurs where the O_2 in the air reduces the metal hydride back to its metallic state before oxidising it again. At $t \approx$ 1150*s*, the sample is exposed to 100% H_2. The initial reduction of the metal hydride is too fast to be recorded, though after purging with air at t = 1300*s*, the same behaviour is repeated. Needless to say that this mechanism is simplified as competition between the hydrogenation and oxidation will occur. Nevertheless, this hypothesis does help describing the data though needs to be confirmed.

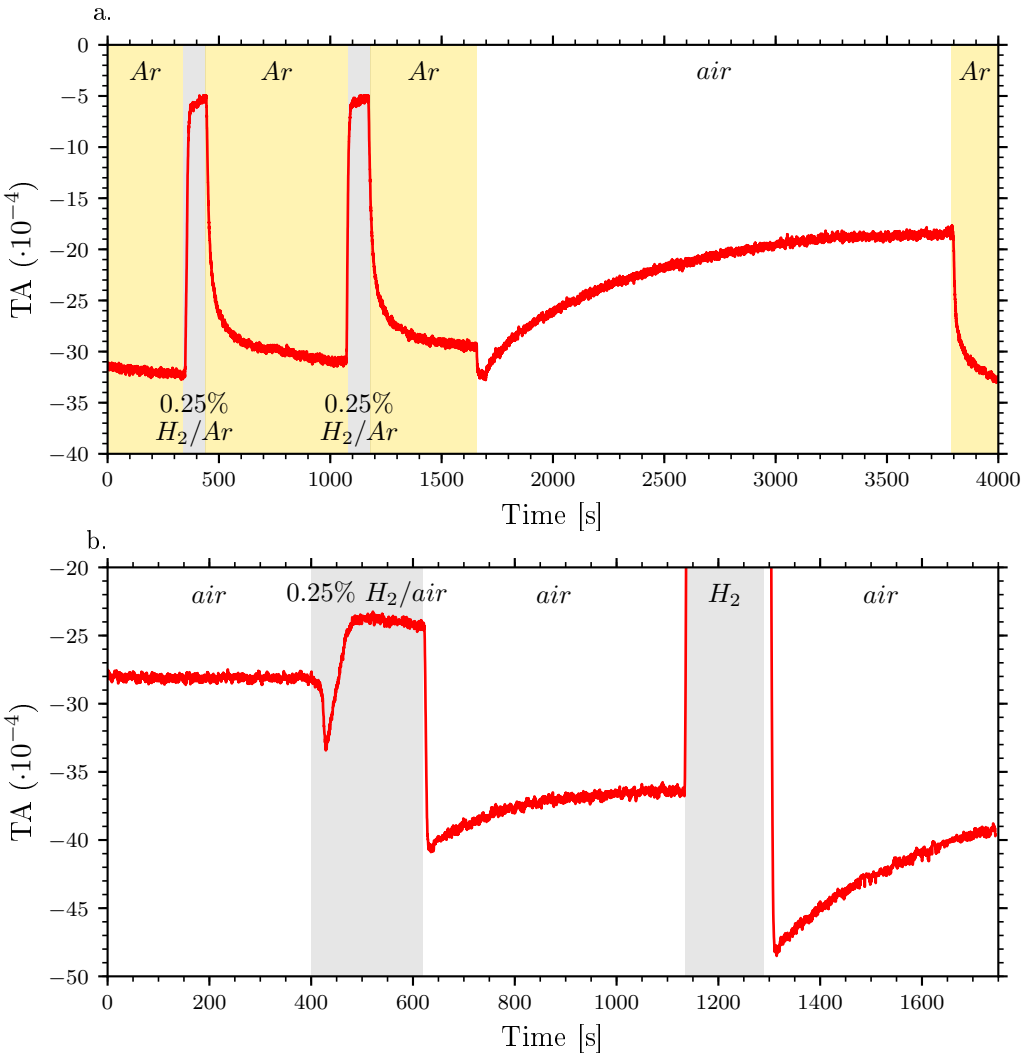

FIGURE 5.33: a. shows the real time cycles initial between Ar and 0.25% H_2 in Ar after which the sample was exposed to pur dry air. b. shows the TA when the sample is exposed to 0.25% H_2 in air after one hour exposure to a dry air flow.

The difference in kinetics between the hydrogenation and oxidation means that the sample is still relatively reactive to H_2 as all the Pd has not yet oxidised. One may wonder, however, how annealing the Pd sample in air helps reactivating its sensing capabilities. According to the literature, the presence of O_2, H_2 and Pd leads to the catalytic formation of H_2O molecules at the surface of the nanoparticles which end up inhibiting the sensing capabilities of Pd [v54], [v68]. Furthermore, Zemlyanov et al. suggested that the oxydation of $Pd(111)$ is thermodynamically driven whereas the $Pd(100)$ is kinetically driven [v69]. This means that increasing the temperature would decrease the oxidation rate in the former and increase it in the latter. In the case of the sample used in this work, it is not evident which facets are dominant. Therefore, the effect of annealing the sample is not straightforward. It can be proposed that O_2 helps reduce the metal hydride and the heat helps evaporate the water. Then, the activation cycles under Ar and H_2/Ar would reduce the present metal oxide. All these results are preliminary and further investigation would be required though it does underline the interfering problem associated with O_2 and H_2O formation regarding H_2 sensing in air.

5.6.2 Effect of humid air on Pd hydrogen sensing

So far the experiments were undertaken in dry synthetic air. For practical application of Pd based LSPR sensors, investigation of the behaviour of the sensor in humid air is a requirement. We have already discussed that water is formed when O_2 reacts with PdH. The water forms a thin chemisorbed layer which inhibits the sample from reacting with H_2. However one may wonder what the reactivity of the sample would be with relatively high humidity. In this section, we repeat the cycles though this time the air is artificially made humid by incorporating water vapour.

The humid air was made by first pumping the mixing bottle down to around $10^{-5}bar$. A flask containing ultra pure water was open and the bottle quickly reached saturation of water vapour around $1.4 \cdot 10^{-2}bar$. The bottle was completed to $2bar$ with dry air. This led to a humidity of about 50%. For H_2 mixture with humid air, the same protocol was followed, though after adding the water vapour, the bottle was filled with $8 \cdot 10^{-2}mbar$ of H_2 which led to a total pressure of $9.4 \cdot 10^{-2}bar$ prior the completion with dry air. This yielded a mixture of 4% H_2 in 50% humid air.

The first test undertaken was to see the effect of the water on the LSPR response. The Pd was purged with dry air, and then humid air was introduced. The results are shown in figure 5.34. The sample has initially been exposed to cycles of H_2 in air, but was purged for $40min$ with dry air. In the figure humid air at 50% was injected at $t = 150s$. The effect seen is very small thus the signal was multiplied by 20 for visibility. The effect of the water was to induce a small increase in the TA with no other distinct behaviour. It would seem water does not have a big effect on the optical response of Pd or in this case of PdO.

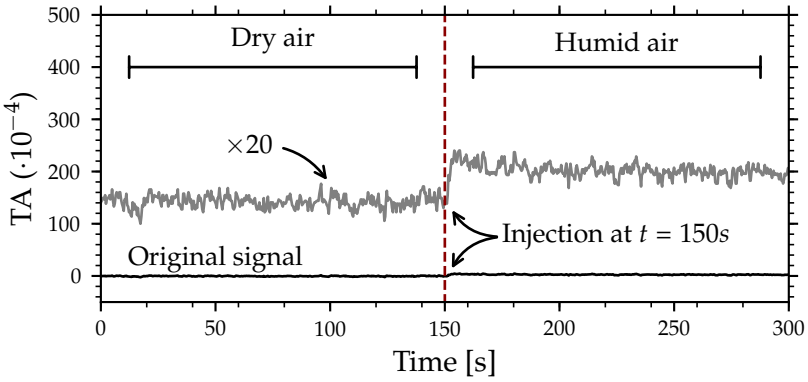

FIGURE 5.34: Real time monitoring of a Pd sample when exposed to dry and humid air. The signal is multiplied by 20 for visibility as the increase in TA when exposed to humid air compared to when exposed to H_2 is much lower. The y axis was chosen to be the same as figure 5.35.

Cycles of H_2 in dry and humid air were done and the raw results are shown in figure 5.35.a. The experiment was done in multiple steps. Initially, two cycles of dry air and H_2 in air at 4% partial pressure were undertaken at $t = 1000$ and $3000s$. Then the sample was purged for the same $40min$ with dry air till $t = 5600s$ when humid air at 50% was injected. At $t = 6000s$, the sample was exposed to 4% H_2 in humid air. The TA is seen to increase to about the same intensity as the previous cycles, however, it takes much longer to saturate. The sample was purged with humid air for about $1000s$ before being re-exposed to the hydrogen mixture at $t = 7800s$. The same increase is seen, though the saturation took even longer.

Figure 5.35.b.c. and d. show the same data adjusted so the absorption and desorption phases are more visible and comparable. If we first look at 5.35.c. and d. we can see that the absorption kinetic for H_2 in humid air is much slower than for dry air. Furthermore, there seem to be an initial fast increase in TA

for about 5*s* before it slows down. The second cycle under humid air is clearly seen to be still slower than the first cycle with the same initial fast jump. Nevertheless, regardless of whether the air is dry or humid, the TA saturates at about the same intensity. On the other hand, looking at the desorption (Fig. 5.35.b), all cycles seem to desorbe at the same rate irrespective of the air humidity.

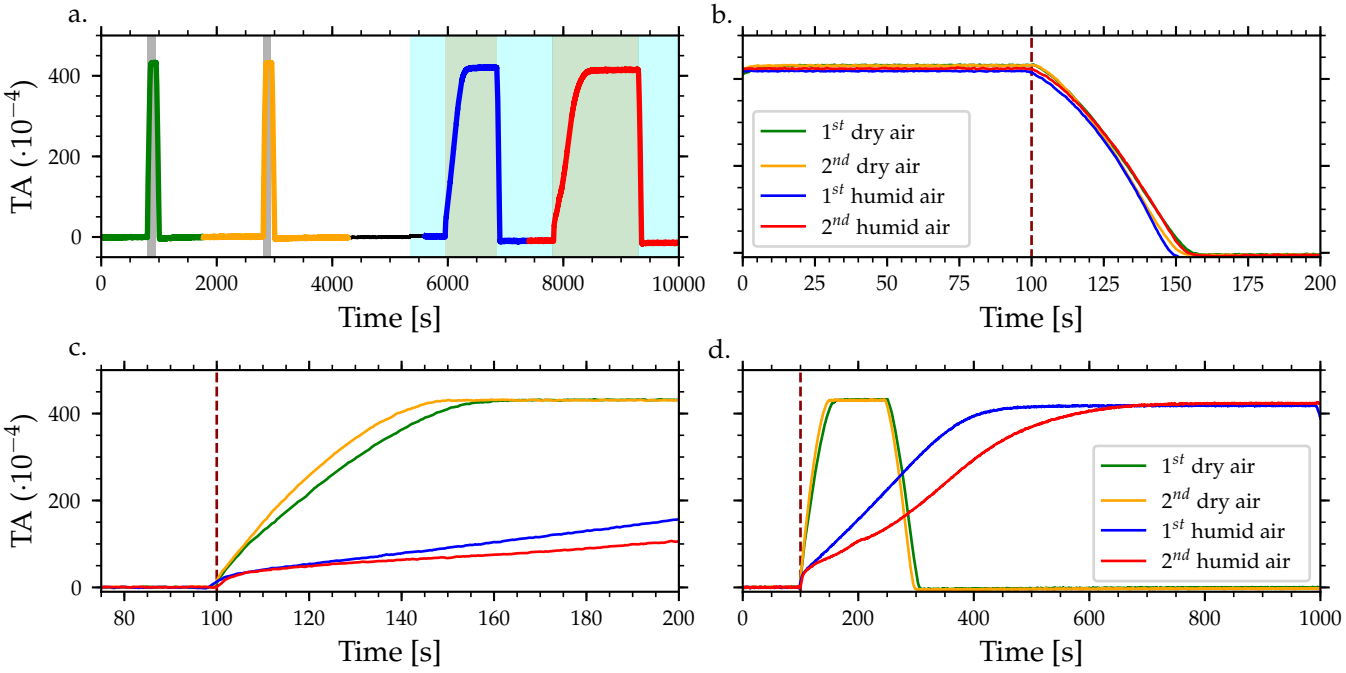

FIGURE 5.35: a. Raw data of the real time monitoring of the Pd sample when exposed to dry and humid air as well as cycles of 4% H_2 in both dry and humid air. b. same data as a. but adjusted in time to align the beginning of the desorption. c-d. same data as a. but adjusted in time to have the absorption start at the same time. c. is a zoomed in view of d. The color code in a. is kept the same throughout all graphs. The humid air was at 50% humidity.

Making sense of these data would require further investigation. The hypothesis that is proposed, although not complete, is that the water does adsorb on the surface of the Pd nanostructure. This leads to the formation of OH groups that would pollute the surface and thus decrease the rate of adsorption of H_2. During the desorption though, the absorbed H still manage to empty from the bulk and since we mainly measure the optical response of the bulk, we cannot see the effect at the surface. This thus indicates that the presence of water does not prevent H to spontaneously empty from the bulk and eventually desorbe to the gas phase. For the moment, there is no explanation for the initial acceleration seen when the sample is exposed to H_2 in humid air.

The experiment was repeated after the sample was left for 24*h* in humid air at a small overpressure of 1.2*bar*. The result is shown in figure 5.36.a. with a zoomed in view in figure 5.36.b. The sample shows a rapid increase when the H_2 is injected however, the intensity is much lower than in the previous experiment. The sample was left for 1100*s* and the sample is seen to initially decrease before steadily increasing. The final intensity reached before the sample was purged with humid air was 45 times lower than the same cycle in figure 5.35.a (red and blue). The sample was then exposed to pure H_2, to see whether it was still reactive. The TA shows that the sample still exhibits a high response to pure H_2.

These results clearly shows that the Pd sample evolved when left in humid air. It is not clear whether it is due to the oxidation of the sample or due to the fact that the water or hydroxyls have poisoned the reactive

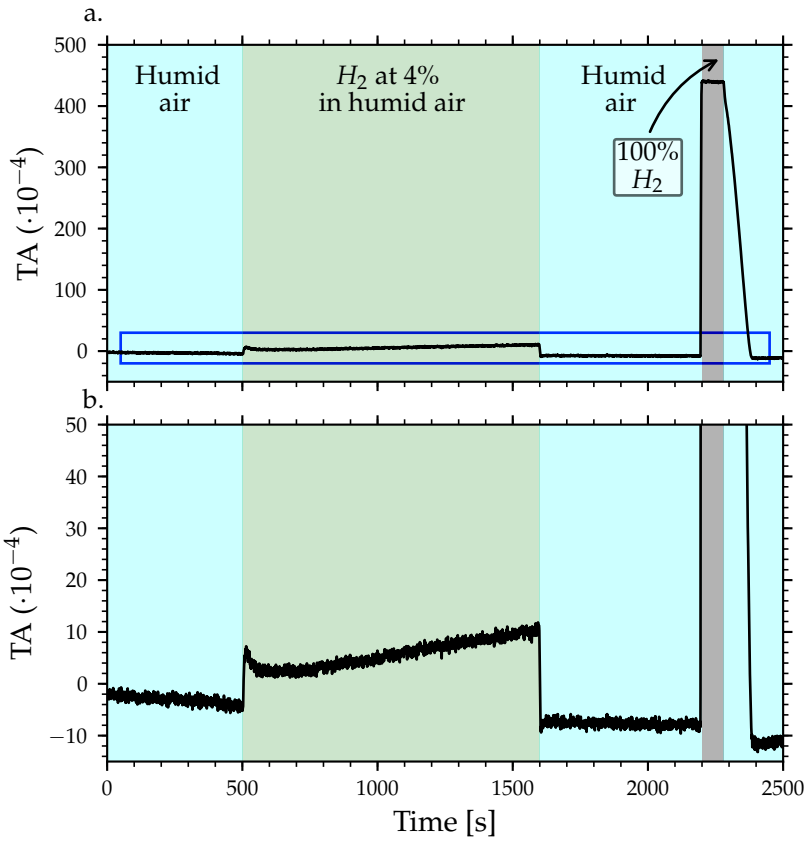

FIGURE 5.36: Real time monitoring of the same sample after being kept for 24*h* in air. The sample is first exposed to 4% H_2 in air at 50% humidity. b. is a zoomed in view of a. as indicated by the blue square.

sites. Nevertheless, these experiment do show that although Pd is indeed sensitive to H_2 in air, there are evidently issues to account for with the presence of water and oxygen. Other contaminants that would need to be investigated, for real world applications, are hydrocarbons since they are known to contaminate Pd fuel cell batteries and thus would also contaminate the Pd sensor. It is however possible to attempt to protect the Pd metal layer as is discussed in the next section.

5.6.3 Use of metal oxide frameworks (MOF) as a protecting layer

A lead to protect the metal film against unwanted contaminants is to use metal oxide frameworks (MOF). These macromolecular compounds form 3D crystalline structures with the corners made of metal complexes and the edges made of organic molecules as illustrated in figure 5.37. A key feature of MOF structures is their very high surface area due to their porosity. The shape, size and composition of these structures are very diverse. They may be tailored for specific chemical and physical properties. For instance, zeolite imidazole framework (zif-8) shown in the illustration has small $\leqslant 0.34nm$ pores and is hydrophobic as discussed by Ortiz et al. [v70]. This would in the case of sensing with Pd, allow permeability to H_2 but not to H_2O and reduce that of O_2.

Such method has been used by Koo et al. to protect Pd nanowires used for H_2 sensing by means of electrical resistance measurements, against H_2O contamination [v71]. The utilisation of a MOF may also be used to concentrate the analyte around a LSPR nanoparticle sensor. Indeed, the MOF layer may behave as

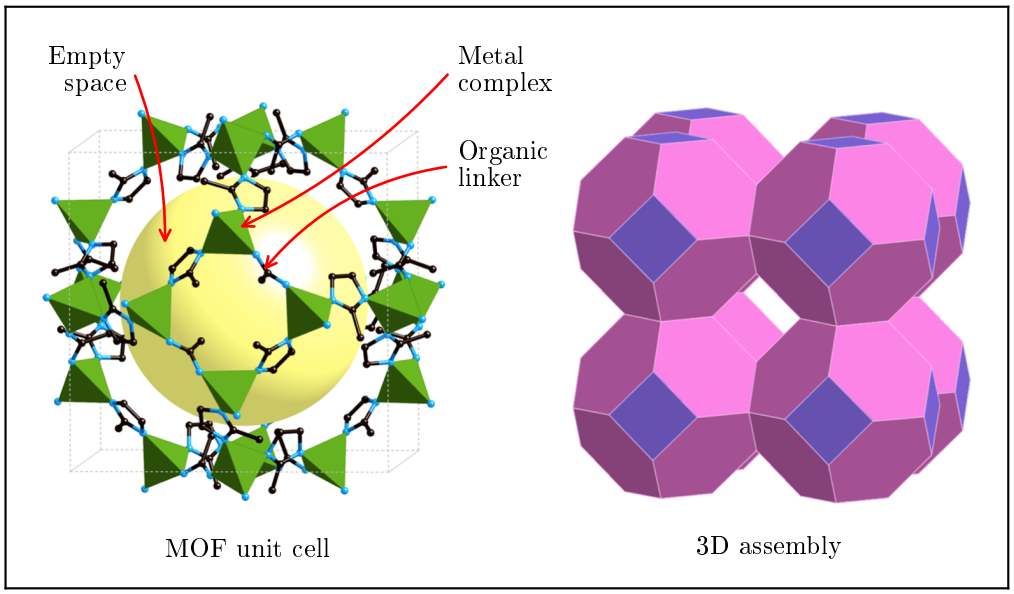

FIGURE 5.37: Molecular model of zif-8 MOF. On the left hand side a unit cell of zif-8 is shown with the metal complexes in green and the organic linker in black and blue (corresponding to the nitrogen and carbon atom respectively). The yellow sphere represent the empty space within the unit cell. On the right hand side, a 3D assembly of four unit cells is shown.

a *sponge* which will increase the refractive index change around the LSPR nanoparticles by concentrating the analyte in their vicinity. This approach has been used by Kreno et al. whom have used the same BTC MOF on Ag nanoparticles to concentrate CO_2 and SF_4 around the transducer which thus enhanced their sensitivity [v72].

In order to protect the Pd nanostructured films, used in this work, against H_2O and possibly O_2 contamination, the samples were coated with zif-8. The protocol is described in the next subsection. This preliminary work has been performed in collaboration with Christian Serre, Antoine Tissot and Shan Dai from the materials institute of Paris ENS for the preparation of the MOF and XRD analysis.

• MOF deposition: protocol

This protocol describes the method used for coating the Pd samples prepared by oblique angle deposition with a layer of zif-8. The glassware was cleaned with aqua regia. A main $200mL$ solution of hydrated zinc nitrate ($Zn(NO_2)_2.6H_2O$) at a concentration of $C_m = 2.78 \cdot 10^{-2} mol \cdot L^{-1}$ were prepared in methanol (CH_3OH). $10mL$ of the zinc solution were pored in a $15mL$ Falcon tube in which $42mg$ of 2-methyl imidazole ($C_4H_6N_2$) were dissolved using ultra sounds. The molar ratio is about 2 part zinc to 1 part imidazole. The MOF precursor solution was pored in a clean beaker and the Pd sample was placed in the beaker for a given amount of time.

Two Pd samples, with a bare glass control, were made and exposed to the MOF solution for different amounts of time.

- Sample (A) was exposed with its glass control substrate in the same beaker for $30min$. A very light white precipitate formed slowly. The samples were then taken out and a new MOF solution was prepared. This time, two beakers were used with one containing the Pd sample and the other containing the glass control substrate. The precipitate formed more rapidly in the control beaker becoming nearly

opaque whereas the beaker containing the Pd sample stayed quite transparent with only a slight hue after 30*min*. The sample was analysed by SEM, X-ray diffraction (XRD) and the TA spectrum was recorded (noted MOF-1). H_2 cycles in air were undertaken and will be discussed in the next section. The sample was then re-exposed again to the MOF solution for two exposures, 40*min* each (noted MOF-2). The same characterisation and sensing test were done afterwards.

- Sample (B) was made of similar Pd sample though it was left in the MOF solution for 3 hours with a glass control. Only the SEM image were recorded for comparison with sample (A).

• Characterisation and gas exposure of the MOF/Pd samples

Figure 5.38.a. and b. shows SEM images of sample (A) before and after the initial MOF coating, respectively, whilst figure 5.38.c. shows the glass control. The first figure shows the Pd nanostructure that we have already characterised in section 5.3. The second image exhibits hexagonal structures, of about 50*nm* in width, have started to form on the surface, though it is not uniformly covered. On the other hand, the control image (Fig. 5.38.c.) exhibits well defined crystalline structures covering the glass substrate. On the upper left hand corner of the SEM image, one may see a MOF nanoparticle deposited on the surface as well as small $\leqslant$ 20*nm* holes in the grain boundaries, on the right hand side. The presence of the large MOF nanoparticle on the control image explains the origin of the white precipitate observed during the synthesis. The sample was indeed covered with such well formed crystals. On the other hand, the Pd sample did not exhibit such particles, though small clusters have started to form. This would indicate that the Pd plays a role in the MOF formation though no further investigation regarding this question was undertaken. AFM measurement showed that the MOF layer was about 65*nm* in height, though the surface does show a high roughness. As a reminder the Pd nanostructure surface was only around 10*nm* in height.

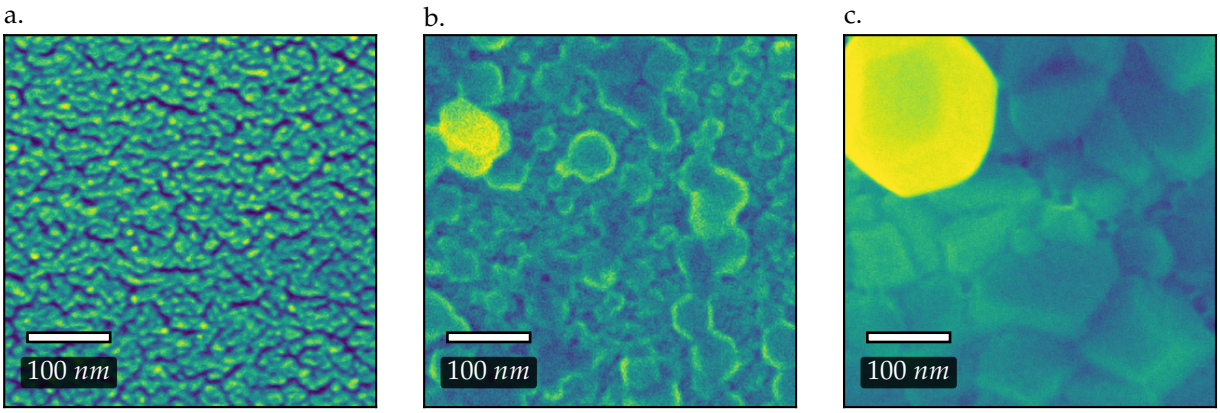

FIGURE 5.38: SEM image of the Pd sample a. before the MOf deposition, the metal nanostructure is clearly visible, b. after two 30*min* dips in the MOF precursor solution, and c. of the glass control which was treated just as the Pd sample.

The TA spectra of the sample before and after MOF coating are plotted in figure 5.39. The spectra are plotted relative to one another in terms of intensity, thus only the slope may be compared. The initial spectrum shows a steep slope going into the IR, whereas after the first coating with MOF, the slope is reduced, though it has the overall same shape.

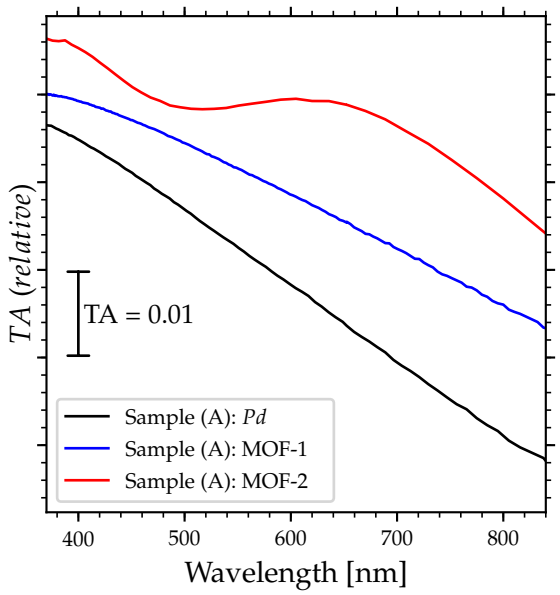

FIGURE 5.39: TA spectra of the Pd sample before exposition MOF coating (black), after the initial MOF coating i.e. two 30*min* dips noted $MOF-1$ (blue) and after the second MOF coating i.e. two 40*min* dips noted $MOF-2$ (red).

The SEM images of the second exposure of sample (A) to the MOF solution as well as sample (B) and its control are shown in figure 5.40.a.b. and c. respectively. Let's first comment figure a. which is of sample (A) after the second two 40*min* exposures to the MOF solution. The SEM image clearly shows that the sample is completely covered with the MOF layer. Although not shown in the image, MOF nanoparticles had formed and were observed deposited on the sample. The profilometric analysis revealed a new thickness of $\approx 300nm$. The TA spectrum after the second exposure is also plotted in figure 5.39. The spectrum, this time, does not have the same shape, but rather exhibits an oscillation due to interference within the now relatively thick MOF layer. Nevertheless, the slope in the near IR is still steep enough for real time TAS measurements. Sample (B) on the other hand exhibits a well crystallised MOF layer, however cracks have formed which reveal the Pd nanostructure beneath it. One has to note though that the charging induced by the SEM increases the separation (images of such effect are shown in appendix A.4). Nevertheless, these cracks would lead to direct exposure of the Pd substrate to the gas mixture, thus defeating the purpose of the protecting layer. Lastly, the control sample for sample (B), shown in figure 5.40.c., shows a completely chaotic deposition of the MOF.

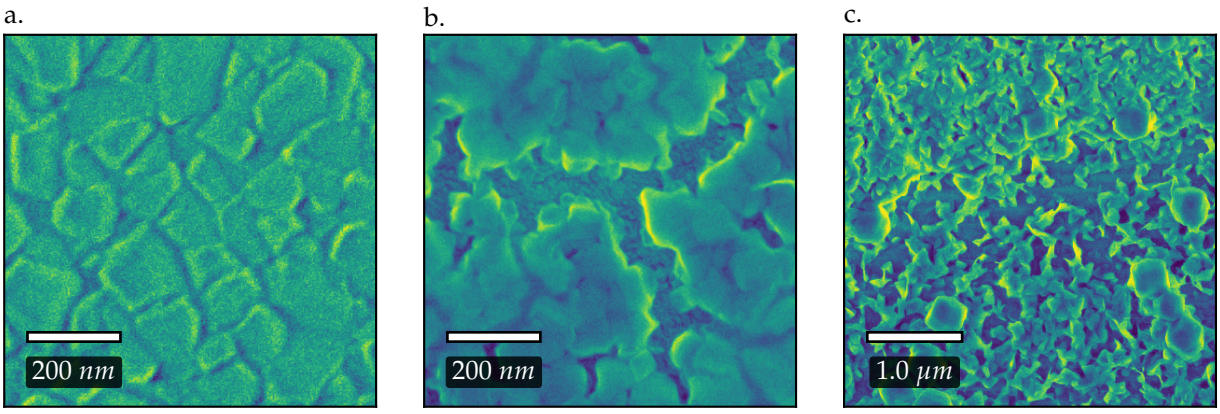

FIGURE 5.40: SEM images of the different samples coated with MOF. a. is the same sample as discussed in figure 5.38 after a second, two 40min dips in the MOF solution, noted $MOF-2$. b. shows the image of another Pd which was exposed for 3 hours to the MOF solution. c. shows the glass control for image b. which was also dipped for 3 hours in the MOF solution.

These morphological results indicate that the multiple dippings of the Pd samples in the MOF solution help making a homogeneous uniform layer free of cracks which the Pd well covered. It also shows that the Pd is a good growing surface for the MOF. XRD spectra were taken at each steps of the synthesis and compared to simulated data taken from ref. [v73]. The results are plotted in figure 5.41. The simulated spectra shows characteristic peaks at 2θ = 7.4, 10.5, 12.8 and 18°. We can see that these main peaks are observed for all samples though for Sample (A): MOF-1 and the control of sample(B), a broad increase in intensity is seen between 2θ = 20 and 30°. This is likely due to poorly crystallised MOF. Furthermore a broad peak is seen on the control substrate at about 2θ = 9.5°, the origin of which is unknown though may come from the poorly formed MOF as seen in figure 5.40.c.

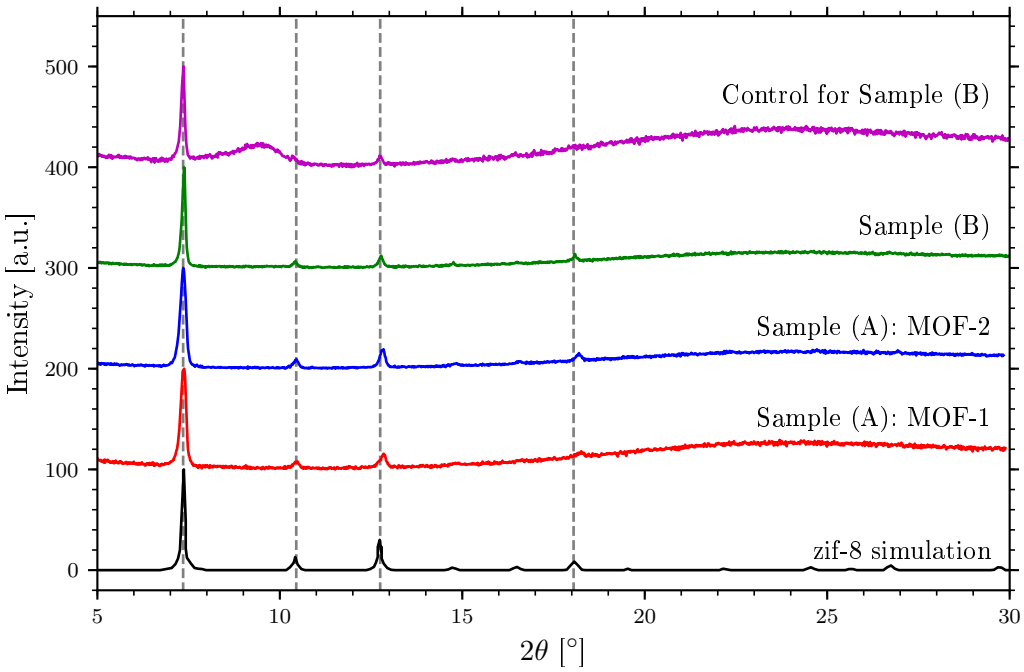

FIGURE 5.41: XRD spectra of all the different samples presented in this section. The simulation of the zif-8 was taken from ref. [v73]. The baselines were adjusted in intensity every 100 for clarity. The measurements were done by Antoine Tissot and Shan Dai at the materials institute of Paris ENS.

• Exposure of the MOF/*Pd* samples to H_2 and air cycles

In order to see the effect of the MOF on the sensing capabilities of the Pd samples, sample (A) was exposed initially to cycles of H_2 in Ar and then to H_2 in air at decreasing partial pressures from 100% H_2 to 0.004% H_2 in air. The results are plotted in figure 5.42 for sample (A) (MOF-1). The initial gas cycles between Ar and H_2/Ar reveal the same behaviour as before with the formation of the $\alpha-$phase yielding an increase in the TA signal. At t = 1400s, the sample was exposed to dry air. The signal is seen to increase slowly to about the same intensity as the initial cycles with H_2/Ar. The effect is thus the same as that see in figure 5.33.a. This indicates that the MOF layer is not impermeable to O_2 and thus does not prevent oxidation of the Pd sample. Nevertheless, two cycles at 100% H_2 and air were undertaken and showed a rapid increase in the signal when exposed to H_2 and decrease when exposed back to air. As seen before, the decrease when exposed to air brings the signal lower as when the H_2 was introduced. The cycles were repeated at 4% H_2/air with the same overall behaviour. At 0.25% though the signal behaves much differently as before. This is best seen in the zoomed in view in figure 5.42.b. The exposure to the H_2 mixture leads to a rapid signal decrease and saturation until the sample is exposed to air. The exposure to the air further changes the behaviour with a sharp second decrease in the signal before a slow increase up to near the signal intensity before exposure to the H_2 mixture. The cycle under 0.25% was repeated three times with the same behaviour. At t = 7800s, the sample was exposed to 0.06% H_2/air. The signal is seen to decrease slower that the precedent cycles. However, this time, the exposure to air, did not lead to a shape decrease before a steady increase, but only the latter effect is seen. Again the cycles at this partial pressure was repeated thrice with the same effect. At partial pressures of 0.015% and 0.004% the same behaviour is seen though with a less intense decrease in signal. A last point to observe is that from the initial exposure to air, till the end of the measurement, the overall signal is steadily increasing.

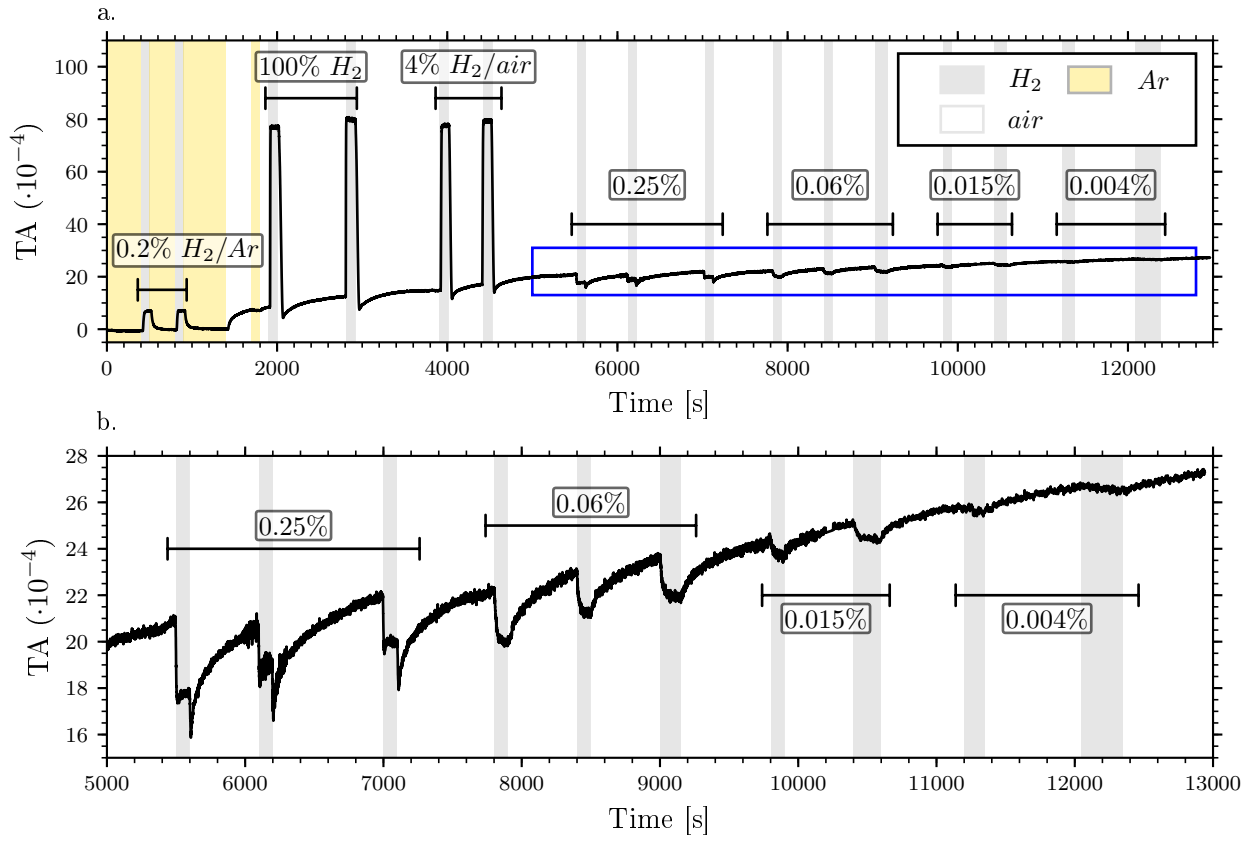

FIGURE 5.42: Real time monitoring of the TA response of sample $MOF-1$ when exposed to different concentration of H_2 in air from 100% H_2 down to 0.004%. b. is a zoomed in view of a. represented by the blue square.

Understanding the data would require much more investigation, though using the mechanism proposed in section 5.6.1, we may propose the following qualitative interpretation. The initial exposure to air leads to a slow oxidation of the Pd sample which is continuous throughout the experiment. The initial exposures to 100% and 4% H_2, then to air, leads to consecutive reduction and oxidation of the metal as previously discussed. At 0.25%, the signal is only seen to decrease, which would indicate that the H_2 in the mixture reduces the Pd near its metallic state and might have started to hydrogenate it. It is also possible that some areas of the metal are hydrogenised whilst others are oxidised. This would explain the rapid decrease after exposure to air, which would rapidly decrease the amount of metal hydride before slowly oxidising the metal. At lower pressures, the H_2 in the mixture is not sufficient to hydrogenise the metal, and thus only the reduction towards a *less* oxidised state is observed. One may note that this mechanism does not account for the possible formation of H_2O, as further investigation would be needed to elucidate the actual reaction mechanism.

Although these results show that the MOF layer investigated here, did not prevent oxidation of the metal surface, the experiment was repeated after three days under a small overpressure of $\approx 1200 mbar$ of air. The question was to see whether the sample was still reactive. Figure 5.43 shows the cycles at 0.25% and 0.06% H_2 in air. On the left hand side the graphs represent the cycles taken from figure 5.42 and on the right hand side, those done after the three day exposure. The intensity of the TA was adjusted to compensate the overall increase of the signal as the sample oxidised. The amplitude of the signals are unchanged. At both partial pressures we can see that the overall behaviour is the same before and after the three day wait.

Indeed at 0.25%, the initial decrease after exposure to the gas H_2 (Fig. 5.43.a.) is also seen on on figure 5.43.b. though the kinetics are slower. Likewise when the sample is re-exposed to air, the signal decreases rapidly and then steadily increases. The same can be said for 0.06% with the overall effect reproduced (Fig. 5.43.c. and d.).

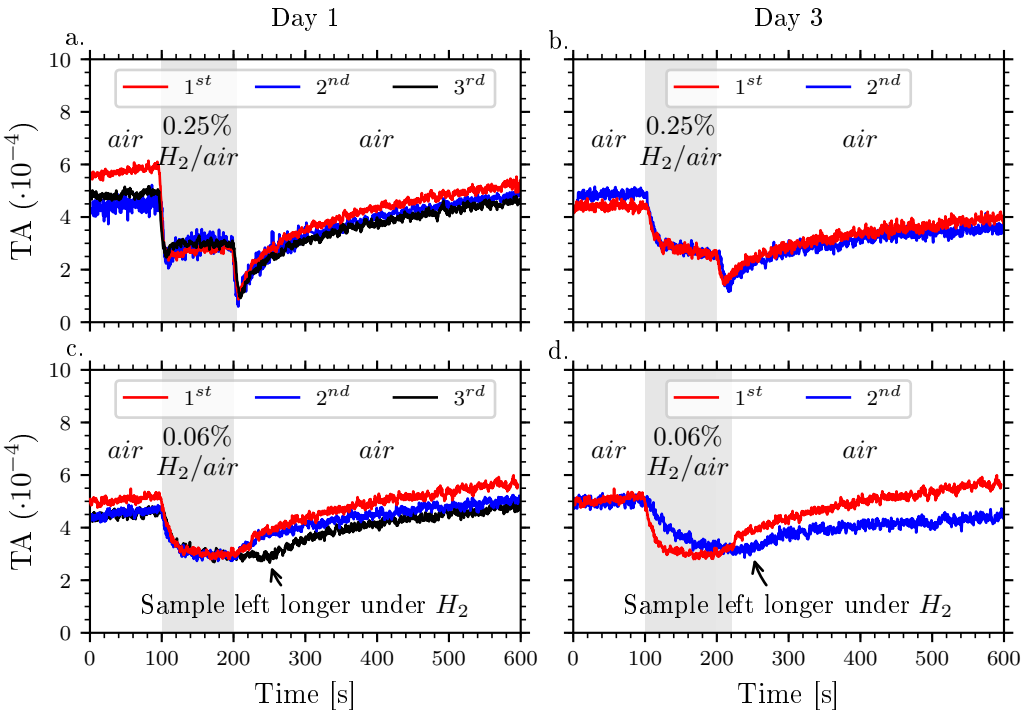

FIGURE 5.43: Cycles done on the $MOF-1$ sample with three days interval at two different concentration of H_2 in air. Multiple cycles were done and are adjusted in time to all start at zero. Their intensity was also adjusted to compensate the steady increase due to the slow oxidation of the sample. The amplitude of the signal was not modified.

Although no data is shown here for the sample without MOF, the sample does not react to the H_2 without initial annealing after being left in air for several days. This means that the use of the MOF coating did indeed help improve the stability of the Pd sensor. Yet, the imperfectly crystallised MOF layer may be responsible for the permeability to O_2 and thus the oxidation of the Pd nanostructure. Thus why sample (A) was re-exposed to MOF in order to complete the protective coating. The H_2/air cycle experiment was repeated on sample (A) after the second exposure to the MOF solution (MOF-2). The results are shown in figure 5.44. Overall the behaviour is the same with a steady increase of the base signal as it undergoes H_2/air cycles meaning that oxidation of the Pd still occurs. The initial exposures to 100% H_2 and 4% H_2/air also exhibit large signal increase. Although the signal is noisier than in the previous experiment (due to unoptimised settings of the TAS), at 0.25% a similar effect, as previously, is observed, that is a rapid initial decrease of the TA signal. However, this time the signal increases whilst still under H_2/air. This may be explained by discrepancies in the H_2/air concentration compared to the previous experiments, and thus enough H_2 is present to initiate a hydrogenation of the Pd metal which would induce an increase in the TA signal. The next exposure to air leads the signal to decrease before steadily increasing again. At lower pressures only the decrease is seen and even at 0.001% partial pressures, a small decrease in the signal may be observed. The interpretation of this data is the same as previously discussed.

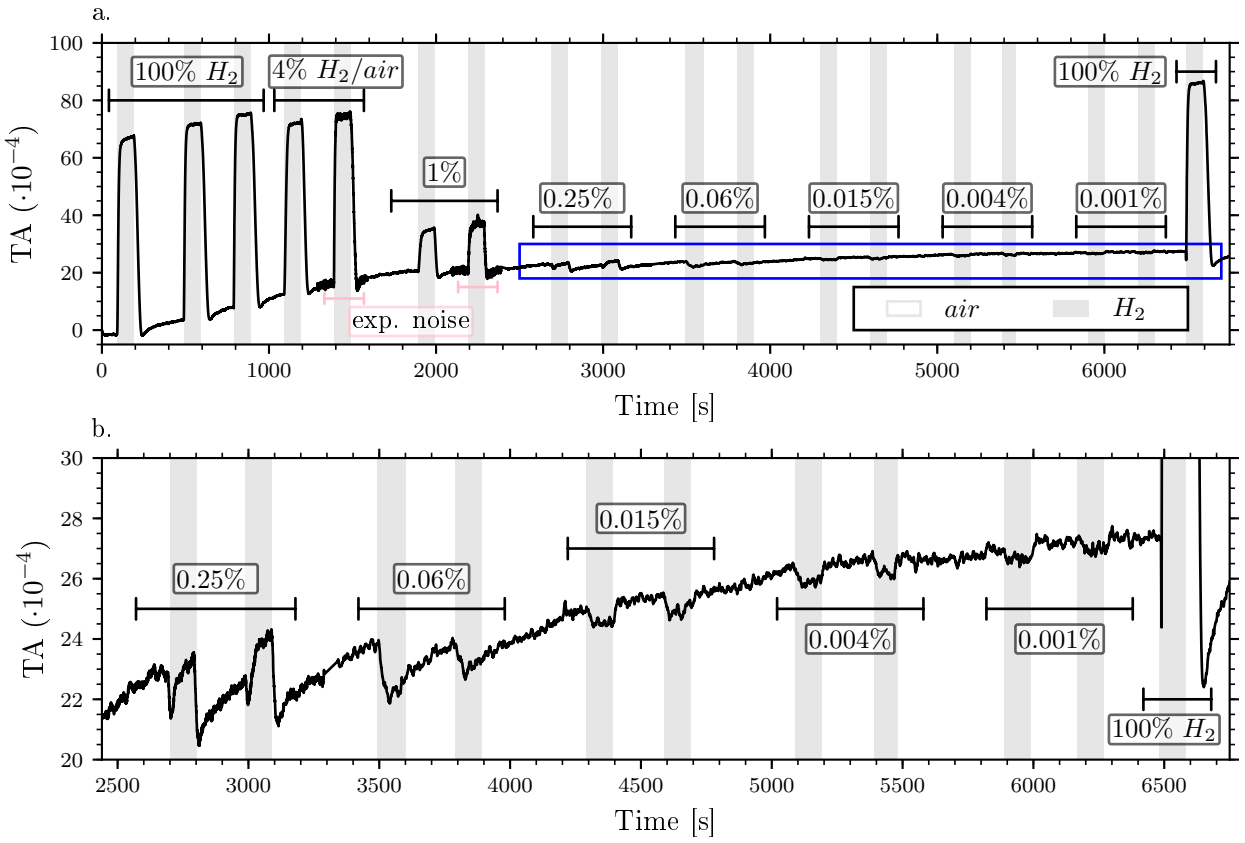

FIGURE 5.44: Real time monitoring of sample $MOF-2$ when exposed to different concentration of H_2 in air from 100% H_2 down to 0.001% of H_2 in air. b. shows a zoomed in view of a. indicated by the blue square. The pink interval corresponds to an increase in the noise of the signal due to a change in the integration constant of the lock-in amplifier.

The steady increase of the signal shows that, although the sample was completely covered with a well formed MOF layer, it was not sufficient to prevent oxidation. Nevertheless, the sensitivity was kept decent, although the signal to noise ratio could be improved. Amelioration of the system may also be done by selecting a MOF with smaller pores which would prevent O_2 from entering the protective layer whilst still allowing H_2 to seep through.

5.7 Summary and perspectives

In this chapter, we have seen than Pd can be used, in conjunction with Au anisotropic LSPR samples, to increase the sample's sensitivity to H_2 in an inert carrier gas. These experiments also demonstrated that increasing the amount of Pd increased the sensitivity of the system down to a few parts per million of H_2. Investigation towards direct Pd sensors revealed that Pd nanostructures do exhibit anisotropic LSPR which could be used for sensing applications.

The absorption of H_2 leads to the formation of palladium hydride. The isotherm reveals that depending on the partial pressure of H_2, different phases are formed. The $\alpha-$phase corresponds to a low amount of diluted H in the metal structure, whereas the $\beta-$phase corresponds to a high amount of adsorbed H. In between the two phases is the hybrid $\alpha+\beta$ phase which relies in a narrow partial pressure interval around

1%. Regardless, the formation of metal hydride leads to a distinct change in the dielectric function of the metal which thus modifies the optical response of the material. Using analytical models, the behaviour of the experimental anisotropic spectra, at different degrees of hydrogenation, could easily be reproduced. This enabled us to verify that the changes in the optical response were indeed due to the absorption of hydrogen which led to a change in the dielectric function of the metal and not due to the known expansion Pd undergoes when it absorbs hydrogen. At least, this effect was found to be minor and was neglected.

Gas cycles of H_2 in Ar, at different partial pressures of H_2, were undertaken whilst monitoring the TA at a single wavelength. With this method partial pressures as low as a 0.001%, equivalent to $10ppm$ could be measured with high reproducibility. Moreover, the sample spontaneously regenerated when purged with Ar to near its initial state. Analysis of the amplitude of the TA change, ΔS, enabled the determination of the H/Pd ratio giving a quantitative characteristic of the method, especially in the $\alpha-$phase, which is indeed most interesting for sensing applications.

The response times were investigated and revealed to be strongly dependent on the partial pressure of H_2. Two characteristic times may be distinguished. On the one hand, t_{detect}, that is the time it takes to register the presence of H_2, yields qualitative information, suitable for leak detection and other safety applications. Depending on the partial pressure, it was less that $1s$ in the $\beta-$phase and in the order of a few dozens of seconds in the $\alpha-$phase. On the other hand, t_{90} , which corresponds to the time it takes to reach 90% of the signal, gives quantitative information on the amount of H_2 in the carrier gas. It is again highly dependent on the partial pressure. For the $\beta-$phase, it was found to be from 4 to $30s$ whilst in the $\alpha-$phase, it was between 1 to 2 minutes. These response times are above the $1s$ mark required for industrial application, however do reveal the potential of the method as it is usable for any partial pressures of H_2, at room temperature, whereas alternative methods, in the literature, did show equivalent if not better response times, though only function in narrow partial pressure intervals and/or require heating at a few hundred degrees Celsius.

In order to investigate the reaction mechanism and thus improvement possibilities, the $\alpha-$phase's kinetics of absorption and desorption were studied. A possible reaction model was drawn to account for the reversible adsorption and desorption on and off the metal surface as well as the absorption and emptying to and from the bulk. By fitting the rate constants, the experimental data were well fitted by considering the partial pressure of H_2 in Ar and fitting the four rate constants. The rigorous model does indeed fit the data and accounted for the decrease in time constant during the absorption when the H_2 partial pressure was decreased. Yet, in order to better understand the mechanisms at play and determine where the bottleneck would occur, two boundary conditions were considered. The first condition was by considering the limiting process being the reactivity of the surface, the second being the reactivity of the bulk. With these considerations, it was proposed that for the desorption process, the limiting process was indeed the surface reactivity, whereas, for the absorption, it was the bulk. To improve the model, one could account for the physisorption step in the reaction mechanism. Indeed, due to the presence of the carrier gas, one could propose that as Ar physisorbs on the surface, it would, thus occupy reactive sites required for the dissociative adsorption of H_2. This does, however, increase the complexity of the model and was not considered as the effect seemed negligible. Nevertheless, it is not straight forwards how the reaction rate could be increased as it is strongly dependent on the chemistry of Pd and not so much on the geometry of the nanoparticles.

Preliminary investigation in O_2 and in dry and humid air were undertaken to see whether the simple Pd sensor can be applicable as is in real world conditions. The results reveal an oxidation of the Pd when it is exposed to O_2. This leads to a competition between the oxidation and hydrogenation of the metal when it is exposed to H_2 in an oxygen containing carrier gas. Both H_2 and O_2 have the same effect of increasing the

TA but with different kinetics. Exposing the sample to water vapour did not, at first prevent the reactivity of Pd as the same amount of hydrogenation was recorded, though the rate of absorption was heavily slowed down. However, long exposure to humid air inhibited the sample's response to low partial pressure of H_2.

Preliminary work was also done with the use of the zif-8 metal oxide framework as a protective layer against contaminants such as water, hydrocarbons and oxygen. The sample was covered with a few hundred nanometres of the MOF. It exhibited a high sensitivity towards H_2 in air compared to the sample without the MOF layer, though it did not prevent oxidation. Further work is required to see its efficiency against humid and contaminated air.

The capability of associating indirect or direct Pd-based sensor with TAS is a promising lead for H_2 sensing. Further work is required to evaluate the large potential of this method as there is room for improvement. One promising perspective would be to substitute the TAS apparatus with a waveplate and a set of two polarisers. This would enable to simplify the set up by using a single wavelength LED and thus remove the monochromator and the bulky lock-in amplifier and thus enable miniaturisation of the apparatus. This point is only mentioned in the perspectives of this chapter as no scientific study was done on the subject.

5.8 References

[v1] B. D. Adams and A. Chen, "The role of palladium in a hydrogen economy", *Materials Today*, vol. 14, no. 6, pp. 282–289, 2011.

[v2] N. P. Brandon and Z. Kurban, "Clean energy and the hydrogen economy", *Philosophical Transactions of the Royal Society A: Mathematical, Physical and Engineering Sciences*, vol. 375, no. 2098, p. 20 160 400, 2017.

[v3] V. G. Dovì, F. Friedler, D. Huisingh, and J. J. Klemeš, "Cleaner energy for sustainable future", *Journal of Cleaner Production*, vol. 17, no. 10, pp. 889–895, 2009.

[v4] I. Dincer and C. Acar, "A review on clean energy solutions for better sustainability", *International Journal of Energy Research*, vol. 39, no. 5, pp. 585–606, 2015.

[v5] G. W. Crabtree, M. S. Dresselhaus, and M. V. Buchanan, "The Hydrogen Economy", *Physics Today*, vol. 57, no. 12, pp. 39–44, 2004.

[v6] A. Midilli and I. Dincer, "Hydrogen as a renewable and sustainable solution in reducing global fossil fuel consumption", *International Journal of Hydrogen Energy*, vol. 33, no. 16, pp. 4209–4222, 2008.

[v7] NASA, "Safety Standard for Hydrogen and Hydrogen Systems", Tech. Rep., 1997, b–37.

[v8] D. Imamura, M. Akai, and S. Watanabe, "Exploration of hydrogen odorants for fuel cell vehicles", *Journal of Power Sources*, vol. 152, no. 1-2, pp. 226–232, 2005.

[v9] T. Hübert, L. Boon-Brett, G. Black, and U. Banach, "Hydrogen sensors – A review", *Sensors and Actuators B: Chemical*, vol. 157, no. 2, pp. 329–352, 2011.

[v10] B. Sharma, A. Sharma, and J.-S. Kim, "Recent advances on H 2 sensor technologies based on MOX and FET devices: A review", *Sensors and Actuators B: Chemical*, vol. 262, pp. 758–770, 2018.

[v11] A. Katsuki and K. Fukui, "H2 selective gas sensor based on SnO2", *Sensors and Actuators B: Chemical*, vol. 52, no. 1-2, pp. 30–37, 1998.

[v12] S. J. McKeown and L. L. Goddard, "Reflective Palladium Nanoapertures on Fiber for Wide Dynamic Range Hydrogen Sensing", *IEEE Journal of Selected Topics in Quantum Electronics*, vol. 23, no. 2, pp. 263–268, 2017.

[v13] N. Javahiraly, "Review on hydrogen leak detection: comparison between fiber optic sensors based on different designs with palladium", *Optical Engineering*, vol. 54, no. 3, p. 030 901, 2015.

[v14] J. Dai, L. Zhu, G. Wang, F. Xiang, Y. Qin, M. Wang, and M. Yang, "Optical Fiber Grating Hydrogen Sensors: A Review", *Sensors*, vol. 17, no. 3, p. 577, 2017.

[v15] Y.-n. Zhang, H. Peng, X. Qian, Y. Zhang, G. An, and Y. Zhao, "Recent advancements in optical fiber hydrogen sensors", *Sensors and Actuators B: Chemical*, vol. 244, pp. 393–416, 2017.

[v16] C. Wadell, S. Syrenova, and C. Langhammer, "Plasmonic Hydrogen Sensing with Nanostructured Metal Hydrides", *ACS Nano*, vol. 8, no. 12, pp. 11 925–11 940, 2014.

[v17] G. Behzadi pour and L. Fekri aval, "Highly sensitive work function hydrogen gas sensor based on PdNPs/SiO_2/Si structure at room temperature", *Results in Physics*, vol. 7, pp. 1993–1999, 2017.

[v18] K. Aoki, "Applicability of palladium membrane for the separation of protium and deuterium", *International Journal of Hydrogen Energy*, vol. 23, no. 5, pp. 325–332, 1998.

[v19] F. D. Manchester, A. San-Martin, and J. M. Pitre, "The H-Pd (hydrogen-palladium) System", *Journal of Phase Equilibria*, vol. 15, no. 1, pp. 62–83, 1994.

[v20] P. Johnson and R. Christy, "Optical constants of transition metals: Ti, V, Cr, Mn, Fe, Co, Ni, and Pd", *Physical Review B*, vol. 9, no. 12, pp. 5056–5070, 1974.

[v21] K. Sugawa, H. Tahara, A. Yamashita, J. Otsuki, T. Sagara, T. Harumoto, and S. Yanagida, "Refractive index susceptibility of the plasmonic palladium nanoparticle: Potential as the third plasmonic sensing material", *ACS Nano*, vol. 9, no. 2, pp. 1895–1904, 2015.

[v22] I. Zorić, E. M. Larsson, B. Kasemo, and C. Langhammer, "Localized Surface Plasmons Shed Light on Nanoscale Metal Hydrides", *Advanced Materials*, vol. 22, no. 41, pp. 4628–4633, 2010.

[v23] R. Bardhan, L. O. Hedges, C. L. Pint, A. Javey, S. Whitelam, and J. J. Urban, "Uncovering the intrinsic size dependence of hydriding phase transformations in nanocrystals", *Nature Materials*, vol. 12, no. 10, pp. 905–912, 2013.

[v24] W. E. Vargas, D. E. Azofeifa, N. Clark, H. Solis, F. Montealegre, and M. Cambronero, "Parametric formulation of the dielectric function of palladium and palladium hydride thin films", *Applied Optics*, vol. 53, no. 24, p. 5294, 2014.

[v25] V. M. Silkin, R. Díez Muiño, I. P. Chernov, E. V. Chulkov, and P. M. Echenique, "Tuning the plasmon energy of palladium–hydrogen systems by varying the hydrogen concentration", *Journal of Physics: Condensed Matter*, vol. 24, no. 10, p. 104 021, 2012.

[v26] N. Clark, W. E. Vargas, and D. E. Azofeifa, "Dielectric function of Pd hydride thin films in terms of hydrogen concentration and film's thickness: A parametric formulation", *Journal of Alloys and Compounds*, vol. 645, no. S1, S320–S324, 2015.

[v27] A. L. Bugaev, A. A. Guda, K. A. Lomachenko, V. V. Srabionyan, L. A. Bugaev, A. V. Soldatov, C. Lamberti, V. P. Dmitriev, and J. A. van Bokhoven, "Temperature- and Pressure-Dependent Hydrogen Concentration in Supported PdH x Nanoparticles by Pd K-Edge X-ray Absorption Spectroscopy", *The Journal of Physical Chemistry C*, vol. 118, no. 19, pp. 10 416–10 423, 2014.

[v28] R. Kirchheim, T. M. I. Tschele, W. Kieninger, T. Mutschele, H. Gleiter, R. Birringer, and T. Koble, "Hydrogen in amorphous and nanocrystalline metals", *Materials Science and Engineering*, vol. 99, no. 1-2, pp. 457–462, 1988.

[v29] N. J. Halas, S. Lal, W.-S. Chang, S. Link, and P. Nordlander, "Plasmons in Strongly Coupled Metallic Nanostructures", *Chemical Reviews*, vol. 111, no. 6, pp. 3913–3961, 2011.

[v30] C. Langhammer, E. M. Larsson, B. Kasemo, and I. Zorić, "Indirect nanoplasmonic sensing: Ultrasensitive experimental platform for nanomaterials science and optical nanocalorimetry", *Nano Letters*, vol. 10, no. 9, pp. 3529–3538, 2010.

[v31] N. Liu, M. L. Tang, M. Hentschel, H. Giessen, and A. P. Alivisatos, "Nanoantenna-enhanced gas sensing in a single tailored nanofocus", *Nature Materials*, vol. 10, no. 8, pp. 631–636, 2011.

[v32] R. Jiang, F. Qin, Q. Ruan, J. Wang, and C. Jin, "Ultrasensitive Plasmonic Response of Bimetallic Au/Pd Nanostructures to Hydrogen", *Advanced Functional Materials*, vol. 24, no. 46, pp. 7328–7337, 2014.

[v33] C. Wadell, F. A. A. Nugroho, E. Lidström, B. Iandolo, J. B. Wagner, and C. Langhammer, "Hysteresis-Free Nanoplasmonic Pd–Au Alloy Hydrogen Sensors", *Nano Letters*, vol. 15, no. 5, pp. 3563–3570, 2015.

[v34] A. Yang, M. D. Huntington, M. F. Cardinal, S. S. Masango, R. P. Van Duyne, and T. W. Odom, "Hetero-oligomer nanoparticle arrays for plasmon-enhanced hydrogen sensing", *ACS Nano*, vol. 8, no. 8, pp. 7639–7647, 2014.

[v35] C. Wadell and C. Langhammer, "Drift-corrected nanoplasmonic hydrogen sensing by polarization", *Nanoscale*, vol. 7, no. 25, pp. 10 963–10 969, 2015.

[v36] H. Fredriksson, Y. Alaverdyan, A. Dmitriev, C. Langhammer, D. S. Sutherland, M. Zäch, and B. Kasemo, "Hole–Mask Colloidal Lithography", *Advanced Materials*, vol. 19, no. 23, pp. 4297–4302, 2007.

[v37] M. Matuschek, D. P. Singh, H.-H. Jeong, M. Nesterov, T. Weiss, P. Fischer, F. Neubrech, and N. Liu, "Chiral Plasmonic Hydrogen Sensors", *Small*, vol. 14, no. 7, p. 1 702 990, 2018.

[v38] S. Syrenova, C. Wadell, and C. Langhammer, "Shrinking-hole colloidal lithography: Self-aligned nanofabrication of complex plasmonic nanoantennas", *Nano Letters*, vol. 14, no. 5, pp. 2655–2663, 2014.

[v39] A. Tittl, P. Mai, R. Taubert, D. Dregely, N. Liu, and H. Giessen, "Palladium-Based Plasmonic Perfect Absorber in the Visible Wavelength Range and Its Application to Hydrogen Sensing", *Nano Letters*, vol. 11, no. 10, pp. 4366–4369, 2011.

[v40] H. K. Yip, X. Zhu, X. Zhuo, R. Jiang, Z. Yang, and J. Wang, "Gold Nanobipyramid-Enhanced Hydrogen Sensing with Plasmon Red Shifts Reaching ≈140 nm at 2 vol% Hydrogen Concentration", *Advanced Optical Materials*, vol. 5, no. 24, p. 1 700 740, 2017.

[v41] D. Aspnes, "Optical properties of thin films", *Thin Solid Films*, vol. 89, no. 3, pp. 249–262, 1982.

[v42] X. Q. Zeng, M. L. Latimer, Z. L. Xiao, S. Panuganti, U. Welp, W. K. Kwok, and T. Xu, "Hydrogen Gas Sensing with Networks of Ultrasmall Palladium Nanowires Formed on Filtration Membranes", *Nano Letters*, vol. 11, no. 1, pp. 262–268, 2011.

[v43] M. Johansson, E. Skúlason, G. Nielsen, S. Murphy, R. M. Nielsen, and I. Chorkendorff, "Hydrogen adsorption on palladium and palladium hydride at 1 bar", *Surface Science*, vol. 604, no. 7-8, pp. 718–729, 2010.

[v44] R. Griessen, N. Strohfeldt, and H. Giessen, "Thermodynamics of the hybrid interaction of hydrogen with palladium nanoparticles", *Nature Materials*, vol. 15, no. 3, pp. 311–317, 2016.

[v45] V. M. Silkin, I. P. Chernov, P. M. Echenique, Y. M. Koroteev, and E. V. Chulkov, "Influence of hydrogen absorption on low-energy electronic collective excitations in palladium", *Physical Review B*, vol. 76, no. 24, p. 245 105, 2007.

[v46] C. K. Gupta, *Chemical Metallurgy*. Wiley-VCH Verlag GmbH & Co. KGaA, 2004, p. 273, ISBN: 9783527602001.

[v47] N. Lopez, Z. Łodziana, F. Illas, and M. Salmeron, "When Langmuir is too simple: H_2 dissociation on Pd(111) at high coverage.", *Physical review letters*, vol. 93, no. 14, p. 146 103, 2004.

[v48] T. Mitsui, M. K. Rose, E. Fomin, D. F. Ogletree, and M. Salmeron, "Dissociative hydrogen adsorption on palladium requires aggregates of three or more vacancies", *Nature*, vol. 422, no. 6933, pp. 705–707, 2003.

[v49] W. J. Buttner, M. B. Post, R. Burgess, and C. Rivkin, "An overview of hydrogen safety sensors and requirements", *International Journal of Hydrogen Energy*, vol. 36, no. 3, pp. 2462–2470, 2011.

[v50] T. Hübert, L. Boon-Brett, V. Palmisano, and M. Bader, "Developments in gas sensor technology for hydrogen safety", *International Journal of Hydrogen Energy*, vol. 39, no. 35, pp. 20 474–20 483, 2014.

[v51] S. S. Kalanur, Y.-A. Lee, and H. Seo, "Eye-readable gasochromic and optical hydrogen gas sensor based on CuS–Pd", *RSC Adv.*, vol. 5, no. 12, pp. 9028–9034, 2015.

[v52] K. Christmann, "Interaction of hydrogen with solid surfaces", *Surface Science Reports*, vol. 9, no. 1-3, pp. 1–163, 1988.

[v53] R. Delmelle and J. Proost, "An in situ study of the hydriding kinetics of Pd thin films", *Physical Chemistry Chemical Physics*, vol. 13, no. 23, p. 11 412, 2011.

[v54] C. Nyberg and C. G. Tengstål, "Adsorption and reaction of water, oxygen, and hydrogen on Pd(100): Identification of adsorbed hydroxyl and implications for the catalytic H_2–O_2 reaction", *The Journal of Chemical Physics*, vol. 80, no. 7, pp. 3463–3468, 1984.

[v55] R. H. Radzilowski and R. D. Pehlke, "Absorption of gaseous oxygen by liquid cobalt, copper, iron and nickel", *Metallurgical Transactions B*, vol. 9, no. 1, pp. 129–137, 1978.

[v56] C. J. Smithells and C. E. Ransley, "The Diffusion of Gases through Metals", *Proceedings of the Royal Society A: Mathematical, Physical and Engineering Sciences*, vol. 150, no. 869, pp. 172–197, 1935.

[v57] F. Mackenzie and J. Mackenzie, *Our changing planet*. Prentice Hall College Div, 1995, ISBN: 0132713217.

[v58] M. Gao, M. Cho, H.-J. Han, Y. S. Jung, and I. Park, "Palladium-Decorated Silicon Nanomesh Fabricated by Nanosphere Lithography for High Performance, Room Temperature Hydrogen Sensing", *Small*, vol. 14, no. 10, p. 1 703 691, 2018.

[v59] A. Baylet, P. Marécot, D. Duprez, P. Castellazzi, G. Groppi, and P. Forzatti, "In situ Raman and in situ XRD analysis of PdO reduction and Pd○ oxidation supported on γ-Al_2O_3 catalyst under different atmospheres", *Physical Chemistry Chemical Physics*, vol. 13, no. 10, p. 4607, 2011.

[v60] D. Wang and T. B. Flanagan, "Diffusion of oxygen in Pd", *Scripta Materialia*, vol. 52, no. 7, pp. 599–601, 2005.

[v61] R. Westerström, C. Weststrate, A. Resta, A. Mikkelsen, J. Schnadt, J. Andersen, E. Lundgren, M. Schmid, N. Seriani, J. Harl, F. Mittendorfer, and G. Kresse, "Stressing Pd atoms: Initial oxidation of the Pd(110) surface", *Surface Science*, vol. 602, no. 14, pp. 2440–2447, 2008.

[v62] G. Zheng and E. Altman, "The oxidation mechanism of Pd(100)", *Surface Science*, vol. 504, pp. 253–270, 2002.

[v63] D. Zemlyanov, B. Aszalos-Kiss, E. Kleimenov, D. Teschner, S. Zafeiratos, M. Hävecker, A. Knop-Gericke, R. Schlögl, H. Gabasch, W. Unterberger, K. Hayek, and B. Klötzer, "In situ XPS study of Pd(111) oxidation. Part 1: 2D oxide formation in 10^{-3}mbar O_2", *Surface Science*, vol. 600, no. 5, pp. 983–994, 2006.

[v64] H. H. Kan and J. F. Weaver, "Mechanism of PdO thin film formation during the oxidation of Pd(111)", *Surface Science*, vol. 603, no. 17, pp. 2671–2682, 2009.

[v65] G. Ketteler, D. F. Ogletree, H. Bluhm, H. Liu, E. L. D. Hebenstreit, and M. Salmeron, "In Situ Spectroscopic Study of the Oxidation and Reduction of Pd(111)", *Journal of the American Chemical Society*, vol. 127, no. 51, pp. 18 269–18 273, 2005.

[v66] H. H. Kan, R. B. Shumbera, and J. F. Weaver, "Adsorption and abstraction of oxygen atoms on Pd(111): Characterization of the precursor to PdO formation", *Surface Science*, vol. 602, no. 7, pp. 1337–1346, 2008.

[v67] P. O. Nilsson, "Optical properties of PdO in the range of 0.5-5.4 eV", *Journal of Physics C: Solid State Physics*, vol. 12, no. 7, pp. 1423–1427, 1979.

[v68] Y.-J. Chiang, K.-C. Li, Y.-C. Lin, and F.-M. Pan, "A mechanistic study of hydrogen gas sensing by PdO nanoflake thin films at temperatures below 250°C.", *Physical chemistry chemical physics : PCCP*, vol. 17, no. 5, pp. 3039–49, 2015.

[v69] D. Zemlyanov, B. Klötzer, H. Gabasch, A. Smeltz, F. H. Ribeiro, S. Zafeiratos, D. Teschner, P. Schnörch, E. Vass, M. Hävecker, A. Knop-Gericke, and R. Schlögl, "Kinetics of Palladium Oxidation in the mbar Pressure Range: Ambient Pressure XPS Study", *Topics in Catalysis*, vol. 56, no. 11, pp. 885–895, 2013.

[v70] A. U. Ortiz, A. P. Freitas, A. Boutin, A. H. Fuchs, and F.-X. Coudert, "What makes zeolitic imidazolate frameworks hydrophobic or hydrophilic? The impact of geometry and functionalization on water adsorption", *Phys. Chem. Chem. Phys.*, vol. 16, no. 21, pp. 9940–9949, 2014.

[v71] W.-T. Koo, S. Qiao, A. F. Ogata, G. Jha, J.-S. Jang, V. T. Chen, I.-D. Kim, and R. M. Penner, "Accelerating Palladium Nanowire H_2 Sensors Using Engineered Nanofiltration", *ACS Nano*, vol. 11, no. 9, pp. 9276–9285, 2017.

[v72] L. E. Kreno, J. T. Hupp, and R. P. Van Duyne, "Metal-Organic Framework Thin Film for Enhanced Localized Surface Plasmon Resonance Gas Sensing", *Analytical Chemistry*, vol. 82, no. 19, pp. 8042–8046, 2010.

[v73] T. Tian, M. T. Wharmby, J. B. Parra, C. O. Ania, and D. Fairen-Jimenez, "Role of crystal size on swing-effect and adsorption induced structure transition of ZIF-8", *Dalton Transactions*, vol. 45, no. 16, pp. 6893–6900, 2016.

Conclusion and perspectives

The aim of this work was to study and develop localised surface plasmon resonance (LSPR) based sensors using anisotropic spectroscopy. In this general conclusion we will summarise the methodology undertaken and introspect on the results to determine the possibilities and capabilities of the technique.

In chapter 1, we have thoroughly discussed the physical property that is LSPR and how it can be used for sensing applications. Indeed, the dependence of a metal's resonance on the changes in environment should it be through changes in the refractive index or due to charge transfers between the metal and adsorbed species inducing a shift in the resonance. Conventionally, this optical shift is measured using UV-Vis spectroscopy. We have seen that several limitations prevent this method from being applicable beyond ideal laboratory conditions. This is due to the fact that these methods measure absolute spectra. This means that they are sensitive to fluctuation in the environment such as the light source, outside light pollution or mechanical vibration. Moreover, the spectral measurement has the consequence that for higher sensitivity, one needs to use a higher resolution monochromator, which thus makes the system more expensive, bulky and overall less practical. Ultimately, the detection limitations are with the use of a monochromator. In order to circumvent these, we use transmission anisotropy spectroscopy (TAS) which measures a differential relative spectrum thus does not have the drawbacks mentioned above, but also enables measurement at a signal wavelength as the change in the anisotropy intensity is easily related to a spectral shift. This is a key property of the method as it therefore leaves the monochromator in the position of a calibration tool and not a measuring tool.

The second key aspect of the methodology is the use of globally anisotropic LSPR nanostructures. In this same chapter, we have discussed how measuring the difference in transmission yields a differential normalised spectrum but requires the sample to be macroscopically anisotropic in contrast to microscopic anisotropy. This can be done by organising or patterning the nanostructures so that the LSPR of the entire sample is polarisation dependent. In chapter 3, we have discussed different methods in the literature to obtain such samples. Nevertheless, the sample's requirements we have set were that the sample needed to be easily fabricated, and have a large covering of the surface with anisotropic nanostructure. The method needed also to yield as small as possible nanostructures in order to increase the surface area for reactivity as LSPR occurs at the surface of the particles. Lastly the method should be controllable and reproducible. All these requirements were set with industrial scalability in mind. The method chosen was oblique angle deposition which consists in evaporating the plasmonic metal at a grazing angle on a glass substrate. This yielded globally anisotropic samples which could be used in conjunction with TAS.

The samples were characterised by UV-Vis and TA spectroscopy for the optical properties, and atomic force (AFM) and scanning electron microscopy (SEM) to determine their morphology. These methods are not ideal to get the absolute representation of the nanostructures. Indeed, due to convolution between the tip and the sample, the AFM images only yields information on the height of the biggest particles, the SEM images on the other hand do show the cross-section of the particle relatively well, but no information regarding the height may be extracted. Furthermore, the fact the substrate is non conductive, the images were prone to charging and thus the resolution was not ideal to gather information on the exact shape of

the particles. Other methods such as transmission electron microscopy (TEM) could not be used as the substrate is part of the sample fabrication. Meaning that depositing the nanoparticles on the grid for TEM measurement is not straightforwards and could result in modification of the particle structure. Two metals were studied: gold and palladium. Due to their wetting properties, these two metals formed different type of nanostructures depending on the amount evaporated. The gold sample yielded isolated nanoparticles of about $10nm$ in width when little was evaporated, and elongated nanostructures when more was evaporated. Palladium, on the over hand, only formed discontinuous nanostructures which still exhibited spectral anisotropy. The use of analytical models enabled to well reproduce the experimental optical properties of the plasmonic nanostructures. Indeed, these methods cannot account for every physical aspect of the sample, and were in consequence simplified. They could, nonetheless, enable the understanding of the origin of the LSPR and determine which aspect could influence the resonance and induce shifts.

To study the capabilities of the method, two study cases were undertaken. The first case considered, in chapter 4, was to use pure gold nanoparticles and expose them to cycles of argon and dihydrogen. The goal was to understand what was the origin of the spectral shift observed when the sample was exposed to dihydrogen. Thanks to the sensitivity of the TAS, it was possible to deduce that, adding to what was known, dihydrogen dissociatively adsorbs on the particle's edges and corners, but also diffuse on the facets of the gold nanoparticles. This effect was not seen before as the sensitivity required for this observation is beyond the capacity of the conventional absolute method. Using analytical models and kinetic analysis, it was possible to determine the actual charge transfer in a single $\mathrm{H-Au}$ bond. This study case was not oriented towards sensing, but to use the high sensitivity to probe the reactivity of gold at the nanoscale, and determine its application for catalytic hydrogenation reactions.

The second case, studied in chapter 5, was to investigate the sensing capabilities of the method. Palladium was used as it selectively and strongly reacts with dihydrogen to form palladium hydride. This property is very much in use when dealing with hydrogen as it has many applications for storing or indeed, sensing. Two types of samples were fabricated. The initial work was to investigate indirect sensors with gold nanoparticles playing the role of the transducer and a thin layer of palladium evaporated on them to play the role of molecular sensors. The first sample only had a monoatomic thick layer and did exhibit a higher response towards dihydrogen enabling the sensing of partial pressures down to 0.001% in argon. Yet, when evaporating a $1nm$ layer, it increased the optical response to hydrogen much more, and the phase isotherm of palladium could be measured. It confirmed the fact that at low partial pressures, the phase obtained known as the $\alpha-$phase, only led to a very small change in optical response of the palladium compared to the $\beta-$phase obtained at higher partial pressures. Nonetheless, the dihydrogen was measured down to about $2ppm$ in argon. This initial work thus demonstrated the high capabilities and sensitivity of the TAS method. The second part of this chapter was to use pure palladium for direct sensing. This enables the simplification of the sample fabrication and was possible since palladium does, by itself, exhibit LSPR which is strongly modified when it absorbs hydrogen. Using thermodynamics studies, it was possible to relate the change in TA with the ratio H/Pd of adsorbed hydrogen. The sensitivity allowed to measure partial pressures down to about $10ppm$ with a rather low response time, less than 3minutes for the most difficult case, that is reaching 90% of the signal at $10ppm$.

The kinetic study of the $\alpha-$phase revealed that multiple mechanisms are at play when the Pd is exposed to $\mathrm{H_2}$. When the sample is exposed to different partial pressures of $\mathrm{H_2}$, the absorption kinetics is seen to be dependent on the partial pressure, as the lower it was, the longer it took to reach saturation. On the other hand, the desorption process was independent of the initial state of the metal hydride. The different steps were modelled by considering the adsorption/desorption from the surface and absorption/emptying

from the bulk. It was possible to fit both the absorption and desorption, which revealed that for either processes, the bulk and the surface, respectively become a bottleneck in the reactivity. The conclusion of this investigation was that the time response of the Pd is evidently strongly dependent on the chemistry of the metal and the diatomic gas. It is therefore not straight forwards how to decrease the response time of the metal for sensing applications as the geometry of the nanoparticle would not strongly change the reactivity. This would require further investigation especially as the effect of temperature, on this system, has not been yet investigated.

To determine the application of the method in *real-world* conditions, the experiment was repeated in dry and humid air at different dihydrogen partial pressures. The presence of dioxygen in these carrier gases led to an oxidation of the palladium which enters in competition with the formation of metal hydride. The sample thus exhibits a lower time response and sensitivity. Moreover, leaving the sample in these oxidising conditions for several days led to the inhibition of the sample towards hydrogen reactivity and it needed to be annealed and reactivated to recover its sensing capabilities.

To protect the sample from contaminants such a water and dioxygen, a metal oxide framework (MOF) zif-8 was deposited on the substrate. By adapting the protocol, it was possible to make a 200nm thick continuous layer on the palladium without cracks. The results revealed that zif-8 did not prevent the oxidation of the sample, but did seem to protect it against water as the sample was still reactive after 3 days left in air. More work is needed to determine the actual performance of this system and see whether a different MOF could be deposited to prevent oxidation altogether.

These study cases underline the capabilities of the method which indeed exhibit better performance than conventional techniques whilst simplifying the optical setup. This nonetheless comes to the detriment of harder sample fabrication.

There are many perspectives and other paths which would be very much interesting to investigate with this technique. Below is a list of such paths which were tested but not investigated.

• The first perspective is of course to elaborate different samples with different composition. For instance, working with metal alloys would enable to further tailor the shape of the anisotropy and increase the anisotropic signal. However, for sensing application, the key part is to investigate different molecular sensors which would be selective to different analytes. The field which would be easier to start this investigation is in the biological's or biomedical's. Indeed, the use of conventional LSPR sensors based on antibodies and enzymes is already quite studied. Applying these molecular compounds with anisotropic samples would be quite feasible. This would enable to increase the sensitivity of the sensing system, as lower shifts are measurable. This perspective inevitably leads to the second bullet.

• Using the TAS system in the liquid phase. Indeed, apart from technical difficulties of working in the liquid phase, it is possible to apply the anisotropic methodology to these media. Preliminary investigation was done in water and ethanol, but not reported here. The first challenge that was encountered was the fact that the change in refraction index of the medium when ethanol was added, led to a strong changes in the transmitted signal which led to artifacts. Furthermore, the presence of trapped bubbles makes it difficult to work in the transmission setup. These are only technical difficulties which can be overcome as they are already in commercial apparatus. Yet, it was realised that working in reflection could also easily circumvent the issue as the anisotropy is still measured and still sensitive to the changes in medium, however, the sensitivity is reduced this the light is not passing twice through the sample anymore. This thus leads to the third bullet.

• Using a mirror in front of the sample to multiply the number of passes. Every time the light passes through the sample, the transmission is elevated by a power of one. Using a mirror in front and behind

the sample, effectively making a mirror cavity would greatly increase the anisotropy. However, apart from the technical difficulty in aligning the optical setup, each passes reduces the intensity of the light due to the absorption of the sample. It is nevertheless feasible to do a few passes which increases the anisotropy and in turn the sensitivity. This point was tested in air, but could not in the gas cell due to the difficulty in alignment.

• As discussed in the last chapter, the use of the MOF layer allowed the protection of the palladium layer. A perspective of research could be to investigate other MOF to take advantage of their physical and chemical properties. Indeed, this field of chemistry is very vast and many types of MOF may be fabricated with the desired properties for protecting the sample. The difficulty resides into fabricating a continuous layer strongly bonded to the metal layer, as some MOF require fabrication conditions not compatible with the palladium sample. Furthermore, these MOF must not prevent light from reaching the sample when working in transmission, and must not exhibit any global anisotropy.

• The use of anisotropy is not limited to chemical sensing nor to metal LSPR. Indeed, a side investigation was to determine the possibilities of the method for gauge sensing, that is sensing the deformation of a sample. The idea was to embed gold nanoparticles in an elastic transparent substrate such a polydiméthylsiloxane (PDMS). If the concentration of nanoparticles is high enough, there should be interactions between the particles, though with no favored direction, which should thus lead to no anisotropic signal. However, by stretching the sample, the nanoparticles would be drawn away in the direction of stretching, which means that the particle-particle interactions would only occur normal to the direction of stretching. This has indeed been reported in the literature, however, with the use of anisotropic spectroscopy, the sensitivity should be increased. Preliminary results confirmed this effect. Moreover, they had also shown that the stretching led to anisotropy appearing in the PDMS, rendering the gold nanoparticles disposable. This illustrates that anisotropy in certain materials may be a way of analysing induced stresses and deformations with this spectroscopic technique.

• The last perspective proposed in this conclusion was mentioned at the end of the last chapter. It regards using a waveplate instead of the photo-elastic modulator (PEM). This wavelength specific waveplate imposes a retardation on the elliptical polarisation induced by the sample. Using the two polarisers and a single wavelength light source such as a laser, or LED would enable the extinction of the light at the detector. Changes in the optical response of the sample would lead to a change in the elliptical polarisation and thus to the increase of the light intensity on the detector. The apparatus is thus simplified as it does not require the use of a monochromator, nor does it need the lock-in amplifier. It thus enables the system to be greatly simplified and miniaturised. The proof of concept was done during this thesis, but further investigation is required to determine the capability of the method and the sensitivity limits for study cases such as that of hydrogen sensing.

This work therefore demonstrated how TAS can be used not only for fundamental analysis of anisotropic crystals but also for more applicable sensing and analysis of chemical reactivity when used in conjunction to plasmonic nanoparticles. It is therefore fair to say that the work undertaken in this thesis is more preliminary than final and much more investigation is possible to truly take advantage of the capabilities of LSPR combined with TAS.

Appendix A

Appendix

A.1 Tabulated dielectric functions for Cu, Ag, Au, Pd and PdH_x

Below are two tables showing the dielectric function values for Cu, Au, Ag and Pd experimentally determined by Johnson and Christy (Tab. A.1) [A1], [A2] as well as the theoretically determined dielectric function for Pd and PdH_x with x = 0.125, 0.333, 0.500 and 0.667 provided by Silkin et al. (Tab. A.2) [A3]. These latter values were taken from the plots provided in their publication.

TABLE A.1: Reproduction of the dielectric constants for copper, silver, gold and palladium provided by Johnson and Christy [A1], [A2]

	Copper		Silver		Gold		Palladium	
Energy [eV]	ε_1	ε_2	ε_1	ε_2	ε_1	ε_2	ε_1	ε_2
0.64	-179.18	29.28	-198.19	6.76	-189.04	25.36	-86.66	66.07
0.77	-123.08	16.90	-140.40	3.56	-125.35	12.56	-64.73	51.71
0.89	-88.73	11.33	-101.99	2.63	-90.43	8.19	-50.68	42.84
1.02	-67.75	7.92	-77.93	1.59	-66.22	5.70	-40.53	36.71
1.14	-51.96	5.20	-60.76	0.62	-51.05	3.86	-33.72	31.90
1.26	-41.13	4.11	-48.89	0.56	-40.27	2.79	-29.22	27.57
1.39	-33.18	3.46	-39.84	0.50	-32.04	1.93	-25.28	24.53
1.51	-26.76	2.69	-32.80	0.46	-25.81	1.63	-22.69	21.38
1.64	-21.70	2.24	-27.48	0.31	-20.61	1.27	-20.11	19.07
1.76	-17.64	1.77	-23.40	0.39	-16.82	1.07	-18.16	17.30
1.88	-13.99	1.65	-20.09	0.45	-13.65	1.04	-16.30	15.91
2.01	-10.18	1.92	-17.24	0.50	-10.66	1.37	-14.66	14.74
2.13	-6.82	3.79	-14.88	0.39	-8.11	1.66	-13.34	13.51
2.26	-5.60	5.26	-12.86	0.43	-5.84	2.11	-12.06	12.60
2.38	-5.41	6.15	-11.05	0.33	-3.95	2.58	-11.08	11.56
2.50	-5.09	6.26	-9.56	0.31	-2.28	3.81	-10.22	10.76
2.63	-4.60	6.21	-8.23	0.29	-1.70	4.84	-9.36	9.90
2.75	-4.21	5.94	-7.06	0.21	-1.76	5.28	-8.64	9.19
2.88	-3.75	5.76	-6.06	0.20	-1.69	5.65	-7.98	8.60
3.00	-3.23	5.65	-5.17	0.23	-1.70	5.72	-7.41	8.06
3.12	-2.74	5.59	-4.28	0.21	-1.65	5.74	-6.89	7.62
3.25	-2.41	5.44	-3.47	0.19	-1.60	5.64	-6.42	7.13
3.37	-2.05	5.37	-2.74	0.23	-1.40	5.61	-5.97	6.80
3.50	-1.79	5.25	-2.00	0.28	-1.23	5.60	-5.51	6.52
3.62	-1.62	5.07	-1.28	0.32	-1.31	5.54	-5.12	6.27
3.74	-1.52	4.88	-0.66	0.28	-1.36	5.57	-4.81	6.00
3.87	-1.27	4.92	0.50	0.64	-1.23	5.85	-4.39	5.86
3.99	-1.09	4.77	0.90	1.39	-1.24	5.79	-4.06	5.69
4.12	-0.86	4.70	0.87	2.58	-1.23	5.78	-3.80	5.50
4.24	-0.65	4.64	0.58	3.23	-1.31	5.60	-3.58	5.26
4.36	-0.56	4.74	0.39	3.56	-1.33	5.49	-3.36	5.14
4.49	-0.58	4.81	0.22	3.75	-1.37	5.28	-3.12	5.07
4.61	-0.68	4.84	0.02	3.79	-1.35	4.98	-3.06	4.87
4.74	-0.87	4.77	-0.10	3.74	-1.24	4.72	-3.01	4.68

4.86	-1.04	4.91	-0.17	3.71	-1.08	4.49	-2.89	4.51
4.98	-1.30	4.89	-0.21	3.64	-0.89	4.34	-2.79	4.30
5.11	-1.44	4.82	-0.21	3.58	-0.74	4.16	-2.72	4.06
5.23	-1.61	4.61	-0.23	3.50	-0.62	4.06	-2.65	3.82
5.36	-1.70	4.41	-0.20	3.47	-0.55	3.89	-2.52	3.61
5.48	-1.73	4.17	-0.22	3.39	-0.42	3.83	-2.39	3.40
5.60	-1.74	3.93	-0.24	3.36	-0.35	3.71	-2.25	3.24
5.73	-1.72	3.67	-0.30	3.26	-0.23	3.61	-2.06	3.09
5.85	-1.64	3.43	-0.32	3.18	-0.13	3.51	-1.93	2.94
5.98	-1.54	3.23	-0.33	3.10	-0.01	3.39	-1.80	2.78
6.10	-1.42	3.07	-0.36	2.98	0.14	3.40	-1.66	2.67
6.22	-1.27	2.93	-0.33	2.91	0.20	3.33	-1.53	2.55
6.35	-1.13	2.79	-0.32	2.81	0.29	3.29	-1.41	2.48
6.47	-1.02	2.64	-0.31	2.71	0.30	3.18	-1.29	2.41
6.60	-0.90	2.51	-0.32	2.59	0.23	3.04	-1.20	2.32

TABLE A.2: Reproduction of the dielectric constants for Palladium and PdH_x with x = 0.125, 0.333, 0.500 and 0.667 provided by Silkin et al., the values were interpolated from the plots available in their publication [A3]

	Palladium		$PdH_{0.125}$		$PdH_{0.333}$		$PdH_{0.500}$		$PdH_{0.667}$	
Energy [eV]	ε_1	ε_2	ε_1	ε_2	ε_1	ε_2	ε_1	ε_2	ε_1	ε_2
1.00	-41.90	36.90	-44.89	43.47	-50.16	50.40	-39.30	31.37	-38.30	40.39
1.05	-38.68	34.60	-40.85	41.75	-45.47	43.11	-35.37	29.09	-34.63	37.27
1.10	-35.89	32.53	-37.82	40.20	-41.65	38.73	-31.51	27.02	-30.82	33.65
1.15	-33.44	30.68	-33.50	38.74	-38.21	35.86	-28.03	25.24	-28.16	30.93
1.20	-31.32	29.01	-30.75	37.30	-34.20	32.97	-24.63	23.75	-25.46	28.38
1.25	-29.49	27.49	-30.16	35.84	-31.43	30.61	-21.44	22.51	-23.29	25.92
1.30	-27.91	26.10	-29.11	34.36	-29.11	28.78	-19.13	21.50	-21.06	24.39
1.35	-26.57	24.84	-27.91	32.79	-26.93	27.23	-17.41	20.65	-19.01	22.84
1.40	-25.40	23.68	-26.19	31.19	-25.01	25.71	-16.06	19.93	-17.73	21.46
1.45	-24.22	22.61	-25.06	29.61	-23.30	24.32	-14.87	19.29	-16.55	20.36
1.50	-23.09	21.61	-24.00	28.10	-21.78	23.05	-13.64	18.70	-15.35	19.47
1.55	-22.02	20.69	-22.99	26.66	-20.39	21.87	-12.42	18.11	-14.27	18.68
1.60	-21.00	19.83	-22.00	25.31	-19.12	20.79	-11.56	17.48	-13.29	17.81
1.65	-20.06	19.02	-21.01	24.08	-17.96	19.77	-10.82	16.94	-12.35	16.96
1.70	-19.16	18.27	-20.06	22.93	-16.89	18.86	-10.16	16.44	-11.41	16.20
1.75	-18.32	17.57	-19.15	21.86	-15.89	18.03	-9.56	15.96	-10.55	15.50
1.80	-17.52	16.91	-18.30	20.88	-14.96	17.28	-8.99	15.52	-9.85	14.85
1.85	-16.77	16.30	-17.52	19.97	-14.10	16.60	-8.43	15.10	-9.22	14.20
1.90	-16.07	15.72	-16.79	19.13	-13.30	15.99	-7.90	14.70	-8.60	13.58
1.95	-15.40	15.18	-16.10	18.36	-12.56	15.43	-7.42	14.33	-7.91	13.01
2.00	-14.77	14.67	-15.46	17.64	-11.88	14.89	-6.97	13.97	-7.21	12.50
2.05	-14.18	14.19	-14.85	16.95	-11.25	14.39	-6.55	13.62	-6.52	12.09
2.10	-13.63	13.72	-14.26	16.28	-10.66	13.94	-6.16	13.29	-5.87	11.75

2.15	-13.11	13.28	-13.69	15.65	-10.12	13.52	-5.80	12.98	-5.25	11.47
2.20	-12.62	12.87	-13.15	15.06	-9.62	13.13	-5.44	12.69	-4.67	11.28
2.25	-12.16	12.46	-12.64	14.50	-9.15	12.78	-5.11	12.42	-4.15	11.15
2.30	-11.73	12.08	-12.14	13.98	-8.71	12.46	-4.80	12.18	-3.70	11.07
2.35	-11.33	11.71	-11.67	13.50	-8.30	12.16	-4.51	11.97	-3.31	11.01
2.40	-10.95	11.35	-11.21	13.05	-7.91	11.89	-4.25	11.78	-3.00	10.94
2.45	-10.58	11.00	-10.74	12.63	-7.56	11.64	-4.02	11.61	-2.76	10.84
2.50	-10.22	10.66	-10.29	12.25	-7.23	11.40	-3.81	11.45	-2.58	10.75
2.55	-9.88	10.33	-9.85	11.89	-6.93	11.17	-3.63	11.30	-2.44	10.68
2.60	-9.56	10.02	-9.44	11.56	-6.66	10.95	-3.50	11.16	-2.34	10.67
2.65	-9.24	9.72	-9.04	11.26	-6.42	10.74	-3.38	11.03	-2.26	10.67
2.70	-8.95	9.44	-8.67	10.98	-6.19	10.50	-3.29	10.88	-2.21	10.66
2.75	-8.66	9.17	-8.33	10.73	-5.99	10.26	-3.21	10.74	-2.16	10.64
2.80	-8.39	8.92	-8.04	10.50	-5.80	10.02	-3.14	10.59	-2.14	10.55
2.85	-8.13	8.68	-7.80	10.29	-5.62	9.79	-3.09	10.45	-2.12	10.42
2.90	-7.88	8.45	-7.58	10.09	-5.45	9.56	-3.05	10.30	-2.11	10.27
2.95	-7.64	8.24	-7.38	9.90	-5.28	9.33	-3.01	10.15	-2.12	10.11
3.00	-7.42	8.03	-7.20	9.71	-5.10	9.11	-2.98	9.99	-2.14	9.95
3.05	-7.20	7.84	-7.03	9.53	-4.92	8.90	-2.95	9.83	-2.21	9.79
3.10	-6.99	7.65	-6.87	9.35	-4.74	8.68	-2.92	9.64	-2.28	9.62
3.15	-6.80	7.47	-6.71	9.13	-4.57	8.48	-2.90	9.45	-2.34	9.45
3.20	-6.60	7.30	-6.54	8.90	-4.40	8.28	-2.88	9.25	-2.36	9.27
3.25	-6.41	7.14	-6.38	8.67	-4.24	8.09	-2.86	9.05	-2.36	9.08
3.30	-6.23	7.00	-6.22	8.44	-4.08	7.90	-2.83	8.85	-2.35	8.88
3.35	-6.05	6.86	-6.07	8.21	-3.92	7.73	-2.81	8.65	-2.33	8.66
3.40	-5.87	6.73	-5.91	7.99	-3.77	7.56	-2.77	8.45	-2.31	8.41
3.45	-5.69	6.60	-5.76	7.77	-3.62	7.42	-2.74	8.25	-2.27	8.16
3.50	-5.52	6.48	-5.60	7.57	-3.47	7.30	-2.71	8.07	-2.22	7.91
3.55	-5.35	6.37	-5.44	7.37	-3.33	7.18	-2.67	7.88	-2.14	7.69
3.60	-5.19	6.26	-5.28	7.18	-3.20	7.07	-2.62	7.70	-2.06	7.48
3.65	-5.03	6.17	-5.12	7.00	-3.07	6.96	-2.56	7.53	-1.99	7.29
3.70	-4.88	6.08	-4.96	6.83	-2.95	6.87	-2.50	7.36	-1.92	7.11
3.75	-4.74	6.00	-4.80	6.67	-2.83	6.77	-2.43	7.19	-1.85	6.96
3.80	-4.60	5.92	-4.64	6.51	-2.73	6.68	-2.37	7.02	-1.78	6.82
3.85	-4.46	5.84	-4.48	6.36	-2.62	6.58	-2.30	6.87	-1.72	6.68
3.90	-4.33	5.76	-4.32	6.23	-2.53	6.48	-2.23	6.72	-1.66	6.56
3.95	-4.21	5.68	-4.17	6.11	-2.43	6.38	-2.16	6.57	-1.59	6.42
4.00	-4.09	5.60	-4.02	6.00	-2.35	6.29	-2.11	6.43	-1.49	6.29
4.05	-3.98	5.54	-3.87	5.89	-2.26	6.19	-2.07	6.29	-1.39	6.16
4.10	-3.88	5.47	-3.73	5.79	-2.19	6.10	-2.02	6.16	-1.30	6.03
4.15	-3.79	5.41	-3.59	5.71	-2.11	6.01	-1.98	6.03	-1.24	5.90
4.20	-3.70	5.35	-3.46	5.62	-2.05	5.92	-1.94	5.90	-1.18	5.76
4.25	-3.61	5.27	-3.34	5.55	-1.98	5.83	-1.90	5.78	-1.13	5.63
4.30	-3.53	5.20	-3.23	5.50	-1.93	5.74	-1.85	5.65	-1.09	5.51
4.35	-3.46	5.13	-3.13	5.45	-1.87	5.66	-1.81	5.54	-1.06	5.38
4.40	-3.38	5.06	-3.03	5.40	-1.82	5.57	-1.76	5.42	-1.02	5.26

4.45	-3.31	4.99	-2.94	5.36	-1.78	5.48	-1.70	5.30	-0.97	5.15
4.50	-3.24	4.93	-2.86	5.32	-1.75	5.40	-1.65	5.19	-0.91	5.05
4.55	-3.17	4.87	-2.79	5.28	-1.72	5.31	-1.60	5.07	-0.86	4.98
4.60	-3.11	4.80	-2.74	5.23	-1.68	5.22	-1.54	4.96	-0.81	4.89
4.65	-3.05	4.74	-2.70	5.18	-1.65	5.12	-1.48	4.84	-0.77	4.80
4.70	-2.99	4.68	-2.66	5.12	-1.61	5.02	-1.42	4.72	-0.73	4.66
4.75	-2.94	4.62	-2.63	5.05	-1.57	4.93	-1.35	4.60	-0.69	4.49
4.80	-2.88	4.56	-2.61	4.98	-1.51	4.83	-1.27	4.48	-0.62	4.31
4.85	-2.83	4.50	-2.58	4.90	-1.45	4.74	-1.20	4.37	-0.56	4.12
4.90	-2.78	4.44	-2.56	4.83	-1.38	4.64	-1.14	4.26	-0.52	3.97
4.95	-2.74	4.38	-2.53	4.75	-1.31	4.55	-1.08	4.15	-0.49	3.84
5.00	-2.69	4.32	-2.48	4.66	-1.23	4.45	-1.02	4.04	-0.47	3.72
5.05	-2.64	4.25	-2.44	4.57	-1.15	4.36	-0.98	3.95	-0.46	3.62
5.10	-2.60	4.19	-2.39	4.48	-1.08	4.27	-1.00	3.85	-0.44	3.54
5.15	-2.55	4.12	-2.34	4.38	-1.00	4.19	-1.02	3.76	-0.44	3.48
5.20	-2.51	4.06	-2.29	4.28	-0.91	4.10	-1.04	3.67	-0.46	3.43
5.25	-2.46	3.99	-2.24	4.19	-0.83	4.02	-1.06	3.58	-0.53	3.36
5.30	-2.41	3.92	-2.20	4.09	-0.76	3.94	-1.07	3.50	-0.61	3.28
5.35	-2.36	3.85	-2.15	4.00	-0.68	3.87	-1.07	3.41	-0.66	3.20
5.40	-2.31	3.77	-2.10	3.91	-0.62	3.81	-1.06	3.32	-0.66	3.12
5.45	-2.25	3.70	-2.06	3.83	-0.55	3.76	-0.96	3.22	-0.59	3.07
5.50	-2.20	3.62	-2.01	3.76	-0.51	3.71	-0.83	3.13	-0.43	3.04
5.55	-2.14	3.54	-1.96	3.69	-0.48	3.66	-0.69	3.04	-0.06	3.03
5.60	-2.08	3.45	-1.92	3.61	-0.46	3.61	-0.54	2.95	0.39	3.02
5.65	-2.01	3.37	-1.87	3.55	-0.44	3.56	-0.37	2.87	0.85	3.02
5.70	-1.94	3.27	-1.82	3.48	-0.42	3.52	-0.20	2.79	1.24	3.02
5.75	-1.86	3.18	-1.77	3.41	-0.40	3.47	-0.03	2.73	1.46	3.02
5.80	-1.79	3.08	-1.72	3.35	-0.37	3.42	0.14	2.67	1.63	3.02
5.85	-1.70	2.98	-1.67	3.28	-0.34	3.37	0.29	2.62	1.79	3.03
5.90	-1.61	2.87	-1.62	3.22	-0.29	3.31	0.45	2.57	1.97	3.04
5.95	-1.52	2.76	-1.57	3.15	-0.25	3.26	0.60	2.54	2.14	3.05
6.00	-1.42	2.64	-1.51	3.09	-0.19	3.21	0.74	2.51	2.28	3.07

A.2 Supplementary information regarding the UV-Vis measurements from section 3.2

In section 3.2, we discussed the fabrication of Au samples using oblique angle deposition. The UV-Vis spectra measured for the samples #1A to #5C before annealing were poorly measured due to technical difficulties. Unfortunately, these same samples were then annealed which meant that the original spectra could not be corrected. Nevertheless, after annealing at 140°C for 10min in air, the samples displayed spectra very similar to the original measurement as shown in figure A.1. Therefore, the measurement cannot give quantitative information on the optical properties of the samples, but it is still reasonable to extract a qualitative behaviour of the samples' optical responses and their dichroic nature.

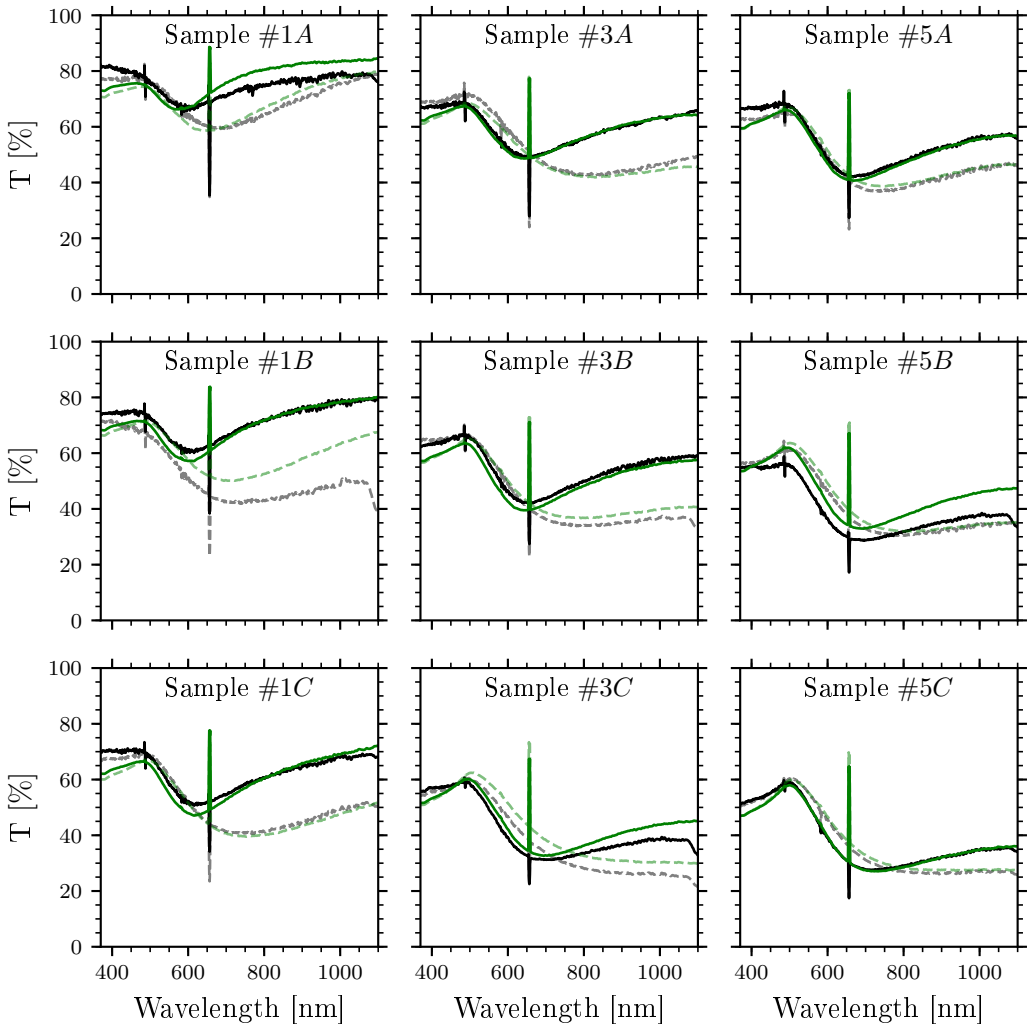

FIGURE A.1: UV-Vis transmission spectra of the Au discussed in section 3.2 before annealing (black) and after annealing for 10min at 140° (green). The spectra were taken using polarised light parallel (solid) and normal (dashed) to the direction of evaporation.

A.3 Example purging of a Au sample with H_2 and Arcycles

Figure A.2 shows an example of purging of the gas cell whilst following the TA of the sample, in this case Au. At first, the sample is exposed to Ar which leads to a decrease of the signal from $\approx 1 \cdot 10^{-4}$ to $\approx -2 \cdot 10^{-4}$. At 250s the sample is exposed to H_2 which leads to another decrease in TO to around -2. At 520s the sample is exposed again to Ar which leads to a last decrease in the TA. After that exposure of about 100s to H_2 are repeated three times at 700s, 1500s and 2800s. The signal is overall increasing though stabilises at the end. The injection of H_2 led to an increase in TA. At 3400s the polariser is relative to adjust the signal back around zero. where the experimental cycles are then undertaken.

The point of this graph is not to try and understand the mechanism occurring in the initial stage. Although it would be interesting to understand why the effect of H_2 is opposite to what expected, the atmosphere is not controlled at first. Nevertheless, the cycles at the end of the purging are reproducible.

It can be noted that the purging is quite rapid and is finished after 1h, however, the reproducibility of the experiment demonstrated that it is sufficient.

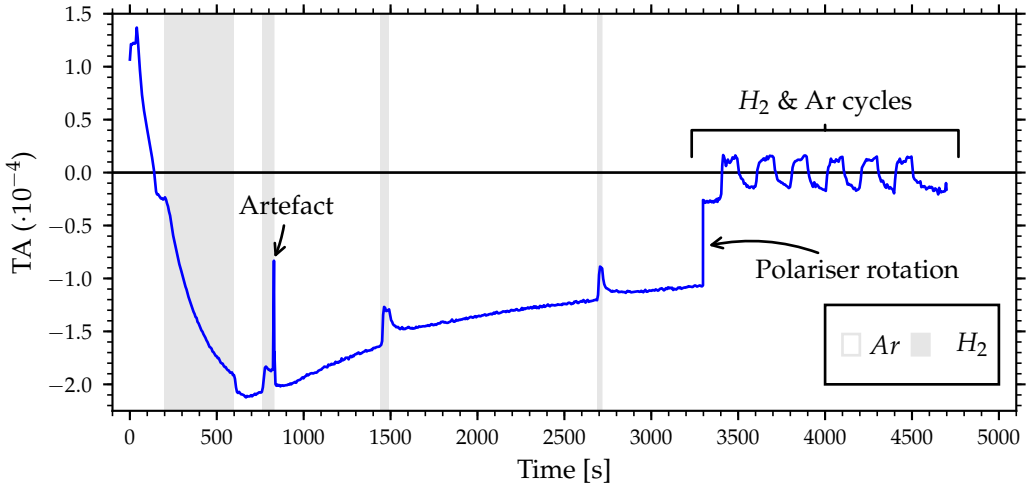

FIGURE A.2: Purging cycle before gas cycles between Ar and H_2 of a Au sample studied in section 4.3

A.4 Effect of charging on SEM images of MOF

In section 5.6.3, we discuss the use of zif-8 metal oxide frameworks for protecting the Pd nanostructure against contaminants for H_2 sensing. For this, we have used SEM to characterise the morphology of the MOF film and determine the coverage quality. In figure 5.40, we see two samples coated with the MOF layer, one having a continuous coverage of the nanostructure, the other exhibiting clear cracks through which the Pd nanostructure may be seen. Through the measurement process, it was revealed that charging of the sample occurred which led to a modification of the MOF layer. This is illustrated in figure A.3, which is exactly the same sample as figure 5.40.b. though measured in a different area. The two images of the figure shown here are of the same location taken a few minutes apart. What can be seen is that, the grain joints of the crystal islands (light yellow) ar charging which led to electronic repulsions and thus to an increase in the cracking of the sample. This image was included in the appendix as it clearly illustrates the effect of the measurement on the morphology, which led, as it was observed to a its modification.

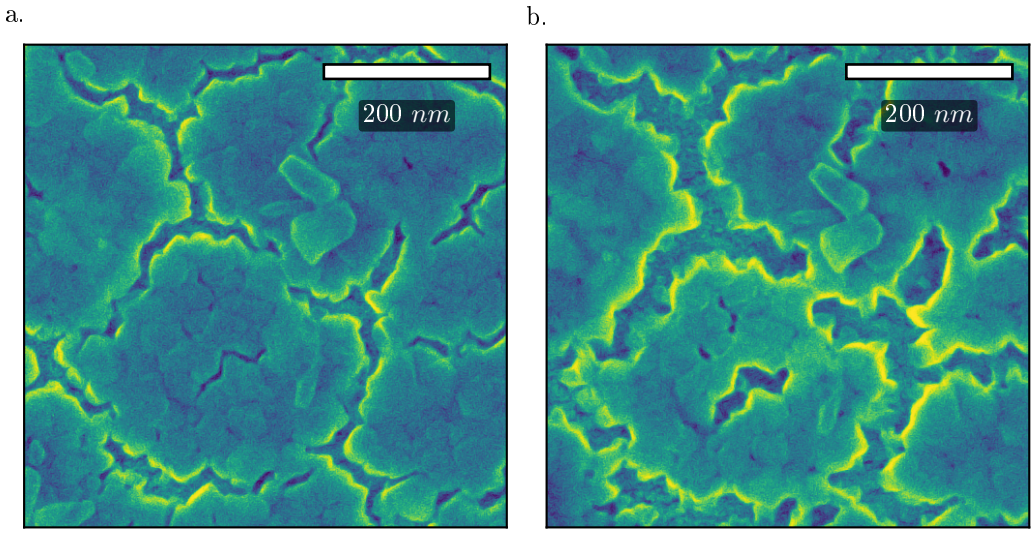

FIGURE A.3: Pd sample exposed for 3 hours to the MOF solution. The image was taken at the same area on the sample a few minutes apart. a. was taken before b. The image shows how charging degrades the MOF layer. This figure is related to section 5.6.3 in the main text

A.5 AFM and SEM images of the Au studied in chapter 4

In chapter 4 we have studied six different samples which were characterised by UV-Vis and TA spectroscopy which are shown for every sample in the main text. To characterise the morphology i.e. the height and average width of the particle, AFM and SEM images were taken for each sample. The former was done by scratching the metal layer with a plastic tweezers to remove the metal and allow the AFM tip to measure the height. A histogram was determined from the SEM images for each sample. In the next pages, the characterisation images are printed for each sample summarised in table A.3.

TABLE A.3: Table summarising six samples with different amount of Au evaporated. The height was determined by AFM and the average diameter using SEM images.

Sample number	Fig. 4.9	*Height* [nm]	d_{eff} [nm]	d_{max} [nm]	$Height/d_{max}$
#1	d.	9.66	16.45	27	0.4
#2	e.	12.34	18.67	34	0.4
#3	a.	7.80	12.12	21	0.4
#4	f.	8.15	13.81	23	0.4
#5	b.	10.00	16.68	28	0.4
#6	c.	8.09	12.54	22	0.4

A.5.1 Sample 1

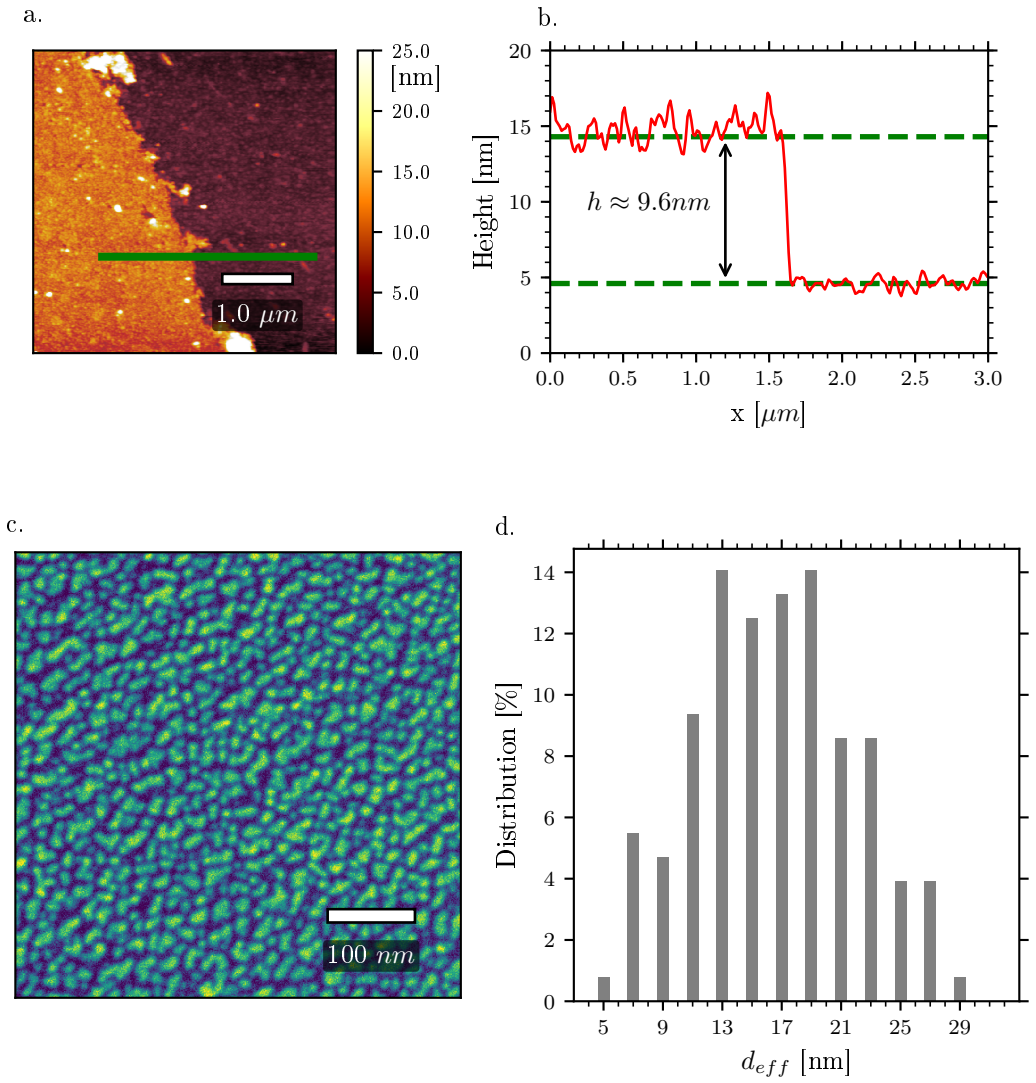

FIGURE A.4: Characterisation images of sample #1. a. shows the AFM image of the sample. The green line shows where the topography shown in b. was recorded and used to measure the height of the sample. c. shows the SEM image of the sample with d. the histogram of the average diameter of the nanoparticles shown in the SEM image.

A.5.2 Sample 2

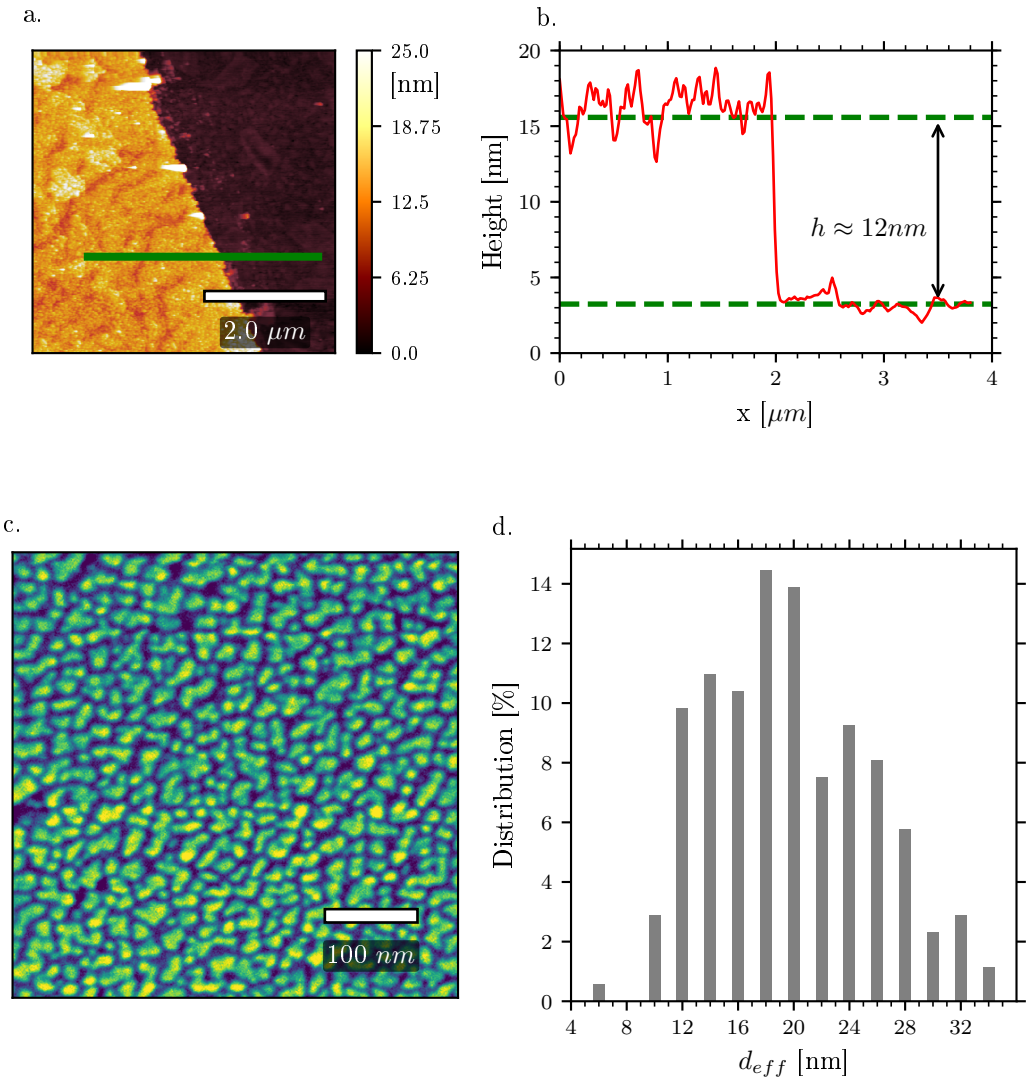

FIGURE A.5: Characterisation images of sample #2. a. shows the AFM image of the sample. The green line shows where the topography shown in b. was recorded and used to measure the height of the sample. c. shows the SEM image of the sample with d. the histogram of the average diameter of the nanoparticles shown in the SEM image.

A.5.3 Sample 3

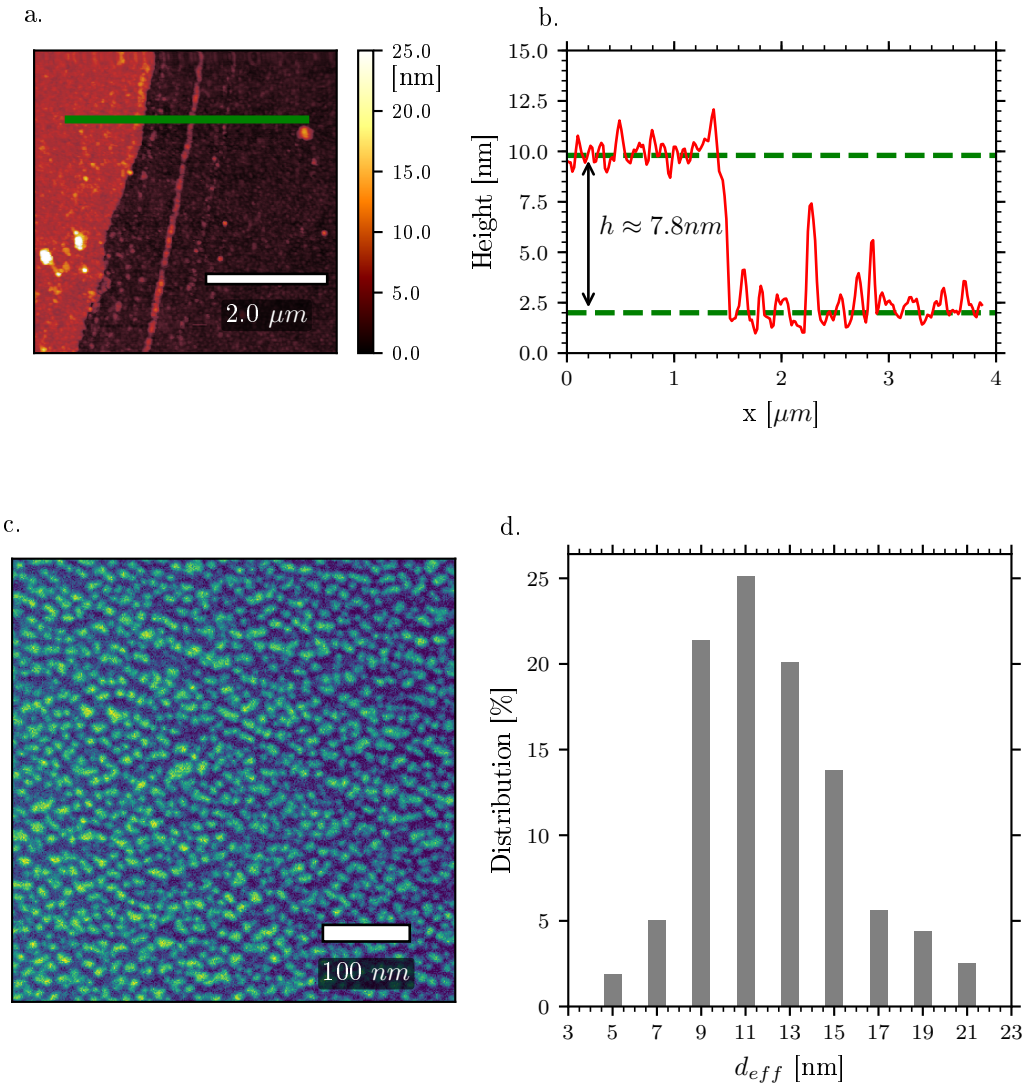

FIGURE A.6: Characterisation images of sample #3. a. shows the AFM image of the sample. The green line shows where the topography shown in b. was recorded and used to measure the height of the sample. c. shows the SEM image of the sample with d. the histogram of the average diameter of the nanoparticles shown in the SEM image.

A.5.4 Sample 4

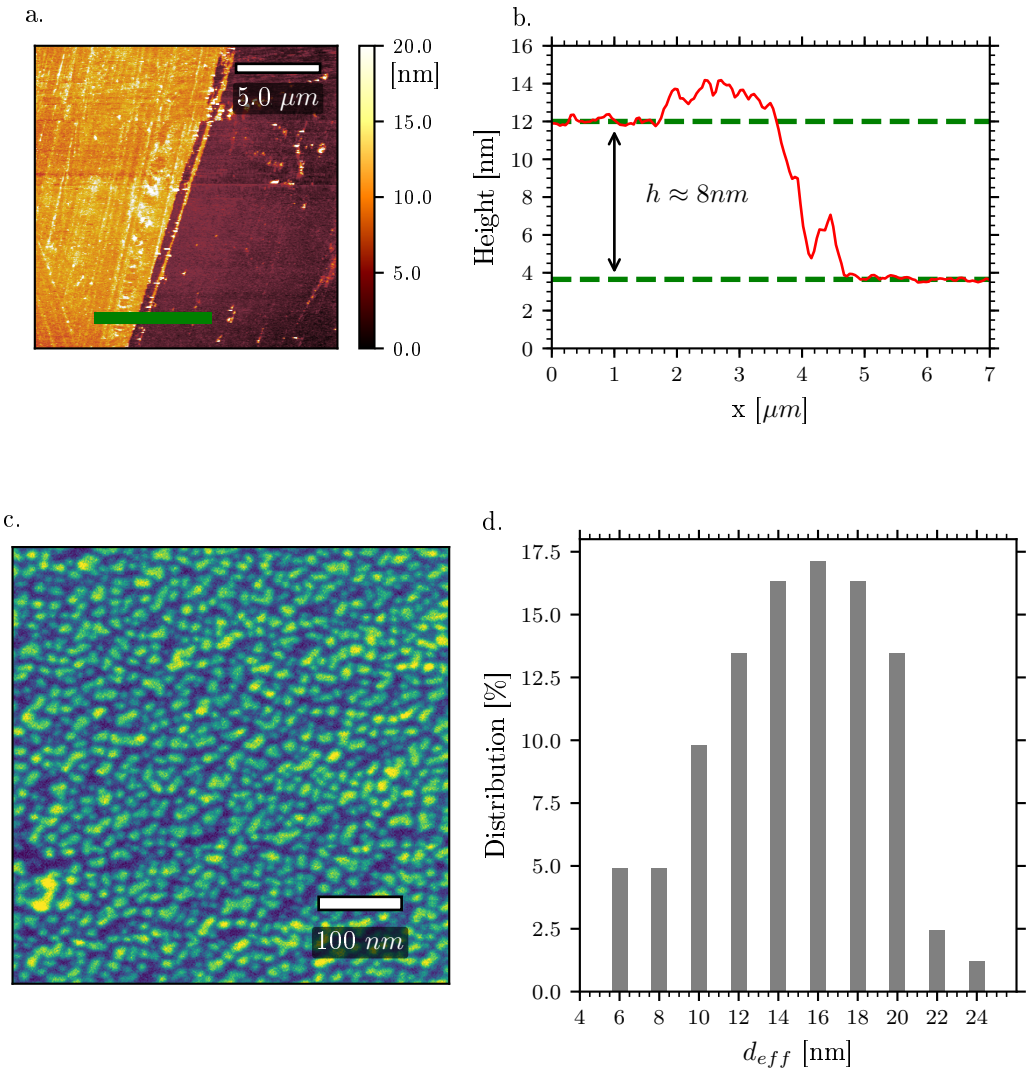

FIGURE A.7: Characterisation images of sample #4. a. shows the AFM image of the sample. The green line shows where the topography shown in b. was recorded and used to measure the height of the sample. c. shows the SEM image of the sample with d. the histogram of the average diameter of the nanoparticles shown in the SEM image.

A.5.5 Sample 5

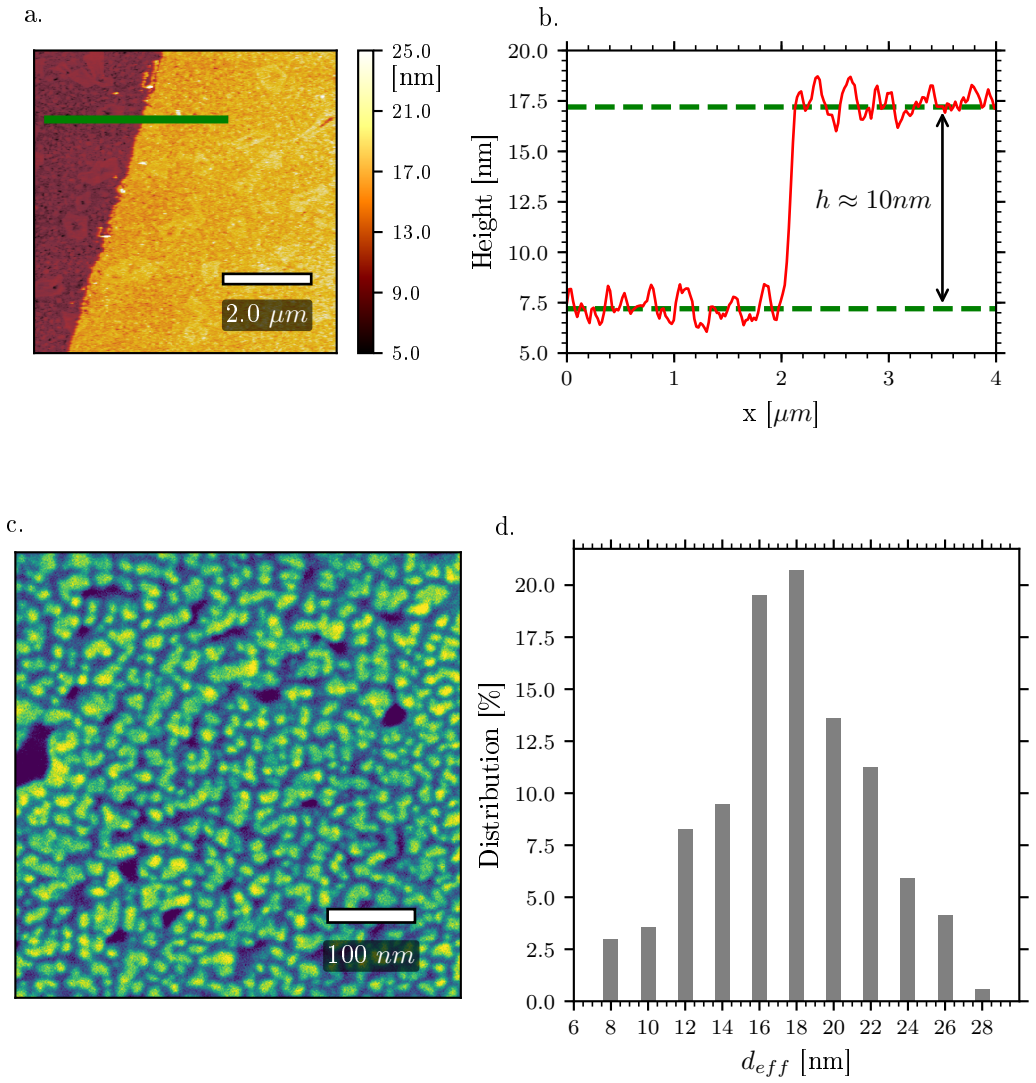

FIGURE A.8: Characterisation images of sample #5. a. shows the AFM image of the sample. The green line shows where the topography shown in b. was recorded and used to measure the height of the sample. c. shows the SEM image of the sample with d. the histogram of the average diameter of the nanoparticles shown in the SEM image.

A.5.6 Sample 6

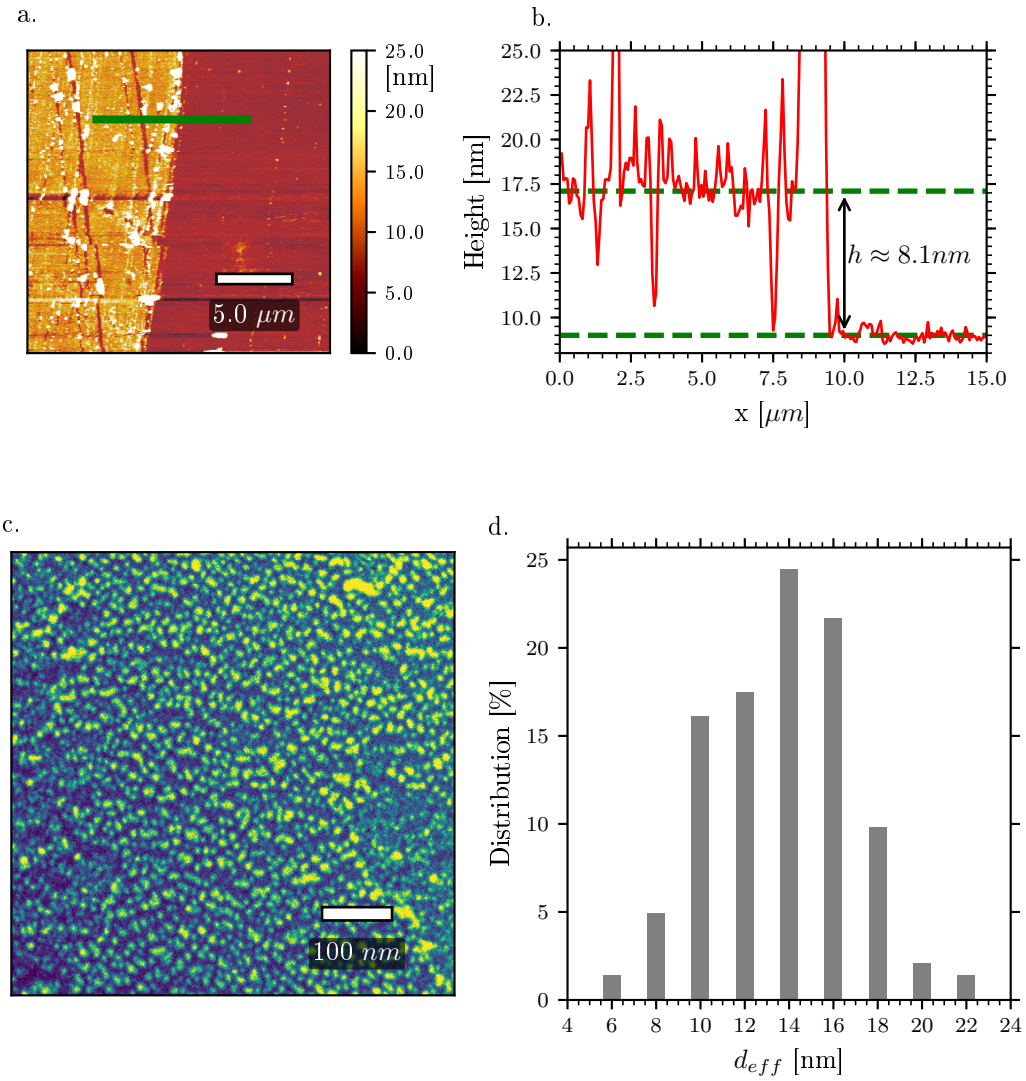

FIGURE A.9: Characterisation images of sample #6. a. shows the AFM image of the sample. The green line shows where the topography shown in b. was recorded and used to measure the height of the sample. c. shows the SEM image of the sample with d. the histogram of the average diameter of the nanoparticles shown in the SEM image.

A.6 References

[vi1] P. B. Johnson and R. W. Christy, "Optical Constants of the Noble Metals", *Physical Review B*, vol. 6, no. 12, pp. 4370–4379, 1972.

[vi2] P. Johnson and R. Christy, "Optical constants of transition metals: Ti, V, Cr, Mn, Fe, Co, Ni, and Pd", *Physical Review B*, vol. 9, no. 12, pp. 5056–5070, 1974.

[vi3] V. M. Silkin, R. Díez Muiño, I. P. Chernov, E. V. Chulkov, and P. M. Echenique, "Tuning the plasmon energy of palladium–hydrogen systems by varying the hydrogen concentration", *Journal of Physics: Condensed Matter*, vol. 24, no. 10, p. 104 021, 2012.

Appendix B

Résumé en français

B.1 Introduction générale et methodologie

Dans le premier chapitre, nous définissons les principes fondamentaux de la résonance plasmonique de surface localisée (LSPR) pour les métaux nobles. Le LSPR est défini comme l'oscillation collective des électrons de conduction excités par un champ électromagnétique. Dans la première partie du chapitre, nous présentons les modèles électrostatiques qui expliquent le concept de polarisabilité permettant le calcul de la section efficace d'absorbance. Le modèle n'est applicable que dans l'approximation quasi-statique et est principalement utilisé avec l'approximation dipolaire. La polarisabilité est basée sur la fonction diélectrique de la particule, l'indice de réfraction du milieu environnant, le volume de la particule et sa forme.

• La fonction diélectrique du métal représente sa réponse optique. C'est une conséquence des transitions électroniques dans la structure de bande et dépend donc de l'élément. Elle est généralement obtenue expérimentalement. Le modèle de Drude permet de reproduire les transitions intrabandes à partir de différents facteurs tels que la densité électronique et le libre parcours moyen de l'électron dans le métal. Avec le modèle de Drude et les transitions interbandes, il est possible d'étudier les effets de chaque paramètre sur le spectre LSPR du métal, ainsi que les effets de confinement lors de la prise en compte de petites nanoparticules.

• La fonction diélectrique du milieu est généralement considérée comme constante, cependant, dans le cas de nanoparticules déposées sur un substrat, le système n'est plus si simple. Une solution consiste à considérer une fonction diélectrique effective moyenne. Il est néanmoins possible, en utilisant l'approximation dipolaire, de considérer le dipôle image généré par la particule dans le substrat et de calculer ainsi l'interaction dipôle-dipôle. Pour aller au-delà de l'approximation dipolaire pour la prise en compte du substrat, il faut tenir compte des résonances multipolaires. Le modèle multipolaire ne peut être résolu que pour des sphéroïdes dont l'axe de révolution est normal au substrat. Dans tous les cas, l'effet du substrat, d'indice de réfraction supérieur au milieu, est d'induire un décalage bathochrome du spectre LSPR.

• Le volume de la particule affecte simplement l'intensité de la section efficace d'absorption. Cependant, il faut tenir compte d'autres effets. En effet, l'approximation quasi-statique ne s'applique que pour des particules beaucoup plus petites que la longueur d'onde incidente, ce qui limite donc les particules à quelques dizaines de nanomètres de largeur. Par contre, lorsque la taille des particules deviennent très petites, il faut maintenant prendre en compte les effets de confinement dans la fonction diélectrique de la particule, ce qui tend à élargir la résonance.

• Le dernier facteur pris en compte dans la polarisabilité est la forme de la particule. Le modèle analytique est limité à des ellipsoïdes. On peut faire valoir que ces formes idéalisées ne peuvent pas être fabriquées expérimentalement, car même les nanosphères colloïdales présentent des facettes et ne sont pas des sphères parfaites. Néanmoins, la méthodologie analytique reproduit bien les résultats expérimentaux, ce qui permet d'étudier des effets tels que les effets de forme, de changements de l'indice de réfraction ou de transferts de charges. Les formes anisotropes présentent également plusieurs pics LSPR en fonction de la direction du champ électrique considéré.

Des systèmes plus complexes tels que l'interaction particules-particules ou les particules cœur-coquille peuvent également être calculés. Pour les premiers, il est encore généralement limité à l'approximation dipolaire, qui ne prend donc pas en compte l'interaction multipolaire qui peut se produire, conduisant à des points chauds générés entre les particules. Les systèmes cœur-coquilles ellipsoïdaux peuvent également être calculés. Il y a cependant une petite conséquence du modèle à considérer, à savoir que l'épaisseur de la coque n'est pas constante. Bien que ce soit un problème mineur, il doit toujours être pris en compte

pour éviter des aberrations de calcules. D'autre part, pour calculer la réponse optique de particules plus grandes où l'approximation quasi-statique ne peut s'appliquer, on peut utiliser la théorie de Mie qui convient à un tel système. Elle tient compte de la résonance multipolaire et de la diffusion, mais reste limitée à des formes simples.

Une approche numérique est requise pour les systèmes plus complexes. La méthode décrite dans le premier chapitre est l'approximation des dipôles discrets (DDA). Cette méthode considère une matrice de dipôles individuels pour reconstruire la forme de la particule. Avec cette méthode, la forme, la composition et la taille du système de particules ne sont plus des facteurs limitants. Cependant, il y a encore des limitations. Le premier est le nombre de dipôles requis pour reproduire correctement la particule qui, lorsqu'elle est grande, augmente le temps de calcul. Par contre, trop peu de dipôles entraînent des aberrations numériques. La deuxième limitation principale est que DDA ne considère pas les éléments semi-infinis tels que les substrats. Néanmoins, il reproduit le champ électrique exalté de la particule LSPR, et permet donc le calcul des effets d'antenne qui amplifient le champ électrique sur des éléments pointus tels que les coins ou entre plusieurs particules en interaction.

Dans la deuxième partie du premier chapitre, nous discutons de l'utilisation du LSPR pour les applications de capteur. Nous avons vu qu'il y avait deux principaux types de détection: la détection indirecte et la détection directe.

• La détection indirecte a lieu lorsque les particules plasmoniques jouent uniquement le rôle de transducteur et utilise des capteurs moléculaires (aussi connus sous le nom de ligants) sélectifs adsorbés à proximité ou sur les nanoparticules pour se lier à l'analyte, ce qui modifie l'indice de réfraction dans le champ exalté du transducteur. L'avantage d'un tel système est la grande polyvalence des capteurs moléculaires et donc des analytes cibles, bien qu'il nécessite généralement une synthèse d'échantillons plus complexe.

• La détection directe utilise les particules LSPR à la fois comme transducteurs et capteurs moléculaires, l'analyte interagissant directement avec les particules. Cela limite les possibilités de détection, en particulier lors de l'utilisation de Au, bien qu'elle permette d'étudier la chimie de la particule, ce qui présente un intérêt dans les domaines tels que la catalyse.

La méthode conventionnelle de capteur LSPR consiste à utiliser la spectroscopie UV-Vis pour mesurer les décalages spectraux de la LSPR lorsque les particules sont exposées à l'analyte. Cela a cependant des limitations majeures intrinsèques. La principale est la nécessité de mesures spectrales qui nécessitent une très bonne reproductibilité. Les mesures étant absolues, celles-ci sont très sensibles aux bruits externes tels que les fluctuations de la source lumineuse, la pollution lumineuse ou les vibrations mécaniques. De plus, lors de la mesure de très petits déplacements du LSPR, la mesure nécessite également un monochromateur haute résolution avec de petites fentes micrométriques. Cela augmente le coût et l'encombrement de la méthode, tout en limitant la quantité de lumière atteignant le détecteur, ce qui conduit à un bruit élevé. Il est aussi possible d'entreprendre des mesures du signal à une longueur d'onde, bien que, en raison de la nature absolue de la mesure, la reproductibilité soit un problème presque impossible à résoudre.

Pour améliorer la sensibilité de cette méthode, des efforts ont été déployés dans la fabrication de nanoparticules présentant un facteur de mérite élevé, qui ont tendance à être plus difficiles à synthétiser et ne résolvent pas les problèmes inhérents à cette méthode spectroscopique. Les particules anisotropes associées à la spectroscopie d'anisotropie de transmission (TAS) offrent cependant une alternative qui surmonte les problèmes susmentionnés.

Les nanoparticules anisotropes présentent un LSPR dépendant de la polarisation de la lumière. Cependant, il faut distinguer l'anisotropie microscopique et macroscopique. En effet, dans ce dernier cas seulement, c'est-à-dire lorsque l'échantillon est globalement anisotrope, les deux polarisations peuvent être découplées avec une lumière polarisée. Ceci est possible soit en orientant des particules anisotropes dans la même direction, soit en organisant des particules isotropes de manière anisotrope, ex. nanochaines de sphères. En utilisant la TAS, il est possible de mesurer directement le spectre différentiel normalisé d'un tel échantillon anisotrope, ce qui présente l'avantage de ne pas être sensible par nature aux fluctuations de la source lumineuse, à la pollution lumineuse ou aux vibrations mécaniques. De plus, il est possible de surveiller en temps réel les changements d'anisotropie à une seule longueur d'onde puisque seule une modification du LSPR induira un décalage spectral facilement lié au changement d'intensité de l'anisotropie, dépassant ainsi les limites d'un monochromateur.

Dans cette thèse, la méthode TAS est utilisée conjointement avec des échantillons LSPR anisotropes pour démontrer la haute sensibilité, la reproductibilité et la stabilité de la méthode en étudiant deux cas particuliers. Le premier est l'utilisation de la méthodologie de détection directe pour analyser le mécanisme chimique de l'adsorption dissociative d'H_2 sur les nanoparticules Au qui ne peut être facilement mesuré avec une méthode spectrale conventionnelle en raison de l'effet très faible de l'hydrogène sur le changement de la LSPR de l'échantillon. Le second cas d'étude montre les capacités de détection réelles de la méthode en détectant de très faibles pressions partielles de H_2 à la fois dans un gaz porteur inerte et dans l'air en utilisant les deux approches directes (Pd) et indirectes ($\mathrm{Au/Pd}$) de détection.

B.2 Fabrication des échantillons

Dans le troisième chapitre, nous discutons la grande variété de méthodes possibles pour fabriquer des échantillons LSPR anisotropes. Cependant, les exigences que nous recherchons sont les suivantes:

- Les échantillons doivent être globalement anisotropes.
- Les échantillons doivent couvrir une grande surface du substrat pour des applications industrielles (au moins quelques millimètres carrés)
- Les métaux doivent être stables lorsqu'ils sont exposés à l'environnement, mais ne doivent pas être recouverts d'un tensioactif qui inhiberait leur réactivité pour la détection directe.
- Les particules doivent être petites pour augmenter la surface active.
- Les particules doivent être déposées sur un substrat qui doit être isotrope, de préférence transparent et chimiquement inerte.
- Les particules doivent être exposées à l'environnement ou, pour la détection indirecte, les capteurs moléculaires doivent être exposés à l'environnement tout en étant à proximité du métal LSPR.

Compte tenu de ces exigences, la méthode choisie a été le dépôt en incidence oblique sur du verre. Cette méthode consiste à évaporer le métal sous vide à un angle rasant par rapport au plan du substrat. Cette méthode donne des échantillons globalement anisotropes qui présentent un LSPR dépendant de la polarisation de la lumière. Les métaux étudiés sont l'Au et le Pd. En effet, en raison des propriétés de mouillage de l'Au sur le verre, des nanoparticules individuelles d'environ $10nm$ de largeur sont fabriquées. En ajustant l'angle de dépôt, la quantité de métal évaporé et le recuit de l'échantillon, les morphologies des particules sont changées formant des particules individuelles ou des nanorubans allongés. Cela permet d'adapter le spectre LSPR dans le domaine visible. En utilisant la méthode TAS, des spectres anisotropes

sont enregistrés, ce qui permet de suivre le signal LSPR à une longueur d'onde. En utilisant du Pd, il est également possible de fabriquer des échantillons anisotropes LSPR, cependant, en raison de la différence de propriétés mouillantes de ce métal sur le verre, les nanostructures obtenues sont des films minces discontinus mais présentant toujours une LSPR dépendant de la polarisation.

En utilisant des modèles théoriques analytiques simples, il est possible de reproduire les spectres expérimentaux pour tous les systèmes et donc de mieux comprendre l'origine du LSPR. De plus, cela permet de comprendre l'origine des changements induits dans la résonance, en raison des modifications des indices de réfraction ou de la fonction diélectrique du métal.

Bien que ces échantillons soient suffisants pour l'investigation entreprise dans les chapitres suivants, d'autres pistes pourraient être étudiées. Un aspect intéressant pourrait être l'utilisation d'une couche de protection diélectrique, telle que la silice, qui serait déposée sur la couche de métal LSPR, en plus des capteurs moléculaires qui seraient adsorbés. Cela permettrait une détection indirecte avec seulement les capteurs moléculaires exposés à l'environnement tandis que la couche de métal LSPR est protégée contre la contamination chimique. Cependant, la difficulté réside dans l'épaisseur de la couche diélectrique. En effet, les particules LSPR ne sont sensibles qu'aux variations de l'indice de réfraction dans leur voisinage proche. L'utilisation de petites nanoparticules nécessiterait une couche diélectrique de quelques nanomètres d'épaisseur qui devient assez difficile à fabriquer. Une autre solution intéressante consisterait à utiliser des alliages métalliques ou des systèmes cœur-coquille. Par exemple, l'Ag et l'Au pourraient donner l'avantage du LSPR de l'argent qui est beaucoup plus intense que celui de l'Au tout en utilisant l'Au pour réduire la réactivité de l'Ag et donner encore plus de flexibilité à la position LSPR.

Dans le chapitre suivant, les échantillons d'Au LSPR fabriqués en utilisant la méthode décrite dans ce chapitre sont utilisés conjointement avec la TAS pour étudier l'interaction de l'H_2 avec l'Au.

B.3 Interaction du dihydrogène avec des nanoparticules d'or

Dans ce travail, la spectroscopie de transmission anisotrope (TAS) est utilisée pour étudier l'interaction de H_2 avec des nanoparticules plasmoniques d'Au. La sensibilité de cette méthode permet de mesurer les décalages spectraux très fins lorsque les échantillons d'Au sont exposés à des cycles d' Ar et d'H_2 à pression atmosphérique. Cela a permis de sonder l'interaction entre l'Au et l'H_2 et de proposer un mécanisme sur le devenir de l'H_2 adsorbé après sa dissociation sur les arêtes des nanoparticules d'Au.

Les échantillons ont été préparés par évaporation à angle oblique. La caractérisation des échantillons a été réalisée par AFM (microscopie à force atomique) et MEB (microscopie électronique à balayage) afin de déterminer la morphologie moyenne des nanoparticules. La spectroscopie UV-Vis montre un dichroïsme pour les deux polarisations orthogonales par rapport à la direction d'évaporation. En effet, la polarisation parallèle à la direction d'évaporation présentait un spectre hypsochrome par rapport à celui mesuré avec une polarisation perpendiculaire à la direction d'évaporation. Le spectre TAS présente l'anisotropie de l'échantillon qui peut être utilisée pour mesurer le décalage du spectre en suivant la variation d'intensité du spectre à une seule longueur d'onde.

Des cycles d'H_2 dans l'Ar ont été réalisés sur plusieurs échantillons de particules de différentes tailles. Lors de l'exposition à l'H_2, le changement de signal est équivalent à un effet bathochrome du spectre LSPR. En revenant à l'Ar, l'anisotropie de transmission (TA) montre une réversibilité du signal au fur et à mesure de son retour à son état initial. Il est donc possible de relier l'intensité du décalage spectral à la variation de la densité électronique de conduction dans la particule. L'observation a montré que lors de l'adsorption

d'H_2 sur la particule, la densité des électrons de conduction est réduite. En mesurant quantitativement ce changement de densité pour chaque échantillon, il est possible de montrer qu'il est proportionnel à la surface moyenne des particules. Cette observation a donc permis de conclure que l'H_2 se dissocie non seulement sur les arêtes des particules d'Au comme le propose la littérature, mais diffuse également à la surface des nanoparticules. En déterminant les différentes énergies de liaison des adatomes d'H sur différentes surfaces de l'Au et en corrélant ces énergies avec la forme probable des particules, le mécanisme proposé est que l'H_2 s'adsorbe et se dissocie sur les bords des nanoparticules d'Au puis diffuse de préférence sur les facettes $Au(100)$ des particules avant de désorber.

L'analyse cinétique des décalages de signal lors de l'exposition à différentes pressions partielles d'H_2 a permis de déterminer le transfert de charge entre l'H adsorbé et l'Au. Ce dernier résultat a révélé que, à pression atmosphérique d'H_2, le transfert de charge négatif moyen de chaque atome de surface d'Au vers l'H est d'environ $-0.06e$ et que la charge rendu localisée sur chaque liaison $Au-H$ est estimée à environ $-0,2e$, ce qui n'est pas en contradiction avec la littérature théorique .

Les résultats obtenus à différentes intensités lumineuses n'ont montré aucune corrélation entre la puissance de la lumière incidente et l'amplitude du décalage, ce qui signifie que le mécanisme observé n'est pas photo-induit. Cependant, une corrélation a été mise en évidence avec la température, avec une diminution de l'amplitude du signal à mesure que la température augmentait, même si elle ne suit pas un mécanisme d'Arrhenius. Elle pourrait néanmoins s'expliquer par une réduction du temps de transit des adatomes d'H sur les facettes (100) et une augmentation de la cinétique de désorption. Cela conduirait à moins d'adatomes d'H sur les surfaces d'Au à un moment donné, donc moins de transfert de charge se produisant, donc à un décalage spectral plus petit.

B.4 Utilisation du palladium pour la détection du dihydrogène

Dans le chapitre 5, nous montrons que le Pd peut être utilisé, en conjonction avec des échantillons d'Au anisotropes, pour augmenter la sensibilité de l'échantillon à l'H_2 dans un gaz porteur inerte. Ces expériences ont également démontré que l'augmentation de la quantité de Pd augmentait la sensibilité du système à quelques ppm d'H_2. Des recherches sur les capteurs directs de Pd ont révélé que les nanostructures de Pd présentent une LSPR anisotrope pouvant être utilisée pour des applications de capteurs.

L'absorption d'H_2 conduit à la formation d'hydrure de palladium. L'isotherme révèle qu'en fonction de la pression partielle d'H_2, différentes phases se forment. La phase α correspond à une faible quantité d'H diluée dans la structure métallique, alors que la phase β correspond à une grande quantité d'H adsorbée. Entre les deux phases se trouve la phase hybride $\alpha+\beta$ obtenue sur un intervalle de pression partielle étroit autour de 1%. Quoi qu'il en soit, la formation d'hydrure métallique entraîne une modification nette de la fonction diélectrique du métal, ce qui modifie la réponse optique du matériau. En utilisant des modèles analytiques, le comportement des spectres anisotropes expérimentaux, à différents degrés d'hydrogénation, peut être facilement reproduit. Cela nous a permis de vérifier que les modifications de la réponse optique étaient bien dues à l'absorption d'hydrogène qui entraînait une modification de la fonction diélectrique du métal et non due à l'expansion connue subie par le Pd lorsque celui-ci absorbe de l'hydrogène. Cet effet s'est révélé mineur et a été négligé.

Des cycles de gaz d'H_2 dans l'Ar, à différentes pressions partielles d'H_2, ont été entrepris tout en surveillant la TA à une longueur d'onde unique. Avec cette méthode, des pressions partielles aussi basses que 0.001%, équivalant à $10ppm$ peuvent être mesurées avec une grande reproductibilité. De plus, l'échantillon se régénère spontanément lorsqu'il est purgé à l'Ar vers de son état initial. L'analyse de l'amplitude du

changement de TA, ΔS, a permis de déterminer le ratio H/Pd donnant une caractéristique quantitative à la méthode, notamment dans la phase α, ce qui est en effet le plus intéressant pour les applications de capteur.

Les temps de réponse ont été étudiés et se sont révélés fortement dépendants de la pression partielle d'H_2. Deux temps caractéristiques peuvent être distingués. D'une part, t_{detect}, c'est-à-dire le temps nécessaire pour enregistrer la présence d'H_2, fournit une informations qualitatives adaptées à la détection de fuites et à d'autres applications de sécurité. Selon la pression partielle, il était inférieur à $1s$ dans la phase β et de l'ordre de quelques dizaines de secondes dans la phase α. Par contre, t_{90}, qui correspond au temps nécessaire pour atteindre 90% du signal, donne des informations quantitatives sur la quantité d'H_2 dans le gaz porteur. Il dépend à nouveau fortement de la pression partielle. Pour la phase β, il se situe entre 4 et $30s$ alors que dans la phase α, il se situe entre 1 et 2 minutes. Ces temps de réponse sont supérieurs au seuil de $1s$ requis pour une application industrielle, mais révèlent le potentiel de la méthode car elle est utilisable pour toute pression partielle d'H_2, à température ambiante, alors que les méthodes alternatives ont montré des temps de réponse équivalents sinon meilleurs, mais ne fonctionnent que dans des intervalles de pression partielle étroits et/ou nécessitent un chauffage à quelques centaines de degrés Celsius.

Afin d'étudier le mécanisme de réaction et donc les possibilités d'amélioration, la cinétique d'absorption et de désorption de la phase α a été étudiée. Un modèle de réaction possible a été établi pour tenir compte de l'adsorption et de la désorption réversibles vers et depuis la surface métallique, ainsi que de l'absorption et du vidage du volume. Les données expérimentales ont été reproduites en considérant la pression partielle d'H_2 dans l'Ar et en ajustant les quatre constantes de cinétiques en jeu. Le modèle reproduit bien les données et a permis de reproduire de la diminution de la constante de temps pendant l'absorption lorsque la pression partielle d'H_2 diminue. Cependant, afin de mieux comprendre les mécanismes en jeu et de déterminer l'étape limitante, deux conditions limites ont été prises en compte. La première condition a été considérer que le processus limitant était la réactivité de la surface, la seconde étant la réactivité dans le volume. Compte tenu de ces considérations, il a été proposé que, pour le processus de désorption, le processus limitant est la réactivité de surface, tandis que, pour l'absorption, il s'agissait du volume. Pour améliorer le modèle, on pourrait considérer l'étape de physisorption dans le mécanisme de réaction. En effet, du fait de la présence du gaz porteur, on pourrait proposer que comme l'Ar physisorbe à la surface, il occuperait ainsi des sites réactifs nécessaires à l'adsorption dissociative de l'H_2. Cela augmente cependant la complexité du modèle et n'a pas été pris en compte à ce stade. Néanmoins, il n'est pas évident que la vitesse de réaction pourrait être augmentée car elle dépend fortement de la chimie du Pd et pas tellement de la géométrie des nanoparticules.

Des recherches préliminaires dans l'O_2 et dans l'air sec et humide ont été entreprises pour voir si le capteur de Pd simple peut être appliqué tel quel dans des conditions réelles. Les résultats révèlent une oxydation du Pd lorsqu'il est exposé à l'O_2. Cela conduit à une compétition entre l'oxydation et l'hydrogénation du métal lorsqu'il est exposé à l'H_2 dans un gaz porteur contenant de l'oxygène. L'H_2 et l'O_2 ont, tous les deux, le même effet qui est d'augmenter le TA mais avec des cinétiques différentes. L'exposition de l'échantillon à la vapeur d'eau n'a pas, au début, empêché la réactivité du Pd puisque la même quantité d'hydrogénation a été enregistrée, bien que la vitesse d'absorption ait été fortement ralentie. Cependant, une longue exposition à l'air humide a inhibé la réponse de l'échantillon à une faible pression partielle d'H_2.

Des travaux préliminaires ont également été réalisés sur l'utilisation de structure d'oxyde metalique (MOF) zif-8 comme couche protectrice contre des contaminants tels que l'eau, les hydrocarbures et l'oxygène. L'échantillon était recouvert de quelques centaines de nanomètres du MOF. Il présent une sensibilité élevée vis-à-vis de l'H_2 dans l'air par rapport à l'échantillon sans couche de MOF, bien que le MOF n'ait pas empêché l'oxydation. Des travaux supplémentaires sont nécessaires pour voir son efficacité dans l'air humide

et contaminé.

La possibilité d'associer un capteur indirect ou direct basé sur le palladium et la TAS est une piste prometteuse pour la détection d'H_2. Des travaux supplémentaires sont nécessaires pour évaluer le potentiel important de cette méthode, car des améliorations sont possibles. Une perspective prometteuse consisterait à remplacer l'appareil TAS par une lame quart d'onde et un ensemble de deux polariseurs. Ceci permettrait de simplifier le système en utilisant une LED ou une diode laser à longueur d'onde fixe, et donc de supprimer le monochromateur et la détection synchrone, tous les deux encombrants, et de permettre ainsi la miniaturisation de l'appareil. Ce point n'est mentionné que dans les perspectives de ce chapitre car aucune étude scientifique n'a été réalisée sur le sujet dans le cadre de ce travail.

Bibliography

References for Chapter 1

[i1] D. B. Harden and J. M. C. Toynbee, "VII.The Rothschild Lycurgus Cup", *Archaeologia*, vol. 97, no. December 1954, pp. 179–212, 1959.

[i2] F. E. Wagner, S. Haslbeck, L. Stievano, S. Calogero, Q. a. Pankhurst, and K. P. Martinek, "Before striking gold in gold-ruby glass", *Nature*, vol. 407, no. 6805, pp. 691–692, 2000.

[i3] R. C. Chirnside and P. M. C. Proffitt, "The Rothschild Lycurgus Cup: an analytical investigation", *Journal of Glass Studies*, vol. 5, pp. 18–23, 1963.

[i4] A. Ruivo, C. Gomes, A. Lima, M. L. Botelho, R. Melo, A. Belchior, and A. Pires de Matos, "Gold nanoparticles in ancient and contemporary ruby glass", *Journal of Cultural Heritage*, vol. 9, pp. 134–137, 2008.

[i5] M. Faraday, "The Bakerian Lecture: Experimental Relations of Gold (and Other Metals) to Light", *Philosophical Transactions of the Royal Society of London*, vol. 147, pp. 145–181, Jan. 1857.

[i6] G. Mie, "Beiträge zur Optik trüber Medien, speziell kolloidaler Metallösungen", *Annalen der Physik*, vol. 330, no. 3, pp. 377–445, 1908.

[i7] R. Gans, "ÜBER DIE FORM ULTRAMIKROSKOPISCHER SILBERTEILCHEN", *Annalen der Physik*, vol. 352, no. 10, pp. 270–284, 1915.

[i8] P. Drude, "Zur Elektronentheorie der Metalle", *Annalen der Physik*, vol. 306, no. 3, pp. 566–613, 1900.

[i9] ——, "Zur Elektronentheorie der Metalle II. Teil. Galvanomagnetische und thermomagnetische Effecte", *Annalen der Physik*, vol. 308, no. 11, pp. 369–402, 1900.

[i10] D. Pines and D. Bohm, "A Collective Description of Electron Interactions: II. Collective vs Individual Particle Aspects of the Interactions", *Physical Review*, vol. 85, no. 2, pp. 338–353, 1952.

[i11] R. Feynman, "There is plenty of room at the bottom (talk tanscript)", *Caltech Engineering and Science*, vol. 23:5, pp. 22–36, 1960.

[i12] F. Wooten, *Optical Properties of solids*. Academic press inc., 1972, ISBN: 9781483220765.

[i13] U. Kreibig and M. Vollmer, *Optical Properties of Metal Clusters*. Springer Berlin Heidelberg, 1995, ISBN: 978-3-642-08191-0.

[i14] J. D. Jackson, *Classical Electrodynamics*. New York ; London : John Wiley, 1999, ISBN: 0471431311.

[i15] C. F. Bohren and D. R. Huffman, *Adsorption and scattering of light by small particles*. New York ; London : John Wiley, 1983, ISBN: 047105772X.

[i16] F. Castro and B. Nabet, "Numerical computation of the complex dielectric permittivity using Hilbert transform and FFT techniques", *Journal of the Franklin Institute*, vol. 336, no. 1, pp. 53–64, 1999.

[i17] P.-O. Nilsson, "Determination of Optical Constants from Intensity Measurements at Normal Incidence", *Applied Optics*, vol. 7, no. 3, p. 435, 1968.

[i18] J. E. Nestell and R. W. Christy, "Optics of Thin Metal Films", *American Journal of Physics*, vol. 39, no. 3, pp. 313–320, 1971.

[i19] P. B. Johnson and R. W. Christy, "Optical Constants of the Noble Metals", *Physical Review B*, vol. 6, no. 12, pp. 4370–4379, 1972.

[i20] P. O. Nilsson, "Studies of AgIn and CuGe Alloys by Optical and Photoemission Techniques", *Physica Scripta*, vol. 1, no. 4, pp. 189–192, 1970.

[i21] G. P. Pells, "Measurement of the optical properties of alloys in ultra-high vacuum", *Journal of Scientific Instruments*, vol. 44, no. 12, pp. 997–1000, 1967.

[i22] J. E. Nestell and R. W. Christy, "Derivation of Optical Constants of Metals from Thin-Film Measurements at Oblique Incidence", *Applied Optics*, vol. 11, no. 3, p. 643, 1972.

[i23] V. M. Silkin, I. P. Chernov, P. M. Echenique, Y. M. Koroteev, and E. V. Chulkov, "Influence of hydrogen absorption on low-energy electronic collective excitations in palladium", *Physical Review B*, vol. 76, no. 24, p. 245 105, 2007.

[i24] V. M. Silkin, R. Díez Muiño, I. P. Chernov, E. V. Chulkov, and P. M. Echenique, "Tuning the plasmon energy of palladium–hydrogen systems by varying the hydrogen concentration", *Journal of Physics: Condensed Matter*, vol. 24, no. 10, p. 104 021, 2012.

[i25] C. Hogan, O. Pulci, P. Gori, F. Bechstedt, D. S. Martin, E. E. Barritt, A. Curcella, G. Prevot, and Y. Borensztein, "Optical properties of silicene, Si/Ag(111), and Si/Ag(110)", *Physical Review B*, vol. 97, no. 19, p. 195 407, 2018.

[i26] A. Marini, R. Del Sole, and G. Onida, "First-principles calculation of the plasmon resonance and of the reflectance spectrum of silver in the GW approximation", *Physical Review B*, vol. 66, no. 11, p. 115 101, 2002.

[i27] H. Ehrenreich and H. R. Philipp, "Optical Properties of Ag and Cu", *Physical Review*, vol. 128, no. 4, pp. 1622–1629, 1962.

[i28] B. R. Cooper, H. Ehrenreich, and H. R. Philipp, "Optical Properties of Noble Metals. II.", *Physical Review*, vol. 138, no. 2A, A494–A507, 1965.

[i29] H. S. Sehmi, W. Langbein, and E. A. Muljarov, "Optimizing the Drude-Lorentz model for material permittivity: Method, program, and examples for gold, silver, and copper", *Physical Review B*, vol. 95, no. 11, p. 115 444, 2017.

[i30] M. Valamanesh, Y. Borensztein, C. Langlois, and E. Lacaze, "Substrate Effect on the Plasmon Resonance of Supported Flat Silver Nanoparticles", *The Journal of Physical Chemistry C*, vol. 115, no. 7, pp. 2914–2922, 2011.

[i31] K. M. Mayer and J. H. Hafner, "Localized Surface Plasmon Resonance Sensors", *Chemical Reviews*, vol. 111, no. 6, pp. 3828–3857, 2011.

[i32] B. Luk'yanchuk, N. I. Zheludev, S. a. Maier, N. J. Halas, P. Nordlander, H. Giessen, and C. T. Chong, "The Fano resonance in plasmonic nanostructures and metamaterials", *Nature Materials*, vol. 9, no. 9, pp. 707–715, 2010.

[i33] R. Kuladeep, L. Jyothi, K. S. Alee, K. L. N. Deepak, and D. N. Rao, "Laser-assisted synthesis of Au-Ag alloy nanoparticles with tunable surface plasmon resonance frequency", *Optical Materials Express*, vol. 2, no. 2, p. 161, 2012.

[i34] L. Bossard-Giannesini, "Mesures et simulation du travail de sortie de nanoparticules d'or fonctionnalisées", PhD thesis, Sorbonne Université, 2018.

[i35] C. Goldmann, R. Lazzari, X. Paquez, C. Boissière, F. Ribot, C. Sanchez, C. Chanéac, and D. Portehault, "Charge Transfer at Hybrid Interfaces: Plasmonics of Aromatic Thiol-Capped Gold Nanoparticles", *ACS Nano*, vol. 9, no. 7, pp. 7572–7582, 2015.

[i36] P. Mulvaney, J. Pérez-Juste, M. Giersig, L. M. Liz-Marzán, and C. Pecharromán, "Drastic Surface Plasmon Mode Shifts in Gold Nanorods Due to Electron Charging", *Plasmonics*, vol. 1, no. 1, pp. 61–66, 2006.

[i37] B. G. Ershov, E. V. Abkhalimov, R. D. Solovov, and V. I. Roldughin, "Gold nanoparticles in aqueous solutions: influence of size and pH on hydrogen dissociative adsorption and Au(III) ion reduction", *Physical Chemistry Chemical Physics*, vol. 18, no. 19, pp. 13 459–13 466, 2016.

[i38] B. S. Hoener, H. Zhang, T. S. Heiderscheit, S. R. Kirchner, A. S. De Silva Indrasekara, R. Baiyasi, Y. Cai, P. Nordlander, S. Link, C. F. Landes, and W.-S. Chang, "Spectral Response of Plasmonic Gold Nanoparticles to Capacitive Charging: Morphology Effects", *The Journal of Physical Chemistry Letters*, vol. 8, no. 12, pp. 2681–2688, 2017.

[i39] A. H. Ali, R. J. Luther, C. A. Foss, and G. B. Chapman, "Optical Properties of Nanoscopic Gold Particles Adsorbed At Electrode Surfaces: the Effect of Applied Potential on Plasmon Resonance Absorption.", *Nanostructured Materials*, vol. 9, no. 5, pp. 559–562, 1997.

[i40] A. H. Ali and J. Colby, A. Foss, "Electrochemically Induced Shifts in the Plasmon Resonance Bands of Nanoscopic Gold Particles Adsorbed on Transparent Electrodes", *Journal of The Electrochemical Society*, vol. 146, no. 2, p. 628, 1999.

[i41] R. Chapman and P. Mulvaney, "Electro-optical shifts in silver nanoparticle films", *Chemical Physics Letters*, vol. 349, no. 5-6, pp. 358–362, 2001.

[i42] T. Miyazaki, R. Hasegawa, H. Yamaguchi, H. Oh-oka, H. Nagato, I. Amemiya, and S. Uchikoga, "Electrical Control of Plasmon Resonance of Gold Nanoparticles Using Electrochemical Oxidation", *The Journal of Physical Chemistry C*, vol. 113, no. 19, pp. 8484–8490, 2009.

[i43] M. Hu, D. P. Linder, M. Buongiorno Nardelli, and A. Striolo, "Hydrogen Adsorption on Platinum–Gold Bimetallic Nanoparticles: A Density Functional Theory Study", *The Journal of Physical Chemistry C*, vol. 117, no. 29, pp. 15 050–15 060, 2013.

[i44] B. T. Draine and P. J. Flatau, "Discrete-Dipole Approximation For Scattering Calculations", *Journal of the Optical Society of America A*, vol. 11, no. 4, p. 1491, 1994.

[i45] H. DeVoe, "Optical Properties of Molecular Aggregates. I. Classical Model of Electronic Absorption and Refraction", *The Journal of Chemical Physics*, vol. 41, no. 2, pp. 393–400, 1964.

[i46] E. M. Purcell and C. R. Pennypacker, "Scattering and Absorption of Light by Nonspherical Dielectric Grains", *The Astrophysical Journal*, vol. 186, p. 705, 1973.

[i47] S. B. Singham and G. C. Salzman, "Evaluation of the scattering matrix of an arbitrary particle using the coupled dipole approximation", *The Journal of Chemical Physics*, vol. 84, no. 5, pp. 2658–2667, 1986.

[i48] S. B. Singham and C. F. Bohren, "Light scattering by an arbitrary particle: a physical reformulation of the coupled dipole method", *Optics Letters*, vol. 12, no. 1, p. 10, 1987.

[i49] K. A. Willets and R. P. Van Duyne, "Localized Surface Plasmon Resonance Spectroscopy and Sensing", *Annual Review of Physical Chemistry*, vol. 58, no. 1, pp. 267–297, 2007.

[i50] J. N. Anker, W. P. Hall, O. Lyandres, N. C. Shah, J. Zhao, and R. P. Van Duyne, "Biosensing with plasmonic nanosensors", *Nature Materials*, vol. 7, no. 6, pp. 442–453, 2008.

[i51] K. Saha, S. S. Agasti, C. Kim, X. Li, and V. M. Rotello, "Gold Nanoparticles in Chemical and Biological Sensing", *Chemical Reviews*, vol. 112, no. 5, pp. 2739–2779, 2012.

[i52] D. Wild, *The Immunoassay Handbook*, Elsevier, Ed. 2005, ISBN: 0080445268.

[i53] J. Satija, N. Punjabi, D. Mishra, and S. Mukherji, "Plasmonic-ELISA: expanding horizons", *RSC Advances*, vol. 6, no. 88, pp. 85 440–85 456, 2016.

[i54] H. Chen, X. Kou, Z. Yang, W. Ni, and J. Wang, "Shape- and Size-Dependent Refractive Index Sensitivity of Gold Nanoparticles", *Langmuir*, vol. 24, no. 10, pp. 5233–5237, 2008.

[i55] B. Rožič, J. Fresnais, C. Molinaro, J. Calixte, S. Umadevi, S. Lau-Truong, N. Felidj, T. Kraus, F. Charra, V. Dupuis, T. Hegmann, C. Fiorini-Debuisschert, B. Gallas, and E. Lacaze, "Oriented Gold

Nanorods and Gold Nanorod Chains within Smectic Liquid Crystal Topological Defects", *ACS Nano*, vol. 11, no. 7, pp. 6728–6738, 2017.

[i56] The Editors of Encyclopaedia Britannica, *Anisotropy*.

[i57] R. Verre, N. Maccaferri, K. Fleischer, M. Svedendahl, N. Odebo Länk, A. Dmitriev, P. Vavassori, I. V. Shvets, and M. Käll, "Polarization conversion-based molecular sensing using anisotropic plasmonic metasurfaces", *Nanoscale*, vol. 8, no. 20, pp. 10 576–10 581, 2016.

References for Chapter 2

[ii1] D. E. Aspnes, J. P. Harbison, A. A. Studna, and L. T. Florez, "Reflectance-difference spectroscopy system for real-time measurements of crystal growth", *Applied Physics Letters*, vol. 52, no. 12, pp. 957–959, 1988.

[ii2] D. E. Aspnes and A. A. Studna, "Anisotropies in the Above—Band-Gap Optical Spectra of Cubic Semiconductors", *Physical Review Letters*, vol. 54, no. 17, pp. 1956–1959, 1985.

[ii3] G. Binnig and C. F. Quate, "Atomic Force Microscope", *Physical Review Letters*, vol. 56, no. 9, pp. 930–933, 1986.

[ii4] R. D. Rodriguez, E. Lacaze, and J. Jupille, "Probing the probe: AFM tip-profiling via nanotemplates to determine Hamaker constants from phase–distance curves", *Ultramicroscopy*, vol. 121, pp. 25–30, 2012.

[ii5] M. R. Ryder, Z. Zeng, K. Titov, Y. Sun, E. M. Mahdi, I. Flyagina, T. D. Bennett, B. Civalleri, C. S. Kelley, M. D. Frogley, G. Cinque, and J.-C. Tan, "Dielectric Properties of Zeolitic Imidazolate Frameworks in the Broad-Band Infrared Regime", *The Journal of Physical Chemistry Letters*, vol. 9, no. 10, pp. 2678–2684, 2018.

References for Chapter 3

[iii1] S. Tawfick, M. De Volder, D. Copic, S. J. Park, C. R. Oliver, E. S. Polsen, M. J. Roberts, and A. J. Hart, "Engineering of Micro- and Nanostructured Surfaces with Anisotropic Geometries and Properties", *Advanced Materials*, vol. 24, no. 13, pp. 1628–1674, 2012.

[iii2] M. C. Traub, W. Longsine, and V. N. Truskett, "Advances in Nanoimprint Lithography", *Annual Review of Chemical and Biomolecular Engineering*, vol. 7, no. 1, pp. 583–604, 2016.

[iii3] B. J. Lin, "The ending of optical lithography and the prospects of its successors", *Microelectronic Engineering*, vol. 83, no. 4-9, pp. 604–613, 2006.

[iii4] V. R. Manfrinato, L. Zhang, D. Su, H. Duan, R. G. Hobbs, E. A. Stach, and K. K. Berggren, "Resolution Limits of Electron-Beam Lithography toward the Atomic Scale", *Nano Letters*, vol. 13, no. 4, pp. 1555–1558, 2013.

[iii5] G. Q. Wallace, S. T. Read, D. M. McRae, S. M. Rosendahl, and F. Lagugné-Labarthet, "Exploiting Anisotropy of Plasmonic Nanostructures with Polarization Modulation Infrared Linear Dichroism Microscopy (μPM-IRLD)", *Advanced Optical Materials*, vol. 6, no. 6, p. 1 701 336, 2018.

[iii6] J. Boneberg, F. Burmeister, C. Schäfle, P. Leiderer, D. Reim, A. Fery, and S. Herminghaus, "The Formation of Nano-Dot and Nano-Ring Structures in Colloidal Monolayer Lithography †", *Langmuir*, vol. 13, no. 26, pp. 7080–7084, 1997.

[iii7] H. Fredriksson, Y. Alaverdyan, A. Dmitriev, C. Langhammer, D. S. Sutherland, M. Zäch, and B. Kasemo, "Hole–Mask Colloidal Lithography", *Advanced Materials*, vol. 19, no. 23, pp. 4297–4302, 2007.

[iii8] Z. Tang and A. Wei, "Fabrication of Anisotropic Metal Nanostructures Using Innovations in Template-Assisted Lithography", *ACS Nano*, vol. 6, no. 2, pp. 998–1003, 2012.

[iii9] R. Verre, N. Maccaferri, K. Fleischer, M. Svedendahl, N. Odebo Länk, A. Dmitriev, P. Vavassori, I. V. Shvets, and M. Käll, "Polarization conversion-based molecular sensing using anisotropic plasmonic metasurfaces", *Nanoscale*, vol. 8, no. 20, pp. 10 576–10 581, 2016.

[iii10] S.-W. Lee, K.-S. Lee, J. Ahn, J.-j. Lee, M.-g. Kim, and Y.-B. Shin, "Highly Sensitive Biosensing Using Arrays of Plasmonic Au Nanodisks Realized by Nanoimprint Lithography", *ACS Nano*, vol. 5, no. 2, pp. 897–904, 2011.

[iii11] S. Park and A. Böker, "Ceramic nanowrinkles via a facile replication process", *Journal of Materials Chemistry*, vol. 21, no. 32, p. 11 734, 2011.

[iii12] S. Y. Chou, "Nanoimprint lithography", *Journal of Vacuum Science & Technology B: Microelectronics and Nanometer Structures*, vol. 14, no. 6, p. 4129, 1996.

[iii13] S. J. Barcelo, W. Wu, X. Li, Z. Li, and R. S. Williams, "Nanoimprint lithography of plasmonic platforms for SERS applications", *Applied Physics A*, vol. 121, no. 2, pp. 443–449, 2015.

[iii14] Y. Yao, H. Liu, Y. Wang, Y. Li, B. Song, A. Bratkovsk, S.-Y. Wang, and W. Wu, "Nanoimprint lithography: an enabling technology for nanophotonics", *Applied Physics A*, vol. 121, no. 2, pp. 327–333, 2015.

[iii15] N. Alayo, A. Conde-Rubio, J. Bausells, X. Borrisé, A. Labarta, X. Batlle, and F. Pérez-Murano, "Nanoparticles with tunable shape and composition fabricated by nanoimprint lithography", *Nanotechnology*, vol. 26, no. 44, p. 445 302, 2015.

[iii16] T. Tomioka, S. Kubo, K. Nagase, M. Hoga, and M. Nakagawa, "Fabrication of Au nanorod and nanogap split-ring structures by reactive-monolayer-assisted thermal nanoimprint lithography involving electrodeposition", *Journal of Vacuum Science & Technology B, Nanotechnology and Microelectronics: Materials, Processing, Measurement, and Phenomena*, vol. 30, no. 6, 06FB02, 2012.

[iii17] J. Turkevich, P. C. Stevenson, and J. Hillier, "A study of the nucleation and growth processes in the synthesis of colloidal gold", *Discussions of the Faraday Society*, vol. 11, no. c, p. 55, 1951.

[iii18] M. Grzelczak, J. Pérez-Juste, P. Mulvaney, and L. M. Liz-Marzán, "Shape control in gold nanoparticle synthesis", *Chemical Society Reviews*, vol. 37, no. 9, p. 1783, 2008.

[iii19] R. Sardar, A. M. Funston, P. Mulvaney, and R. W. Murray, "Gold Nanoparticles: Past, Present, and Future", *Langmuir*, vol. 25, no. 24, pp. 13 840–13 851, 2009.

[iii20] M. C. M. Daniel and D. Astruc, "Gold nanoparticles: Assembly, supramolecular chemistry, quantum-size related properties and applications toward biology, catalysis and nanotechnology", *Chemical Reviews*, vol. 104, pp. 293–346, 2004.

[iii21] J. Pérez-Juste, B. Rodríguez-González, P. Mulvaney, and L. M. Liz-Marzán, "Optical Control and Patterning of Gold-Nanorod-Poly(vinyl alcohol) Nanocomposite Films", *Advanced Functional Materials*, vol. 15, no. 7, pp. 1065–1071, 2005.

[iii22] E. Boisselier and D. Astruc, "Gold nanoparticles in nanomedicine: preparations, imaging, diagnostics, therapies and toxicity", *Chemical Society Reviews*, vol. 38, no. 6, p. 1759, 2009.

[iii23] Z. Nie, D. Fava, E. Kumacheva, S. Zou, G. C. Walker, and M. Rubinstein, "Self-assembly of metal–polymer analogues of amphiphilic triblock copolymers", *Nature Materials*, vol. 6, no. 8, pp. 609–614, 2007.

[iii24] M. a. Correa-Duarte, J. Pérez-Juste, A. Sánchez-Iglesias, M. Giersig, and L. M. Liz-Marzán, "Aligning Au Nanorods by Using Carbon Nanotubes as Templates", *Angewandte Chemie International Edition*, vol. 44, no. 28, pp. 4375–4378, 2005.

[iii25] M. A. Correa-Duarte, N. Sobal, L. M. Liz-Marzán, and M. Giersig, "Linear Assemblies of Silica-Coated Gold Nanoparticles Using Carbon Nanotubes as Templates", *Advanced Materials*, vol. 16, no. 23-24, pp. 2179–2184, 2004.

[iii26] E. Lacaze, O. Merchiers, Y. Borensztein, and D. Coursault, "Trapping of gold nanoparticles within arrays of topological defects: evolution of the LSPR anisotropy", *Rendiconti Lincei*, vol. 26, no. S2, pp. 183–191, 2015.

[iii27] D. Coursault, J. Grand, B. Zappone, H. Ayeb, G. Lévi, N. Félidj, and E. Lacaze, "Linear Self-Assembly of Nanoparticles Within Liquid Crystal Defect Arrays", *Advanced Materials*, vol. 24, no. 11, pp. 1461–1465, 2012.

[iii28] J. H. Park and Y. L. Joo, "Tailoring nanorod alignment in a polymer matrix by elongational flow under confinement: simulation, experiments, and surface enhanced Raman scattering application", *Soft Matter*, vol. 10, no. 19, p. 3494, 2014.

[iii29] G.-W. Hsieh, J. Wang, K. Ogata, J. Robertson, S. Hofmann, and W. I. Milne, "Stretched Contact Printing of One-Dimensional Nanostructures for Hybrid Inorganic–Organic Field Effect Transistors", *The Journal of Physical Chemistry C*, vol. 116, no. 12, pp. 7118–7125, 2012.

[iii30] J. Li, S. Liu, Y. Liu, F. Zhou, and Z.-y. Li, "Anisotropic and enhanced absorptive nonlinearities in a macroscopic film induced by aligned gold nanorods", *Applied Physics Letters*, vol. 96, no. 26, p. 263 103, 2010.

[iii31] C. J. Murphy and C. J. Orendorff, "Alignment of Gold Nanorods in Polymer Composites and on Polymer Surfaces", *Advanced Materials*, vol. 17, no. 18, pp. 2173–2177, 2005.

[iii32] J. Y. Chung, A. J. Nolte, and C. M. Stafford, "Surface Wrinkling: A Versatile Platform for Measuring Thin-Film Properties", *Advanced Materials*, vol. 23, no. 3, pp. 349–368, 2011.

[iii33] A. Schweikart, A. Horn, A. Böker, and A. Fery, "Controlled Wrinkling as a Novel Method for the Fabrication of Patterned Surfaces", in *Advances in Polymer Science*, 2012, 2009, pp. 75–99, ISBN: 9781118056776.

[iii34] A. Horn, H. G. Schoberth, S. Hiltl, A. Chiche, Q. Wang, A. Schweikart, A. Fery, and A. Böker, "Nanostructured wrinkled surfaces for templating bionanoparticles—controlling and quantifying the degree of order", *Faraday Discussions*, vol. 143, p. 143, 2009.

[iii35] M. Tebbe, M. Mayer, B. a. Glatz, C. Hanske, P. T. Probst, M. B. Müller, M. Karg, M. Chanana, T. A. F. König, C. Kuttner, and A. Fery, "Optically anisotropic substrates via wrinkle-assisted convective assembly of gold nanorods on macroscopic areas", *Faraday Discussions*, vol. 181, no. 0, pp. 243–260, 2015.

[iii36] C. Hanske, M. B. Müller, V. Bieber, M. Tebbe, S. Jessl, A. Wittemann, and A. Fery, "The Role of Substrate Wettability in Nanoparticle Transfer from Wrinkled Elastomers: Fundamentals and Application toward Hierarchical Patterning", *Langmuir*, vol. 28, no. 49, pp. 16 745–16 750, 2012.

[iii37] C. Hanske, M. Tebbe, C. Kuttner, V. Bieber, V. V. Tsukruk, M. Chanana, T. A. F. König, and A. Fery, "Strongly Coupled Plasmonic Modes on Macroscopic Areas via Template-Assisted Colloidal Self-Assembly", *Nano Letters*, vol. 14, no. 12, pp. 6863–6871, 2014.

[iii38] M. Mueller, M. Tebbe, D. V. Andreeva, M. Karg, R. A. Alvarez Puebla, N. Pazos Perez, and A. Fery, "Large-Area Organization of pNIPAM-Coated Nanostars as SERS Platforms for Polycyclic Aromatic Hydrocarbons Sensing in Gas Phase", *Langmuir*, vol. 28, no. 24, pp. 9168–9173, 2012.

[iii39] L. Anghinolfi, R. Moroni, L. Mattera, M. Canepa, and F. Bisio, "Flexible Tuning of Shape and Arrangement of Au Nanoparticles in 2-Dimensional Self-Organized Arrays: Morphology and Plasmonic Response", *The Journal of Physical Chemistry C*, vol. 115, no. 29, pp. 14 036–14 043, 2011.

[iii40] L. Anghinolfi, L. Mattera, M. Canepa, and F. Bisio, "Plasmon dispersion in self-organized Au nanoparticle arrays", *Physical Review B*, vol. 85, no. 23, p. 235 426, 2012.

[iii41] R. Verre, K. Fleischer, O. Ualibek, and I. V. Shvets, "Self-assembled broadband plasmonic nanoparticle arrays for sensing applications", *Applied Physics Letters*, vol. 100, no. 3, 2012.

[iii42] R. Verre, K. Fleischer, J. F. McGilp, D. Fox, G. Behan, H. Zhang, and I. V. Shvets, "Controlled in situ growth of tunable plasmonic self-assembled nanoparticle arrays", *Nanotechnology*, vol. 23, no. 3, p. 035 606, 2012.

[iii43] R. Verre, K. Fleischer, R. G. S. Sofin, N. McAlinden, J. F. McGilp, and I. V. Shvets, "In situ characterization of one-dimensional plasmonic ag nanocluster arrays", *Physical Review B - Condensed Matter and Materials Physics*, vol. 83, no. 12, p. 125 432, 2011.

[iii44] N. Semaltianos and E. Wilson, "Investigation of the surface morphology of thermally evaporated thin gold films on mica, glass, silicon and calcium fluoride substrates by scanning tunneling microscopy", *Thin Solid Films*, vol. 366, no. 1-2, pp. 111–116, 2000.

[iii45] H. Sun, M. Yu, X. Sun, G. Wang, and J. Lian, "Effective Temperature Sensing by Irreversible Morphology Evolution of Ultrathin Gold Island Films", *The Journal of Physical Chemistry C*, vol. 117, no. 7, pp. 3366–3373, 2013.

[iii46] A. Schaub, P. Slepička, I. Kašpárková, P. Malinský, A. Macková, and V. Švorčík, "Gold nanolayer and nanocluster coatings induced by heat treatment and evaporation technique", *Nanoscale Research Letters*, vol. 8, no. 1, p. 249, 2013.

[iii47] R. Gupta, M. J. Dyer, and W. A. Weimer, "Preparation and characterization of surface plasmon resonance tunable gold and silver films", *Journal of Applied Physics*, vol. 92, no. 9, pp. 5264–5271, 2002.

[iii48] Y. He, J. Fu, and Y. Zhao, "Oblique angle deposition and its applications in plasmonics", *Frontiers of Physics*, vol. 9, no. 1, pp. 47–59, 2014.

[iii49] T.-C. Peng, W.-C. Lin, C.-W. Chen, D. P. Tsai, and H.-P. Chiang, "Enhanced Sensitivity of Surface Plasmon Resonance Phase-Interrogation Biosensor by Using Silver Nanoparticles", *Plasmonics*, vol. 6, no. 1, pp. 29–34, 2011.

[iii50] J.-X. Fu, A. Collins, and Y.-P. Zhao, "Optical Properties and Biosensor Application of Ultrathin Silver Films Prepared by Oblique Angle Deposition", *The Journal of Physical Chemistry C*, vol. 112, no. 43, pp. 16 784–16 791, 2008.

[iii51] M. Born and E. Wolf, "A homogeneous dielectric film", in *Principles of Optics*, P. Press, Ed., 3rd, 1965, pp. 60–63.

[iii52] U. Kreibig and M. Vollmer, *Optical Properties of Metal Clusters*. Springer Berlin Heidelberg, 1995, ISBN: 978-3-642-08191-0.

[iii53] R. G. Barrera, M. del Castillo-Mussot, G. Monsivais, P. Villaseor, and W. L. Mochán, "Optical properties of two-dimensional disordered systems on a substrate", *Physical Review B*, vol. 43, no. 17, pp. 13 819–13 826, 1991.

[iii54] S. Grésillon, L. Aigouy, A. C. Boccara, J. C. Rivoal, X. Quelin, C. Desmarest, P. Gadenne, V. A. Shubin, A. K. Sarychev, and V. M. Shalaev, "Experimental Observation of Localized Optical Excitations in Random Metal-Dielectric Films", *Physical Review Letters*, vol. 82, no. 22, pp. 4520–4523, 1999.

[iii55] B. Lamprecht, G. Schider, R. T. Lechner, H. Ditlbacher, J. R. Krenn, A. Leitner, and F. R. Aussenegg, "Metal Nanoparticle Gratings: Influence of Dipolar Particle Interaction on the Plasmon Resonance", *Physical Review Letters*, vol. 84, no. 20, pp. 4721–4724, 2000.

[iii56] M. O. Stetsenko, L. S. Maksimenko, S. P. Rudenko, I. M. Krishchenko, A. A. Korchovyi, S. B. Kryvyi, E. B. Kaganovich, and B. K. Serdega, "Surface Plasmon's Dispersion Properties of Porous Gold Films", *Nanoscale Research Letters*, vol. 11, no. 1, p. 116, 2016.

[iii57] R. Esteban, R. W. Taylor, J. J. Baumberg, and J. Aizpurua, "How Chain Plasmons Govern the Optical Response in Strongly Interacting Self-Assembled Metallic Clusters of Nanoparticles", *Langmuir*, vol. 28, no. 24, pp. 8881–8890, 2012.

[iii58] F. Abelès, Y. Borensztein, and T. López-Rios, "Optical properties of discontinuous thin films and rough surfaces of silver", in *Advances in Solid State Physics*, vol. 125, Springer Berlin Heidelberg, 1984, pp. 93–117.

[iii59] M. Jebari, Y. Borensztein, and G. Vuye, "Anomalous optical absorption in porous metal films", *Physica A: Statistical Mechanics and its Applications*, vol. 157, no. 1, pp. 371–376, 1989.

[iii60] T. V. Teperik, V. V. Popov, and F. J. García de Abajo, "Void plasmons and total absorption of light in nanoporous metallic films", *Physical Review B*, vol. 71, no. 8, p. 085 408, 2005.

[iii61] D. Aspnes, "Optical properties of thin films", *Thin Solid Films*, vol. 89, no. 3, pp. 249–262, 1982.

[iii62] P. Johnson and R. Christy, "Optical constants of transition metals: Ti, V, Cr, Mn, Fe, Co, Ni, and Pd", *Physical Review B*, vol. 9, no. 12, pp. 5056–5070, 1974.

References for Chapter 4

[iv1] W. L. Watkins and Y. Borensztein, "Mechanism of hydrogen adsorption on gold nanoparticles and charge transfer probed by anisotropic surface plasmon resonance", *Phys. Chem. Chem. Phys.*, vol. 19, no. 40, 2017.

[iv2] B. Hammer and J. K. Norskov, "Why gold is the noblest of all the metals", *Nature*, vol. 376, no. 6537, pp. 238–240, 1995.

[iv3] B. Hammer and J. Norskov, "Theoretical surface science and catalysis — calculations and concepts", *Advances in Catalysis*, vol. 45, pp. 71–129, 2000.

[iv4] L. Barrio, P. Liu, J. A. Rodríguez, J. M. Campos-Martín, and J. L. G. Fierro, "A density functional theory study of the dissociation of h_2 on gold clusters: Importance of fluxionality and ensemble effects", *Journal of Chemical Physics*, vol. 125, no. 16, pp. 12–16, 2006.

[iv5] A. Corma, M. Boronat, S. González, and F. Illas, "On the activation of molecular hydrogen by gold: A theoretical approximation to the nature of potential active sites.", *Chemical communications (Cambridge, England)*, no. 32, pp. 3371–3373, 2007.

[iv6] L. Stobiński, L. Zommer, and R. Duś, "Molecular hydrogen interactions with discontinuous and continuous thin gold films", *Applied Surface Science*, vol. 141, no. 3-4, pp. 319–325, 1999.

[iv7] A. G. Sault, R. J. Madix, and C. T. Campbell, "Adsorption of oxygen and hydrogen on au(110)-(1x2)", *Surface Science*, vol. 169, no. 2-3, pp. 347–356, 1986.

[iv8] M. Haruta, "When gold is not noble: Catalysis by nanoparticles", *Chemical Record*, vol. 3, no. 2, pp. 75–87, 2003.

[iv9] T. Fujitani, I. Nakamura, T. Akita, M. Okumura, and M. Haruta, "Hydrogen dissociation by gold clusters", *Angewandte Chemie - International Edition*, vol. 48, no. 50, pp. 9515–9518, 2009.

[iv10] A. Corma and H. Garcia, "Supported gold nanoparticles as catalysts for organic reactions", *Chemical Society Reviews*, vol. 37, no. 9, pp. 2096–2126, 2008.

[iv11] G. C. Bond, "Hydrogenation by gold catalysts: An unexpected discovery and a current assessment", *Gold Bulletin*, vol. 49, no. 3-4, pp. 53–61, 2016.

[iv12] M. Manzoli, A. Chiorino, F. Vindigni, and F. Boccuzzi, "Hydrogen interaction with gold nanoparticles and clusters supported on different oxides: A ftir study", *Catalysis Today*, vol. 181, no. 1, pp. 62–67, 2012.

[iv13] S. Mukherjee, F. Libisch, N. Large, O. Neumann, L. V. Brown, J. Cheng, J. B. Lassiter, E. A. Carter, P. Nordlander, and N. J. Halas, "Hot electrons do the impossible: Plasmon-induced dissociation of h_2 on au", *Nano Letters*, vol. 13, no. 1, pp. 240–247, 2013.

[iv14] S. Mukherjee, L. Zhou, A. M. Goodman, N. Large, C. Ayala-Orozco, Y. Zhang, P. Nordlander, and N. J. Halas, "Hot-electron-induced dissociation of h_2 on gold nanoparticles supported on sio_2", *Journal of the American Chemical Society*, vol. 136, no. 1, pp. 64–67, 2014.

[iv15] M. L. Brongersma, N. J. Halas, and P. Nordlander, "Plasmon-induced hot carrier science and technology", *Nature Nanotechnology*, vol. 10, no. 1, pp. 25–34, 2015.

[iv16] L. Leandro, R. Malureanu, N. Rozlosnik, and A. Lavrinenko, "Ultrathin, Ultrasmooth Gold Layer on Dielectrics without the Use of Additional Metallic Adhesion Layers", *ACS Applied Materials and Interfaces*, vol. 7, no. 10, pp. 5797–5802, 2015.

[iv17] G. A. Somorjai, *Introduction to surface chemistry and catalysis.* Nov. 1994, p. 369, ISBN: 0-471-03192-5.

[iv18] S. S. E. Collins, M. Cittadini, C. Pecharromán, A. Martucci, and P. Mulvaney, "Hydrogen spillover between single gold nanorods and metal oxide supports: A surface plasmon spectroscopy study", *ACS Nano*, vol. 9, no. 8, pp. 7846–7856, 2015.

[iv19] D. Sil, K. D. Gilroy, A. Niaux, A. Boulesbaa, S. Neretina, and E. Borguet, "Seeing is believing: Hot electron based gold nanoplasmonic optical hydrogen sensor", *ACS Nano*, vol. 8, no. 8, pp. 7755–7762, 2014.

[iv20] E. Bus, J. T. Miller, and J. A. Van Bokhoven, "Hydrogen chemisorption on Al2O3-supported gold catalysts", *Journal of Physical Chemistry B*, vol. 109, no. 30, pp. 14 581–14 587, 2005.

[iv21] P. Ferrin, S. Kandoi, A. U. Nilekar, and M. Mavrikakis, "Hydrogen adsorption, absorption and diffusion on and in transition metal surfaces: A dft study", *Surface Science*, vol. 606, no. 7-8, pp. 679–689, 2012.

[iv22] X. Shen, Y. Li, X. Liu, D. Zhang, J. Gao, and T. Liang, "Hydrogen diffusion into the subsurfaces of model metal catalysts from first principles", *Phys. Chem. Chem. Phys. Phys. Chem. Chem. Phys*, vol. 19, no. 19, pp. 3557–3564, 2017.

[iv23] L. Kristinsdóttir and E. Skúlason, "A systematic dft study of hydrogen diffusion on transition metal surfaces", *Surface Science*, vol. 606, pp. 1400–1404, 2012.

[iv24] Y. Santiago-Rodríguez, J. A. Herron, M. C. Curet-Arana, and M. Mavrikakis, "Atomic and molecular adsorption on au(111)", *Surface Science*, vol. 627, no. 2, pp. 57–69, 2014.

[iv25] E. Del, V. Gómez, S. Amaya-Roncancio, L. B. Avalle, D. H. Linares, and M. Cecilia Gimenez, "Dft study of adsorption and diffusion of atomic hydrogen on metal surfaces", *Applied Surface Science*, vol. 420, pp. 1–8, 2017.

[iv26] M. N 'dollo, P. S. Moussounda, T. Dintzer, and F. Garin, "A density functional theory study of methoxy and atomic hydrogen chemisorption on au(100) surface", *Journal of Modern Physics*, vol. 4, pp. 409–417, 2013.

[iv27] A. S. Barnard and Y. Chen, "Kinetic modelling of the shape-dependent evolution of faceted gold nanoparticles", *Journal of Materials Chemistry*, vol. 21, no. 33, p. 12 239, 2011.

[iv28] G. D. Barmparis and I. N. Remediakis, "First-principles atomistic Wulff constructions for gold nanoparticles", Nov. 2011. arXiv: 1111.4667.

[iv29] G. D. Barmparis, K. Honkala, and I. N. Remediakis, "Thiolate adsorption on Au(hkl) and equilibrium shape of large thiolate-covered gold nanoparticles", *The Journal of Chemical Physics*, vol. 138, no. 6, p. 064 702, 2013.

[iv30] T. Kizuka and N. Tanaka, "Atomic process of epitaxial growth of gold on magnesium oxide studied by cross-sectional time-resolved high-resolution electron microscopy", *Physical Review B - Condensed Matter and Materials Physics*, vol. 56, no. 16, pp. 10 079–10 088, 1997.

[iv31] S. Giorgio, M. Cabié, and C. R. Henry, "Dynamic observations of au catalysts by environmental electron microscopy", *Gold Bulletin*, vol. 41, no. 2, pp. 167–173, 2008.

[iv32] D. A. King and M. G. Wells, "Reaction mechanism in chemisorption kinetics: Nitrogen on the plane of tungsten", *Proceedings of the Royal Society A: Mathematical, Physical and Engineering Sciences*, vol. 339, no. 1617, pp. 245–269, 1974.

[iv33] H. C. Kang and W. H. Weinberg, "Dynamic monte carlo simulations of surface-rate processes", *Accounts of Chemical Research*, vol. 25, no. 6, pp. 253–259, 1992.

[iv34] X.-J. Kuang, X.-Q. Wand, and G.-B. Liu, "A comparative study between all-electron scalar relativistic calculation and all-electron calculation on the adsorption of hydrogen molecule onto small gold clusters", *Journal of Chemical Sciences*, vol. 125, no. 2, pp. 401–411, 2013.

[iv35] A. Lyalin and T. Taketsugu, "A computational investigation of h_2 adsorption and dissociation on au nanoparticles supported on tio_2 surface", *Faraday Discussions*, vol. 152, no. 0, p. 26, 2011, ISSN: 1359-6640.

[iv36] S. Zhao, Y. Ren, Y. Ren, J. Wang, and W. Yin, "Density functional study of hydrogen binding on gold and silver-gold clusters", *The Journal of Physical Chemistry A*, vol. 114, no. 14, pp. 4917–4923, 2010.

[iv37] F. Libisch, J. Cheng, and E. A. Carter, "Electron-transfer-induced dissociation of h_2 on gold nanoparticles: Excited-state potential energy surfaces via embedded correlated wavefunction theory", *Zeitschrift für Physikalische Chemie*, vol. 227, 2013.

[iv38] M. Hu, D. P. Linder, M. Buongiorno Nardelli, and A. Striolo, "Hydrogen Adsorption on Platinum–Gold Bimetallic Nanoparticles: A Density Functional Theory Study", *The Journal of Physical Chemistry C*, vol. 117, no. 29, pp. 15 050–15 060, 2013.

References for Chapter 5

[v1] B. D. Adams and A. Chen, "The role of palladium in a hydrogen economy", *Materials Today*, vol. 14, no. 6, pp. 282–289, 2011.

[v2] N. P. Brandon and Z. Kurban, "Clean energy and the hydrogen economy", *Philosophical Transactions of the Royal Society A: Mathematical, Physical and Engineering Sciences*, vol. 375, no. 2098, p. 20 160 400, 2017.

[v3] V. G. Dovì, F. Friedler, D. Huisingh, and J. J. Klemeš, "Cleaner energy for sustainable future", *Journal of Cleaner Production*, vol. 17, no. 10, pp. 889–895, 2009.

[v4] I. Dincer and C. Acar, "A review on clean energy solutions for better sustainability", *International Journal of Energy Research*, vol. 39, no. 5, pp. 585–606, 2015.

[v5] G. W. Crabtree, M. S. Dresselhaus, and M. V. Buchanan, "The Hydrogen Economy", *Physics Today*, vol. 57, no. 12, pp. 39–44, 2004.

[v6] A. Midilli and I. Dincer, "Hydrogen as a renewable and sustainable solution in reducing global fossil fuel consumption", *International Journal of Hydrogen Energy*, vol. 33, no. 16, pp. 4209–4222, 2008.

[v7] NASA, "Safety Standard for Hydrogen and Hydrogen Systems", Tech. Rep., 1997, b–37.

[v8] D. Imamura, M. Akai, and S. Watanabe, "Exploration of hydrogen odorants for fuel cell vehicles", *Journal of Power Sources*, vol. 152, no. 1-2, pp. 226–232, 2005.

[v9] T. Hübert, L. Boon-Brett, G. Black, and U. Banach, "Hydrogen sensors – A review", *Sensors and Actuators B: Chemical*, vol. 157, no. 2, pp. 329–352, 2011.

[v10] B. Sharma, A. Sharma, and J.-S. Kim, "Recent advances on H 2 sensor technologies based on MOX and FET devices: A review", *Sensors and Actuators B: Chemical*, vol. 262, pp. 758–770, 2018.

[v11] A. Katsuki and K. Fukui, "H2 selective gas sensor based on SnO2", *Sensors and Actuators B: Chemical*, vol. 52, no. 1-2, pp. 30–37, 1998.

[v12] S. J. McKeown and L. L. Goddard, "Reflective Palladium Nanoapertures on Fiber for Wide Dynamic Range Hydrogen Sensing", *IEEE Journal of Selected Topics in Quantum Electronics*, vol. 23, no. 2, pp. 263–268, 2017.

[v13] N. Javahiraly, "Review on hydrogen leak detection: comparison between fiber optic sensors based on different designs with palladium", *Optical Engineering*, vol. 54, no. 3, p. 030 901, 2015.

[v14] J. Dai, L. Zhu, G. Wang, F. Xiang, Y. Qin, M. Wang, and M. Yang, "Optical Fiber Grating Hydrogen Sensors: A Review", *Sensors*, vol. 17, no. 3, p. 577, 2017.

[v15] Y.-n. Zhang, H. Peng, X. Qian, Y. Zhang, G. An, and Y. Zhao, "Recent advancements in optical fiber hydrogen sensors", *Sensors and Actuators B: Chemical*, vol. 244, pp. 393–416, 2017.

[v16] C. Wadell, S. Syrenova, and C. Langhammer, "Plasmonic Hydrogen Sensing with Nanostructured Metal Hydrides", *ACS Nano*, vol. 8, no. 12, pp. 11 925–11 940, 2014.

[v17] G. Behzadi pour and L. Fekri aval, "Highly sensitive work function hydrogen gas sensor based on PdNPs/SiO_2/Si structure at room temperature", *Results in Physics*, vol. 7, pp. 1993–1999, 2017.

[v18] K. Aoki, "Applicability of palladium membrane for the separation of protium and deuterium", *International Journal of Hydrogen Energy*, vol. 23, no. 5, pp. 325–332, 1998.

[v19] F. D. Manchester, A. San-Martin, and J. M. Pitre, "The H-Pd (hydrogen-palladium) System", *Journal of Phase Equilibria*, vol. 15, no. 1, pp. 62–83, 1994.

[v20] P. Johnson and R. Christy, "Optical constants of transition metals: Ti, V, Cr, Mn, Fe, Co, Ni, and Pd", *Physical Review B*, vol. 9, no. 12, pp. 5056–5070, 1974.

[v21] K. Sugawa, H. Tahara, A. Yamashita, J. Otsuki, T. Sagara, T. Harumoto, and S. Yanagida, "Refractive index susceptibility of the plasmonic palladium nanoparticle: Potential as the third plasmonic sensing material", *ACS Nano*, vol. 9, no. 2, pp. 1895–1904, 2015.

[v22] I. Zorić, E. M. Larsson, B. Kasemo, and C. Langhammer, "Localized Surface Plasmons Shed Light on Nanoscale Metal Hydrides", *Advanced Materials*, vol. 22, no. 41, pp. 4628–4633, 2010.

[v23] R. Bardhan, L. O. Hedges, C. L. Pint, A. Javey, S. Whitelam, and J. J. Urban, "Uncovering the intrinsic size dependence of hydriding phase transformations in nanocrystals", *Nature Materials*, vol. 12, no. 10, pp. 905–912, 2013.

[v24] W. E. Vargas, D. E. Azofeifa, N. Clark, H. Solis, F. Montealegre, and M. Cambronero, "Parametric formulation of the dielectric function of palladium and palladium hydride thin films", *Applied Optics*, vol. 53, no. 24, p. 5294, 2014.

[v25] V. M. Silkin, R. Díez Muiño, I. P. Chernov, E. V. Chulkov, and P. M. Echenique, "Tuning the plasmon energy of palladium–hydrogen systems by varying the hydrogen concentration", *Journal of Physics: Condensed Matter*, vol. 24, no. 10, p. 104 021, 2012.

[v26] N. Clark, W. E. Vargas, and D. E. Azofeifa, "Dielectric function of Pd hydride thin films in terms of hydrogen concentration and film's thickness: A parametric formulation", *Journal of Alloys and Compounds*, vol. 645, no. S1, S320–S324, 2015.

[v27] A. L. Bugaev, A. A. Guda, K. A. Lomachenko, V. V. Srabionyan, L. A. Bugaev, A. V. Soldatov, C. Lamberti, V. P. Dmitriev, and J. A. van Bokhoven, "Temperature- and Pressure-Dependent Hydrogen Concentration in Supported PdH x Nanoparticles by Pd K-Edge X-ray Absorption Spectroscopy", *The Journal of Physical Chemistry C*, vol. 118, no. 19, pp. 10 416–10 423, 2014.

[v28] R. Kirchheim, T. M. I. Tschele, W. Kieninger, T. Mutschele, H. Gleiter, R. Birringer, and T. Koble, "Hydrogen in amorphous and nanocrystalline metals", *Materials Science and Engineering*, vol. 99, no. 1-2, pp. 457–462, 1988.

[v29] N. J. Halas, S. Lal, W.-S. Chang, S. Link, and P. Nordlander, "Plasmons in Strongly Coupled Metallic Nanostructures", *Chemical Reviews*, vol. 111, no. 6, pp. 3913–3961, 2011.

[v30] C. Langhammer, E. M. Larsson, B. Kasemo, and I. Zorić, "Indirect nanoplasmonic sensing: Ultrasensitive experimental platform for nanomaterials science and optical nanocalorimetry", *Nano Letters*, vol. 10, no. 9, pp. 3529–3538, 2010.

[v31] N. Liu, M. L. Tang, M. Hentschel, H. Giessen, and A. P. Alivisatos, "Nanoantenna-enhanced gas sensing in a single tailored nanofocus", *Nature Materials*, vol. 10, no. 8, pp. 631–636, 2011.

[v32] R. Jiang, F. Qin, Q. Ruan, J. Wang, and C. Jin, "Ultrasensitive Plasmonic Response of Bimetallic Au/Pd Nanostructures to Hydrogen", *Advanced Functional Materials*, vol. 24, no. 46, pp. 7328–7337, 2014.

[v33] C. Wadell, F. A. A. Nugroho, E. Lidström, B. Iandolo, J. B. Wagner, and C. Langhammer, "Hysteresis-Free Nanoplasmonic Pd–Au Alloy Hydrogen Sensors", *Nano Letters*, vol. 15, no. 5, pp. 3563–3570, 2015.

[v34] A. Yang, M. D. Huntington, M. F. Cardinal, S. S. Masango, R. P. Van Duyne, and T. W. Odom, "Hetero-oligomer nanoparticle arrays for plasmon-enhanced hydrogen sensing", *ACS Nano*, vol. 8, no. 8, pp. 7639–7647, 2014.

[v35] C. Wadell and C. Langhammer, "Drift-corrected nanoplasmonic hydrogen sensing by polarization", *Nanoscale*, vol. 7, no. 25, pp. 10 963–10 969, 2015.

[v36] H. Fredriksson, Y. Alaverdyan, A. Dmitriev, C. Langhammer, D. S. Sutherland, M. Zäch, and B. Kasemo, "Hole–Mask Colloidal Lithography", *Advanced Materials*, vol. 19, no. 23, pp. 4297–4302, 2007.

[v37] M. Matuschek, D. P. Singh, H.-H. Jeong, M. Nesterov, T. Weiss, P. Fischer, F. Neubrech, and N. Liu, "Chiral Plasmonic Hydrogen Sensors", *Small*, vol. 14, no. 7, p. 1 702 990, 2018.

[v38] S. Syrenova, C. Wadell, and C. Langhammer, "Shrinking-hole colloidal lithography: Self-aligned nanofabrication of complex plasmonic nanoantennas", *Nano Letters*, vol. 14, no. 5, pp. 2655–2663, 2014.

[v39] A. Tittl, P. Mai, R. Taubert, D. Dregely, N. Liu, and H. Giessen, "Palladium-Based Plasmonic Perfect Absorber in the Visible Wavelength Range and Its Application to Hydrogen Sensing", *Nano Letters*, vol. 11, no. 10, pp. 4366–4369, 2011.

[v40] H. K. Yip, X. Zhu, X. Zhuo, R. Jiang, Z. Yang, and J. Wang, "Gold Nanobipyramid-Enhanced Hydrogen Sensing with Plasmon Red Shifts Reaching ≈140 nm at 2 vol% Hydrogen Concentration", *Advanced Optical Materials*, vol. 5, no. 24, p. 1 700 740, 2017.

[v41] D. Aspnes, "Optical properties of thin films", *Thin Solid Films*, vol. 89, no. 3, pp. 249–262, 1982.

[v42] X. Q. Zeng, M. L. Latimer, Z. L. Xiao, S. Panuganti, U. Welp, W. K. Kwok, and T. Xu, "Hydrogen Gas Sensing with Networks of Ultrasmall Palladium Nanowires Formed on Filtration Membranes", *Nano Letters*, vol. 11, no. 1, pp. 262–268, 2011.

[v43] M. Johansson, E. Skúlason, G. Nielsen, S. Murphy, R. M. Nielsen, and I. Chorkendorff, "Hydrogen adsorption on palladium and palladium hydride at 1 bar", *Surface Science*, vol. 604, no. 7-8, pp. 718–729, 2010.

[v44] R. Griessen, N. Strohfeldt, and H. Giessen, "Thermodynamics of the hybrid interaction of hydrogen with palladium nanoparticles", *Nature Materials*, vol. 15, no. 3, pp. 311–317, 2016.

[v45] V. M. Silkin, I. P. Chernov, P. M. Echenique, Y. M. Koroteev, and E. V. Chulkov, "Influence of hydrogen absorption on low-energy electronic collective excitations in palladium", *Physical Review B*, vol. 76, no. 24, p. 245 105, 2007.

[v46] C. K. Gupta, *Chemical Metallurgy*. Wiley-VCH Verlag GmbH & Co. KGaA, 2004, p. 273, ISBN: 9783527602001.

[v47] N. Lopez, Z. Łodziana, F. Illas, and M. Salmeron, "When Langmuir is too simple: H_2 dissociation on Pd(111) at high coverage.", *Physical review letters*, vol. 93, no. 14, p. 146 103, 2004.

[v48] T. Mitsui, M. K. Rose, E. Fomin, D. F. Ogletree, and M. Salmeron, "Dissociative hydrogen adsorption on palladium requires aggregates of three or more vacancies", *Nature*, vol. 422, no. 6933, pp. 705–707, 2003.

[v49] W. J. Buttner, M. B. Post, R. Burgess, and C. Rivkin, "An overview of hydrogen safety sensors and requirements", *International Journal of Hydrogen Energy*, vol. 36, no. 3, pp. 2462–2470, 2011.

[v50] T. Hübert, L. Boon-Brett, V. Palmisano, and M. Bader, "Developments in gas sensor technology for hydrogen safety", *International Journal of Hydrogen Energy*, vol. 39, no. 35, pp. 20 474–20 483, 2014.

[v51] S. S. Kalanur, Y.-A. Lee, and H. Seo, "Eye-readable gasochromic and optical hydrogen gas sensor based on CuS–Pd", *RSC Adv.*, vol. 5, no. 12, pp. 9028–9034, 2015.

[v52] K. Christmann, "Interaction of hydrogen with solid surfaces", *Surface Science Reports*, vol. 9, no. 1-3, pp. 1–163, 1988.

[v53] R. Delmelle and J. Proost, "An in situ study of the hydriding kinetics of Pd thin films", *Physical Chemistry Chemical Physics*, vol. 13, no. 23, p. 11 412, 2011.

[v54] C. Nyberg and C. G. Tengstål, "Adsorption and reaction of water, oxygen, and hydrogen on Pd(100): Identification of adsorbed hydroxyl and implications for the catalytic H_2–O_2 reaction", *The Journal of Chemical Physics*, vol. 80, no. 7, pp. 3463–3468, 1984.

[v55] R. H. Radzilowski and R. D. Pehlke, "Absorption of gaseous oxygen by liquid cobalt, copper, iron and nickel", *Metallurgical Transactions B*, vol. 9, no. 1, pp. 129–137, 1978.

[v56] C. J. Smithells and C. E. Ransley, "The Diffusion of Gases through Metals", *Proceedings of the Royal Society A: Mathematical, Physical and Engineering Sciences*, vol. 150, no. 869, pp. 172–197, 1935.

[v57] F. Mackenzie and J. Mackenzie, *Our changing planet*. Prentice Hall College Div, 1995, ISBN: 0132713217.

[v58] M. Gao, M. Cho, H.-J. Han, Y. S. Jung, and I. Park, "Palladium-Decorated Silicon Nanomesh Fabricated by Nanosphere Lithography for High Performance, Room Temperature Hydrogen Sensing", *Small*, vol. 14, no. 10, p. 1 703 691, 2018.

[v59] A. Baylet, P. Marécot, D. Duprez, P. Castellazzi, G. Groppi, and P. Forzatti, "In situ Raman and in situ XRD analysis of PdO reduction and Pd○ oxidation supported on γ-Al_2O_3 catalyst under different atmospheres", *Physical Chemistry Chemical Physics*, vol. 13, no. 10, p. 4607, 2011.

[v60] D. Wang and T. B. Flanagan, "Diffusion of oxygen in Pd", *Scripta Materialia*, vol. 52, no. 7, pp. 599–601, 2005.

[v61] R. Westerström, C. Weststrate, A. Resta, A. Mikkelsen, J. Schnadt, J. Andersen, E. Lundgren, M. Schmid, N. Seriani, J. Harl, F. Mittendorfer, and G. Kresse, "Stressing Pd atoms: Initial oxidation of the Pd(110) surface", *Surface Science*, vol. 602, no. 14, pp. 2440–2447, 2008.

[v62] G. Zheng and E. Altman, "The oxidation mechanism of Pd(100)", *Surface Science*, vol. 504, pp. 253–270, 2002.

[v63] D. Zemlyanov, B. Aszalos-Kiss, E. Kleimenov, D. Teschner, S. Zafeiratos, M. Hävecker, A. Knop-Gericke, R. Schlögl, H. Gabasch, W. Unterberger, K. Hayek, and B. Klötzer, "In situ XPS study of Pd(111) oxidation. Part 1: 2D oxide formation in 10^{-3}mbar O_2", *Surface Science*, vol. 600, no. 5, pp. 983–994, 2006.

[v64] H. H. Kan and J. F. Weaver, "Mechanism of PdO thin film formation during the oxidation of Pd(111)", *Surface Science*, vol. 603, no. 17, pp. 2671–2682, 2009.

[v65] G. Ketteler, D. F. Ogletree, H. Bluhm, H. Liu, E. L. D. Hebenstreit, and M. Salmeron, "In Situ Spectroscopic Study of the Oxidation and Reduction of Pd(111)", *Journal of the American Chemical Society*, vol. 127, no. 51, pp. 18 269–18 273, 2005.

[v66] H. H. Kan, R. B. Shumbera, and J. F. Weaver, "Adsorption and abstraction of oxygen atoms on Pd(111): Characterization of the precursor to PdO formation", *Surface Science*, vol. 602, no. 7, pp. 1337–1346, 2008.

[v67] P. O. Nilsson, "Optical properties of PdO in the range of 0.5-5.4 eV", *Journal of Physics C: Solid State Physics*, vol. 12, no. 7, pp. 1423–1427, 1979.

[v68] Y.-J. Chiang, K.-C. Li, Y.-C. Lin, and F.-M. Pan, "A mechanistic study of hydrogen gas sensing by PdO nanoflake thin films at temperatures below 250°C.", *Physical chemistry chemical physics : PCCP*, vol. 17, no. 5, pp. 3039–49, 2015.

[v69] D. Zemlyanov, B. Klötzer, H. Gabasch, A. Smeltz, F. H. Ribeiro, S. Zafeiratos, D. Teschner, P. Schnörch, E. Vass, M. Hävecker, A. Knop-Gericke, and R. Schlögl, "Kinetics of Palladium Oxidation in the mbar Pressure Range: Ambient Pressure XPS Study", *Topics in Catalysis*, vol. 56, no. 11, pp. 885–895, 2013.

[v70] A. U. Ortiz, A. P. Freitas, A. Boutin, A. H. Fuchs, and F.-X. Coudert, "What makes zeolitic imidazolate frameworks hydrophobic or hydrophilic? The impact of geometry and functionalization on water adsorption", *Phys. Chem. Chem. Phys.*, vol. 16, no. 21, pp. 9940–9949, 2014.

[v71] W.-T. Koo, S. Qiao, A. F. Ogata, G. Jha, J.-S. Jang, V. T. Chen, I.-D. Kim, and R. M. Penner, "Accelerating Palladium Nanowire H_2 Sensors Using Engineered Nanofiltration", *ACS Nano*, vol. 11, no. 9, pp. 9276–9285, 2017.

[v72] L. E. Kreno, J. T. Hupp, and R. P. Van Duyne, "Metal-Organic Framework Thin Film for Enhanced Localized Surface Plasmon Resonance Gas Sensing", *Analytical Chemistry*, vol. 82, no. 19, pp. 8042–8046, 2010.

[v73] T. Tian, M. T. Wharmby, J. B. Parra, C. O. Ania, and D. Fairen-Jimenez, "Role of crystal size on swing-effect and adsorption induced structure transition of ZIF-8", *Dalton Transactions*, vol. 45, no. 16, pp. 6893–6900, 2016.

References for the Appendix

[A1] P. B. Johnson and R. W. Christy, "Optical Constants of the Noble Metals", *Physical Review B*, vol. 6, no. 12, pp. 4370–4379, 1972.

[A2] P. Johnson and R. Christy, "Optical constants of transition metals: Ti, V, Cr, Mn, Fe, Co, Ni, and Pd", *Physical Review B*, vol. 9, no. 12, pp. 5056–5070, 1974.

[A3] V. M. Silkin, R. Díez Muiño, I. P. Chernov, E. V. Chulkov, and P. M. Echenique, "Tuning the plasmon energy of palladium–hydrogen systems by varying the hydrogen concentration", *Journal of Physics: Condensed Matter*, vol. 24, no. 10, p. 104 021, 2012.

Study and development of localised surface plasmon resonance based sensors using anisotropic spectroscopy

Localised surface plasmon resonance (LSPR) is defined as the collective oscillation of the conduction electron cloud induced by an external electric field. In the case of nanoparticles composed of noble metals such as gold, silver, or copper, the resonance is located in the visible or near UV range. The polarisability of a nanoparticle is directly proportional to four key parameters: its volume, its composition, its shape and its surrounding environment. It is these properties that make LSPR useful for sensor applications.

In the case of isotropic particles, such as spheres, the LSPR spectrum shows only one absorption peak. In the case of an anisotropic particle, such as an ellipsoid, the absorption spectrum has two or more distinct peaks. If the absorption cross-section is measured with unpolarised light, multiple maxima are obtained. The key point for these type of systems is the possibility to decouple the resonances using polarised light. In this description the anisotropic system is considered microscopic, i.e. it is only made of one or two particles. In the case of a macroscopic sample, such as a colloidal solution of ellipsoids or nanorods, the absorption spectrum will always have multiple absorption maxima, and they cannot be decoupled because the sample is not globally anisotropic. On the other hand, if the sample has a global anisotropy such as aligned nanorods, or nanosphere organised in lines, it is possible to have a plasmon spectrum dependent on the light polarisation. Being able to decouple the resonances of an anisotropic sample makes it possible to measure a differential spectrum by taking the difference of the two absorption spectra. This is experimentally possible by using anisotropic transmission spectroscopy which measures the optical anisotropy. The advantage is to obtain a relative and differential spectrum more stable and reproducible. Moreover, it is now possible to follow the evolution of the optical response of the plasmonic particles no longer by measuring a spectral shift but by measuring the change in intensity of the signal at a fixed wavelength.

This method is used on two case studies which are the measurement of the interaction of dihydrogen with gold nanoparticles, as well as the detection of low partial pressure of dihydrogen in a carrier gas (argon, and air) using palladium nanoparticles, for hydrogen sensing applications

Keywords: LSPR, plasmon, sensor, hydrogen, gold, anisotropy, spectroscopy, palladium, optic, nanoparticles

Étude et développement de capteurs basés sur la résonance de plasmon de surface localisée en conjonction à la spectroscopie anisotrope

La résonance de plasmon de surface localisée (LSPR) est définie comme l'oscillation collective du nuage d'électrons de conduction induite par un champ électrique externe. Dans le cas de nanoparticules composé de métaux nobles tels que l'or, l'argent, ou le cuivre,la résonance est localisée dans le visible ou le proche UV. La polarisabilité d'une nanoparticule est directement proportionnelle à quatre paramètres clefs : son volume, sa composition, sa forme et son milieu environnant. Ce sont ces propriétés qui font que la LSPR peut être utilisée à des fin de capteur.

Dans le cas d'une particule isotrope, tel que la sphère, le spectre LSPR montre un seul pic d'absorption. Dans le cas d'une particule anisotrope, tel qu'une ellipsoïde, le spectre d'absorption a deux maxima distincts. Si on calcule la section efficace d'absorption en considèrant une lumière non polarisée, on obtient deux maxima. Le point clef de ce type de système est la possibilité de découpler les deux résonances en utilisant une lumière polarisée. Dans cette description le système anisotrope est considéré comme microscopique, c'est à dire qu'il ne s'agit que d'une ou deux particules. Dans le cas d'un échantillon macroscopique, tel qu'une solution colloïdale d'ellipsoïdes ou nanotiges, le spectre d'absorption aura toujours deux maxima d'absorption, mais ceux-ci ne pourront pas être découplés car l'échantillon n'est pas globalement anisotrope. En revanche, si l'échantillon présente une anisotropie globale telle que des nanotiges alignés, ou des nanosphères organisées en ligne, il est possible d'avoir un spectre de plasmon dépendant de la polarisation de la lumière. Être capable de découpler les résonances d'un échantillon anisotrope permet de mesurer un spectre différentiel en prenant la différence des deux spectres d'absorption. Cela est expérimentalement possible en utilisant la spectroscopie de transmission anisotrope qui permet la mesure de l'anisotropie optique. L'avantage est d'obtenir un spectre relative et différentiel donc plus stable et reproductible. De plus il est maintenant possible de suivre l'évolution de la réponse optique des particules plasmoniques, non plus en mesurant un déplacement spectral, mais en mesurant le changement d'intensité du signal à une longueur d'onde fixe.

Cette méthode est utilisée pour deux cas d'études qui sont la mesure de l'interaction du dihydrogène avec des nanoparticules d'or, ainsi que la détection de faible pression partielle de dihydrogène dans un gaz porteur (argon, et air) à l'aide de palladium, pour des applications de capteur d'hydrogène.

Mots clés : LSPR, plasmon, capteur, hydrogen, or, anisotropie, spectroscopie, palladium, optique, nanoparticules